

**GEOFORSCHUNGSZENTRUM POTSDAM**  
STIFTUNG DES ÖFFENTLICHEN RECHTS

---

# Scientific Technical Report

ISSN 1610-0956

*Retrieval of Earthquake Source Parameters in  
Inhomogeneous Anisotropic Media with Application  
to Swarm Events in West Bohemia in 2000*

DISSERTATION

ZUR ERLANGUNG DES AKADEMISCHEN GRADES  
DOKTOR DER NATURWISSENSCHAFTEN  
(DR. RER. NAT.)  
IN DER WISSENSCHAFTSDISZIPLIN GEOPHYSIK

EINGEREICHT AN DER  
MATHEMATISCH-NATURWISSENSCHAFTLICHEN FAKULTÄT  
DER UNIVERSITÄT POTSDAM

VON

*Dirk Rößler*

GEBOREN AM 28.05.1976 IN LEIPZIG

POTSDAM, AM 24. AUGUST 2006





*Ein zarter Schrei,  
ein leises Lächeln.  
Kraftvoll dein Anspruch  
und deine Sehnsucht nach  
Leben und Geborgenheit,  
deine Neugier auf  
den nächsten Moment.  
Vorbereitet,  
alles zu erkunden  
und zu erlernen,  
was sich dir bieten wird,  
alles in dich aufzunehmen  
und mit deinem Verstand  
und deinem Herzen  
zu beurteilen,  
dich einzusetzen,  
für deine Welt.*

FÜR K. UND C. S. ZUM 03.01.2006



# Zusammenfassung

Bisherige Standardverfahren zur Bestimmung der Mechanismen von Erdbeben gehen von isotropen Gesteinseigenschaften aus. Momententensoren dienen dabei der Beschreibung von Kräften, die das abgestrahlte Wellenfeld erklären. Es werden in der Regel Scherbrüche entlang von Herdflächen beobachtet. Daneben finden sich in speziellen Fällen wie in Westböhmen an der deutsch-tschechischen Grenze und anderen vulkanisch aktiven Gebieten auch Erdbeben, die anscheinend Volumenänderung aufweisen (tensile Quellen).

Im Gegensatz zur Annahme seismischer Isotropie wird Anisotropie, d.h. Richtungsabhängigkeit elastischer Parameter, als Eigenschaft der Erdkruste und des Mantels häufig beobachtet, wie z.B. auch in Westböhmen. Anisotropie führt im Vergleich zu isotropen Medien zur Veränderung der Wellenamplituden und -polarisierungen und zum Aufspalten von Scherwellen.

In der vorliegenden Arbeit werden der Einfluss seismischer Anisotropie auf wahre oder scheinbar auftretende tensile Quellanteile untersucht und Erdbebenmechanismen unter Berücksichtigung seismischer Anisotropie bestimmt. Es wird gezeigt, dass der Momententensor und die Abstrahlmuster eines Scherbruches im anisotropen Medium denen eines tensilen Bruches im isotropen Medium ähneln können. Umgekehrt treten Ähnlichkeiten tensiler Beben in anisotropen Gesteinen mit Scherbrüchen in isotropen Medien auf. Damit existieren Mehrdeutigkeiten beobachteter tensiler Quellanteile. Die Effekte von Anisotropie hängen von der Orientierung des Bruches und vom Grad der Anisotropie ab. Außerdem beeinflusst Anisotropie das Moment eines Bebens.

Die Orientierung von Herdflächen kann auch dann verlässlich bestimmt werden, wenn man Isotropie statt Anisotropie annimmt und die Spektren von Kompressionswellen verwendet. Bei Hinzunahme der Spektren von Scherwellen treten hierbei jedoch größere Probleme auf. Beschränkt sich Anisotropie auf das Medium in unmittelbarer Quellnähe, können dessen elastische Eigenschaften aus Momententensoren verschieden orientierter Beben abgeleitet werden.

Beispiele zeigen, dass die tensilen Quellanteile, welche für Schwarmbeben in Westböhmen im Jahr 1997 beobachtet wurden, nicht allein durch moderate Anisotropie erklärt werden können. Weiterhin wurden früher beobachtete Momententensoren induzierter Beben nahe der Kontinentalen Tiefbohrung (KTB), BR Deutschland, unter Annahme anisotroper Eigenschaften reinterpretiert. Die Beben werden einheitlich als Scherbrüche charakterisiert, obwohl deren Momententensoren tensile Bestandteile enthalten, die als scheinbar angesehen werden.

Diese Resultate verdeutlichen die Notwendigkeit, seismische Anisotropie zu berücksichtigen, um tensile Anteile von Erdbeben eindeutig zu bestimmen. Ein daher neu entwickelter Inversionsalgorithmus wurde getestet, erfolgreich auf 112 Erdbeben angewandt und deren Herdparameter ermittelt. Dabei wurden isotrope und anisotrope Geschwindigkeitsmodelle verwendet. Die untersuchten Beben ereigneten sich während der letzten intensiven Schwarmepisode im Jahr 2000 in Westböhmen. Die bestimmten Lokalmagnituden der Beben liegen zwischen 1,6 und 3,2. Die Herdflächenlösungen sind zueinander ähnlich und durch linkslateralen Versatz auf steil einfallenden, Nord-Süd orientierten Bruchflächen gekennzeichnet. Die Fallwinkel nehmen oberhalb 8,4 km Tiefe an Steilheit ab.

Zusammen mit dem Momententensor, wurde die Slip Inklinationswinkel, d.h. der Winkel zwischen Bruchrichtung und der Senkrechten zur Bruchfläche, als wichtiger Parameter zur Quantifizierung von Volumenänderungen in der Quelle abgeleitet. Für über 60% der betrachteten Erdbeben werden tensile Quellanteile mit Volumenvergrößerung beobachtet. Die tensilen Komponenten zeigen Abhängigkeiten von Herdzeit und -ort. Sie sind zu Beginn des Schwarms sowie in Tiefen unterhalb 8,4 km besonders signifikant und nehmen später an Bedeutung ab.

Abgeleitete Hauptspannungsachsen enthalten P Achsen mit nordwestlicher und T Achsen mit südwestlicher Streichrichtung. Sie ähneln denen in Mitteleuropa. Es werden tiefenabhängige Fallwinkel beobachtet. Die Änderungen erfolgen für die P Achsen graduell von 50° hin zu flacheren Fallwinkeln bei tieferen Beben. Sie erfolgen jedoch abrupt für die T Achsen von etwa 8° oberhalb einer Tiefe von etwa 8,4 km zu 21° einfallend unterhalb dessen.

Mit dieser Arbeit werden erstmals zeitliche und räumliche Veränderungen tensiler Quellanteile und Spannungszustände im Vogtland für Erdbeben im Jahr 2000 beobachtet. Diese haben auch dann Bestand, wenn seismische Anisotropie berücksichtigt wird. Sie können durch Fluide erklärt werden, die in die Bruchflächen eindringen.

## Summary

Currently used standard techniques for the retrieval of earthquake source mechanisms assume isotropic rock properties. By means of moment tensors, equivalent forces acting at the source are used to explain the radiated wavefield. Usually, shear sources have been observed. Besides, in certain areas such as in West Bohemia at the German-Czech border and other volcanic areas earthquakes have been reported that apparently comprise additional volumetric changes (tensile earthquakes).

In contrast to the assumption of isotropy, anisotropy, i.e. directional dependence of elastic parameters, has been often observed as a property of the earth's crust and mantle, such as in West Bohemia. In comparison to isotropic media, anisotropy causes changes in wave amplitudes and polarisations, and shear-wave splitting.

In this work, effects of seismic anisotropy on true or apparent tensile source components of earthquakes are investigated. Earthquake source parameters are determined considering anisotropy. It is shown that moment tensors and radiation patterns due to shear sources in anisotropic media may be similar to those of tensile sources in isotropic media. Conversely, similarities between tensile earthquakes in anisotropic rocks and shear sources in isotropic media may exist. As a consequence, the interpretation of tensile source components is ambiguous. The effects that are due to anisotropy depend on the orientation of the earthquake source and the degree of anisotropy. In addition, the moment of an earthquake is influenced by anisotropy.

The orientation of fault planes can be reliably determined even if isotropy instead of anisotropy is assumed and if the spectra of the compressional waves are used. Greater difficulties arise when the spectra of shear waves are additionally included. If anisotropy is restricted to the region in the vicinity of the source, the anisotropic elastic properties may be determined from retrieved moment tensors of differently oriented sources.

Examples show that the tensile source components determined for events in West Bohemia in 1997 can only partly be attributed to the effects of moderate anisotropy.

Furthermore, moment tensors determined earlier for earthquakes induced at the German Continental Deep Drilling Program (KTB) were reinterpreted under assumption of anisotropic rock properties near the borehole. The events can be consistently identified as shear sources, although their moment tensors comprise tensile components that are considered to be apparent.

These results show the necessity to consider anisotropy if a unique determination of tensile source parameters is desired. Therefore, a new inversion algorithm has been developed, tested, and successfully applied to 112 earthquakes. Their source mechanisms have been retrieved using isotropic and anisotropic velocity models. The earthquakes occurred during the most recent intense swarm episode in West Bohemia in 2000. The determined local magnitudes are in the range between 1.6 and 3.2. Fault-plane solutions are similar to each other and characterised by left-lateral faulting on steeply dipping, roughly North-South oriented rupture planes. Their dip angles decrease above a depth of about 8.4 km.

Together with the moment tensor the slip inclination, i.e. the angle between the direction of rupture and the normal to the fault plane, is retrieved as an important parameter to quantify volume changes at the source. Tensile source components indicating positive volume changes are found for more than 60% of the considered earthquakes. Their size depends on source time and location. They are significant at the beginning of the swarm and at depths below 8.4 km but they decrease in importance later in the course of the swarm.

Determined principle stress axes include P axes striking Northeast and T axes striking Southeast. They resemble those found earlier in Central Europe. However, depth-dependence in plunge is observed. Plunge angles of the P axes decrease gradually from  $50^\circ$  towards shallow angles with increasing depth. In contrast, the plunge angles of the T axes change rapidly from about  $8^\circ$  above a depth of 8.4 km to  $21^\circ$  below this depth.

By this thesis, spatial and temporal variations in tensile source components and stress conditions have been reported for the first time for swarm earthquakes in West Bohemia in 2000. They also persist, when anisotropy is assumed and can be explained by intrusion of fluids into the opened cracks during tensile faulting.



# Contents

<b>1</b>	<b>Introduction</b>	<b>3</b>
1.1	Motivation and scope of this study . . . . .	3
1.2	Description of seismic point sources . . . . .	5
1.2.1	Equivalent forces . . . . .	6
1.2.2	Properties of the source tensor . . . . .	9
1.2.3	Properties of the moment tensor . . . . .	10
1.3	Excitation of body waves by seismic point sources . . . . .	14
1.3.1	Radiation due to moment-tensor sources in isotropic media . . . . .	15
1.3.2	Radiation due to moment-tensor sources in anisotropic media . . . . .	17
1.3.3	Numerical implementation . . . . .	21
1.4	Geoscientific observations in the Vogtland/West Bohemia . . . . .	22
1.4.1	Tectonic evolution . . . . .	22
1.4.2	Observations of fluids . . . . .	23
1.4.3	Observations of gravity . . . . .	25
1.4.4	Seismic structure and observations of anisotropy . . . . .	25
1.4.5	Observations of seismicity . . . . .	27
<b>2</b>	<b>Moment tensors and radiation patterns</b>	<b>32</b>
2.1	Introduction . . . . .	32
2.2	Theoretical background . . . . .	33
2.3	Effects of anisotropy on point-source radiation . . . . .	36
2.4	Case study: Modeling of effects in the W-Bohemian earthquake region . . . . .	42
2.5	Conclusions . . . . .	46
<b>3</b>	<b>Source retrieval assuming isotropy</b>	<b>48</b>
3.1	Introduction . . . . .	49
3.2	Theory . . . . .	49
3.3	Synthetic example . . . . .	52
3.4	Generalisation . . . . .	57
3.4.1	Properties of generated moment tensors . . . . .	57
3.4.2	Properties of retrieved moment tensors . . . . .	57
3.5	Interpretation of moment tensors for events at the KTB borehole . . . . .	63
3.6	Inversion for elastic constants in the source area . . . . .	64
3.7	Discussion . . . . .	67
<b>4</b>	<b>Source retrieval assuming anisotropy</b>	<b>70</b>
4.1	Introduction . . . . .	71
4.2	Inversion scheme . . . . .	71
4.3	Source retrieval for an earthquake from West Bohemia . . . . .	74
4.4	Discussion and conclusions . . . . .	86
4.5	Appendix . . . . .	87
4.5.1	Equations for source retrieval . . . . .	87
4.5.2	Slip and fault normal from the source tensor . . . . .	87
4.5.3	Parameters of seismic stations in West Bohemia in 2000 . . . . .	88
<b>5</b>	<b>Earthquake source parameters in West Bohemia in 2000</b>	<b>89</b>



5.1	Data selection . . . . .	89
5.2	Data preparation . . . . .	90
5.3	Computation of synthetic seismograms . . . . .	90
5.4	Retrieved source parameters . . . . .	91
5.4.1	Misfit reduction . . . . .	93
5.4.2	Size of events . . . . .	93
5.4.3	Fault-plane solutions . . . . .	94
5.4.4	Tensile source components . . . . .	95
5.4.5	Properties of determined moment tensors . . . . .	99
5.4.6	Interpretation of source parameters . . . . .	101
5.5	Reliability of determined source parameters . . . . .	102
5.5.1	Jackknife and bootstrap tests . . . . .	103
5.5.2	Uncertainties due to simplified assumptions . . . . .	105
5.6	Principle directions of the local stress field . . . . .	107
<b>6</b>	<b>Discussion and conclusions</b>	<b>109</b>
6.1	Source components in anisotropic media . . . . .	109
6.2	Implications from swarm earthquakes in West Bohemia . . . . .	110
6.3	Outlook . . . . .	113
	<b>Acknowledgments</b>	<b>114</b>
	<b>Bibliography</b>	<b>115</b>
<b>A</b>	<b>Glossary</b>	<b>129</b>
<b>B</b>	<b>Elastic constants and model specifications</b>	<b>131</b>
B.1	Isotropic media . . . . .	132
B.2	Description of weak-anisotropy parameters . . . . .	132
B.3	Generic transversely isotropic models . . . . .	133
B.4	Models I and II for West Bohemia . . . . .	135
B.5	Model III for West Bohemia . . . . .	137
B.6	Anisotropy model at the KTB borehole . . . . .	138
<b>C</b>	<b>Source retrieval in West Bohemia</b>	<b>140</b>
C.1	Station information . . . . .	140
C.2	Hypocentre parameters . . . . .	141
C.3	Fault-plane solutions, principle stress axes, and matched polarities . . . . .	145
C.4	Determined seismic moments, local magnitudes, and potencies . . . . .	152
C.5	Determined slip inclinations and rupture planes . . . . .	155
C.6	Determined moment-tensor components . . . . .	160
C.7	Bootstrap tests for events in the West Bohemia . . . . .	165
C.8	Standard deviations for retrieved source parameters . . . . .	176
C.9	Source parameters determined by means of MTINVERS . . . . .	181
C.10	Principle stress axes in West Bohemia for models I, II, and III . . . . .	183
	<b>Curriculum Vitae</b>	<b>187</b>

# 1 Introduction

## 1.1 Motivation and scope of this study

Earthquakes have an enormous hazard potential for human society by the generation of destructive ground motions and/or Tsunamis. Indicating dynamic processes within our dynamically active planet earth, they occur at tectonic plate boundaries, within continents, in volcanic regions or deep in the earth's mantle. Furthermore, humans themselves are responsible for some seismic events such as mine collapses (e.g. the rock burst near Teutschenthal/Halle, FR Germany, 1996, *Tittel et al.*, 2001), underground nuclear explosions, quarry blasts or earthquakes induced by extraction of hydrocarbons. Accurate characterisation of earthquakes contributes to assess potential hazards and to constrain other geoscientific observations. Indisputable detection of nuclear explosions in the frame of the comprehensive nuclear-test-ban-treaty has a vast social and political impact. These tasks require a profound physical understanding of the mechanisms of seismic sources. Therefore, determination of earthquake source parameters is a major geoscientific subject and topic of current intensive research.

Seismic sources are commonly described by equivalent force models. The moment tensor - being special case - represents seismic sources that are equivalent to couples of forces. It is derived from observations of body- and surface-wave seismograms, namely their polarities, amplitudes, amplitude ratios, or complete seismograms. Hereby, isotropic medium properties are usually assumed. However, indicated by directional variations of wave travel-times and shear-wave splitting seismic anisotropy has been identified in many regions of the earth's crust and mantle. Seismic anisotropy causes complexity in wavefields and may obscure the moment tensor of an earthquake. Considering isotropy instead of anisotropy states a simplification of the model. It may have an impact on retrieval and interpretation of source models.

For most tectonic earthquakes, material failure by shearing along a fault surface within the crust or the mantle is observed. Such seismic sources are called shear sources. They are described by the double-couple components of moment tensors. In addition to double-couple components, non-double-couple moment-tensor components have been frequently reported. They are often attributed to noisy data and/or to effects that are due to mismodelling of the wavefield by unknown earth's structure. In other cases, mainly in regions of earthquake swarm activity or in volcanic areas, they are related to volumetric source changes that may happen by additional opening or closure of the fault surface during faulting. These events are called tensile earthquakes. Possible scenarios causing such phenomena include magmatic dyke intrusion or injection of high-pressure fluids into a fault during rupturing. Moreover, complex source geometries, collapses of cavities, events due to sudden mineral-phase changes in the earth's mantle, and explosion-type sources such as quarry blasts or underground nuclear explosions are candidates to produce non-double-couple moment-tensor components.

As an example, seismic anisotropy and large non-double-couple moment-tensor components have been reported for many events in the swarm earthquake area Vogtland/West Bohemia at the German-Czech border in Central Europe. Observations of local seismicity and the content of gas springs indicate migration of fluids that rise up. Fluids possibly played an important role for the initiation of the earthquake swarm in 2000 and for the spatiotemporal distribution of events. Such fluids have also been

frequently related to changes in pore pressure that may control earthquake triggering and that may lead to non-shear source components. However, because anisotropy has not been considered so far during source retrieval, the existence of real tensile source components in the Vogtland/West Bohemia is questioned here.

Therefore, the aim and subject of this work is a study of effects that are due to seismic anisotropy on real or apparent non-shear source components and the accurate determination of tensile components for earthquakes in anisotropic media. Their robust interpretation is an important issue because they allow for a variety of interpretations and tectonic implications. It is to be clarified if observed non-double components in moment tensors of events in West Bohemia may be equally explained as artefacts of seismic anisotropy near the earthquake source and/or along the ray path or if they can also be supported when anisotropy is considered.

To study this issue in detail, influences of anisotropy on moment tensors and radiated body-wave amplitudes due to combinations of special cases of anisotropy and synthetic point sources are investigated in Section 2.

Assuming more general conditions, effects of anisotropy on moment tensors due to shear and tensile sources are studied systematically in Section 3. Synthetic waveforms radiated from sources in different anisotropic media are generated exploiting asymptotic ray theory for anisotropic media. They are inverted for the moment tensors and the fault orientations. These quantities are compared with those of the true sources that were originally used for waveform generation. Hereby, standard inversion techniques are applied assuming isotropy instead of anisotropy. Moment tensors retrieved earlier at the KTB borehole, FR Germany, are re-interpreted in terms of their faulting mechanism under assumption of observed anisotropy.

In Section 4, an inversion algorithm is developed to retrieve the geometry of dislocation point sources in general inhomogeneous anisotropic media. The algorithm is tested and applied to one event that occurred during the earthquake swarm in the Vogtland/West Bohemia in 2000.

Exploiting the new inversion algorithm, source parameters for 112 major events of this swarm are determined in Section 5. Much attention is paid to quantify possible tensile source components as well as their spatial and temporal variations. Making assumptions on structural models including differences in anisotropy and data quality, the significance of the observed parameters is assessed.

Section 6 finally summarises conclusions of this work and discusses implications for West Bohemia.

Abbreviations and symbols frequently utilised herein are listed in Appendix A. Continuitive or supplementary explanations and information on data and results of this work that are of further interest can be found in Appendices B and C. Closed descriptions of used velocity models and elastic parameters are given in Appendix B. Tables and figures in Appendix C summarise details of seismic stations, hypocentres, and source parameters retrieved for events in West Bohemia and highlight further aspects of source parameters and of the local stress field.

Sections 2, 3, and 4 contain contributions that have been published or are submitted for publication in the scientific literature. Therefore, these parts can be seen as ‘stand-alone’ work. Essential theory and geoscientific facts are only shortly resumed and

referenced therein. However, many details of the theory that are useful for a profound understanding are missing. They are presented in a comprehensive form in Sections 1.2 and 1.3. A more elaborate introduction to geoscientific observations made earlier in the Vogtland/West Bohemia and that further challenge and justify this study is given in Section 1.4. Repetition of some formulae and facts is thus inevitable in some parts of this thesis. I wish the disposed reader may excuse this redundancy. Referenced in these sections, findings of others are used extensively to outline a modern state of the art. Note that the region of the Vogtland/West Bohemia is sometimes also conveniently referred to as Vogtland or West Bohemia.

## 1.2 Description of seismic point sources

In earthquake seismology, a general seismic dislocation source is often described by a model of a planar fault surface and a slip across the fault. In this model fault and slip may have any orientation. By rapid faulting a seismic wavefield is radiated from the source that can be recorded on the earth's surface. If the extension of the source is small compared to the observed wavelengths of the radiated wavefield, we speak of an effective point source (*Aki and Richards, 2002*). In this work only point sources are considered.

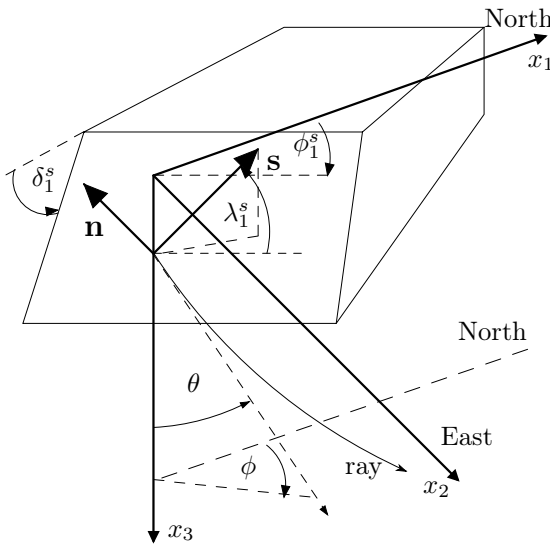


Figure 1.1: Definition of the coordinate system ( $NEZ \Leftrightarrow x_1x_2x_3$ ) and the angles that define dislocation on a fault (strike:  $0 \leq \Phi_1^s \leq 2\pi$ , dip:  $0 \leq \delta_1^s \leq \pi/2$ , rake:  $-\pi \leq \lambda_1^s \leq \pi$ ), after *Aki and Richards (2002)*. The strike forms an angle with the fault dipping down to the right of the strike direction. Strike and azimuth  $\phi$  are measured in clockwise direction from North, the dip is measured down from the horizontal, and the rake is measured in the fault plane as the angle between the direction of strike and slip. Vectors  $\mathbf{n}$  and  $\mathbf{s}$  are the fault normal and the direction of the slip, respectively. Angles  $\phi$  and  $\theta$  describe the direction of the departing ray.

The orientation of the fault and the projection of the slip onto the fault-plane are given by the angles of strike  $\Phi_1^s$ , dip  $\delta_1^s$ , and rake  $\lambda_1^s$  (see Fig. 1.1 for a definition of these angles). Three categories are commonly used to characterise shear sources by the sense of the dislocation, namely, strike-slip faulting, normal faulting, and reverse faulting (see Fig. 1.2, *Lay and Wallace, 1995; Scholz, 2002*). For strike-slip faulting, the two sides of a fault move horizontally relative to each other ( $\lambda_1^s = 0^\circ, 180^\circ$ ) and in addition  $\delta_1^s = 90^\circ$  for vertical strike slip. Left-lateral (sinistral) slip occurs when, looking in strike direction, the left side of the fault is offset towards the point of observation. Offset in opposite direction is called right-lateral (dextral). Faulting with a vertical component of relative faulting is called dip-slip faulting. For  $\lambda_1^s = 90^\circ$ , shortening occurs and the hanging wall moves upwards causing reverse faulting. Similarly, normal faulting is connected to  $\lambda_1^s = -90^\circ$ , extension, and downwards movement of the hanging wall.

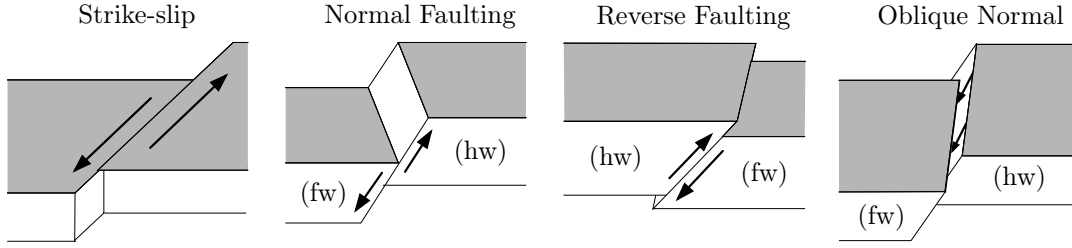


Figure 1.2: Examples of the end-member styles of faulting for different slip orientations. The position of the hanging wall and the foot wall of the fault are indicated by (hw) and (fw), respectively. The relative dislocation along the fault is indicated by arrows.

Where  $\lambda_1^s$  has values different from these cases the motion is called oblique slip. The dominant character of the event is described by concatenating appropriate terms, e.g. left-lateral oblique normal faulting.

More general, the geometry and the size of a dislocation point source can be described by the unit vector that points normal to the fault, the normal to the fault plane  $n_i$ , the direction of the slip  $s_i$ , the length of the slip  $s$ , and the area of the fault  $A_0$  (see Fig. 1.3). The slip vector  $s'_i$  is given as  $s'_i = ss_i$ . The quantity  $sA_0$  is also called the potency (*Ben-Zion, 2001; Aki and Richards, 2002*). Note that  $A_0 \neq 0$  for point sources. The slip inclination  $\delta$  refers to the angle between  $n_i$  and  $s_i$ . This description includes dislocation sources with volumetric components.

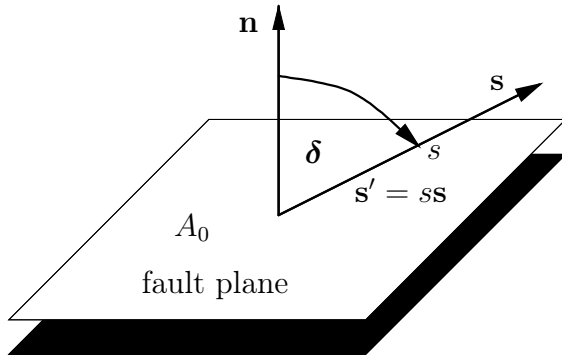


Figure 1.3: Geometry of a dislocation source described by the normal to the fault plane  $n_i$ , the slip direction  $s_i$ , the size of the slip  $s$ , and the area of the fault  $A_0$ . Fault normal and slip direction can point in any direction forming an angle  $\delta$ , the slip inclination. The product  $sA_0$  is called potency and  $s'_i$  is the slip vector. For volumetric source components  $\delta \geq 90^\circ$ . Otherwise, pure shearing occurs.

### 1.2.1 Equivalent forces

The dislocation process is regarded as a sudden change in the stress-strain relations (see Appendix B) that causes rapid changes in the stress field. The resulting disequilibrium leads to the radiation of waves. In the absence of external forces and disregarding effects due to gravity the Navier-Stokes equation in the frequency domain relates causative forces at point  $\mathbf{x}_0$  to the displacement  $u_i$  at point  $\mathbf{x}$  (*Ben-Menahem et al., 1991; Julian et al., 1998*)

$$\rho\omega^2 u_j + \frac{\partial}{\partial x_i} \left( c_{ijkl} \frac{\partial u_k}{\partial x_l} \right) = -\delta(\mathbf{x} - \mathbf{x}_0) \delta_{jm} f_m(\omega), \quad (1.1)$$

where  $c_{j k p q}$  is the elastic tensor that describes the elastic properties in the surrounding of the source (see *Aki and Richards, 2002*, and Appendix B),  $\rho$  density, and  $\omega$  is the angular frequency. The  $f_m$  have the form of a body-force density. Equation (1.1) is

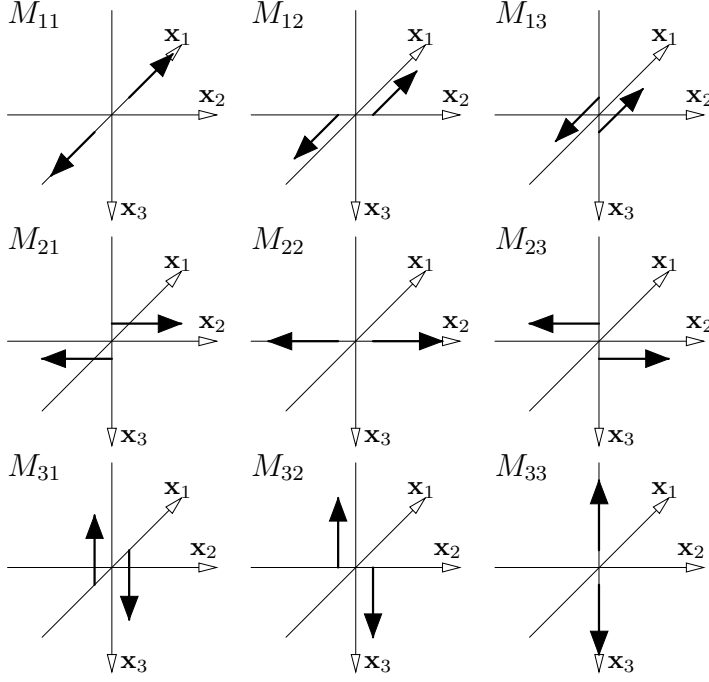


Figure 1.4: The moment-tensor components represent nine force couples. They are required to obtain equivalent forces for a generally oriented dislocation point source in anisotropic media (after *Aki and Richards, 2002*).

valid in general inhomogeneous anisotropic elastic media. A Green's tensor  $G_{np}$  can be defined as the response of the medium between  $\mathbf{x}$  and  $\mathbf{x}_0$  due to a unidirectional unit  $\delta$ -Dirac impulse in space and time such that  $u_j = G_{jm}f_m$

$$\rho \frac{\partial^2 G_{jm}}{\partial t^2} - \frac{\partial}{\partial x_i} \left( c_{ijkl} \frac{\partial G_{km}}{\partial x_l} \right) = -\delta(\mathbf{x} - \mathbf{x}_0) \delta_{jm} \delta(t - t_0). \quad (1.2)$$

The response of the earth due to the internal forces  $f_m$  at point  $\mathbf{x}_0$  and time  $\tau$  at the source is a solution to (1.1) (*Aki and Richards, 2002*)

$$u_i(\mathbf{x}, t) = \int \int \int_V G_{ij}(\mathbf{x}, t - \tau, \mathbf{x}_0, 0) * f_j(\mathbf{x}_0, \tau) d\mathbf{x}_0^3, \quad (1.3)$$

where  $u_i(\mathbf{x}, t)$  are the components of the displacement at point  $\mathbf{x}$  and time  $t$ ;  $*$  is the convolution symbol. By Taylor expansion about the source position (1.3) becomes

$$u_i(\mathbf{x}, t) = G_{ij}(\mathbf{x}, t - \tau, 0, 0) * F_j(\tau) + G_{ij,k}(\mathbf{x}, t - \tau, 0, 0) * M_{jk}(\tau) + \dots, \quad (1.4)$$

where higher-order terms are assumed to be negligibly small. The net forces  $F_j(\tau)$  are forces due to effects of gravity and mass advection (*Julian et al., 1998*) and  $M_{jk}$  is the second-order moment tensor that describes a superposition of 9 elementary force couples (see Fig. 1.4). Assuming zero net torque due to the source, the moment tensor is symmetric about the diagonal. If net forces  $F_j(t)$  and higher-order terms are neglected, (1.4) reads

$$u_i(\mathbf{x}, t) = G_{ij,k}(\mathbf{x}, t - \tau, 0, 0) * M_{jk}(\tau). \quad (1.5)$$

The displacement that is due to a dislocation source with slip  $s'_i = ss_i$  across a fault surface  $\Sigma$  is found as a solution to (1.1) (*Aki and Richards, 2002*)

$$u_i(\mathbf{x}, t) = \int_{-\infty}^{\infty} d\tau \int \int_{\Sigma} c_{jkpq} s'_p(\mathbf{x}_0, \tau) n_q \frac{\partial}{\partial x_{0k}} G_{ij}(\mathbf{x}, t - \tau; \mathbf{x}_0, 0) d\Sigma. \quad (1.6)$$

Partial integration over  $d\tau$  in (1.6) and using relation (1.2) yields (*Aki and Richards, 2002; Dahm, 1993*)

$$u_i(\mathbf{x}, t) = \int \int_{\Sigma} m_{jk}(\mathbf{x}_0, \tau) * G_{ij,k}(\mathbf{x}, t - \tau; \mathbf{x}_0, 0) d\Sigma, \quad (1.7)$$

where  $G_{np,q}$  is the spatial derivative of  $G_{np}$  with respect to  $x_{0q}$ . The quantities

$$m_{jk}(\mathbf{x}_0, \tau) = c_{j k p q} s'_p(\mathbf{x}_0, \tau) n_q \quad (1.8)$$

define the components of the moment density tensor in general anisotropic media. They are required to obtain the equivalent force model to explain the wavefield due to a general dislocation source. For an effective point source the contributions from all  $d\Sigma$  to the radiated wavefield are approximately in phase and the whole surface  $\Sigma$  is considered as a system of couples at one point.

The moment tensor of a dislocation point source in general anisotropic media is defined as (see Fig. 1.4)

$$M_{jk}(\tau) = \int \int_{\Sigma} m_{jk}(\mathbf{x}_0, \tau) d\Sigma = c_{j k p q} s_p n_q s A_0 h(\tau). \quad (1.9)$$

In (1.9) it is assumed that all components of the moment tensor share the same time-dependence,  $M_{jk}(\tau) = M_{jk} h(\tau)$ , which is expressed by the source-time function  $h(\tau)$  ( $h(0) = 0$  and  $h(\infty) = 1$ ). The time it takes  $h(t)$  to reach the maximum is called the rise time. Then (1.5) and (1.7) read (*Aki and Richards, 2002*)

$$u_i(\mathbf{x}, t) = M_{jk} h(\tau) * G_{ij,k}(\mathbf{x}, t - \tau; \mathbf{x}_0, 0). \quad (1.10)$$

The spatial derivative of  $G_{ij,k}$  is formed by its partial derivatives (*Dahm, 1993*)

$$G_{ij,k}(\mathbf{x}, t - \tau; \mathbf{x}_0, 0) = \frac{\partial G_{ij}}{\partial x_l} \frac{\partial x_l}{\partial x_{0k}} + \frac{\partial G_{ij}}{\partial t} \frac{\partial t}{\partial x_{0k}}. \quad (1.11)$$

Due to spherical divergence of waves that are radiated from point sources the second term on the right-hand side of (1.11) decays with distance  $r$  from the source as  $G_{ij} r^{-1}$  (*Dahm, 1993; Aki and Richards, 2002*). The first term on the right-hand side of (1.11) decays with higher order of  $r$ . Therefore, at large distances ( $r > \lambda/(2\pi)$ , where  $\lambda$  is the considered wavelength, *Wielandt, 2001*) amplitudes of the second term will dominate the first term and

$$G_{ij,k}(\mathbf{x}, t - \tau; \mathbf{x}_0, 0) \approx \frac{\partial G_{ij}}{\partial t} \frac{\partial t}{\partial x_{0k}} = \dot{G}_{ij} p_k, \quad (1.12)$$

where  $p_k$  is the slowness vector. Equation (1.12) is the far-field approximation of (1.11). The far-field approximation is used to re-write (1.10)

$$\begin{aligned} u_i(\mathbf{x}, t) &= M_{jk} h(\tau) * \dot{G}_{ij}(\mathbf{x}, t - \tau; \mathbf{x}_0, 0) p_k \\ &= M_{jk} \dot{h}(\tau) * G_{ij}(\mathbf{x}, t - \tau; \mathbf{x}_0, 0) p_k. \end{aligned} \quad (1.13)$$

It shows that the displacement due to a wave in the far-field is proportional to the rise time of the source.

If the considered periods of the Green's functions are large compared to the source duration, a Taylor expansion of (1.13) about the source time  $\tau^0$  with  $0 \leq \tau^0 \leq \tau^\infty$  is useful. Neglecting terms of higher order, the expansion reads (Nabalek, 1984; Dahm, 1993)

$$u_i(\mathbf{x}, t) = M_{jk}^0 h(\infty) G_{ij}(\mathbf{x}, t - \tau_0; \mathbf{x}_0, 0) p_k + M_{jk}^0 \dot{G}_{ij}(\mathbf{x}, t - \tau_0; \mathbf{x}_0, 0) p_k \int_0^\infty \dot{h}(\tau) (\tau - \tau_0) d\tau. \quad (1.14)$$

$\tau_0$  can be chosen such that the integral in (1.14) disappears (Dahm, 1993)

$$u_i(\mathbf{x}, t) = M_{jk}^0 G_{ij}(\mathbf{x}, t; \mathbf{x}_0, 0) p_k. \quad (1.15)$$

$M_{jk}^0$  is an approximation of  $M_{jk}$ . Note that equation (1.15) provides a linear relation between the forces acting at the source and the displacement field. If the medium that determines the Green's functions is appropriately known and sufficient data are available, retrieval of  $M_{jk}^0$ ,  $\mathbf{x}_0$ , and  $\tau_0$  is feasible.

### 1.2.2 Properties of the source tensor

Substituting the parameters  $s_i$ ,  $n_i$ , and  $sA_0$  that define the geometry of a point source by the source tensor  $D_{pq}$ , Eq. (1.9) can be written as

$$M_{jk} = c_{jkpq} D_{pq}. \quad (1.16)$$

The source tensor  $D_{pq}$  is formed by the dyadic product of the slip vector and the fault normal (see Fig. 1.3)

$$D_{pq} = \frac{1}{2} s A_0 \begin{pmatrix} 2\sigma_1 & \sigma_2 & \sigma_3 \\ \sigma_2 & 2\sigma_4 & \sigma_5 \\ \sigma_3 & \sigma_5 & 2\sigma_6 \end{pmatrix}, \quad (1.17)$$

where  $\sigma_i$  are the elements of the source vector

$$\boldsymbol{\sigma}^T = (s_1 n_1, s_1 n_2 + s_2 n_1, s_1 n_3 + s_3 n_1, s_2 n_2, s_2 n_3 + s_3 n_2, s_3 n_3). \quad (1.18)$$

A singular value decomposition of  $D_{pq}$  in (1.17) yields the eigenvalues (compare Vavryčuk, 2005)

$$\nu_1 = \frac{sA_0}{4} (\mathbf{s} + \mathbf{n}) \cdot (\mathbf{s} + \mathbf{n}), \quad \nu_2 = 0, \quad \nu_3 = \frac{sA_0}{4} (\mathbf{s} - \mathbf{n}) \cdot (\mathbf{s} - \mathbf{n}). \quad (1.19)$$

Because  $n_i n_i = s_i s_i = 1$ , the eigenvalues take the form

$$\nu_1 = \frac{sA_0}{2} (s_i n_i + 1), \quad \nu_2 = 0, \quad \nu_3 = \frac{sA_0}{2} (s_i n_i - 1). \quad (1.20)$$

The corresponding normalised eigenvectors are

$$\mathbf{e}_1 = \frac{\mathbf{s} + \mathbf{n}}{|\mathbf{s} + \mathbf{n}|}, \quad \mathbf{e}_2 = \frac{\mathbf{s} \times \mathbf{n}}{|\mathbf{s} \times \mathbf{n}|}, \quad \mathbf{e}_3 = \frac{\mathbf{s} - \mathbf{n}}{|\mathbf{s} - \mathbf{n}|}, \quad (1.21)$$



where  $\times$  is the vectorial cross product and  $|\mathbf{x}|$  denotes the length of a vector  $x_i$ . Equations (1.19)-(1.21) are used to determine the slip direction  $s_i$ , the fault normal  $n_i$ , and the potency  $sA_0$  from a given source tensor (1.17)

$$\mathbf{s} = \frac{\mathbf{e}_1\sqrt{\nu_1} + \mathbf{e}_3\sqrt{|\nu_3|}}{|\mathbf{e}_1\sqrt{\nu_1} + \mathbf{e}_3\sqrt{|\nu_3|}|}, \quad \mathbf{n} = \frac{\mathbf{e}_1\sqrt{\nu_1} - \mathbf{e}_3\sqrt{|\nu_3|}}{|\mathbf{e}_1\sqrt{\nu_1} - \mathbf{e}_3\sqrt{|\nu_3|}|}, \quad sA_0 = \nu_1 - \nu_3. \quad (1.22)$$

However, it is not possible to distinguish between  $s_i$  and  $n_i$  from observations of waveforms. This ambiguity arises from the symmetry of the source tensor and the wavefield that is radiated from such a seismic source (see Section 1.3). Two conjugate fault planes always exist that are described by the same source tensor. For pure shear in isotropic media they correspond to the nodal planes in the symmetric P-wave radiation pattern (see Section 1.3). Rupturing on these two surfaces can equally explain the observed wavefield. Without further information it is therefore impossible to distinguish between the fault plane on which the rupture occurred (principle fault plane) and the conjugate fault plane (auxiliary fault plane). The orientations of these two surfaces are given by the angle of strike  $\Phi_1^s/\Phi_2^s$ , dip  $\delta_1^s/\delta_2^s$ , and rake  $\lambda_1^s/\lambda_2^s$  (subscripts  $_1$  and  $_2$  refer to the rupture plane and the auxiliary fault plane, respectively). Following *Aki and Richards (2002)*, these quantities are calculated as the planes perpendicular to the slip direction  $s_i$  and the fault normal  $n_i$ , respectively (compare Fig. 1.1). Since  $s_i$  and  $n_i$  are generally oriented, retrieved fault planes can form any angle and are not necessarily perpendicular to each other.

The angle between the slip direction and the fault normal is called the slip inclination  $\delta$  with  $\cos(\delta) = |s_i n_i|$ . It is calculated from the eigenvalues of  $D_{ij}$  in (1.20)

$$\cos(\delta) = \frac{\nu_1 + \nu_3}{\nu_1 - \nu_3}. \quad (1.23)$$

If the slip vector lies within the fault plane, the source has the type of a shear source where the volume around the source does not change during faulting. Then,  $\mathbf{n} \perp \mathbf{s}$  and  $\delta = 90^\circ$ . When a combination of shear source and tension crack occurs the slip is directed off the fault plane and  $\delta \geq 90^\circ$ . Here, volumetric source changes occur. For  $\delta < 90^\circ$  the slip vector points out of the fault plane and the crack opens. Consequently, closure of the crack is connected with  $\delta > 90^\circ$ . This type of source is called tensile earthquake (e.g. *Vavryčuk, 2001*). Expressions (1.16)-(1.23) are later used in Sections 4 and 5 to describe geometric properties of events in the Vogtland.

### 1.2.3 Properties of the moment tensor

The model of dislocation point sources allows simple geometric interpretation of the source. However, the moment tensor describes more generally the force model that acts on the source during rupturing. By that, source types that are not included in the dislocation model, such as explosions, can be described. In isotropic media  $c_{j k p q}$  is given by only 2 independent elastic moduli, the Lamé parameters  $\lambda$  and  $\mu$  (see Appendix B) and the moment tensor (1.9) for a general dislocation point source simplifies to

$$M_{jk} = \lambda s_p n_p \delta_{jk} s A_0 + \mu (s_j n_k + s_k n_j) s A_0 \quad (1.24)$$

For pure shear sources, it reads

$$M_{jk} = \mu (s_j n_k + s_k n_j) s A_0 \quad (1.25)$$

An extension to the general dislocation model is given by *Dufumier and Rivera (1997)*

$$M_{jk} = \lambda s_p n_p \delta_{jk} s A_0 + \mu (s_j n_k + s_k n_j) s A_0 + E \delta_{jk}, \quad (1.26)$$

where  $E$  is an isotropic component of non-tectonic nature. Note that the extension is equivalent for sources in anisotropic media. By (1.26) mixed sources that consist of a dislocation component and an explosion or implosion can be described. Coupling occurs between the Lamé parameters and  $E$ .

In isotropic media the radiated wavefield due to shear faulting is explained by two conjugate force couples. Shear sources are therefore also called double-couple sources. Similarly, shear faulting on two conjugate faults produces exactly the same moment tensor. For this reason two fault-plane solutions are obtained from moment tensors that are determined for earthquakes. Concerning the identification of the rupture plane and the auxiliary plane, the same ambiguity exists for the moment tensor of a dislocation source and the source tensor. The fault-plane on which the actual rupture occurs must be identified from other observations such as the distribution of aftershocks or seismicity prior to the determined event.

The scale of a seismic event can be described, for instance, by the scalar seismic moment  $M_0$  (*Aki and Richards, 2002*), the total seismic moment  $M_T$  (*Silver and Jordan, 1982*), the moment magnitude  $M_w$ , the local magnitude  $M_L$  and other magnitudes scales that are based on amplitude observations of body and surface waves (see *Bormann, 2002*, for a more complete description)

$$\begin{aligned} M_0 &= \mu s A_0, \text{ for shear sources,} \\ M_T &= \sqrt{\sum_{j,k} M_{jk} M_{jk} / 2}, \\ M_w &= 2/3(\log M_0 - 9.1). \end{aligned} \quad (1.27)$$

For shear (double-couple) sources in isotropic media  $M_0 = M_T$ . A local magnitude scale  $M_L$  for the Vogtland is given as (*Hainzl and Fischer, 2002*)

$$M_0 = 10^{11.265 + 1.052 M_L}. \quad (1.28)$$

The total seismic moment provides physical scaling for earthquake sources whereas magnitudes are based on empirical relations. They are influenced by local effects and effects due different frequencies used for their determination, e.g., magnitude saturation (*Aki and Richards, 2002; Bormann, 2002*). However, the seismic moment has a simple shortcoming by the dependence on the elastic moduli in the surrounding of the source. Therefore, the potency  $s A_0$  in (1.22) has been suggested as another useful scaling parameter for the description of the size of a seismic source (*Ben-Zion, 2001; Aki and Richards, 2002*). Provided the stress drop during faulting is known and a circular fault plane can be assumed, the radii  $r$  of the fault area can be approximated by the relation (*Scholz, 2002*)

$$M_0 = 16/7 \Delta \sigma r^3. \quad (1.29)$$

Geometric properties of the source that is described by the moment tensor are obtained by a decomposition of the moment tensor. It can be uniquely decomposed into the deviatoric  $M_{ij}^{DEV}$  and the isotropic moment tensor  $M_{ij}^{ISO}$  (ISO) (see e.g.

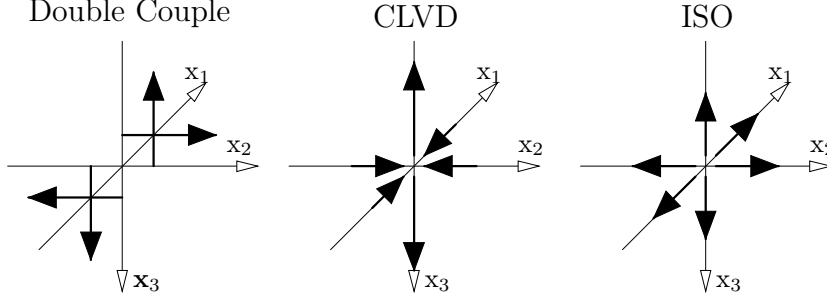


Figure 1.5: Possible orientations of moment-tensor components. The double couple is formed of 2 force couples. The compensated linear vector dipole (CLVD) consists of one large force couple with twice the strength of the two other force couples that point in the opposite direction with respect to the source. For a positive CLVD component the large force couple is directed away from the source. Directions are reversed for a negative CLVD component. The isotropic moment tensor (ISO) is given by three force couples of equal strength. The force couples point radially away from the source for positive sign of the isotropic moment-tensor component (explosion) and towards the source for a negative sign (implosion).

*Aki and Richards, 2002*). However, further decomposition of  $M_{ij}^{DEV}$  is non-unique and several methods exist, see Figure 3 in *Julian et al. (1998)* for an overview or *Silver and Jordan (1982)*, *Jost and Herrmann (1989)*, and *Vavryčuk (2002)*. They include decomposition into the double-couple  $M_{ij}^{DC}$  (DC) and the compensated-linear-vector-dipole component  $M_{ij}^{CLVD}$  (CLVD) or into a major and minor double couple ( $M_{ij}^{MAJ}$  and  $M_{ij}^{MIN}$ ) such that

$$\begin{aligned} M_{ij} &= M_{ij}^{ISO} + M_{ij}^{DEV} \\ &= M_{ij}^{ISO} + M_{ij}^{DC} + M_{ij}^{CLVD} \\ &= M_{ij}^{ISO} + M_{ij}^{MAJ} + M_{ij}^{MIN}. \end{aligned} \quad (1.30)$$

In this work the decomposition suggested by *Knopoff and Randall (1970)* is used. It makes the major axis of the CLVD coincide with the corresponding axis of the DC such that both components share the same P and T axes (*Julian et al., 1998*)

$$\begin{pmatrix} \nu'_1 \\ \nu'_2 \\ \nu'_3 \end{pmatrix} = M^{DC} \begin{pmatrix} 0 \\ -1 \\ 1 \end{pmatrix} + M^{CLVD} \begin{pmatrix} -1/1 \\ -1/2 \\ 1 \end{pmatrix}, \quad (1.31)$$

where  $\nu'_i$  are the eigenvalues of the deviatoric moment tensor ( $|\nu'_1| \leq |\nu'_2| \leq |\nu'_3|$ ),  $M^{DC} = \nu'_1 - \nu'_2$ , and  $M^{CLVD} = -2\nu'_1$ . The moment-tensor components are compared by their size to the moment of the complete moment tensor *Vavryčuk (2002)*

$$\begin{aligned} \text{ISO} &= \frac{1}{3} \frac{\text{Tr}(\mathbf{M})}{|\nu'_{max}|} \times 100\%, \\ \text{CLVD} &= -2 \frac{\nu'_{min}}{|\nu'_{max}|} (100\% - |\text{ISO}|), \\ \text{DC} &= 100\% - |\text{ISO}| - |\text{CLVD}|, \end{aligned} \quad (1.32)$$

with  $|\text{ISO}| + |\text{DC}| + |\text{CLVD}| = 100\%$ . In (1.32)  $\text{Tr}(\mathbf{M})$  is the trace of  $M_{ij}$ . It is calculated from the eigenvalues  $\nu_i$  of  $M_{ij}$  ( $\text{Tr}(\mathbf{M}) = \nu_1 + \nu_2 + \nu_3$ ). Consequently, the eigenvalues

of  $M_{ij}^{DEV}$  are  $\nu'_i = \nu_i - \text{Tr}(\mathbf{M})/3$ . Subscripts  $_{|min|}$  and  $_{|max|}$  refer to the minima and the maxima of the absolute values of  $\nu_i$  and  $\nu'_i$ .

By the definition of the moment tensor, see (1.9) and (1.26), coupling occurs between the elastic moduli of the medium at the source and the parameters describing the geometry of a source. Therefore, moment tensors for sources in anisotropic media may be more complicated than in isotropic media.

In isotropic media double-couple moment tensors represent shearing on a fault plane where the slip lies within the fault plane (see Fig. 1.5 and #1, Tab. 1.1). The force model of an isotropic moment tensor is equivalent to an explosive or implosive source (see Fig. 1.5). For crustal earthquakes it can be also indicative of pore-pressure changes during faulting or faulting on a non-planar fault plane. Implosional source mechanisms have been found and associated with collapse of cavities in mines (*Stickney and Sprenke, 1993*). The CLVD is more difficult to interpret and is often attributed to effects of noise in the data or inappropriate representation of the velocity model (see Fig. 1.5 and *Julian et al., 1998*). However, it can be also due to transformational faulting caused by sudden mineral phase changes (*Kawasaki, 1991; Kirby et al., 1991*), tensile faulting due to high-pressure fluids (*Kanamori et al., 1993; Foulger et al., 2004*), faulting on non-planar fault planes, or composite events with faulting on different fault planes (see #5, Tab. 1.1). The latter may form ring faults with anomalous moment tensors and large CLVD (*Sipkin, 1986b; Ekström, 1994; Nettles and Ekström, 1998*). If the net-volumetric effects due to tensile faulting are compensated by implosive sources or injection of fluids, the isotropic components may be small or insignificant and only the compensated-linear-vector-dipole components remain (see *Foulger and Long, 1984; Kanamori et al., 1993*, and #7 in Tab. 1.1). Large non-double-couple moment-tensor components including isotropic and CLVD components have been reported for volcanic areas and areas of earthquake swarms (see e.g. *Julian et al., 1997; Miller et al., 1998; Dahm et al., 2000; Horálek et al., 2000b; Foulger et al., 2004; Dziak et al., 2006; Templeton and Dreger, 2006*). See also (*Julian et al., 1998*) for an overview on non-double-couple earthquakes.

For tensile sources in isotropic media different  $v_p/v_s$  ratios cause variation in the moment-tensor components. Hereby, the isotropic components are most sensitive (see Tab. 1.1 for examples). In addition, properties of the moment-tensor components may differ for sources in anisotropic and isotropic media. The interpretation of the moment tensor may be difficult if inappropriate elastic properties near the source are assumed. The moment-tensor components may be further influenced by the co-existence of dislocation and non-dislocation sources (compare (1.26) and Tab. 1.1). Effects that are due to anisotropic elastic material properties on moment tensors of dislocation sources and consequences for their interpretation are discussed in Sections 2 and 3. The discussion is not prerecorded here.

Calculations of net-volume changes  $\delta V$  due to volume sources depend on the source model itself, on the elastic properties at the source and on the assumed equivalent force system representing volume change (*Müller, 1973; Julian, 1983; Müller, 2001; Richards and Kim, 2005*). Assuming a spherically symmetric, explosive, or implosive source in an isotropic medium gives (*Müller, 1973*)

$$\delta V = M^{ISO}/(\lambda + 2\mu), \quad (1.33)$$

where  $M^{ISO}$  is the isotropic moment.

Table 1.1: Moment-tensor components (1.32) for exemplary sources in isotropic media and different  $v_p/v_s$  ratios. Sources #1-#4 are dislocation sources (see Eqs. (1.25), (1.24)). Source #1: pure shear source. The percentage of moment-tensor components is independent of  $v_p/v_s$ . Sources #2-#4: tensile dislocations (crack opening,  $\delta \approx 79^\circ$ ). Moment-tensor components depend on  $v_p/v_s$ . Source #5: composite source consisting of 2 shear dislocations on different fault planes. Sources #6-#7 are composed of a dislocation source and an additional isotropic source component  $E$  (see Eq. (1.26)). Source #6: shear source plus an explosive source.  $E$  has the strength of the double-couple that is due to the shear source. Source #7: the same tensile source as for #2-#4 plus an implosive source that compensates the isotropic moment-tensor component of the dislocation source. Orientation of the simple dislocation source component: fault normal  $n_i = (0, 1, 0)$ , slip vectors  $s'$  are given separately.

no.	source specification	DC [%]	ISO [%]	CLVD [%]	$v_p/v_s$ $v_p/v_s$
#1	$s_i = (1, 0, 0)$	100.0	0.0	0.0	$\forall v_p/v_s$
#2	$s'_i = (1, 0.2, 0)$	62.1	7.7	20.2	$\sqrt{2.5}$
#3		57.7	23.5	18.8	$\sqrt{3}$
#4		52.2	30.8	17.0	$\sqrt{3.75}$
#5	$s_i^{(1)} = (-\frac{1}{2}, \frac{1}{2}, \frac{1}{\sqrt{2}}), n_i^{(1)} = (\frac{1}{2}, -\frac{1}{2}, \frac{1}{\sqrt{2}})$ $s_i^{(2)} = (-\frac{1}{\sqrt{2}}, 0, \frac{1}{\sqrt{2}}), n_i^{(2)} = (\frac{1}{\sqrt{2}}, 0, \frac{1}{\sqrt{2}})$	70.7	0.0	29.3	$\sqrt{3}$
#6	$s'_i = (1, 0, 0), E = M_{12}$	50.0	50.0	0.0	$\forall v_p/v_s$
#7	$s'_i = (1, 0.2, 0), E = -1/3M_{12}$	75.5	0.0	24.5	$\sqrt{3}$

The principle axes of the local stress field at the source,  $\sigma_i$ , are determined by the directions of the eigenvectors of the moment tensor that is retrieved for the source. The pressure axis  $\sigma_1$  (P axis) and the tension axis  $\sigma_3$  (T axis) point in the directions of the eigenvectors corresponding to the smallest and the largest eigenvalue, respectively. Perpendicular to  $\sigma_1$  and  $\sigma_3$ , the  $\sigma_2$  axis (B axis) has the orientation of the eigenvector that corresponds to the intermediate eigenvalue of  $\mathbf{M}$ . The three principle stress directions also represent the principle axes of the stress tensor  $\tau_{ij}$  (see Appendix B).

### 1.3 Excitation of body waves by seismic point sources

If rupturing at a source is fast enough, seismic waves that can be recorded on the earth's surface are excited and radiated (*Aki and Richards, 2002*). As a condition

$$|\mathbf{k}| \leq \omega/c, \quad (1.34)$$

where  $c$  is the phase velocity of the generated wave along the rupture plane,  $\omega$  is the considered circular frequency, and  $\mathbf{k}$  is the projection of the wavenumber vector on the rupture plane. Otherwise, if rupturing is too slow, waves are trapped in the source region. Therefore, slow rupturing and mineral creeping are not detected within the frequency band of modern seismographs.

Equations (1.1) and (1.10) provide the base to predict the wavefield that is generated by seismic sources. However, only for few specific cases the Green's functions and their derivatives can be determined analytically. If no analytic solution exists, they are either solved by complete methods such as finite difference approaches or by approximate solutions such as ray methods. Ray methods provide good asymptotic approximations to the wavefield. The theory is well established and has found a wide

range of applications (see e.g. Červený *et al.*, 1977; Kendall, 1991; Gajewski, 1993; Pšenčík and Teles, 1996; Červený, 2001; Aki and Richards, 2002). In ray methods it is assumed that body-wave propagation is controlled by local properties, such as wave speed, along a ray path that is defined by Snell's law. Several rays form wavefronts. They arrive with amplitudes that are determined by the geometrical spreading of the ray between the source and the receiver (Aki and Richards, 2002).

The accuracy of asymptotic ray methods is frequency-dependent. Their validity is based on the condition (Ben-Menahem *et al.*, 1991)

$$\frac{1}{\omega} \left| \frac{\partial \left\{ \frac{c_{ijkl}(\mathbf{x})}{\rho} \right\}}{\partial x_i} \right| \ll 1. \quad (1.35)$$

This means that the considered wavelengths (or frequencies) must be small (or high) with respect to the spatial variation of the elastic properties of a medium. Therefore, asymptotic ray theory provides a high-frequency approximation of a wavefield.

### 1.3.1 Radiation of body waves from moment-tensor sources in infinite homogeneous isotropic media

If the medium around the source is infinite, homogeneous, and isotropic, an exact analytical solution to (1.10) can be found for amplitudes of body waves radiated from a source that is described by a moment tensor (Aki and Richards, 2002)

$$\begin{aligned} u_i(\phi, \theta, r, t) &= M_{jk} * G_{ij,k} \\ &= \left( \frac{15\gamma_i\gamma_j\gamma_k - 3\gamma_i\delta_{jk} - 3\gamma_j\delta_{ik} - 3\gamma_k\delta_{ij}}{4\pi\rho} \right) \frac{1}{r^4} \int_{r/v_p}^{r/v_s} \tau M_{jk}(t - \tau) d\tau \\ &\quad + \left( \frac{6\gamma_i\gamma_j\gamma_k - \gamma_i\delta_{jk} - \gamma_j\delta_{ik} - \gamma_k\delta_{ij}}{4\pi\rho v_p^2} \right) \frac{1}{r^2} M_{jk} \left( t - \frac{r}{v_p} \right) \\ &\quad - \left( \frac{6\gamma_i\gamma_j\gamma_k - \gamma_i\delta_{jk} - \gamma_j\delta_{ik} - \gamma_k\delta_{ij}}{4\pi\rho v_s^2} \right) \frac{1}{r^2} M_{jk} \left( t - \frac{r}{v_s} \right) \\ &\quad + \frac{\gamma_i\gamma_j\gamma_k}{4\pi\rho v_p^3} \frac{1}{r} \dot{M}_{jk} \left( t - \frac{r}{v_p} \right) \\ &\quad + \frac{(\delta_{ij} - \gamma_i\gamma_j)\gamma_k}{4\pi\rho\beta^3} \frac{1}{r} \dot{M}_{jk} \left( t - \frac{r}{v_s} \right), \end{aligned} \quad (1.36)$$

where  $r$  is the distance from the source and the angles  $\phi$  and  $\theta$  describe the ray direction (compare Fig. 1.1). The direction cosines  $\gamma_i$  ( $\gamma_i = -\partial r / \partial x_{0i}$ ) may be defined in a right-handed coordinate system as

$$\gamma_1 = \sin \theta \cos \phi, \quad \gamma_2 = \sin \theta \sin \phi, \quad \gamma_3 = \cos \theta. \quad (1.37)$$

The quantities  $v_p$  and  $v_s$  denote velocities of the P and the S wave, respectively, in isotropic media (see Appendix B) and  $\delta_{jk}$  is the Kronecker symbol. Note that in this representation the particle motion due to general moment-tensor sources, including dislocation sources and explosions or implosions is given. Whereas dislocation sources in homogeneous isotropic media generate P and S waves, pure explosion sources generate only P but no S waves (Aki and Richards, 2002). In (1.36), the first and the

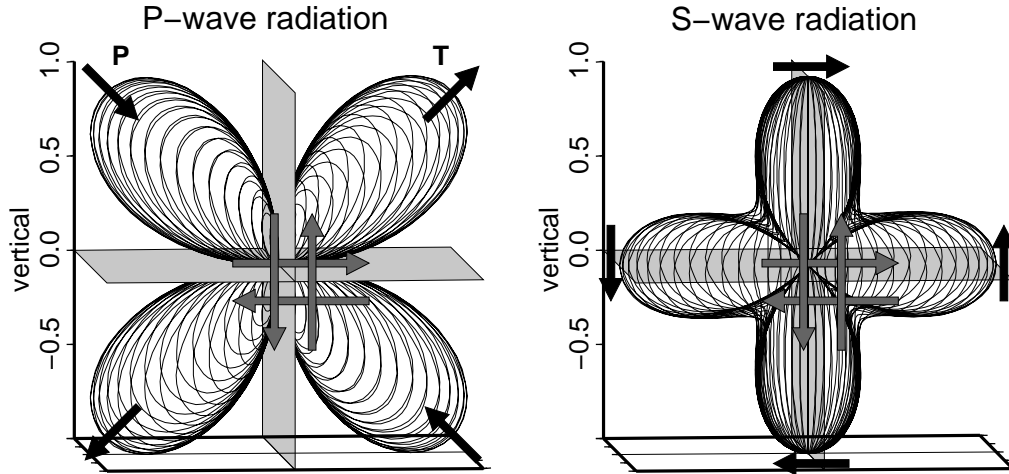


Figure 1.6: Perspective view on P- and S-wave amplitude radiation patterns in the far-field due to a double-couple source on a vertical (dip slip) or a horizontal rupture plane. Amplitudes are normalised and calculated along the plotted lines. Polarisation is indicated at maximum amplitudes by black arrows. Grey planes indicate the two conjugate fault planes that coincide with the nodal planes of the P-wave radiation. Grey arrows show relative dislocation and equivalent force couples at the source. The orientation of the P- and T-axes are also marked.

second term are proportional to higher orders of  $r$ . They are small at large distances and therefore called the near-field and the intermediate-field term, respectively. The last two terms represent the amplitudes in the far-field approximation for the P and the S waves given in (1.13).

The radiation pattern of a point source is commonly calculated as the amplitude of the particle motion in the direction of the ray on a sphere with unit radius from the source (*Aki and Richards, 2002*). Because the moment tensor is symmetric, the radiation pattern of P and S waves also show symmetry (see Fig. 1.6 and Section 2). The radiation pattern of the P wave due to a double-couple source in a homogenous isotropic medium consists of 4 lobes with alternating polarisation that are separated by the two nodal planes. They correspond to two fault planes. Rupturing on these two plane produces exactly the same radiation pattern. Polarisation of the displacement that points away from the source is called compression and otherwise dilatation. Amplitudes of S waves due to a shear source are non-zero everywhere except in the directions where the lobes of the P waves radiation are at their maximum. For shear source in isotropic media the principle stress axes point in the directions of maximum dilatation ( $\sigma_1$  axis) and maximum compression ( $\sigma_3$  axis) of the P waves (see Fig. 1.6).

Because velocities of P and S waves in isotropic media are independent of direction waves form circular wavefronts. The direction of energy propagation equals the normal to the wavefront. It also follows that P waves are polarised in the direction of wave propagation. The polarisation of S wave is determined by the source. It lies within the wavefront.

### 1.3.2 Asymptotic ray approximation of seismic body waves due to moment-tensor sources in anisotropic media

In anisotropic media no analytic solution to (1.10) exists. However, the complex-valued displacement in the far-field can be given in the ray-theoretical high-frequency

approximation (*Pšenčík and Teles, 1996*)

$$u_i(\mathbf{x}, t) = g_i(\mathbf{x}) \left[ \frac{\rho(\mathbf{x}_0)c(\mathbf{x}_0)}{\rho(\mathbf{x})c(\mathbf{x})} \right]^{1/2} \frac{Df^{(A)}(t - \tau(\mathbf{x}))}{|\Omega_M(\mathbf{x})|^{1/2}} \exp \left[ i\frac{\pi}{2}k_s - i\frac{\pi}{2}k(\mathbf{x}_0, \mathbf{x}) \right]. \quad (1.38)$$

Actual seismograms are given by the real part of the displacement  $\Re(u_i(\mathbf{x}, t))$ . In (1.38)  $g_i$  is the vector of polarisation,  $\Omega_M$  is related to the relative geometrical spreading  $|\Omega_M|$ ,  $f^{(A)}$  is the analytical signal corresponding to the source time function. The quantities  $k$  and  $k_s$  are the indices of the trajectory and of the source, respectively, that describe the shape of the slowness surface (see *Pšenčík and Teles, 1996*, for a detailed description). Equation (1.38) is valid in inhomogeneous, generally anisotropic media for which condition (1.35) holds. In homogeneous anisotropic media

$$\Omega_M = (v/c)^2 Kr^2. \quad (1.39)$$

Here,  $c$  is the phase velocity,  $v$  is the group velocity and  $K$  is the Gaussian curvature of the slowness surface in the direction specified by the slowness vector  $p_i$  of the considered wave type. In a homogeneous isotropic medium (1.39) simply reads

$$\Omega_M = c^2 r^2. \quad (1.40)$$

The scalar quantity  $D$  in (1.38) denotes the so called directivity. It is given by

$$D(\mathbf{x}_0, \theta, \phi) = \frac{g_j(\mathbf{x}_0)M_{jk}p_k(\mathbf{x}_0)}{4\pi\rho(\mathbf{x}_0)c(\mathbf{x}_0)}. \quad (1.41)$$

The directivity (1.41) represents a spreading-free amplitude at the source. It should not be confused with the directional dependence of amplitudes due to source finiteness. It depends on the moment tensor  $M_{jk}$ , the polarisation and the slowness vectors  $g_j$  and  $p_k$ , respectively, as well as the phase velocity  $c$  and the density  $\rho$  at the source. The radiation patterns of body waves due to point sources in anisotropic media may be deformed by the effects of anisotropy on the moment tensor and ray-related quantities in (1.38). Some of these effects and consequences on the interpretation of observed body-wave amplitudes are studied in Section 2. They are not described here. As another consequence of anisotropy, S waves may be excited by explosions or implosions in a homogeneous anisotropic medium (*Ben-Menahem et al., 1991; Gajewski, 1993*) because the directivity  $D$  can be non-zero for many directions.

Equation (1.38) is used to model P and S waves for different sources in inhomogeneous anisotropic media in Section 2 and 3. It is also the base for the software package ANRAY (*Pšenčík, 1998*) that is utilised for computations of synthetic seismograms in Sections 4 and 5. The basic theory and equations needed to compute quantities on the right-hand side of (1.38) are given in the following. They are condensed from work found in a number of places, such as *Musgrave (1970)*, *Ben-Menahem et al. (1991)*, *Kendall (1991)*, *Gajewski (1993)*, *Červený (2001)*, and *Aki and Richards (2002)*.

In the absence of internal forces ( $F_i = 0$ ) Eq. (1.1) yields the wave equation in the frequency domain

$$\rho\omega^2 u_j + \frac{\partial}{\partial x_j} \left( c_{ijkl} \frac{\partial u_k}{\partial x_l} \right) = 0. \quad (1.42)$$



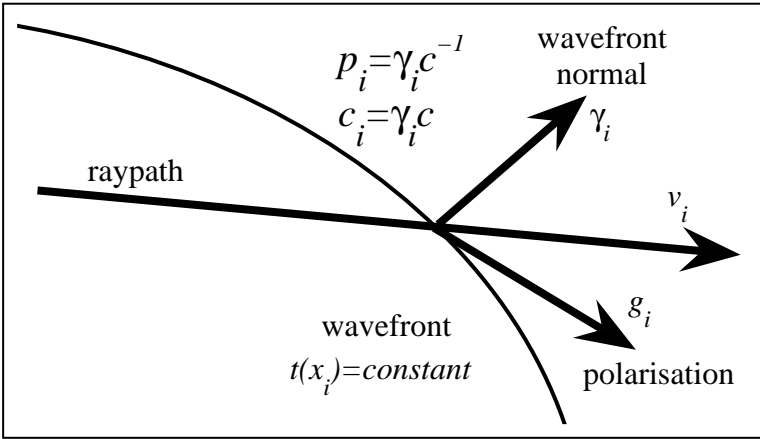


Figure 1.7: Important quantities and directions at the wavefront  $t(x_i) = \text{constant}$  of quasi P waves (qP) in anisotropic media. The normal to the wavefront  $\gamma_i$  is parallel to the slowness  $p_i$  and the phase velocity  $c_i$ . The raypath points in the direction of the group velocity  $v_i$ . The polarisation  $g_i$  forms an oblique angle with the direction of the ray.

If condition (1.35) applies, an approximate solution to (1.42) can be found for high frequencies. This yields the Christoffel's equation

$$(a_{ijkl}p_i p_l - \delta_{jk}) g_k = 0, \quad (1.43)$$

where  $a_{ijkl} = c_{ijkl}/\rho$ . The Eikonal equation is given by

$$G(x_n, p_n) = a_{ijkl}p_i p_l g_j g_k = 1 \quad \text{or} \quad c^2 = a_{ijkl}\gamma_i \gamma_l g_j g_k. \quad (1.44)$$

A non-trivial solution of (1.43) requires

$$\det |a_{ijkl}\gamma_i \gamma_l - c^2 \delta_{jk}| = 0. \quad (1.45)$$

For a given set of direction cosines  $\gamma_i$  (or take-off angles) in (1.37) the three solutions of the cubic equation (1.45) are the roots of  $c^2$ . They define phase velocities  $c$  corresponding to three different waves, one P and two S waves, namely qP, qS1, and qS2. The slowness vector  $p_i$  of these wave types are immediately calculated as

$$p_i = \frac{\partial t}{\partial x_i} = \frac{\gamma_i}{c(\gamma_j)}. \quad (1.46)$$

The polarisation vector  $g_i$  corresponding to the slowness  $p_i$  of one of the three wave types is obtained as a solution to the Christoffel equation (1.43). For a given set of take-off angles the polarisation vectors of the three wave types are mutually perpendicular. If the two eigenvalues of (1.43) that define the speed of the S-waves degenerate, only one S-wave velocity is obtained and the polarisation is determined by the source. The surfaces of the slownesses and phase velocities corresponding to qP, qS1, and qS2 are defined by the end points of  $p_i$  and  $c_i$ , respectively, for all  $\gamma_j$ .

The group velocity  $v_i$  of a surface-area element of the wavefront is calculated as

$$v_i = \frac{dx_i}{dt} = a_{ijkl}p_l g_j g_k. \quad (1.47)$$

From (1.46) and (1.47) it follows that for directions given by  $\theta$  to a surface element

$$v_i p_i = \frac{|v_i| \sin \theta}{c} = 1. \quad (1.48)$$

For a given  $p_i$ , a plane in the  $\mathbf{v}$ -space is defined by (1.48) to which  $p_i$  is normal. The wavefront  $t(x_i) = \text{constant}$  of a wavetype is the envelope of all planes that are defined by all possible  $p_i$ . Therefore,  $p_i$  is normal to the wavefront,  $v_i$  is normal to the slowness surface and  $v_i dp_i = 0$  and  $p_i dv_i = 0$  (see Fig. 1.7). The direction of the ray is determined by the direction of  $v_i$ . In anisotropic media phase and group velocities are in general different (see Appendix B for plots of phase and group velocities as well as slowness surfaces). The direction of the wave-front normal (and the direction defined by the take-off angles) differs from the ray direction. The ray directions of the 3 wave types that correspond to one set of take-off angles are mutually different. As a consequence, the polarisation vectors of qP, qS1, and qS2 are in general not perpendicular for rays in the same direction. P waves in isotropic media are polarised in the direction of the ray. In anisotropic media the polarisation of the qP wave may differ from the ray direction. It is ‘quasi’ longitudinal, giving raise to the term ‘qP’ wave (see Fig. 1.7). Similarly, the qS1 and the qS2 waves are ‘quasi’ transversely polarised.

Equation (1.45) can be alternatively written as

$$B_{jk} (a_{ijkl} p_i p_l - \delta_{jk}) = 0, \quad (1.49)$$

where  $B_{ij}$  are cofactors of the determinant

$$B_{ij} = \frac{1}{6} \epsilon_{ikl} \epsilon_{jmn} (\Gamma_{km} - \delta_{km}) (\Gamma_{ln} - \delta_{ln}), \quad (1.50)$$

with  $\Gamma_{jk} = a_{ijkl} p_i p_l$  and  $a_{ijkl} p_i p_l B_{jk} = B_{qq}$ . The  $\epsilon_{ikl}$  is the third-order alternating tensor (Levi-Civita’s tensor). Then, the group velocity (1.47) can be also formulated as

$$v_i = \frac{a_{ijkl} p_l B_{jk}}{B_{pp}}. \quad (1.51)$$

In this work equation (1.51) is used to calculate  $v_i$ .

The calculation of the Gaussian curvature  $K$  of the slowness surfaces to compute the geometrical spreading  $\Omega_M$  (1.39) requires evaluation of the first- and second-order spatial derivatives of the slowness vector  $p_i$  and the first-order spatial derivative of the group velocity  $v_i$ .

A vector  $\alpha_J$ ,  $J = 1, 2$ , is defined as the vector of the initial parameters (take-off angles at the source) with  $\alpha_1 = \theta$ ,  $\alpha_2 = \phi$ , and  $\gamma_i = \gamma_i(\alpha_J)$  in (1.37). Using (1.46) the first-order spatial derivative of the slowness with respect to  $\alpha_J$  is

$$\frac{\partial p_i}{\partial \alpha_J} = \frac{\partial}{\partial \gamma_j} \left( \frac{\gamma_i}{c} \right) \frac{\partial \gamma_j}{\partial \alpha_J} = \left( \frac{1}{c} \frac{\partial \gamma_i}{\partial \gamma_j} - \frac{\gamma_i}{c^2} \frac{\partial c}{\partial \gamma_j} \right) \frac{\partial \gamma_j}{\partial \alpha_J}. \quad (1.52)$$

With (1.44) and (1.47)

$$\frac{\partial c}{\partial \gamma_j} = v_i \frac{\partial \gamma_i}{\partial \gamma_j}. \quad (1.53)$$

Then (1.52) reads

$$\frac{\partial p_i}{\partial \alpha_J} = \frac{1}{c} \left( \frac{\partial \gamma_i}{\partial \alpha_J} - p_i v_k \frac{\partial \gamma_k}{\partial \alpha_J} \right). \quad (1.54)$$

The second-order derivatives of  $p_i$  with respect to  $\alpha_J$  are formed from (1.54)

$$\begin{aligned} \frac{\partial^2 p_i}{\partial \alpha_J \partial \alpha_L} = & -\frac{1}{c^2} v_k \frac{\partial \gamma_k}{\partial \alpha_L} \left( \frac{\partial \gamma_i}{\partial \alpha_J} - p_i v_k \frac{\partial \gamma_k}{\partial \alpha_J} \right) \\ & + \frac{1}{c} \left( \frac{\partial^2 \gamma_k}{\partial \alpha_J \partial \alpha_L} - \frac{\partial p_i}{\partial \alpha_L} \frac{\partial \gamma_k}{\partial \alpha_J} v_k - p_i \frac{\partial v_k}{\partial \alpha_L} \frac{\partial \gamma_k}{\partial \alpha_J} - p_i v_k \frac{\partial^2 \gamma_k}{\partial \alpha_J \partial \alpha_L} \right). \end{aligned} \quad (1.55)$$

The derivatives of the wave normal  $\gamma_i$  with respect to  $\alpha_J$  are obtained from (1.37). To compute  $\partial v_k / \partial \alpha_L$  in (1.55) the Eikonal equation (1.44) and (1.47) are used

$$\begin{aligned} \frac{\partial v_k}{\partial \alpha_L} = & \frac{\partial}{\partial \alpha_L} \left( \frac{dx_k}{dt} \right) = \frac{\partial}{\partial \alpha_L} \left( \frac{1}{2} \frac{\partial G}{\partial p_k} \right) \\ = & \frac{1}{2} \left( \frac{\partial^2 G}{\partial p_k \partial x_j} \frac{\partial x_j}{\partial \alpha_L} + \frac{\partial^2 G}{\partial p_k \partial p_j} \frac{\partial p_j}{\partial \alpha_L} \right). \end{aligned} \quad (1.56)$$

For point sources  $\partial x_j / \partial \alpha_L = 0$  at the source position  $x_i = x_{0i}$  and

$$\frac{\partial v_k}{\partial \alpha_L} = \frac{1}{2} \left( \frac{\partial^2 G}{\partial p_k \partial p_j} \frac{\partial p_j}{\partial \alpha_L} \right). \quad (1.57)$$

The second order derivatives in (1.57) are calculated from the geometric spreading equations (see (2.28)-(2.31) in *Kendall, 1991*).

The Gaussian curvature  $K$  is then calculated as

$$K = \frac{e_{11}e_{22} - e_{12}^2}{b_{11}b_{22} - b_{12}^2}, \quad (1.58)$$

where

$$b_{IJ} = \frac{\partial p_i}{\partial \alpha_I} \frac{\partial p_i}{\partial \alpha_J}, \quad e_{IJ} = N_i \frac{\partial^2 p_i}{\partial \alpha_I \partial \alpha_J} \quad \text{and} \quad N_i = v_i/v. \quad (1.59)$$

The two principle curvatures of the slowness surface  $k_1$  and  $k_2$  are obtained as a solution to the quadratic equation

$$k^2 - 2Hk + K = 0 \quad (1.60)$$

with

$$H = \frac{b_{11}e_{22} - 2b_{12}e_{12} + b_{22}e_{11}}{2(b_{11}b_{22} - b_{12}^2)}. \quad (1.61)$$

The Gaussian curvature can be also computed as  $K = k_1 k_2$ . It is therefore zero where  $k_1$  and/or  $k_2$  are zero. For  $K = 0$  Eq. (1.38) becomes singular. Therefore, approximate ray theory fails to compute wave amplitudes in these directions.

The index of the source  $k_s$  in (1.38) can attain values of 0, 1, and 2:

$$\begin{aligned} k_s = 0 & \quad \forall \quad k_1 < 0 \wedge k_2 < 0, \\ k_s = 1 & \quad \forall \quad k_1 < 0 \wedge k_2 > 0 \quad \text{or} \quad k_1 > 0 \wedge k_2 < 0, \\ k_s = 2 & \quad \forall \quad k_1 > 0 \wedge k_2 > 0. \end{aligned} \quad (1.62)$$

The slowness surface in a given direction at the source is convex if  $k_s = 0$ , it is saddle-shaped if  $k_s = 1$ , and it is concave if  $k_s = 2$ . In the latter case parabolic points occur for the corresponding directions and (1.38) is not directly applicable. The region of inapplicability is frequency dependent. Equivalent conditions apply for the index of the trajectory  $k$  in (1.38).

### 1.3.3 Numerical implementation

Equation (1.38) is used in Section 2 to compute the radiation patterns of P and S waves for different sources. For a given set of direction cosines all quantities are calculated numerically as described in Sections 1.3.1 and 1.3.2. Vertical sections through slowness, group, and phase velocity surfaces are given in Appendix B for the anisotropic media used in this thesis.

To calculate amplitudes of P and/or S waves at a station, the components of the slowness vectors and the direction cosines in (1.43) and (1.44) that determine the ray from the source to the station must be found. In homogeneous isotropic media this task can be solved without additional effort because the directions of the ray and of the slowness vector are equal for P and S waves. In the homogeneous anisotropic medium ray directions are computed for a range of direction cosines that point in the vicinity of the ray direction. The ray that arrives closest to the station is identified and the corresponding slowness vector is used to further calculate the remaining quantities in (1.38). This is easily done by a rotation of the slowness surface towards the required ray. Then, the  $p_3$  components of the slownesses in the rotated coordinate system point in the direction of the ray. Because of the relation (1.48), the desired slowness direction is found at extrema of  $p_3$ . In the cases where anisotropy is restricted to the region near the source and the medium is otherwise isotropic (inhomogeneous media in Sections 2 and 3) it is assumed that the extent of the source region is small and the transition to the isotropic medium is smooth. There, anisotropic properties near the source are used to compute the directivity  $D$  in (1.41). Isotropic properties are assumed to determine the spreading as well as velocity and polarisation along the ray. The source-time function is approximated by the Brüstle signal (*Brüstle and Müller, 1983*)

$$h(t) = \frac{9}{16} \left[ 1 - \cos \left( \frac{\pi t}{T} \right) \right] + \frac{1}{9} \left[ \cos \left( \frac{3\pi t}{T} \right) - 1 \right]. \quad (1.63)$$

The effects on wave amplitudes and phases due to reflection of waves at the free surface are accounted for (*Ben-Menahem and Singh, 1981; Gajewski and Pšenčík, 1987*).

## 1.4 Geoscientific observations in the Vogtland/West Bohemia

### 1.4.1 Tectonic evolution

The Vogtland/West Bohemia located at the border of FR Germany and the Czech Republic is situated at the transition between the Erzgebirge (Krušné Hory) and the Fichtelgebirge (Smrčiny). It forms a synform in the Saxothuringian Zone of the western part of the Bohemian Massif (see Fig. 1.8 for the location of the Vogtland and a geological map). The latter comprises the Saxothuringian Zone, the Moldanubian Zone, and the Mariánské Lázně Complex, a suture separating the Saxothuringian Zone from the Teplá-Barrandian unit. These zones are major units of the European Variscan Belt. Detailed descriptions of the geological evolution and of geoscientific observations in the region can be found, e.g. in *Vrána and Štědrá (1997)* and *Franke et al. (2000)*.

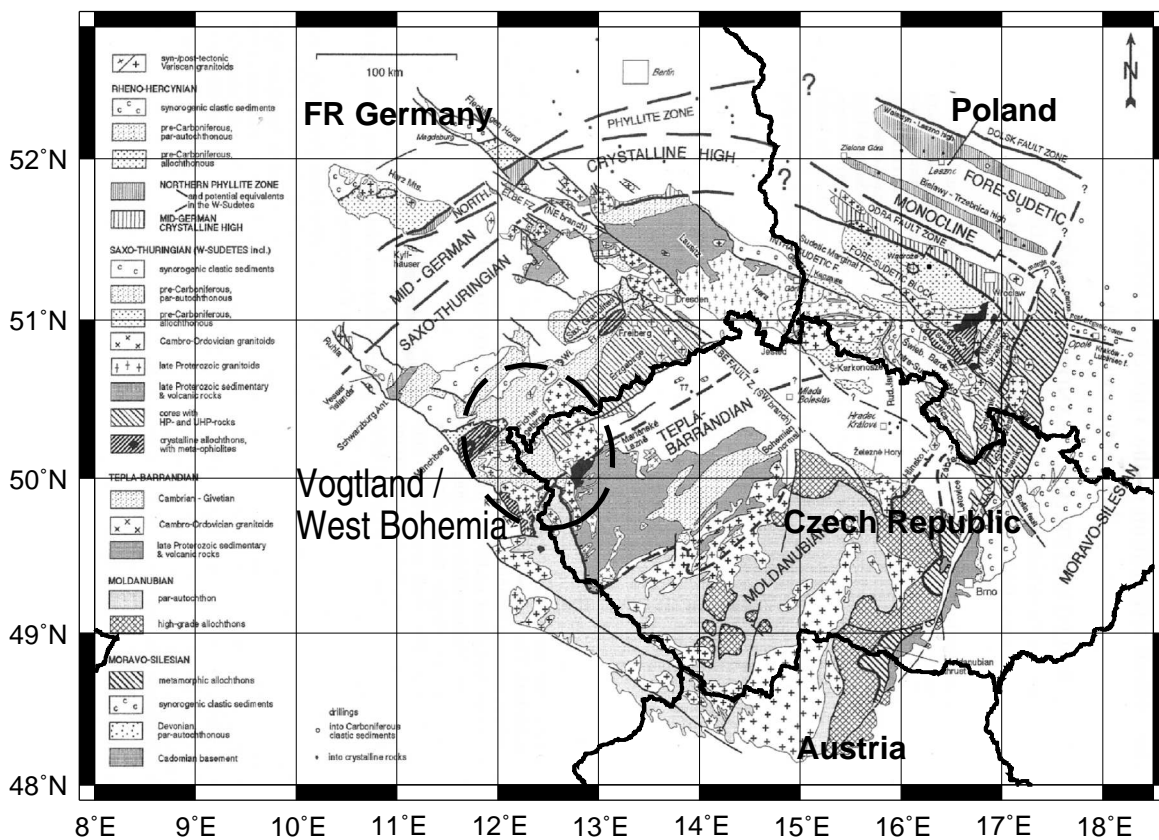


Figure 1.8: Geological Map of the Bohemian Massif (modified after *Franke and Źelaźniewicz, 2000*). The area of the Vogtland/West Bohemia located at the border between FR Germany and the Czech Republic is indicated by the dashed ellipse. It forms a syncline in the Saxothuringian zone of the Bohemian Massif.

The Bohemian Massif is the largest outcrop of the Variscan Orogenic Belt that formed after Ordovician rifting of Gondwana subcontinents and subsequent late Palaeozoic construction of Pangaea by ocean closure–collision of Laurasia and Gondwana in the Carboniferous and the Permian period (*Hirschmann, 1995; O'Brien and Carswell, 1993; Vrána and Štědra, 1998*). Models of deep subduction of continental lithosphere, breaking and exhumation by upward extrusion due to buoyancy forces and erosion are discussed for instance in *Matte (1998), Franke and Stein (2000), Hirschmann (1993), Linnemann et al. (2000), and O'Brien (2000)*. Oceanic NNW–SSE sub-

duction occurred 400 Ma b.p. followed by continental collision (380-360 Ma), slab break-off and buoyant upthrusting (350 Ma) and collapse of thickened crust (320-300 Ma). Indications for dipping palaeo-subduction zones have been also found from observations of seismic anisotropy in the upper mantle (*Plomerová et al.*, 1998; *Babuška and Plomerová*, 2001; *Plomerová et al.*, 2005). In the region of Münchberg, Wildenfels, and Frankenberg allochthon nappe can be found on autochthon and lower allochthon structures (*Franke and Stein*, 2000). They were also confirmed by interpretation of gravity anomalies (*Švancara et al.*, 2000; *Hofmann et al.*, 2003).

Internal zones were overprinted by late orogenic collapse and modifications resulting from the Alpine tectonic event. The NE–SW oriented, NW-tilted Erzgebirge formed by uplifting along the Erzgebirge fault at Tertiary Period (*Grünthal et al.*, 1990; *Peterek et al.*, 1994). The Ohře (Eger) Graben formed at the resulting slope to the SW as part of the European Cenozoic rift system. The post-Oligocene sedimentary fill reaches up to 400 m in the Cheb Basin to the West of Nový Kostel. At Cretaceous period (79-49 Ma) the pre-rifting volcanic event produced ultra-alkaline magma. The Cenozoic riftogenic event (42-9 Ma) was accompanied by voluminous alkaline intraplate volcanism (*Ulrych et al.*, 1999). The two quarternary volcanoes, Železná Hůrka and Komorní Hůrka, located in the Cheb basin were most recently active at 0.45-0.9 Ma and at 0.17-0.4 Ma, respectively (see Fig. 1.9, *Kopecký*, 1978; *Špičák et al.*, 1999; *Ulrych et al.*, 2003).

The main tectonic faults in this region developed mostly during Palaeozoic and pre-Palaeozoic time and were reactivated later during the Alpine orogeny (*Grünthal et al.*, 1990). Those faults mainly oriented NW and N are characterised by sinistral sense of faulting, such as the Mariánské Lázně fault zone in Fig. 1.9, the Počatky-Plesná fault zone, and the Schöneck fault. Perpendicular to this (ENE) in the direction of the Ohře Graben faults exhibit dextral sense of faulting (*Grünthal et al.*, 1990; *Špičáková et al.*, 2000; *Bankwitz and Schneider*, 2000; *Bankwitz et al.*, 2002, 2003). As indicated by GPS-measured lateral (< 2 mm/a) and vertical movements and by the location of hypocentres (compare Fig. 1.9) some of these faults have been recently aseismically and/or seismically active (*Ellenberg*, 1992; *Mrlina*, 2000; *Bankwitz et al.*, 2003). The amount of vertical offset varies between the different swarm episodes and during periods of seismic quiescence (see Section 1.4.5 for an overview on the seismicity). For instance in the Nový Kostel area (zone 1 in Fig. 1.9) subsidence ( $\approx -6$  mm) in 1995-1996 and uplift (< 4 mm) in 1996-1997 occurred (*Mrlina*, 2000). In general, vertical movements are increased during swarm activity.

#### 1.4.2 Observations of fluids

Numerous mineral springs and dry gas vents rich in CO<sub>2</sub> (> 99 vol.% CO<sub>2</sub>, mofettes) can be found in the Vogtland (Fig. 1.9). Showing high gas flux (> 85000 l/h, *Weinlich et al.*, 1999) and temperatures (> 60°C) some gas spring are even commercially exploited, for instance in the spa resorts of Mariánské Lázně and Františkovy Lázně in the Cheb Basin, West of Nový Kostel. According to *Bankwitz et al.* (2003) many vents and springs are located at junctions of tectonic faults. *Bankwitz et al.* (2002) defined Riedel-anti shears connected to active faults in Tertiary clay formation as a prerequisite for degassing. For the earthquake swarms in 1994 and in 2000 *Bräuer et al.* (2003) and *Bräuer et al.* (2005) found correlation between variations in

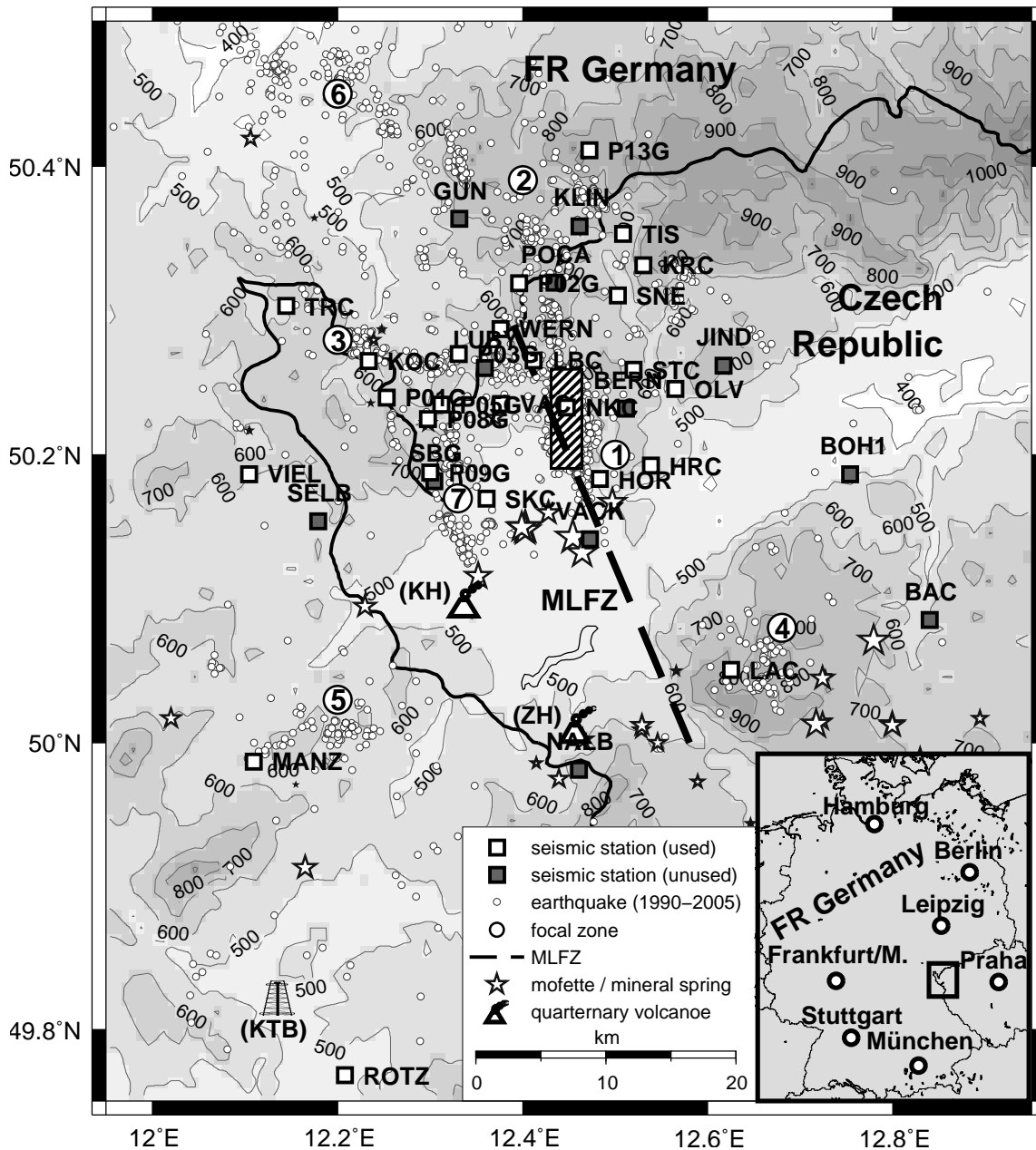


Figure 1.9: Topography and seismicity (1990-2005) of the Vogtland/West Bohemia located at the German-Czech borderline (rectangle in the overview map, lower right corner). Seismic stations installed during the swarm are annotated and shown at their locations by squares (see Tab. C.1 for information on stations). White-filled/grey-filled squares: stations used/not used during inversion. Hatched rectangle: focal area near Nový Kostel (enlarged in Fig. 1.11), small circles: hypocentres of earthquakes (Neunhöfer, 2000; Boušková, 2005), number 1-7 in large circles: locations of the epicentral zones (1: Nový Kostel, 2: Kraslice, 3: Adorf, 4: Mariánské Lázně, 5: Marktredwitz, 6: Plauen, 7: Bad Brambach). The Mariánské Lázně fault zone (MLFZ) is approximately drawn by a dashed line. Sites of the quaternary volcanoes Komorní Hůrka (KH) and Železná Hůrka (ZH) as well as the ICDP super-deep drillhole (KTB) are shown. Sites of mofettes and mineral springs (flux rate > 11/h) are given by stars (size scales logarithmically with gas flux rate, after Geissler *et al.*, 2005). Main degassing occurs near the epicentral zones 1 and 7.

gas content of gas/mineral springs ( $\delta^{13}\text{C}_{\text{CO}_2}$ , He,  $\text{CH}_4$ ) and recorded earthquake activity. The estimated fluid transport velocity (from depth to the surface) is highest in the Cheb basin (400 m/day at the Bublák mofette) and lowest at the periphery of the degassing area (e.g. 50 m/day at Eisenquelle mineral spring). High  $^3\text{He}/^4\text{He}$  ratios ( $^3\text{He}/^4\text{He} \leq 5.9 \pm 0.17 \text{ Ra}$ ) as well as observations of  $-4.0\text{‰} \leq \delta^{13}\text{C}_{\text{CO}_2} \leq -1.8\text{‰}$  and of  $\delta^{15}\text{N} = -4.0 \pm -1.0\text{‰}$  are compatible with a mixing of atmospheric and mantle derived volatiles (*Bräuer et al.*, 2004). These and a number of other geochemical investigations suggest that the fluid emanating on the surface have subcrustal origin (*Weinlich et al.*, 1993; *Kämpf et al.*, 1999; *Weinlich et al.*, 1999; *Weise et al.*, 2001; *Bräuer et al.*, 2003, 2004).

### 1.4.3 Observations of gravity

Densities of crustal rocks in the Vogtland vary between  $2450 \text{ kgm}^{-3}$  of sediments in the Cheb Basin and  $3000 \text{ kgm}^{-3}$  in the lower crust (*Švancara et al.*, 2000; *Hofmann et al.*, 2003). Near Nový Kostel the Mariánské Lázně fault separates low-density granites of the Fichtelgebirge from higher-density nappes of the Erzgebirge. Three dimensional modelling the Bouguer-gravity field *Hofmann et al.* (2003) suggest a low-density body at the crust-mantle boundary (MOHO) with the properties of a magma chamber. The magma concentrated at the MOHO might ascend from the mantle where it is produced by partial melting. The position of this body also coincides with the area of gas emanations on the surface (compare Section 1.4.2).

### 1.4.4 Seismic structure and observations of anisotropy

The seismic structure of the crust and the mantle in the Vogtland has been subject to intensive research in the last years by means of active and passive experiments. Seismic models derived for West Bohemia and the area near Nový Kostel, Czech Republic clearly show the 3D-character of the upper-crustal velocity structure (*Málek et al.*, 2000, 2004). They commonly exhibit strong vertical velocity gradients in the uppermost crustal layers and high velocities (above  $5.5 \text{ km s}^{-1}$ ) below  $\approx 2 \text{ km}$  depth with generally low gradients (see, e.g., *Novotný*, 1996; *Málek et al.*, 2000, 2004, for a review and Fig. 4.2). The DEKORP seismic reflection and the Granu95 seismic refraction profiles traversing the northern Erzgebirge (Krušné Hory) and NE-Bavaria revealed dipping low-velocity zones in the upper and lower crust (*DEKORP Research Group*, 1988; *Enderle et al.*, 1998; *DEKORP Research Group*, 1994). On the Czech side the 9HR deep seismic reflection profile shows reflectors in the upper mantle at 35, 42, and 56 km depth (*Tomek et al.*, 1997) which were later confirmed by receiver function studies (*Geissler*, 2005; *Heuer et al.*, 2006). These reflections were interpreted as the degassing source region for uprising fluids that emanate on the surface (*Kämpf et al.*, 1999). In the western Bohemian Massif *Heuer et al.* (2006) found a  $3.7 \pm 1.0\%$  velocity decrease at  $\approx 65 \text{ km}$  depth covering an area of  $5300 \text{ km}^2$  which they interpreted as an uplifted lithosphere-asthenosphere boundary and/or an area of partial melting. A 3D-tomographic image will be derived for the upper mantle in the frame of the project BOHEMA (*Babuška et al.*, 2003; *Plomerová et al.*, 2003). However, no direct evidence for a low-velocity body that might correspond to a magma chamber which is suggested by the interpretation of the gas content of fluids (Sec. 1.4.2) and the gravity



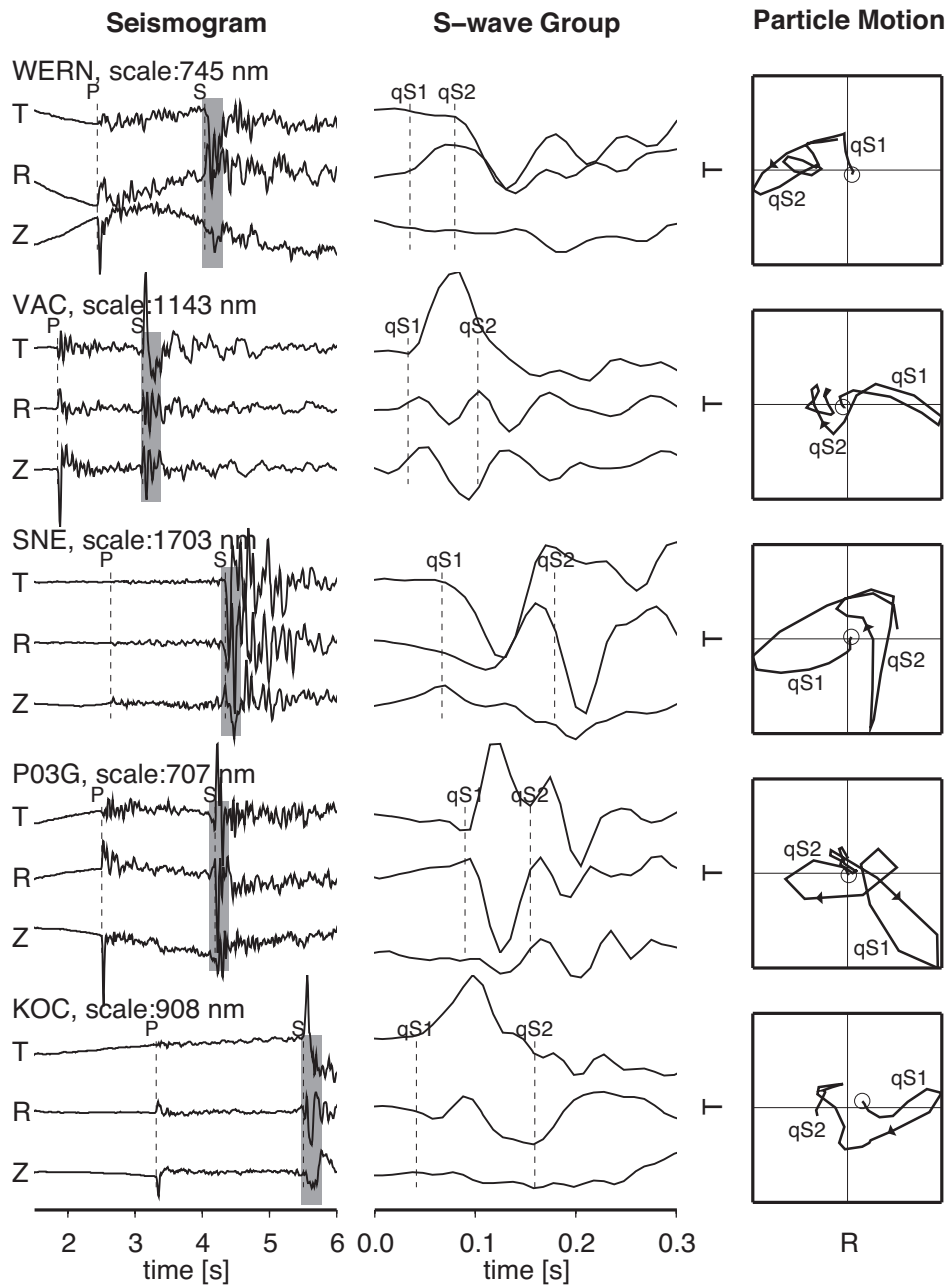


Figure 1.10: Observations of S-wave splitting due to anisotropy at stations KOC, P03G, SNE, VAC, and WERN (compare Fig. 1.9 for station locations). Left: raw, three-component displacement seismograms (vertical, radial, and transverse component) with marked onsets of the P and the S wave. Event time (October 17, 2000, 14:22:31) is at 0 s. S-wave groups are grey shaded. Middle: details of the S-wave group. Onsets of the split qS1 and qS2 waves are marked. Right: particle motion of the S-wave group on the (horizontal) radial and transverse components. Circles mark the start of the seismogram. Arrows indicate the sense of motion.

field (Sec. 1.4.3) was found so far in the upper mantle (*Babuška et al.*, 2004). To date, a 3D-crustal velocity model is lacking.

The depth of the Mohorovičić discontinuity (MOHO) defining the crustal thickness increases from NW (31 km) to SE (38 km) of the Bohemian Massif. Local  $\approx 40$  km wide updoming of the MOHO to at least 27 km beneath the Cheb Basin was observed by receiver function imaging (*Geissler*, 2005; *Geissler et al.*, 2005; *Heuer et al.*, 2006). The position of this updoming coincides with a seismic reflector that has only diffuse character as compared to an otherwise pronounced MOHO (*DEKORP Research Group*, 1988; *Tomek et al.*, 1997) and with the magma-body-like structural feature interpreted from observed gravity anomalies (Sec. 1.4.3). In contrast, (*Hrubcová et al.*, 2005) found a MOHO depths greater than 35 km. They interpreted strong lower-crustal reflections as a highly reflective laminated layer below 25 km depth and above the MOHO.

Seismic anisotropy can be identified by shear-wave splitting (compare Section 1.2). It is also observed in the Vogtland (see Fig. 1.10). A model of moderate crustal anisotropy of 5-6% for P and S waves due to the parallel alignment of stress-induced cracks was derived from measurements of S-wave splitting times and S-P travel-time differences (anisotropy in terms of an effective-medium property, *Vavryčuk*, 1993). Using blasts and tectonic earthquakes *Málek et al.* (2005) determined parameters for an inhomogeneous anisotropic velocity model based on measurements of P-wave travel-time variations (*Málek et al.*, 2005). Laboratory experiments on samples of local metamorphic and magmatic rocks revealed high and extreme P-wave anisotropy of up to 49% due to the alignment of minerals (*Martínková et al.*, 2000; *Chlupáčová et al.*, 2003). More regionally, azimuthal variation of crustal P velocities was reported by *Růžek et al.* (2003). Using teleseismic methods (analysis of SKS splitting and P-wave travel times) *Plomerová et al.* (1998), *Plomerová et al.* (2000), *Babuška* and *Plomerová* (2001), *Plenefisch et al.* (2001), and *Plomerová et al.* (2005) observed anisotropy also in the upper mantle below the Bohemian Massif.

### 1.4.5 Observations of seismicity

The Vogtland/West Bohemia is well-known for outstanding seismic activity within an otherwise seismically quiet area in the Centre of Europe (see Fig. 1.9). Therefore, the region has been subject to extensive studies by research groups of different geoscientific disciplines including passive and active seismic experiments. Seismic monitoring of the region has been carried out since the start of the installation of local seismic networks, e.g. the Vogtland network (start: 1956, *Neunhöfer* and *Güth*, 1988), WEBNET (start: 1986, *Hampel et al.*, 1995), KRASNET (start: 1991), East Thuringian Seismic Network (start: 1997), Saxonian Seismic Network (start: 2000), and Bavarian Network (start: 2000). Today, observations from dense networks of modern digital seismic stations are available.

Earthquake swarms are sequences of earthquakes that often start and end gradually and in which no single earthquake dominates in size (*Scholz*, 2002). Several intense earthquake swarms with maximum magnitudes of 3 to 4.8, e.g. in the years 1903, 1908, 1985/86, 1997, and 2000 occurred during the last decades in the Vogtland/West Bohemia (*Neunhöfer* and *Güth*, 1988; *Grünthal et al.*, 1990; *Horálek et al.*, 2000a; *Tittel* and *Wendt*, 2003; *Fischer*, 2003). Earthquakes with single-event or swarm-like character between consecutive intensive swarms have also been observed.

The most recent (minor) swarm was observed in June, 2005. Located close to the foci of the year 2000 swarm the activity lasted for 3 days (*Fischer*, pers. comm.).

Since 1990 most seismicity has been concentrated in 7 main epicentral areas on either sides of the German-Czech borderline (Fig. 1.9) between 3 and 23 km depth. The shallowest and the deepest events have occurred in zone 1 and zone 7, respectively. However, the most intense swarms of the last 2 decades in 1985/86, 1997, and 2000 were focused in the Nový Kostel area, zone 1 (*Neunhöfer* and *Güth*, 1989; *Fischer* and *Horálek*, 2000; *Fischer*, 2003). Earthquakes in zone 1 follow the depth level where the allochthonous part of the Saxothuringian Zone is thrust over the parautochthon part at the eastern margin of the Fichtelgebirge (see Sections 1.4.1 and 1.4.3).

A common characteristic of an earthquake population is the  $b$ -value that describes the frequency-magnitude distribution of the events (*Gutenberg* and *Richter*, 1956)

$$\log_{10}N = a - bM, \quad (1.64)$$

where  $N$  is the cumulative number of earthquakes with magnitudes greater or equal to  $M$ . World-wide  $b \approx 1$  is observed (*Scholz*, 2002). Triggering of swarm earthquakes is often attributed to over-pressurised fluids leading to increased pore pressures (*Foulger et al.*, 2004; *Miller*, 2004; *Hainzl* and *Ogata*, 2005; *Parotidis et al.*, 2005; *Templeton* and *Dreger*, 2006) and a decrease in normal stress at the fault (*Scholz*, 2002). Therefore, events occur at low stress levels and no dominant earthquake can occur. For this reason swarm earthquakes often show unusually large  $b$ -values (*Scholz*, 1968). For West Bohemia, however, the  $b$ -values vary between 0.7 (swarm in 1973) and 1.5 (swarm in 1968) indicating complexity in swarm formation (*Neunhöfer* and *Güth*, 1988). Focal mechanisms determined by *Špičák et al.* (1999), *Dahm et al.* (2000), *Horálek et al.* (2000b), *Wirth et al.* (2000), *Plenefisch* and *Klinge* (2003), and *Fischer* and *Horálek* (2005) show variations between different swarms but also between separated phases within one swarm episode. Based upon these focal mechanisms *Wirth et al.* (2000), *Havříř* (2000), *Vavryčuk* (2002), and *Plenefisch* and *Klinge* (2003) determined the local stress field. They found that the stress regime in the focal area is characterised by a horizontal SE-NW orientated direction of compressive stress. Therefore, it does not differ substantially from the regional stress regime in Central Europe (see *Hinzen*, 2003, and references therein). By now, the earthquake sequence in 1997 is probably the best investigated swarm in terms of focal mechanisms (e.g. *Horálek et al.*, 2000b; *Dahm et al.*, 2000; *Wirth et al.*, 2000). Interpreting the full moment tensor *Dahm et al.* (2000) and *Horálek et al.* (2000b) found significant non-double-couple moment tensor-components of up to 50%. They are possibly related to over-pressurised pore fluids at focal depth (*Vavryčuk*, 2001, 2002).

The year 2000 earthquake swarm occurred in the focal zone 1 near Nový Kostel at depths of 7-11 km (Figs. 1.9, 1.11). Lasting for about 3 month from August 28 until December 30, 2000 it forms the most recent period of intense seismic activity in the seismoactive area Vogtland/West Bohemia (Fig. 1.12). To enhance the existing networks of permanent seismic stations (Bavarian Network, East-Thuringian Network, KRASNET, Saxony Seismic Network, and WEBNET) a maximum number of 6 additional stations were installed by the University of Potsdam after September 11, 2000 and later replaced by the GeoForschungsZentrum Potsdam. More additional instruments were provided by the Seismological Central Observatory (SZGRF) and the WEBNET (see

Fig. 1.9 and Tab. C.1).

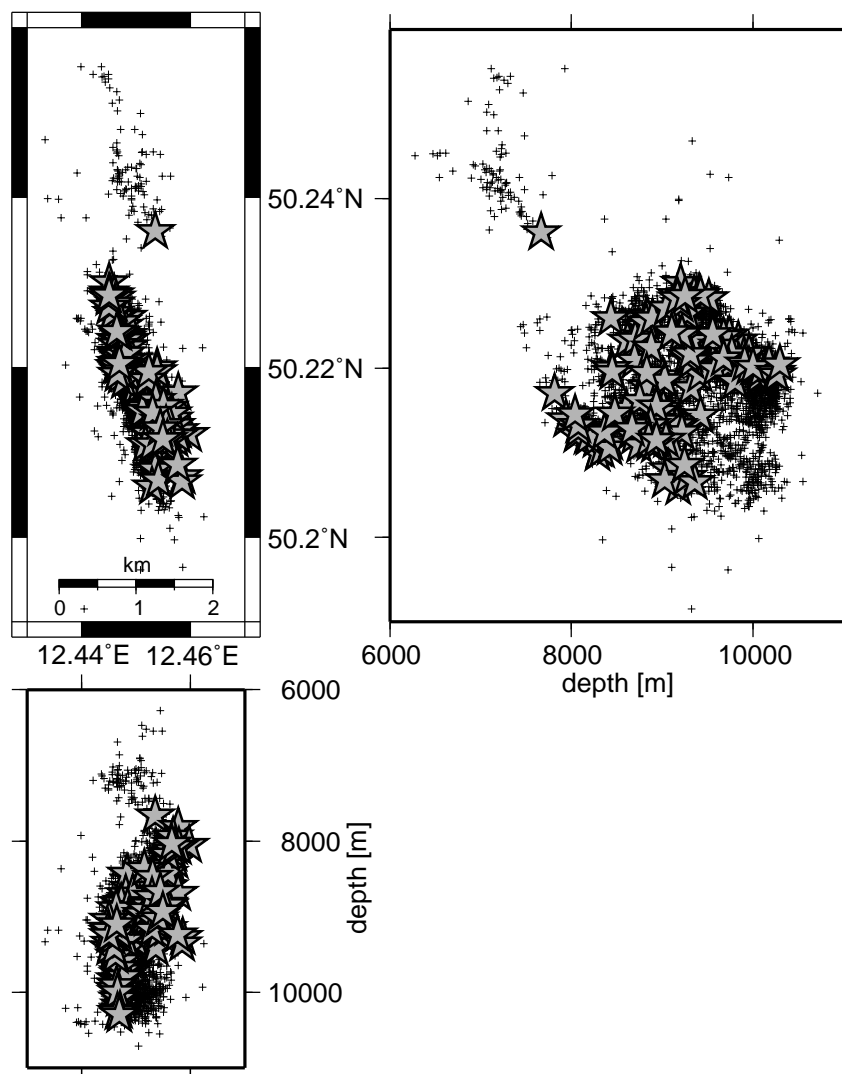


Figure 1.11: Event locations for about 5,000 events of the Vogtland swarm in 2000 (crosses +). Stars (★) correspond to the 112 events that are studied in this work in Sections 4 and 5 (see also Fig. 1.9 and Tab. C.2). Note the almost planar shape of the fault zone. Locations are provided by *Fischer* (pers. comm.).

About 10,000 events could be recorded by stations at local distances (*Tittel and Wendt, 2003; Fischer and Horálek, 2005*). According to *Fischer* (2003) the events are separated into 9 swarm phases (*Tittel and Wendt* (2003) distinguish only 7 phases). The great majority of all events were located on an almost planar NNW striking and steeply dipping fault zone (Fig. 1.11). They lie on a contiguous rupture surface. Starting at the bottom tip of this surface and first propagating north and upwards the foci of the events continued to propagate in anti-clockwise direction on a circular shape (when looking from East) before they returned back to the initially broken area. Interestingly, only little spatial overlap exists between the ruptured zones (*Fischer and Horálek, 2005*).

The largest events of the entire swarm occurred during the 8<sup>th</sup> phase in November, 2000. For the separate phases, the largest events are found near the phase onsets (see

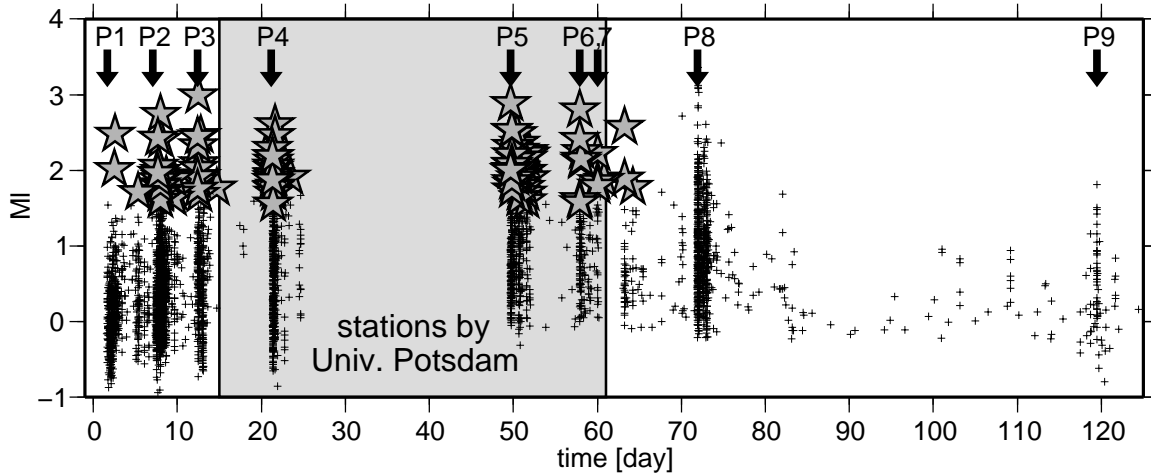


Figure 1.12: Magnitude–time distribution of events in Fig. 1.11. The onset of the 9 swarm phases are marked by arrows. From September 11, 2000 to October 24, 2000 seismic stations were installed by the University of Potsdam (highlighted in grey). Time equal 0 corresponds to August 28, 2000, 00:00:00. Event times and  $M_L$  are provided by *Fischer* (pers. comm.).

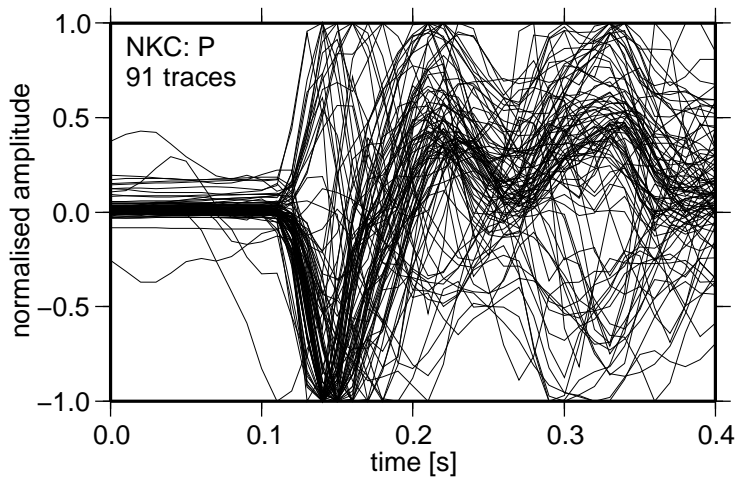


Figure 1.13: Normalised vertical-displacement seismograms of P waves recorded at station NKC for 91 events with  $M_L \geq 1.7$  processed in this work (see Figs. 1.11, 1.12, and Tab. C.2 for hypocentre parameters). Data are unfiltered. Note the high data quality and variable polarity of the P waves. For events of missing traces, NKC was not available.

Fig. 1.12). Observed magnitudes differ between stations used for their determination with an uncertainty of about  $\pm 0.2$ . *Tittel* and *Wendt* (2003) and *Fischer* (2003) report peak magnitudes of 4.2 at station VIE (Vienna) and of 3.3 at WEBNET stations, respectively (hypocentre time: 06/11/2000, 22:07:19.72, phase 8). Magnitudes determined at the German Regional Network station CLL (Collm, see *Tittel* and *Wendt*, 2003) are on average larger by 0.27 than local magnitudes determined by *Fischer* (2003).

Source duration and waveforms of P waves are very similar for the largest events with  $M_L \geq 1.7$  of the phases 1-7 (Fig. 1.13) and also throughout the whole swarm (*Fischer*, 2003). However, varying P-wave polarities indicate differences in source mechanism.

Coherence analyses of Sg and coda waves of *Eckhardt* (2004) revealed similarities between events within but differences between the separate swarm phases indicating similarities and differences, respectively, in source mechanisms and/or ray-path.

The swarm character is manifested by the time between two consecutive events (inter-event time). For the inter-event times *Tittel* and *Wendt* (2003) found  $< 1$  min for

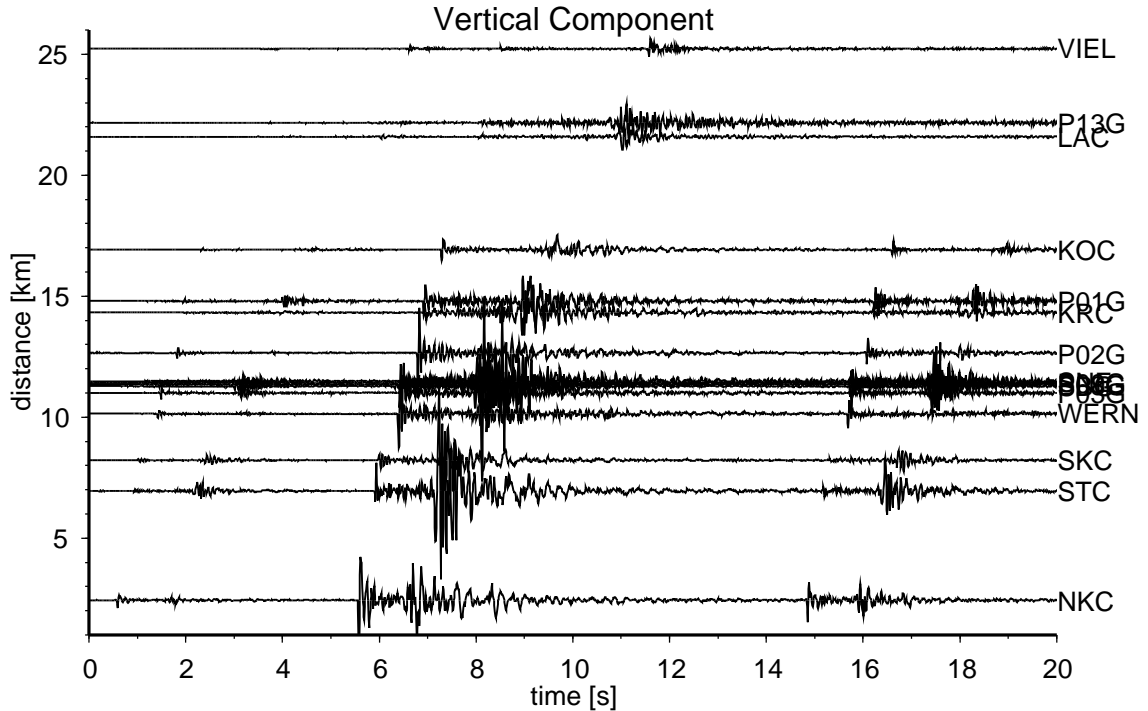


Figure 1.14: Seismogram example typical for events of the Vogtland swarm in 2000 (vertical component of the particle velocity) where short interevent times can be observed. Start time: October 16, 2000, 18:01:34. The dominating wavetrains between 5 and 12s correspond to event 83 in Tab. C.2. Seismograms are sorted by distance from the hypocentre of event 83. Stations are annotated at the respective trace (see Fig. 1.9 Tab. C.2 for details on stations).

80% of all events and  $< 10$  s for more than 5,000 events (see Fig. 1.14 for a seismogram example). Using empirical Green's functions *Fischer* (2005) identified 54 multiple-events from earthquakes in the magnitude range  $1.2 \leq M_L \leq 3.3$ . At least 18 of these events occurred as double events or triplets. Resulting in complicated waveforms they are separated in time and space by less than 0.1 s and 320 m, respectively. Due to the small inter-event times interference of waves generated by different events may occur making phase picking and their interpretation difficult.

*Hainzl* and *Fischer* (2002) found significant changes in the frequency-magnitude distribution expressed by large  $b$ -values for the onset (phase 1,  $b = 1.4$ ) and smaller  $b$ -values at the end of the swarm (phase 8,  $b = 0.8$ ). The decrease in  $b$ -value was explained by either pore-pressure increase due to fluid migration or stress accumulation at the rupture front. By a spatiotemporal analysis of the swarm sequence *Hainzl* and *Fischer* (2002) found that earthquakes trigger aftershocks at the edge of the rupture area of preceding events. Overpressurised fluids causing increase in pore pressure are found to be responsible for the triggering and propagation of the swarm events. This idea is compatible with indications of volumetric source components found for the earlier 1997 earthquake swarm. It is also supported by independent observations of fluid-driven aftershocks in northern Italy (*Miller*, 2004).

Inverting polarities and amplitudes of P and S phases using the FOCMEC algorithm (*Snoke*, 2003), *Fischer* and *Horálek* (2005) found that source mechanisms are dominated by faulting on a N-S oriented fault that can be associated with the Mariánské Lázně Fault Zone. However, no information on possible volumetric source components

were determined. *Plenefisch et al.* (2003) determined full moment tensors using the relative method by *Dahm* (1996). Their findings partially contradict orientations of fault planes given in *Plenefisch* and *Klinge* (2003) and *Fischer* and *Horálek* (2005).

## 2 Ambiguous moment tensors and radiation patterns in anisotropic media with applications to the modeling of earthquake mechanisms in W-Bohemia

Dirk Rößler<sup>1\*</sup>, Georg Rümpker<sup>2</sup>, Frank Krüger<sup>1</sup>

<sup>1</sup>Department of Earthsciences, University of Potsdam, K.-Liebknecht-Str. 24, 14476 Golm, FR Germany

<sup>2</sup>Department of Meteorology and Geophysics, University of Frankfurt/Main, Feldbergstr. 47, 60323 Frankfurt/Main, FR Germany

\*corresponding author

Published 2004 in *Studia Geophysica et Geodaetica*, 48(1), pp. 233-250

### Abstract

Anisotropic material properties are usually neglected during inversions for source parameters of earthquakes. In general anisotropic media, however, moment tensors for pure-shear sources can exhibit significant non-double-couple components. Such effects may be erroneously interpreted as an indication for volumetric changes at the source. Here we investigate effects of anisotropy on seismic moment tensors and radiation patterns for pure-shear and tensile-type sources. Anisotropy can significantly influence the interpretation of the source mechanisms. For example, the orientation of the slip within the fault plane may affect the total seismic moment. Also, moment tensors due to pure-shear and tensile faulting can have similar characteristics, depending on the orientation of the elastic tensor. Furthermore, the tensile nature of an earthquake can be obscured by near-source anisotropic properties. As an application, we consider effects of inhomogeneous anisotropic properties on the seismic moment tensor and the radiation patterns of a selected type of micro-earthquakes observed in W-Bohemia. The combined effects of near-source and along-path anisotropy cause characteristic amplitude distortions of the P, S1 and S2 waves. However, the modeling suggests that neither homogeneous nor inhomogeneous anisotropic properties alone can explain the observed large non-double-couple components.

The results also indicate that a correct analysis of the source mechanism, in principle, is achievable by application of anisotropic moment tensor inversions.

*Keywords: anisotropy, radiation pattern, seismic moment tensor, W-Bohemia*

### 2.1 Introduction

Most present studies of seismic source mechanisms are based on the assumption that the material in which the rupture occurs, as well as the medium along the ray path are isotropic. On the other hand, seismic anisotropy is a widely observed characteristic of crustal rocks and mantle material (*Babuška and Cara, 1991*). Preferred



mineral orientation due to frozen-in material flux, non-hydrostatic pressure, layering, and fracturing with preferred orientation are among the possible causes. A clear observation of crustal anisotropy has been reported for the W-Bohemian region, where observations of shear-wave splitting from the 1985/86 swarm episode were interpreted in terms of the Schoenberg–Douma fracture model (Vavryčuk, 1993). This model suggests transverse isotropy of about 6% for S waves with a horizontal axis of symmetry pointing N31°E.

Anisotropic material properties affect the earthquake radiation pattern and may influence the interpretation of the source mechanism. Non-double-couple components of the seismic moment tensor have been frequently observed in volcanic regions (see e.g. Sykes, 1967; Solomon and Julian, 1974; Julian et al., 1997; Vavryčuk, 2002). Such observations are often interpreted in terms of volumetric changes in the source region related to e.g. tensile faulting, explosions, or volume collapses. However, apparent volumetric source effects may also be caused by multiple shearing on non-planar faults, heterogenous focal areas, and anisotropic elastic properties (Julian et al., 1998). The latter is supported by the modeling of Kawasaki and Tanimoto (1981) who found significant non-quadrant-type radiation patterns for pure shear sources in anisotropic media. Further studies on source radiation by Ben-Menahem et al. (1991); Gajewski (1993) endorse these findings.

For the 1997 swarm episode in W-Bohemia, moment tensor solutions for 70 earthquakes were found to be characterized by pure shear sources as well as by significant non-double-couple components (Dahm et al., 2000; Horálek et al., 2000b; Vavryčuk, 2002). The latter were interpreted by a certain amount of tensile faulting, i.e. slip within a fault plane accompanied by crack opening or closing (Vavryčuk, 2002).

In the following, we will investigate possible effects of anisotropy on moment tensors and radiation patterns for earthquakes of the W-Bohemia region. Anisotropic material properties at the source can be different from those of the surrounding material (Julian et al., 1998; Scholz, 2002). We will take this into account by applying expressions for the ray-theoretical Green’s function in inhomogeneous anisotropic media (Pšenčík and Teles, 1996). After a brief review of the theoretical background, we consider moment tensors and radiation patterns for pure-shear and tensile faulting. Effects of a rotation of the elastic tensor on the radiation are considered in some detail. Subsequently, we consider possible scenarios for anisotropic structures in the W-Bohemia region. The resulting radiation patterns are used to assess the significance of anisotropic effects on moment-tensor inversions for this region.

## 2.2 Theoretical background

The far-field displacement  $u_i$  generated by a seismic source is expressed in terms of a convolution of the spatial derivative of the Green’s function  $G_{ij,k}$  with the seismic moment tensor  $M_{jk}$ , which represents the equivalent forces at the source (Aki and Richards, 2002)

$$u_i(\mathbf{x}, t) = G_{ij,k}(\mathbf{x}, t, \mathbf{x}_0, t_0) * M_{jk}(\mathbf{x}_0, t). \quad (2.1)$$

Following (*Pšenčík and Teles, 1996*), for inhomogeneous anisotropic media eq. (2.1) can be given in the form

$$u_i(\mathbf{x}, t) = g_i(\mathbf{x}) \left[ \frac{\rho(\mathbf{x}_0)c(\mathbf{x}_0)}{\rho(\mathbf{x})c(\mathbf{x})} \right]^{1/2} \frac{Df^{(A)}(t - \tau(\mathbf{x}))}{|\Omega_M(\mathbf{x})|^{1/2}} \exp \left[ i\frac{\pi}{2}k_s - i\frac{\pi}{2}k(\mathbf{x}_0, \mathbf{x}) \right], \quad (2.2)$$

which is a high-frequency approximation to the solution of the wave equation. Here  $g_i$  is the polarization vector,  $\rho$  is the density,  $c$  is the phase velocity,  $\mathbf{x}$  is the spatial coordinate and  $f^{(A)}$  is the analytical signal corresponding to the source-time function. The index 0 denotes quantities at the source. Depending on the principle curvature of the slowness surface for a particular wavetype  $k_s$  and  $k$  can attain values of 0,1,2 (see *Pšenčík and Teles (1996)* for details). The force equivalents, polarizations and elastic properties at the source are given in terms of the directivity  $D$ . For a moment tensor source,  $D$  is given by (*Pšenčík and Teles, 1996*):

$$D(\mathbf{x}_0, \theta, \phi) = \frac{g_j(\mathbf{x}_0)M_{jk}p_k(\mathbf{x}_0)}{4\pi\rho(\mathbf{x}_0)c(\mathbf{x}_0)} \quad (2.3)$$

with components of the slowness vector  $p_k$ . Angles  $\theta$  and  $\phi$  specify the direction of the wavefront normal and the slowness vector, respectively. The quantity  $\Omega_M$  in eq. (2.2) describes the geometrical spreading. For a homogeneous anisotropic medium

$$\Omega_M = (v/c)^2 Kr^2 \quad (2.4)$$

which simplifies to  $\Omega_M = (rc)^2$  in the isotropic case. Here,  $v$  is the group velocity,  $r$  is the hypocentral distance, and  $K$  is the Gaussian curvature of the slowness surface. The latter can be calculated using equations given by (e.g.) *Gajewski (1993)*, where the corresponding expression (see eq. 2.2) for a homogeneous medium can also be found.

For an effective point source, the seismic moment tensor given in eq. (2.3) depends on the slip  $s_i$ , the normal to the fault plane  $n_i$ , and the elastic parameters of the source medium  $c_{ijkl}$ :

$$M_{jk} = s_p n_q c_{pqjk} A_0, \quad (2.5)$$

where the quantities  $s_i$ ,  $n_i$  and  $c_{ijkl}$  are constant everywhere on the fault surface  $A_0$ . A decomposition of the moment tensor into its double-couple (DC), compensated linear vector dipole (CLVD) and isotropic (ISO) components is often used to characterize the source in terms of pure shear and volumetric changes. This can be performed using formulas given in *Jost and Herrmann (1989)* and *Vavryčuk (2002)*.

**Effects of the slip direction on the total seismic moment.** The total seismic moment  $M_T$  may be defined by (*Silver and Jordan, 1982*)

$$M_T = \sqrt{\sum_{j,k} M_{jk} M_{jk} / 2}. \quad (2.6)$$

Consider, for example, a pure-shear point source within an anisotropic medium of orthorhombic (or higher) symmetry, where the axes of symmetry are parallel to the coordinate axes. Using the crystallographic representation ( $c_{ijkl} \rightarrow C_{ij}$ , Voigt notation),

the elastic tensor may be expressed as

$$C_{ij} = \begin{pmatrix} C_{11} & C_{12} & C_{13} & 0 & 0 & 0 \\ C_{12} & C_{22} & C_{23} & 0 & 0 & 0 \\ C_{13} & C_{23} & C_{33} & 0 & 0 & 0 \\ 0 & 0 & 0 & C_{44} & 0 & 0 \\ 0 & 0 & 0 & 0 & C_{55} & 0 \\ 0 & 0 & 0 & 0 & 0 & C_{66} \end{pmatrix}. \quad (2.7)$$

Further assuming slip  $sl_1$  with  $\mathbf{s} = s(1, 0, 0)$  and fault normal  $\mathbf{n} = (0, 0, 1)$  (see Fig. 2.1), we obtain the moment tensor from (2.5) and (2.7)

$$\mathbf{M} = \begin{pmatrix} 0 & 0 & C_{55} \\ 0 & 0 & 0 \\ C_{55} & 0 & 0 \end{pmatrix} A_0 s. \quad (2.8)$$

On the other hand, assuming slip  $sl_2$  with  $\mathbf{s} = s(0, 1, 0)$  and  $\mathbf{n} = (0, 0, 1)$  (see Fig. 2.1), we find

$$\mathbf{M} = \begin{pmatrix} 0 & 0 & 0 \\ 0 & 0 & C_{44} \\ 0 & C_{44} & 0 \end{pmatrix} A_0 s. \quad (2.9)$$

While these two examples represent force equivalents of pure double-couple characteristic, the resulting total seismic moments (2.6) differ as, in contrast to the isotropic case,  $C_{44} \neq C_{55}$ . Consequently, if anisotropy is not accounted for, quantities deduced from the observed total seismic moment (e.g. slip, strain, stress drop) may be biased.

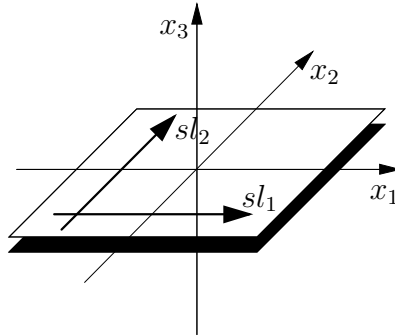


Figure 2.1: Fault in the  $x_1$ - $x_2$ -plane with slip in  $x_1$  (slip  $sl_1$ ) and  $x_2$  direction (slip  $sl_2$ ).

Table 2.1: Density normalized elastic constants  $a_{ij}$  taken from Vavryčuk (1993) for W-Bohemia (M1) and for a synthetic TI medium (M2) with 10% of anisotropy (Rümpker and Kendall, 2002).  $[a_{ij}] = \text{km}^2/\text{s}^2$ ,  $[\rho] = \text{kg}/\text{m}^3$ ;  $C_{ij} = a_{ij} * \rho * 10^6$ .

medium	$a_{11}$	$a_{12}$	$a_{13}$	$a_{22}$	$a_{23}$	$a_{33}$	$a_{44}$	$a_{55}$	$a_{66}$	$\rho$
M1	23.5	7.8	7.8	31.9	9.9	31.9	11.0	10.8	10.8	2850
M2	39.7	13.2	13.2	39.7	13.2	32.5	10.8	10.8	13.2	2850

Taking the elastic constants derived from earthquakes in the W-Bohemia region (see Tab. 2.1, M1) as an example, the total seismic moments calculated from (2.8) and (2.9) are  $30.8 \cdot 10^9$  Nm and  $31.4 \cdot 10^9$  Nm, respectively (assuming unit values for  $s$  and  $A_0$ ). Here the differences can be considered negligible. However, more significant effects can be generated from different orientations of the elastic tensor or for sources in regions with stronger anisotropy.

**Effects of a rotation of symmetry axes on the moment tensor.** Up to this point, we have assumed that the symmetry axes of the (orthorhombic) elastic tensor are oriented parallel or perpendicular to the slip and the fault normal, respectively. Effects of a rotation of the elastic tensor with respect to the coordinate axes are elucidated by the following examples. For a general orientation of the elastic tensor in (2.5) with slip  $s_{l_1}$  the moment tensor (2.8) takes the form

$$\mathbf{M} = \begin{pmatrix} C_{15} & C_{56} & C_{55} \\ C_{56} & C_{25} & C_{45} \\ C_{55} & C_{45} & C_{35} \end{pmatrix} A_0 s, \quad (2.10)$$

where it is understood that the  $C_{ij}$  denote components of the rotated elastic tensor. In general, the trace of (2.10) will lead to a non-vanishing isotropic component of the moment tensor after decomposition.

We now consider a source medium given by the elastic constants derived for W-Bohemia (Tab. 2.1, M1). In a first example, we apply a rotation of  $-45^\circ$  (clockwise, the resulting medium is denoted M1<sup>-</sup>) about the  $x_2$ -axis to the elastic tensor. Equation (2.10) leads to

$$\mathbf{M} = \begin{pmatrix} 6.0 & 0.0 & 28.4 \\ 0.0 & 3.0 & 0.0 \\ 28.4 & 0.0 & 6.0 \end{pmatrix} A_0 s \cdot 10^9 \text{ Pa}. \quad (2.11)$$

Following *Vavryčuk* (2002) this tensor decomposes into components DC=73.9%, ISO=14.5%, and CLVD=11.6%. Interestingly, similar values can be obtained for a tensile-type source in the original (unrotated) anisotropic medium. A unit slip, incorporating 11.5% crack opening in the  $x_3$  direction [i.e.  $\mathbf{s} = (0.993, 0, 0.115)$ ], would generate a seismic moment tensor with almost identical characteristics (DC=73.8%, ISO=14.5%, and CLVD=11.7%).

However, the same tensile-type source can create a moment tensor with nearly vanishing non-double-couple components if the original elastic tensor is rotated by  $+40^\circ$  (counterclockwise, M1<sup>+</sup>) about the  $x_2$ -axis. In this case the decomposition leads to values that would be expected for pure shear in an isotropic medium (DC=99.4%, ISO=0.3%, and CLVD=0.3%).

In conclusion, pure shear sources in generally oriented anisotropic media may lead to significant isotropic moment tensor components. The isotropic components can be of similar size as those produced by tensile-type source mechanisms. On the other hand, under certain circumstances, the tensile nature of a source may also be obscured due to anisotropy.

### 2.3 Effects of anisotropy on point-source radiation

In the following, we investigate effects of weak anisotropy on point-source radiation based on the different moment tensors discussed in the previous section. The radiation

patterns are calculated from the length of the displacement vector for a particular ray direction.

**Anisotropic inclusion.** Anisotropy in the immediate neighborhood of the source is accounted for by the directivity function  $D$  (see eq. 2.3). To investigate and isolate the effects of near-source anisotropy (i.e. an anisotropic inclusion) on the radiation pattern, we first consider isotropic material properties in the medium surrounding the inclusion. We thereby assume a smooth transition of elastic properties from the spherical anisotropic source region to the isotropic full space (i.e. along-path medium). In this model, coupling between wavetypes is considered negligible such that effects due to converted phases are not significant. It is further assumed that the ray (or group-velocity) direction is determined by the anisotropic properties of the inclusion. The isotropic properties of the along-path medium are calculated by averaging the anisotropic elastic constants (M1, Tab. 2.1) according to  $v_p^2 = (c_{11} + c_{22} + c_{33})/(3\rho)$  and  $v_s^2 = (c_{44} + c_{55} + c_{66})/(3\rho)$ . Vertical cross-sections of the radiation patterns (within the  $x_1$ - $x_3$ -plane) are given in Fig. 2.2. To cover the complete angular range we also show contour lines in a mercator projection (Fig. 2.3).

- i) The pure shear source (slip  $sl_1$  in Fig. 2.1) in the (unrotated) anisotropic medium (M1, Figs. 2.2a, 2.3a) produces symmetric radiation patterns with crossing nodal lines (quadrant-type characteristic) for the P wave and nodal points for the S wave. The radiation patterns are similar to those found for isotropic media (see *Aki and Richards, 2002*). Note, that in this case the symmetry axis of the medium M1 is parallel to the slip direction.
- ii) The same pure shear source in the rotated anisotropic medium (M1<sup>-</sup>) generates considerable apparent isotropic components (Figs. 2.2b, 2.3b). Amplitudes in the directions of compression are similar to those in the previous case, whereas the amplitudes in dilatational directions are decreased. The nodal lines do not intersect which is typical for tensile sources (non-quadrant-type characteristic). However, this is in contrast to the pure-shear nature of the event. S-wave amplitudes are slightly distorted but still very similar to those in the unrotated medium.
- iii) The tensile source [i.e.  $\mathbf{s} = (0.993, 0, 0.115)$ ] in the unrotated medium (M1) produces the strongest modifications in the radiation patterns (Figs. 2.2c, 2.3c). P-wave amplitudes in the directions of compression are significantly enlarged, whereas they are decreased in the directions of dilatation. As in the previous case, nodal lines of the P-wave amplitudes do not intersect. In comparison (see *ii*), the amplitudes of the S waves are slightly more distorted.
- iv) For most angular ranges, the P and S amplitudes of the same tensile source in the rotated medium (M1<sup>+</sup>, Figs. 2.2d, 2.3d) are deformed in a way similar to the previous case. However, nodal lines of the P-wave amplitudes that nearly close up are an important feature of this source. Thus, this radiation pattern is more similar to that for the shear source in the unrotated medium (see *i*).

Generally, the findings agree with the previous results from the decomposition of the moment tensors for the different source mechanisms. The P-wave radiation patterns

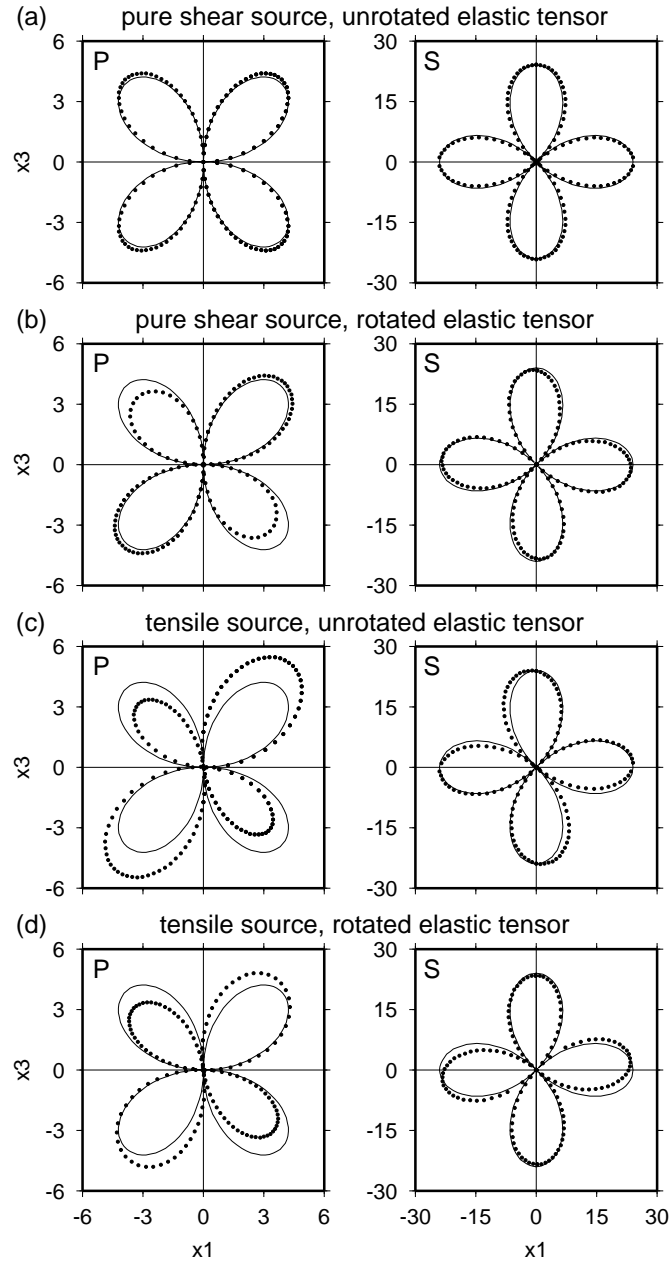


Figure 2.2: Radiation patterns (dots) in the  $x_1$ - $x_3$ -plane for P and S waves caused by four different dislocation point sources in the anisotropic inclusion (elastic constants are given in Tab. 2.1, medium M1). The surrounding (along-path) medium is assumed isotropic. (a) A pure-shear source within the anisotropic inclusion with elastic properties given by medium M1. (b) The elastic tensor within the inclusion (medium M1<sup>-</sup>) is rotated by  $-45^\circ$  (clockwise) about the  $x_2$ -axis. (c) The shear source is accompanied by 11.5% crack opening in the anisotropic inclusion (tensile faulting). The elastic tensor is given by medium M1. (d) The same tensile source as in (c). The elastic tensor within the inclusion is rotated by  $40^\circ$  (counterclockwise) about the  $x_2$ -axis (medium M1<sup>+</sup>). For comparison radiation patterns for a pure-shear source in a homogeneous isotropic medium are shown (solid line). Units are given in  $\mu\text{m}$ .

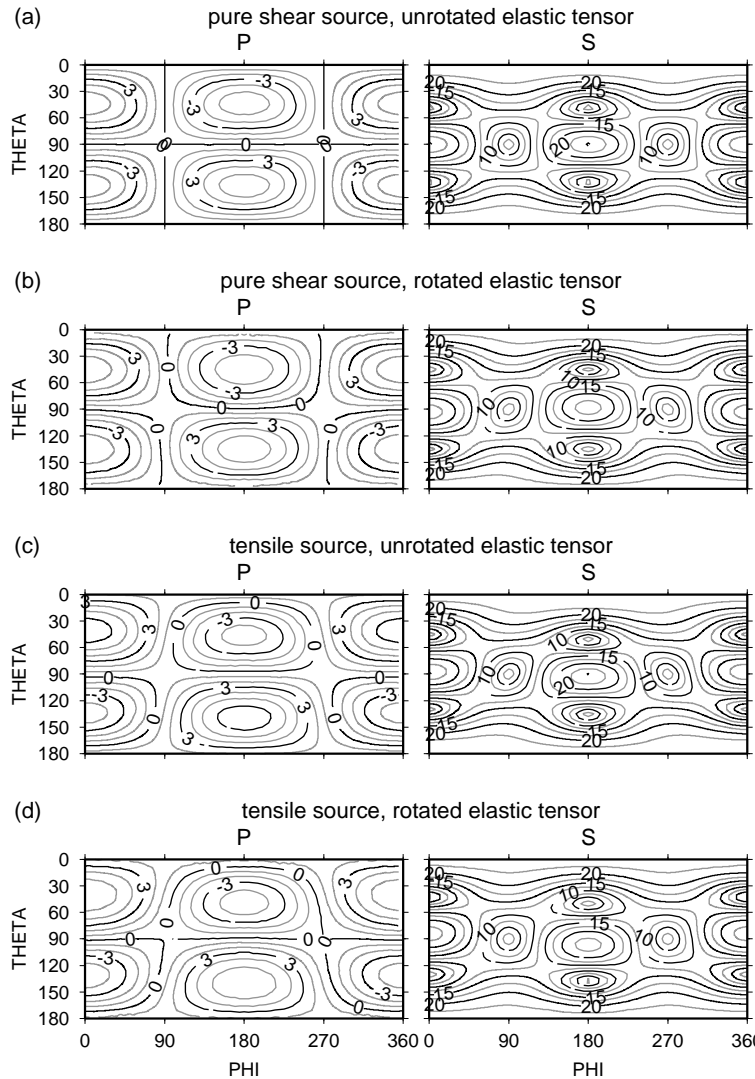


Figure 2.3: Mercator projection of the P and S-wave radiation patterns for sources given in Fig. 2.2. Positive signs in P correspond to compressional first motion. Note that the projection leads to strong distortions in the vicinity of  $\theta = 0^\circ$  and  $180^\circ$ . Units of contour lines are given in  $\mu\text{m}$ .

are usually more distorted. A possible explanation for this could be that (as in the isotropic case) compression and dilatation away from the source are transmitted by P rather than S waves.

**Homogeneous anisotropic medium.** In this section the isotropic elastic tensor in the full-space is replaced by the anisotropic tensor at the source (inclusion) such that the medium becomes homogeneous. Due to the anisotropy in the medium along the ray path we now consider radiation patterns for three wavetypes P, S1, S2 (see Figs. 2.4 and 2.5 for the corresponding cross sections and contour plots).

In general, the P-wave radiation patterns in the homogeneous anisotropic case are similar to those in the previous section. The amplitude variations are slightly more pronounced. For all cases in the  $x_1$ - $x_3$ -plane only one type of S wave (S2) is excited. The slip lies in this plane, which also corresponds to a symmetry plane of the elastic tensor. Thus, the slow S2 wave exhibits SV polarization.

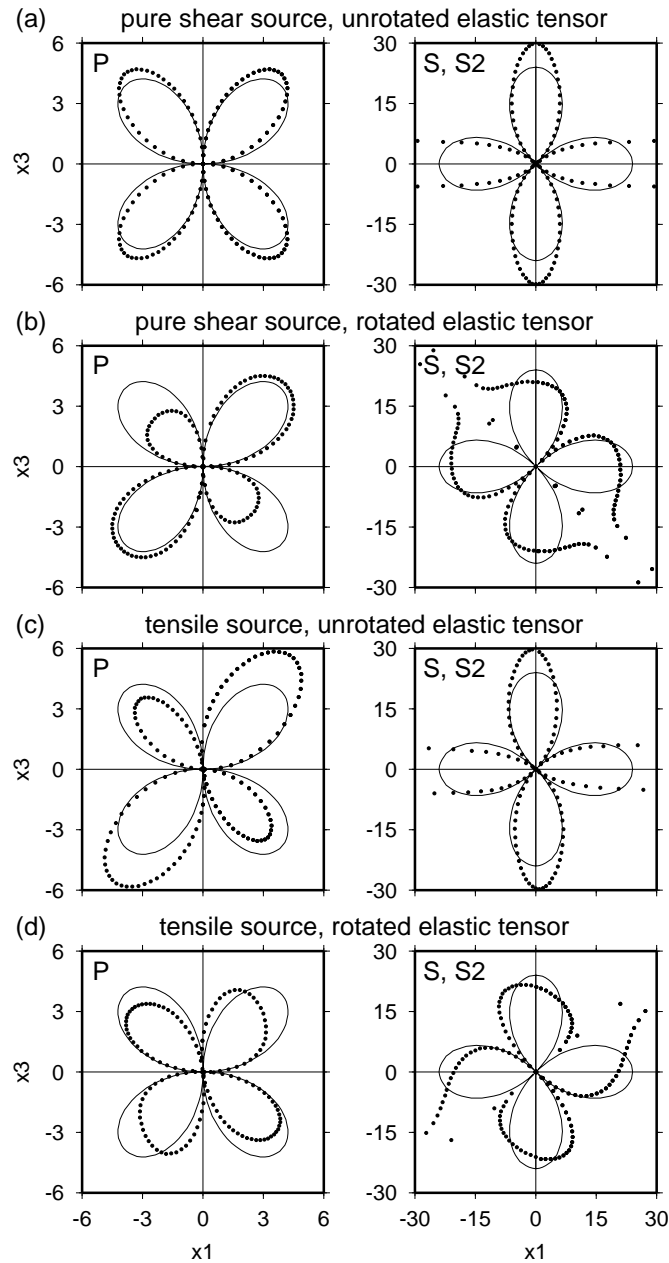


Figure 2.4: Radiation patterns for the case of homogeneous anisotropy (the same anisotropic properties are used for the inclusion and the along-path medium). Otherwise as in Fig. 2.2.



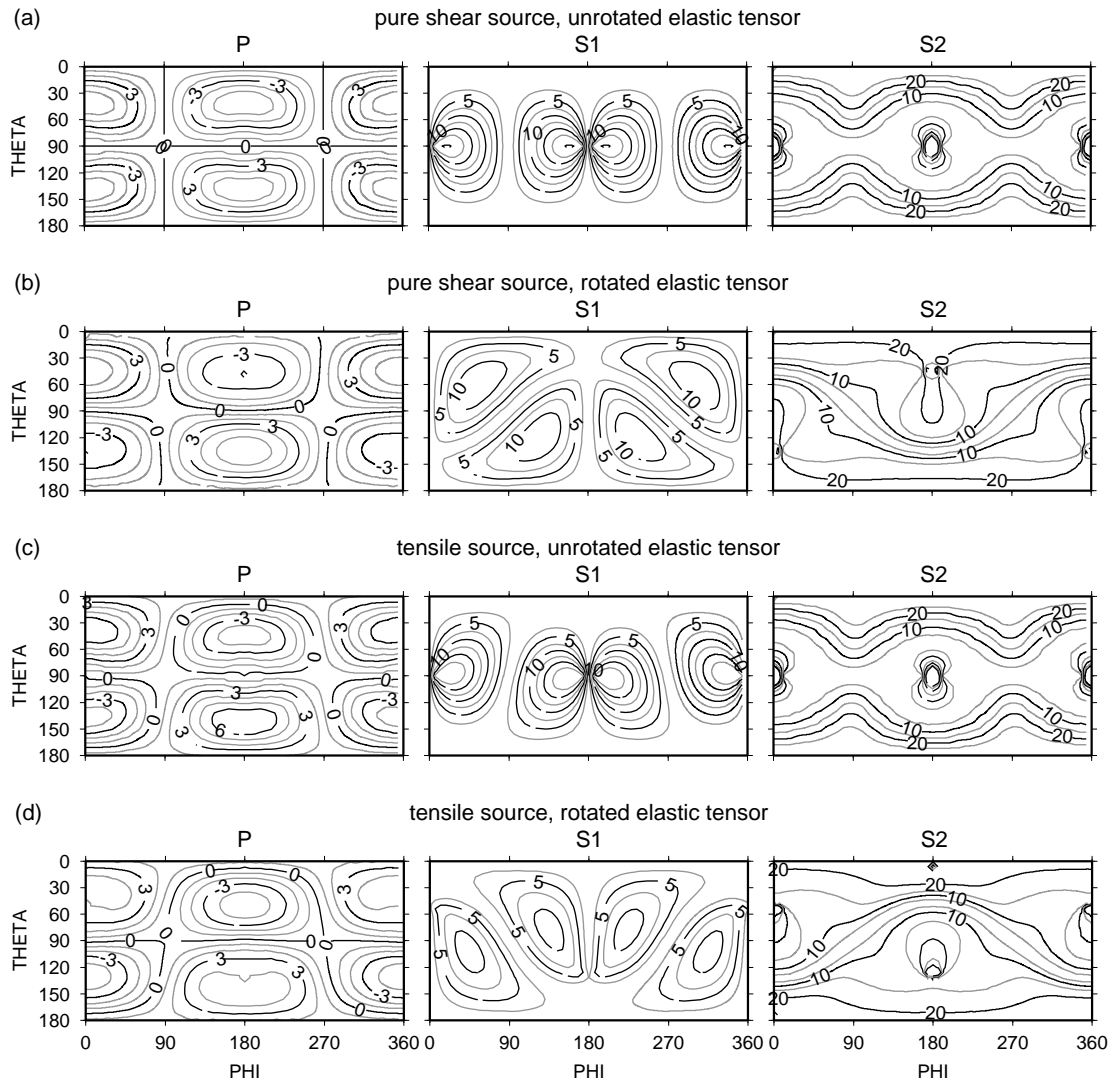


Figure 2.5: Radiation patterns for the case of homogeneous anisotropy. Otherwise as in Fig. 2.3. The S-wave amplitudes for values of  $\phi = 0^\circ$  ( $, 360^\circ$ ),  $180^\circ$  have to be considered with care, as they may correspond to directions of slowness-surface singularities.

For certain directions, which are related to shear-wave slowness-surface singularities in the vicinity of the  $x_1$ -axis, the high-frequency approximation for the computation of the anisotropic Green's function breaks down, leading to unphysically large values for the radiation amplitudes. For these directions the shear waves do not propagate independently leading to frequency dependent amplitude effects. The application of more complete solutions for the displacements based on integral representations is necessary to describe the corresponding waveform. These complications are not considered in the present paper.

Contours of the radiation patterns (Fig. 2.5) may be characterized as follows.

- i) For the shear source in the unrotated medium (M1) we find quadrant-type P-wave radiation; the corresponding radiation patterns for S1 and S2 are symmetric with respect to  $\theta = 90^\circ$ , which corresponds to the  $x_1$ - $x_2$ -plane.
- ii) For the shear-source in rotated medium (M1<sup>-</sup>) the P-wave radiation is of non-quadrant type; the previous symmetry for the S1 and S2 radiation is lost.
- iii) For the tensile source in the unrotated medium the P-wave radiation is of non-quadrant type; the S1 and S2 radiation patterns are similar to case (i).
- iv) For the tensile source in the rotated medium (M1<sup>+</sup>), quadrant-type P radiation dominates (even more clearly as in the previous section), which could be considered a characteristic of pure shear sources. The S1 and S2 radiation patterns are distorted in a characteristic fashion.

For P waves the discrimination between quadrant and non-quadrant type radiation is obvious. For the S waves the interpretation is less clear due to the occurrence of two wavetypes. A more conclusive interpretation of the results should be based on waveform calculations and their inversion. This will be studied in more detail in a forthcoming paper.

## 2.4 Case study: Modeling of anisotropic effects in the W-Bohemian earthquake region

The earthquakes of the W-Bohemian swarm episode of 1997 show two spatially distinct event clusters with different focal mechanisms of either small (type A) or up to about 50% (type B) non-double-couple components (see *Vavryčuk, 2002; Dahm et al., 2000; Horálek et al., 2000b*). The latter have been interpreted as tensile earthquakes due to hydrofracturing (*Vavryčuk, 2002*). However, since anisotropy is also present in this region (*Vavryčuk, 1993*), we are interested in the possible consequences for the interpretation of the source mechanism. The effects of anisotropy on isotropic moment-tensor-inversion schemes have recently been investigated by *Šílený* and *Vavryčuk* (2002) in great detail. Here, we use a more exemplary approach, which is limited to the forward problem, but also accounts for the previously omitted effects of anisotropy on the moment tensor itself. We further consider effects of inhomogeneous anisotropic properties due to distinct near-source anisotropy (an inclusion). As before, we assume a smooth change of the elastic properties from the source to the medium along the ray path such that effects due to wavetype conversion can be neglected. We assume that the ray direction is determined by the anisotropic properties of the along-path medium.

In the following, we present radiation patterns for pure shear sources based on the source geometry defined by events of type B. The computation of radiation patterns is carried out using eq. (2.2). In our modeling, coordinates are chosen such that the  $x_1$ -axis points to the east, the  $x_2$ -axis points north, and the  $x_3$ -axis is taken positive upwards. The elastic properties of the medium along the ray-path are defined by the Schoenberg-Douma's model for the W-Bohemian swarm earthquake region of *Vavryčuk* (1993). Here, the elastic tensor (M1, see Tab. 2.1) is rotated by  $59^\circ$  (counterclockwise) about the  $x_3$ -axis such that the horizontal symmetry axis points N31°E in agreement with the findings of *Vavryčuk* (1993).

We further adopt a fault geometry similar to that for events of type B by choosing strike= $45^\circ$ , dip= $90^\circ$ , and rake= $45^\circ$ . This corresponds to a slip vector  $\mathbf{s} = (1/2, 1/2, 1/\sqrt{2})$  and a fault normal  $\mathbf{n} = (1/\sqrt{2}, -1/\sqrt{2}, 0)$ . We consider four cases:

*Case A0:* In this reference case the along-path medium is characterized by average isotropic elastic properties, whereas the anisotropic inclusion exhibits the elastic properties of medium M1. This includes a rotation about the vertical axis such that the horizontal symmetry axis aligns parallel to N31°E.

*Case A1:* For this homogeneous anisotropic model the entire medium exhibits the same elastic properties as the anisotropic inclusion of case A0.

*Case A2 (inhomogeneous anisotropic model I):* Here we assume that the fracture zone (modeled by the inclusion) exhibits strong P and S-wave anisotropy of 10% (*Crampin*, 1994) due to extreme deformation and remineralization. Further assuming mineralization in layers parallel to the fault plane, we take a generic transversely isotropic (TI) elastic tensor (M2, see Tab. 2.1) with symmetry axis parallel to the fault normal. Here, the symmetry axis corresponds to the slow direction for both P and S waves. In the surrounding medium, along the ray path, we assume the same anisotropic elastic properties as in the previous case (A1). Thus, the symmetry axis at the source lies oblique to that in the along-path medium.

*Case A3 (inhomogeneous anisotropic model II):* Recent studies indicate that the foci of the swarm events in W-Bohemia are located in a N-S striking shear zone (*Bankwitz et al.*, 2002; *Bankwitz and Schneider*, 2000). Considering the same orienting mechanisms as in the previous case (A2), the properties of the inclusion may be characterized by TI anisotropy with an E-W oriented symmetry axis. Outside of the inclusion we assume equal anisotropic elastic properties as in the previous cases (A1 and A2).

Radiation patterns for the different cases are given in Figs. 2.6 and 2.7, respectively. The cross-sections shown in Fig. 2.6 correspond to the vertical E-Z plane. Note that, unlike the previous section, the fault plane is oblique to the E-Z plane such that the typical four-lobe pattern is not apparent in this representation. The findings can be summarized as follows:

- i) The source for cases A0 and A1 leads to a seismic moment tensor which is dominated by double-couple components (DC=94.1%). However, due to the oblique orientation of the fault with respect to the anisotropic symmetry planes, volumetric components (ISO=5.1%) are created (see Tab. 2.2 for the moment tensor decomposition). The volumetric effects are relatively small; they are most apparent for P waves in Figures 2.7a-b, where the nodal lines are separated. The

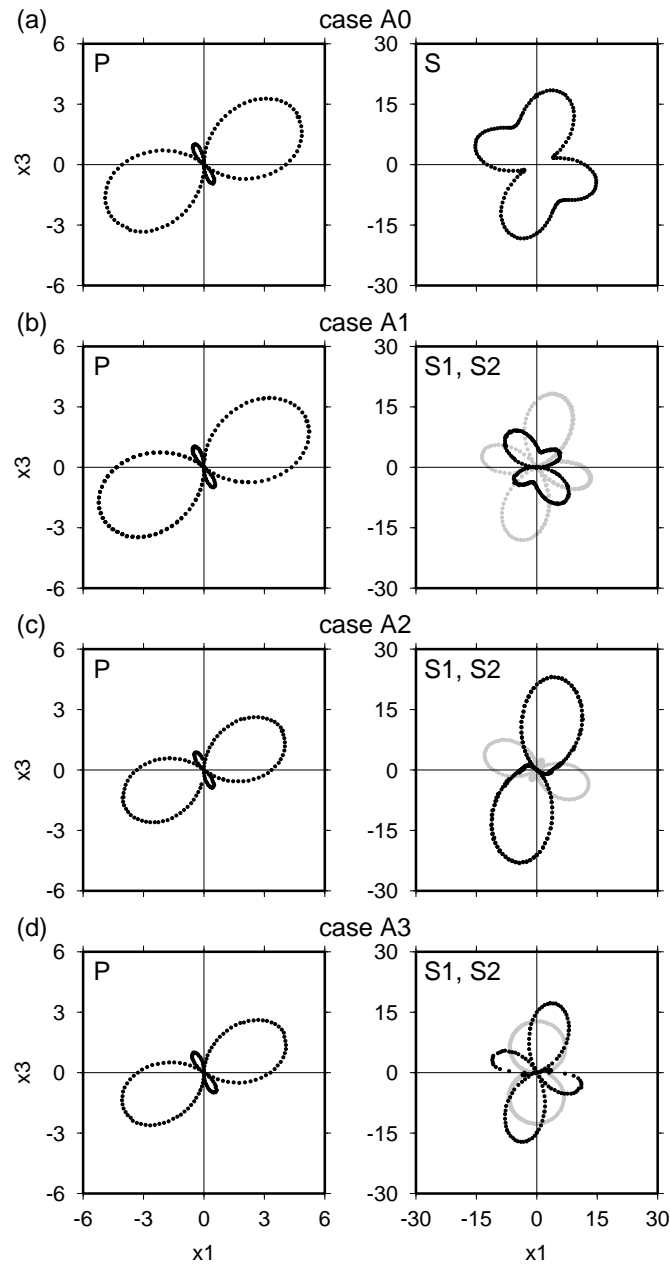


Figure 2.6: Radiation patterns of the P, S1 (grey), and S2 (black) waves for faulting of type B. Here,  $x_1$  points to the east,  $x_3$  points upwards, oblique to the fault normal and the slip. Case A0 corresponds to the anisotropic inclusion with elastic properties given by medium M1. The surrounding along-path medium is assumed isotropic. Case A1 corresponds to homogeneous anisotropy with properties given by medium M1. Case A2 corresponds to a transversely isotropic inclusion with properties given by medium M2; the axis of symmetry is aligned with the fault normal. Case A3 corresponds to a transversely isotropic inclusion given by medium M2; the axis of symmetry points east. The surrounding medium for cases A1-A3 is given by the same elastic tensor (medium M1, see text for details). Apparent gaps in the radiation patterns are due to the irregular sampling interval in this non-symmetry plane. Units are given in  $\mu\text{m}$ .

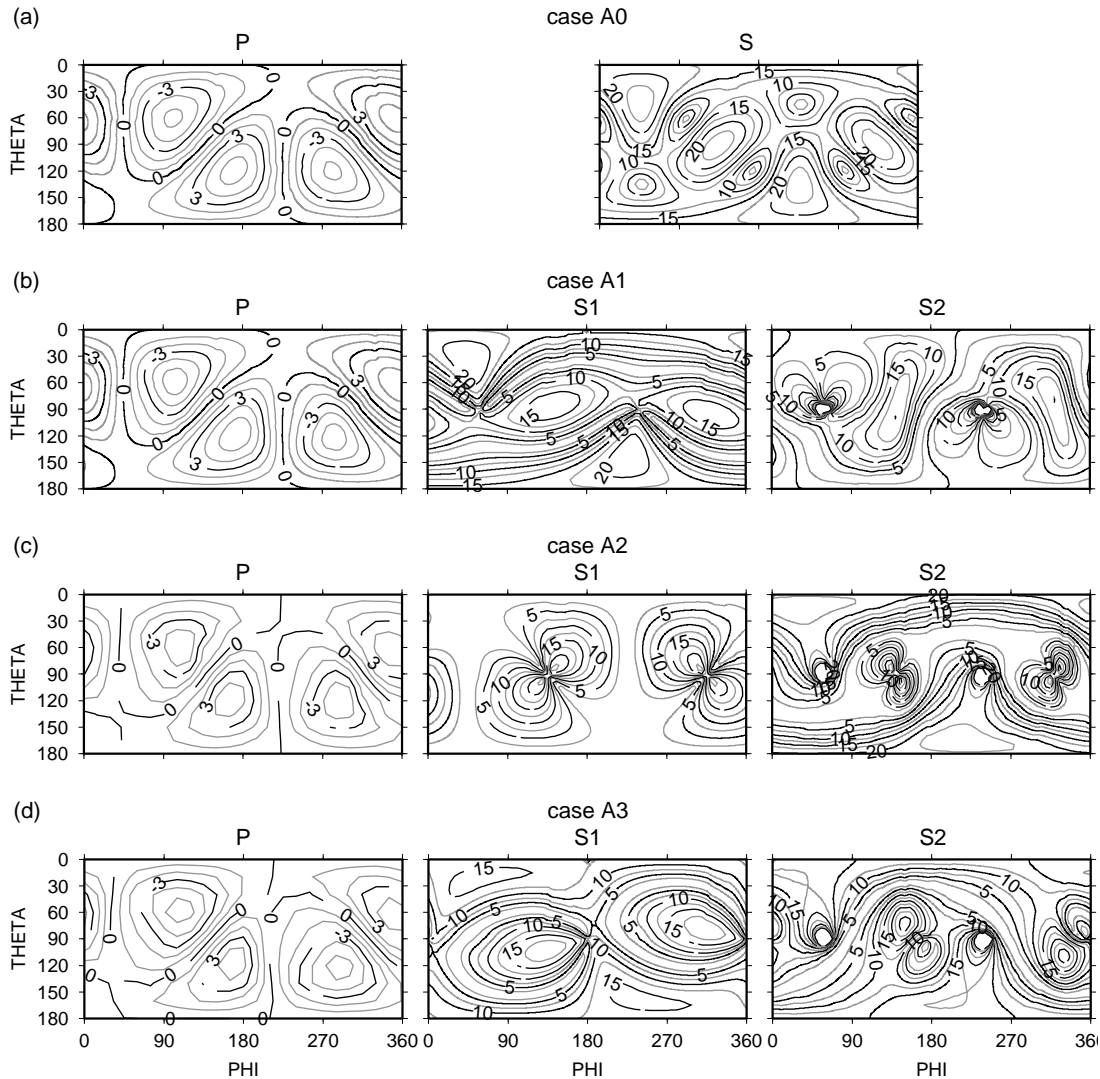


Figure 2.7: Mercator projection of radiation patterns. Otherwise as in Fig. 2.6. Note singular directions for S waves near  $\theta = 90^\circ$  in (b)-(d).

amplitude values in dilatational and compressional regions are almost the same. While the anisotropic properties of along-path medium have little effect on the P-wave radiation (A1), they do cause S-wave splitting which is expected to significantly affect waveforms. However, from the cross-sections it becomes apparent that summing-up the contributions from the two S waves (case A1) will lead to similar S-wave radiation patterns as in the previous case (A0).

- ii) For case A2, the isotropic component of the moment tensor vanishes (see Tab. 2.2). This is because the anisotropy (TI) in the inclusion exhibits a symmetry axis parallel to the fault normal (see section 2). Contours of the P-wave radiation show closely-spaced nodal lines and nearly equal amplitudes for regions of compression and dilatation (Fig. 2.7c). Radiation patterns for the two S waves exhibit relatively strong differences compared to case A1.

- iii) For case A3, the oblique orientation between source anisotropy and fault plane

causes significant (negative) non-double-couple components of the moment tensor (DC=77.9%, ISO=-6.5%, CLVD=-15.6%; see Tab. 2.2). The P-wave radiation pattern is intermediate between cases A1 and A2. The nodal lines are not as close as in the previous inhomogeneous case, but slightly less separated than in the homogenous case. Again, the direct interpretation of the S-wave pattern is difficult. However, comparison with the previous cases (A1, A2) suggests, that they are most sensitive to changes in anisotropic properties of the inclusion.

Table 2.2: Moment tensor decomposition for synthetic faulting of fault type B.

case	DC (%)	ISO (%)	CLVD (%)
A0, A1	94.1	5.1	-0.8
A2	100.0	0.0	0.0
A3	77.9	-6.5	-15.6

## 2.5 Conclusions

- 1) For pure-shear sources in anisotropic media the total seismic moment is sensitive to the slip direction. The decomposition of the moment tensor can lead to significantly different non-double-couple components depending on the orientation of the fault with respect to the anisotropic symmetry planes.
- 2) In cases where anisotropic material properties are limited to the immediate source region (i.e. an anisotropic inclusion), effects on the radiation patterns are most pronounced for P waves. The examples show that the occurrence of apparent volumetric components for pure-shear sources is determined by the orientation of the anisotropic tensor with respect to the fault and the slip. Effects of true tensile faulting may be hidden for certain orientations of the near-source anisotropy with respect to the fault.
- 3) Anisotropic properties in the along-path medium cause pronounced distortions of the S-wave radiation due to effects related to slowness-surface curvature and S-wave splitting. However, to better assess the possible consequences for the interpretation of source mechanisms, the calculation of complete waveforms is required. The P-wave radiation in the homogeneous anisotropic medium is similar to the case, where anisotropy is limited to the inclusion. This indicates that little information can be gained from P-wave radiation on the extent of the anisotropic region.
- 4) The inhomogeneous anisotropic models for the W-Bohemia region cause significantly different radiation patterns for S waves. The P-wave amplitudes are relatively uniform. Their interpretation under isotropic assumptions would yield seismic moment tensors with dominating double-couple components and could, therefore, reveal the correct source mechanism. However, it seems possible that a moment tensor inversion for anisotropic media under inclusion of S waves can significantly improve the interpretation in view of source anisotropy and source

mechanism. Such algorithm is currently under development and will be based on waveform calculations for anisotropic media.

- 5) In our modeling of anisotropy in W-Bohemia, the moment tensor decomposition yields non-double-couple components of up to 22%, which includes isotropic (i.e. volumetric) components of up to 6%. These estimates cannot explain the observed large non-double-couple components. However, the moment tensor decomposition does not account for the possibly significant effects due to anisotropy of the along-path medium. Shear wave splitting and related frequency-dependent amplitude effects will affect P/S-amplitude ratios, which are indicative of volumetric effects in isotropic media. To estimate the significance of apparent tensile contributions more precisely, it would be necessary to apply a conventional isotropic inversion algorithm to synthetic waveforms for the models presented here (see Šílený and Vavryčuk, 2002).

## Acknowledgments

We would like to thank I. Pšenčík, T. Dahm and the two anonymous referees for very helpful comments and suggestions. This work was supported by the Deutsche Forschungsgemeinschaft, grant KR 1935.

### 3 Retrieval of moment tensors due to dislocation point sources in anisotropic media using standard techniques

Dirk Rößler<sup>1\*</sup>, Frank Krüger<sup>1</sup>, Georg Rümpker<sup>2</sup>

<sup>1</sup>Department of Earthsciences, University of Potsdam, K.-Liebknecht-Str. 24, 14476 Golm, FR Germany

<sup>2</sup>Department of Meteorology and Geophysics, University of Frankfurt/Main, Feldbergstr. 47, 60323 Frankfurt/Main, FR Germany

\*corresponding author

Submitted for publication in *Geophysical Journal International*

#### Summary

Anisotropic material properties are commonly neglected during moment tensor inversion. On the other hand, anisotropy is a widely observed rock property. We show that anisotropy may greatly influence characteristics of moment tensors. For the inversion we apply a method based on amplitude spectra of waveforms in isotropic media. We investigate effects of anisotropy on seismic moment, moment-tensor components, and apparent slip inclination of dislocation point sources. The direct calculation of moment tensors for shear sources in anisotropic regions shows spurious non-double-couple components that may be mistaken as an indication of (apparent) opening or closing of the fracture plane. On the other hand real volumetric components may be increased but also hidden in the presence of anisotropy. These effects as well as the seismic moment depend on the orientation of the elastic tensor relative to the fault plane and the slip direction. If anisotropy is present near the source but isotropy is assumed during inversion, the properties of the moment tensor can still be obtained in a good approximation. In the case where anisotropy extends to the medium along the ray path, only the fault orientation can be successfully retrieved by inverting qP waves to derive the deviatoric moment tensor. The inversions show that retrieved moment tensors can deviate systematically from moment tensors of shear and tensile sources expected in isotropic media. Further complications may arise when qS waves are included in the inversion process. We account for near-source anisotropy to re-interpret moment tensors derived for two events at the KTB super deep drill hole, SE-Germany. The obtained source mechanisms are close to shear faulting although the moment tensors comprise non-double-couple components. We interpret the volumetric moment-tensor components partly as a result of anisotropy. This indicates that for detailed studies of volumetric source components anisotropy should be considered during inversion. In addition, we show that for shear sources in anisotropic media the elastic properties near the source can also be derived from inverted moment tensors in media where anisotropy is restricted to the source region.

*Keywords: earthquake-source mechanism, seismic anisotropy, seismology, synthetic waveforms, seismic moment tensor*



### 3.1 Introduction

Seismic moment tensors describe earthquakes in terms of point sources (*Aki and Richards, 2002*). They are used to characterise the orientation of the faulting process, the strength of the event, and they may be indicative of possible volumetric changes. Effects of seismic anisotropy near the source and along the ray-path are commonly neglected during inversion for moment tensors. The source mechanisms of tectonic earthquakes often reveal dislocations that lie purely within the fault plane (double couple sources). However, components of faulting related to opening or closing of the fracture zone (volumetric sources, tensile faulting) are frequently observed in volcanic environments or for complex geometries (e.g., *Sykes, 1967; Solomon and Julian, 1974; Julian et al., 1997, 1998; Miller et al., 1998; Horálek et al., 2000a; Dahm et al., 2000; Vavryčuk, 2002; Foulger et al., 2004*). Seismic anisotropy in the near source region can significantly obscure the properties of the seismic moment tensor and may distort the radiation pattern (*Kawasaki and Tanimoto, 1981; Ben-Menahem et al., 1991; Gajewski, 1993; Rößler et al., 2004; Vavryčuk, 2004*). Thus, amplitudes of seismic waves excited by pure shear faults may be falsely interpreted to result from tensile faulting (*Rößler et al., 2004*). The characteristic effects on the radiated amplitudes that arise from anisotropy at the source and along the ray path are discussed in detail in, e.g., *Gajewski (1993); Pšenčík and Teles (1996)* and *Rößler et al. (2004)*.

In this paper we investigate effects on moment tensor inversion of body waves if anisotropy in the near source region and along the ray path is not accounted for. We therefore perform inversions of synthetic seismograms for dislocation point sources in anisotropic media using an isotropic standard technique. The applied inversion code (*Dahm et al., 1999; Krüger and Dahm, 2002*) aims to fit the spectra of body or surface waves. In our examples the seismic sources are located within an anisotropic host medium. Along the ray path the elastic medium is either isotropic or anisotropic but always anisotropic near the source. We first apply the inversion to specific examples of an earlier paper (*Rößler et al., 2004*) and then generalise by systematically varying the orientation of the elastic tensor in the complete medium. From the retrieved moment tensors the characteristic properties such as seismic moment, source orientation, slip inclination (the angle between the fault normal and the slip direction) as well as double-couple (DC), isotropic (ISO), and compensated linear vector dipole (CLVD) components are determined. These properties are compared with the synthetic moment tensors used in the forward modelling of the waveforms. Using a given set of elastic stiffness parameters (*Rabbell et al., 2004*) we interpret the moment tensor determined by *Jost et al. (1998)* for two events at the KTB borehole, southeast Germany. We further explain how inverted moment tensors can be used to derive the anisotropic elastic constants in the source region. However, if the medium along the ray path is anisotropic we suggest to account for anisotropy during inversion if a detailed study of volumetric source components is required.

### 3.2 Theory

The moment tensor  $\mathbf{M}$  for an effective dislocation point source in a general anisotropic medium can be written as (*Aki and Richards, 2002*):

$$M_{jk} = s_p n_q c_{pqjk} s A_0. \quad (3.1)$$

Here,  $c_{pqjk}$  are the elastic constants that describe properties of the anisotropic medium at the source,  $s_p$  and  $s$  are the direction and the length of the slip,  $n_q$ , and  $A_0$  denote the fault normal and the area of the fault, respectively. Note that in this representation  $s_p$  can point in any direction and is not restricted to lie within the fault plane. Therefore, pure shear faulting as well as shearing that is accompanied by opening or closing of a crack (tensile faulting) can be described by (3.1). In isotropic media Eq. (3.1) reduces to

$$M_{jk} = \lambda s A_0 s_p n_p \delta_{jk} + \mu s A_0 (s_j n_k + s_k n_j), \quad (3.2)$$

where  $\lambda$  and  $\mu$  are the Lamé's constants and  $\delta_{jk}$  denotes the Kronecker symbol. If no volumetric changes are induced by the source  $s_j$  and  $n_k$  are perpendicular and  $s_p n_p = 0$ . Then (3.2) simplifies to

$$M_{jk} = \mu s A_0 (s_j n_k + s_k n_j). \quad (3.3)$$

For tectonic sources in isotropic media that also contain a non-tectonic part  $E$ , such as an explosive source, the moment tensor reads (*Dufumier and Rivera, 1997*)

$$M_{jk} = \lambda s A_0 s_p n_p \delta_{jk} + \mu s A_0 (s_j n_k + s_k n_j) + E \delta_{jk}. \quad (3.4)$$

The seismic moment tensor is used to calculate the seismic moment  $M_0$  which is a measure of the size of the seismic event (*Silver and Jordan, 1982*)

$$M_0 = \sqrt{M_{jk} M_{jk} / 2}. \quad (3.5)$$

The moment tensor can be decomposed into its double-couple (DC) and non-double-couple, i.e. the isotropic (ISO) and the compensated linear vector dipole (CLVD) component. For decomposition various formulae exist (*Silver and Jordan, 1982; Jost and Herrmann, 1989*). Here, we use formulae given in *Vavryčuk (2002)* to calculate the percentage of each component:

$$\text{ISO} = \frac{1}{3} \frac{\text{Tr}(\mathbf{M})}{|\nu'_{max}|} \times 100\%, \quad (3.6)$$

$$\text{CLVD} = -2 \frac{\nu'_{min}}{|\nu'_{max}|} (100\% - |\text{ISO}|), \quad (3.7)$$

$$\text{DC} = 100\% - |\text{ISO}| - |\text{CLVD}|, \quad (3.8)$$

where  $\text{Tr}(\mathbf{M})$  denotes the trace of  $\mathbf{M}$ . It can be calculated from the eigenvalues  $\nu_i$  corresponding to  $\mathbf{M}$  so that  $\text{Tr}(\mathbf{M}) = \nu_1 + \nu_2 + \nu_3$ . Using this, the eigenvalues of the deviatoric component of  $\mathbf{M}$  are calculated from  $\nu'_i = \nu_i - \text{Tr}(\mathbf{M})/3$ . In (3.6) and (3.7), subscripts  $|min|$  and  $|max|$  refer to the minima and the maxima of the absolute values of  $\nu_i$  and  $\nu'_i$ . We see from (3.2) and (3.3) that in isotropic media tensile faulting generates moment tensors with non-double-couple components ( $\text{DC} < 100\%$ ) whereas for pure shear faulting  $\text{Tr}(\mathbf{M}) = 0$  and  $\text{DC} = 100\%$ . In the case of anisotropy it follows from (3.1) that apparent non-double-couple components can be created by pure shear faulting ( $\text{DC} < 100\%$ ). On the other hand, real volumetric source changes due to the opening or closure of the fault may be hidden (*Rößler et al., 2004*). Additional ambiguity

in the origin of the isotropic component may arise from the trade-off between the Lamé parameters  $(\lambda, \mu)$  and an explosion-type source component  $E$  in (3.4). However, we only consider dislocation point sources in this paper but not such cases where dislocation and explosion-type sources can occur during the same event, e.g. during nuclear explosions or collapses of cavities.

Another quantitative measure of the character of a dislocation point source is the (apparent) angle  $\alpha$  between the slip vector and the normal to the fault plane (slip inclination). It may be directly derived from the eigenvalues of the deviatoric moment tensor (*Dufumier and Rivera, 1997*):

$$90^\circ - \alpha = \arcsin \left( 3 \frac{\nu'_{max} + \nu'_{min}}{\nu'_{max} - \nu'_{min}} \right). \quad (3.9)$$

Therefore, the slip inclination is independent of the isotropic moment tensor. Eq. (3.9) can be used to relate the decomposed moment tensor to the source properties. In isotropic media  $\alpha = 90^\circ$  for pure shear faulting,  $\alpha < 90^\circ$  for the opening, and  $\alpha > 90^\circ$  for the closure of cracks. However, for moment tensors of shear sources in general anisotropic media  $\alpha \neq 90^\circ$  can be expected. Notice that depending on the strength of the ISO and CLVD components (apparent) slip inclinations indicating opening or closure of the fault can occur for both, positive and negative isotropic (ISO) components of moment tensors.

In anisotropic media three distinct wave types exist (qP, qS1, qS2). For each wavetype the far-field displacement  $u_i$  due to a source at  $\mathbf{x}_0$  in an inhomogeneous anisotropic medium can be approximated at any location  $\mathbf{x}$  and time  $t$  (*Pšenčík and Teles, 1996*) by

$$u_i(\mathbf{x}, t) = g_i(\mathbf{x}) \left[ \frac{\rho(\mathbf{x}_0)c(\mathbf{x}_0)}{\rho(\mathbf{x})c(\mathbf{x})} \right]^{1/2} \frac{Df^{(A)}(t - \tau(\mathbf{x}))}{|\Omega_M(\mathbf{x})|^{1/2}} \exp \left[ i\frac{\pi}{2}k_s - i\frac{\pi}{2}k(\mathbf{x}_0, \mathbf{x}) \right]. \quad (3.10)$$

The quantity  $D$  is called the directivity function referring to the spreading free amplitude at the source (*Pšenčík and Teles, 1996*). It shall not be confused with the directional dependence of radiated amplitudes due to fault propagation of finite sources (*Lay and Wallace, 1995*). The directivity function is dependent on elastic properties near the source. In (3.10)  $\Omega_M$  is the geometrical spreading,  $g_i$  is the vector of polarisation at  $x_i$ ,  $\rho$  is the density,  $c$  is the phase velocity, and  $f^{(A)}$  is the analytical signal corresponding to the source time function. The integer quantities  $k$  and  $k_s$  are the indices of the trajectory and of the source (see *Pšenčík and Teles, 1996*, for a detailed description). Note that Eq. (3.10) fails in directions coinciding with singularities of the slowness surfaces of the qS waves (singular directions) or wherever the anisotropy is weak and coupling between qS1 and qS2 occurs (see *Pšenčík and Dellinger, 2001*). For a moment tensor source

$$D(\mathbf{x}_0, \theta, \phi) = \frac{g_j(\mathbf{x}_0)M_{jk}p_k(\mathbf{x}_0)}{4\pi\rho(\mathbf{x}_0)c(\mathbf{x}_0)}, \quad (3.11)$$

where the  $p_k$  denote the components of the slowness vector. If anisotropy is present along the ray path

$$\Omega_M = (v/c)^2 Kr^2 \quad (3.12)$$

which simplifies to  $\Omega_M = (rc)^2$  in the isotropic case. In (3.12)  $v$  is the group velocity,  $K$  is the principal curvature of the slowness surface (for details see *Gajewski, 1993; Pšenčík and Teles, 1996*), and  $r$  is the distance from the source to the receiver. We approximate the corresponding isotropic velocities:  $v_p = \sqrt{(A_{11} + A_{22} + A_{33})/3}$ ,  $v_s = \sqrt{(A_{44} + A_{55} + A_{66})/3}$ , where  $A_{ij}$  represent the density normalised elastic tensor in the Voigt notation (e.g., *Bos et al., 2004*).

### 3.3 Synthetic example

In the following we investigate effects of anisotropy on retrieved seismic moment tensors if anisotropy is neglected during the inversion process. We concentrate on the determination of the fault orientation as well as on moment tensor characteristics for exemplary conditions. As in *Rößler et al. (2004)* we consider two basic source types located at 10 km depth (see Fig. 3.1 for the orientation of both sources and the coordinate system): pure shear faulting within a horizontal plane (type 1) and tensile faulting, i.e. shearing with a minor component (10%) of crack opening (type 2). We assume that the source region is transversely isotropic. The corresponding anisotropic elastic constants used in our calculations are derived from seismograms recorded during the 1985/86 swarm episode in W-Bohemia, Czech Republic (transversely isotropic medium M1, see Table 3.1, *Vavryčuk, 1993*).

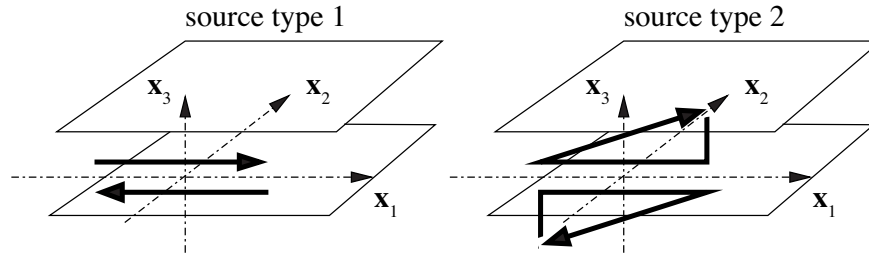


Figure 3.1: Schematic sketch of a shear fault with slip in the  $\mathbf{x}_1$ - $\mathbf{x}_2$  plane (source type 1) and a tensile fault with slip out of the  $\mathbf{x}_1$ - $\mathbf{x}_2$  plane (source type 2).

Table 3.1: Density normalised elastic constants  $A_{ij}$  in Voigt notation for West Bohemia (medium M1, *Vavryčuk, 1993*), for the generic transversely isotropic media with 1% (medium M2) or 10% (medium M3) anisotropy (*Rümpker and Kendall, 2002*), and for the KTB borehole at 7.9-8.2 km depth (medium M4, *Rabbel et al., 2004*).  $[A_{ij}] = \text{km}^2/\text{s}^2$ ,  $[\rho] = \text{kg}/\text{m}^3$ ;  $C_{ij} = A_{ij} * \rho * 10^6$ .

medium	$A_{11}$	$A_{12}$	$A_{13}$	$A_{22}$	$A_{23}$	$A_{33}$	$A_{44}$	$A_{55}$	$A_{66}$	$\rho$
M1	23.5	7.8	7.8	31.9	9.9	31.9	11.0	10.8	10.8	2850
M2	35.6	11.9	11.9	35.6	11.9	36.4	12.1	12.1	11.9	2650
M3	39.7	13.2	13.2	39.7	13.2	32.5	10.8	10.8	13.2	2650
M4	37.3	9.1	9.1	37.3	9.1	26.1	9.8	9.8	14.1	2750

We consider 4 different combinations of source type and near-source anisotropy to compute moment tensors from Eq. (3.1) and their characteristics using Eqs. (3.5)-(3.9) (compare Table 3.2):

(A1) source type 1; the symmetry axis of the elastic tensor is parallel to the slip direction ( $\mathbf{x}_1$ -axis, unrotated elastic tensor). Therefore, this moment tensor contains no apparent non-double-couple components.

(A2) source type 1; the elastic tensor is rotated by  $\gamma = -45^\circ$  about  $\mathbf{x}_2$  (clockwise rotation, see Fig. 3.1). The symmetry axis of the elastic tensor is neither aligned with the slip direction nor with the fault normal. This combination causes (apparent) non-double-couple components due to anisotropy.

(A3) source type 2; unrotated elastic tensor. Non-double-couple components exist due to tensile faulting. They are of similar size as apparent non-double-couple components observed for (A2).

(A4) source type 2; elastic tensor is rotated by  $\gamma = +40^\circ$  about  $\mathbf{x}_2$  (counterclockwise). For this combination non-double-couple source components are hidden in the moment tensor due to anisotropy. The characteristics of the moment tensors of this source are therefore comparable to (A1).

Based on these 4 cases (A1)-(A4) we generate synthetic waveforms applying (3.10) and invert them for the moment tensor. Hereby, we neglect anisotropy and assume that the complete medium is isotropic. The receivers are situated at the free surface in a specific configuration rather ideal to avoid further complications due to insufficient station coverage (see Figs. 3.2 and 3.3). To discriminate the effects of anisotropy at the source and along the ray path, waveforms are calculated assuming that the source region is anisotropic and the medium outside the source is either isotropic (inhomogeneous model) or anisotropic with the same properties as in the source region (homogeneous model).

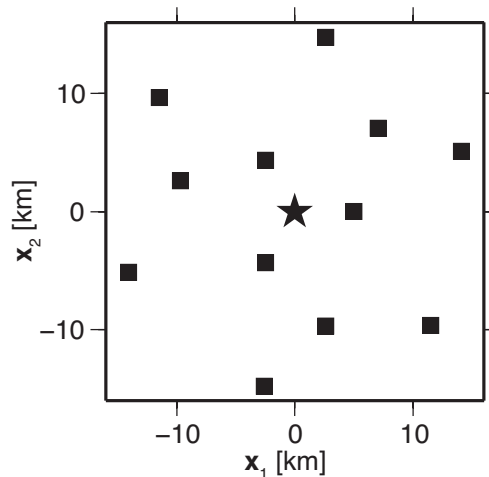


Figure 3.2: Distribution of stations (squares) and event at 10 km depth (star) for computation of synthetic seismograms.

The moment tensor inversion is performed by fitting the amplitude spectra of the synthetic waveforms (Dahm *et al.*, 1999; Krüger and Dahm, 2002). We consider the complete signal of the respective type of wave and frequencies up to 40 Hz. Compared to other methods working in the time domain (e.g., Langston *et al.*, 1982; Šílený and Vavryčuk, 2000; Pinar *et al.*, 2003) this method avoids complications introduced by erroneously determined traveltimes. Moreover, instead of fitting S waves for isotropic media to the waveform of one recorded qS wave only (qS1 or qS2) the spectra of both qS waves can be matched simultaneously. However, the spectral con-

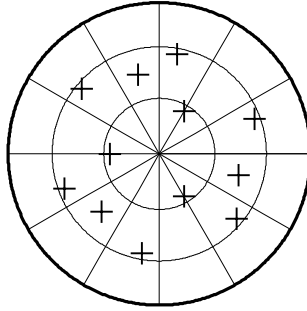


Figure 3.3: Ray take-off angles in lower hemispherical projection for stations and event in Fig. 3.2.

tent of one S wave in an isotropic medium differs from the two split qS1 and qS2 waves in an anisotropic medium. In addition, the polarisation of the particle motion in anisotropic and isotropic media are different. Therefore, we expect biasing by this method when neglecting anisotropy during inversion of qP and especially of the qS waves. It is further possible to either invert for all 6 independent elements of  $\mathbf{M}$  or to apply mathematical constraints, e.g. by suppressing the isotropic part of  $\mathbf{M}$  forcing  $\text{Tr}(\mathbf{M}) = 0$ . In seismological practice, the latter option is frequently applied to stabilise the inversion. The inversion is linearised and iterative. Therefore, during inversion we consider many starting models ( $3^6$ ) for the moment tensor. Depending on the shape of the misfit function we may obtain different moment tensors and residuals from the solutions for different starting models. The inversions are carried out using the vertical component of the P waves (P and qP). In our figures and tables results are referred to as P\* and P for inversions of vertical component of P (isotropy along the ray path) and qP (anisotropy along the ray path), respectively. Additionally, the transverse components of the S waves (S and qS) are included. The results are similarly referred to as P+S\* (isotropy along the ray path) and P+S (anisotropy along the ray path). Results obtained by using the transverse and the radial components of the S waves in addition to the P waves is referred to as P+SS\* (isotropy along the ray path) and P+SS (anisotropy along the ray path).

We invert for the moment tensor and compare the results with the true moment tensor used to calculate the synthetic waveforms (see Fig. 3.4 and Table 3.2). First we consider the fault-plane solutions of retrieved moment tensors with similar residuals (Fig. 3.4). If the medium along the ray path is isotropic and the medium surrounding the source is anisotropic we find that the fault orientation may be reliably determined from P and S waves within few degrees (see Fig. 3.4). Here, the correct fault-plane solution is connected with the smallest residual. To test the stability of inversion we use different components of seismograms. We use the vertical component of the P waves alone, the vertical component of the P waves together with the transverse component of the S waves, or the vertical component of the P waves together with the transverse and the radial component of the S waves. For isotropy along the ray path (cases P\*, P+S\*, and P+SS\* in Fig. 3.4) obtained results are similar. The correct fault-plane solution can be derived. However, 2 groups of solutions with similar misfit exist for the sources of type A1 and A2 when only P waves are used for inversion. Among these 2 groups the correct solutions are associated with the smallest misfit. Here, mismodelling of the fault orientation (strike-slip solution with strike direction  $\approx 45^\circ$  instead of dip slip) is

compensated by large non-double-components ( $DC < 50\%$ ). Using S wave information improves the uniqueness of fault-plane solutions. Ambiguity rises where anisotropy is present along the ray path (cases P, P+S, and P+SS in Fig. 3.4). Here, different focal mechanisms may fit the data (amplitude spectra) with similar residuals. Using qS waves during inversion intensifies this effect where anisotropy is more complex, e.g. in cases (A2) and (A4). This problem can be overcome by applying the constraint  $\text{Tr}(\mathbf{M}) = 0$ , i.e. by inverting for the deviatoric moment tensor. If moment tensors are retrieved only from qP waves forcing  $\text{Tr}(\mathbf{M}) = 0$  the fault-plane solutions corresponding to the smallest residuals coincide well with the true fault planes (see Fig. 3.4). Thus, they can be determined even if anisotropy is present along the ray path. Therefore, if evidences for anisotropy are observed we suggest to first determine the orientation of the fault plane applying the constraint  $\text{Tr}(\mathbf{M}) = 0$ . In the next step the data are inverted for the 6 independent elements of  $\mathbf{M}$  (no constraint); the moment tensor is chosen from the set of best-fitting inversion results by comparing the obtained fault-plane solutions with the fault orientation retrieved before. This processing flow was important for the homogeneous model (anisotropic medium along the ray path and in the source region) to identify the correct focal mechanism from the set of solutions. The non-double-couple components of retrieved moment tensors may vary considerably even for fault-plane solutions with similar misfit. Choosing an incorrect fault-plane solution might therefore lead to erroneous interpretation of the source in terms of its tensile character.

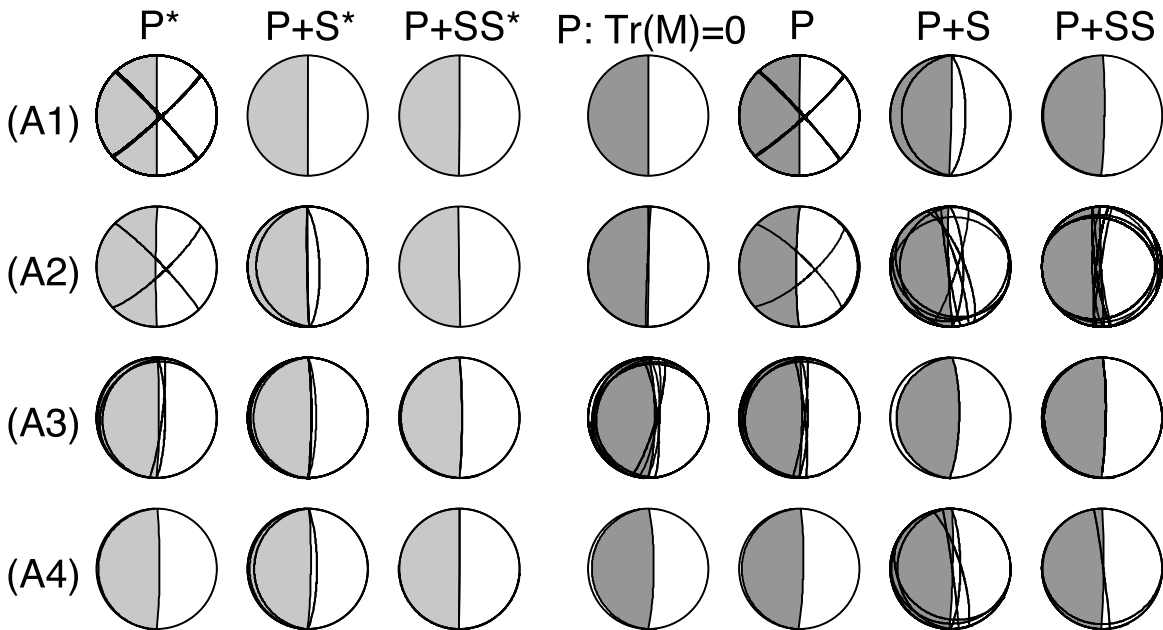


Figure 3.4: Best double-couple solutions (gray-shaded) of retrieved moment tensors (s. Table 3.2) for the sources in the medium M1 and for source models (A1)-(A4). Notations as in Table 3.2, lower-hemisphere projection. Fault planes obtained from inversions with different starting models and with residuals smaller than 1.5 times the residual of the best solutions are also plotted (black lines). Additionally, fault-plane solutions based on inversion of qP (homogeneous anisotropic models) forcing  $\text{Tr}(\mathbf{M}) = 0$  are presented (referred to as P:  $\text{Tr}(\mathbf{M}) = 0$ ).

If anisotropy is restricted to the source area (inhomogeneous models) it appears that the slip inclination rather than the moment-tensor components are retrieved with

confidence (see Tab. 3.2). Shear and tensile faulting are clearly separated and can be identified after inversion. Moment tensors retrieved for the sources in the rotated media (A2 and A4 in Tab. 3.2) are similar to the calculated moment tensors of the same sources in the unrotated medium (A1 and A2).

Anisotropy along the ray path (homogeneous models) and greater medium complexity by rotation of the elastic tensor (A2 and A4 in Tab. 3.2) lead to decreasing agreement of retrieved and true source properties when using qP (case P in Tab. 3.2). Mainly the CLVD components and the slip inclination show large variability and are difficult to interpret. Owing to more complicated radiation patterns (*Rößler et al.*, 2004) this effect is even intensified when additionally using qS waves (cases P+S and P+SS in Table 3.2). In this case a decrease in solution uniqueness may be an indicator for the importance of anisotropy along the ray path.

Table 3.2: Characteristics of true and inverted moment tensors for combinations of source type and near-source anisotropy (A1)-(A4) (see Eqs. 3.1, 3.7-3.8, 3.9). Source type 1:  $\mathbf{s} = (1,0,0)$ ,  $\mathbf{n} = (0,0,1)$ , source type 2:  $\mathbf{s} = (0.99,0,0.12)$ ,  $\mathbf{n} = (0,0,1)$ . P\*/P: inversions are only based on the vertical component of P/qP; P+S\*/P+S: the transverse components of S/qS waves are additionally used; P+SS\*/P+SS: the transverse and the radial components of S/qS waves are additionally used. The moment-tensor components inverted from waveforms calculated for inhomogeneous models (anisotropic at the source, isotropic along the ray path) are marked with asterisks. Otherwise the medium is homogeneously anisotropic.

model specification		true m.t.	retrieved moment tensor					
			isotropic medium along ray path			anisotropic medium along ray path		
			P*	P+S*	P+SS*	P	P+S	P+SS
(A1) source:	DC [%]	100	96	98	99	94	89	88
type 1	ISO [%]	0	0	0	1	0	1	-5
medium:	CLVD [%]	0	4	-1	1	6	-10	7
unrotated	$\alpha$ [°]	90	88	91	89	87	95	87
	residual		0.01	0.01	0.02	0.01	0.03	0.04
(A2) source:	DC [%]	74	89	84	93	68	64	86
type 1	ISO [%]	14	8	9	7	12	18	13
medium:	CLVD [%]	12	3	-7	0	20	-18	0
rotation by	$\alpha$ [°]	90	89	93	90	80	99	90
$\gamma = -45^\circ$	residual		0.01	0.01	0.02	0.01	0.14	0.13
(A3) source:	DC [%]	74	74	69	71	72	57	69
type 2	ISO [%]	14	14	16	18	14	13	24
medium:	CLVD [%]	12	12	15	10	14	29	7
unrotated	$\alpha$ [°]	83	84	82	84	83	74	86
	residual		0.01	0.01	0.02	0.02	0.03	0.04
(A4) source:	DC [%]	99	76	70	73	74	60	46
type 2	ISO [%]	0	9	9	14	8	7	4
medium:	CLVD [%]	0	15	20	14	-18	33	50
rotation by	$\alpha$ [°]	83	82	80	83	99	73	63
$\gamma = +40^\circ$	residual		0.01	0.01	0.02	0.01	0.06	0.09

m.t.=moment tensor



### 3.4 Generalisation

After analysing results of moment tensor inversions for specific anisotropic models we now present characteristic features of moment tensors for shear and tensile faulting under more general conditions. We concentrate on moment tensors retrieved from synthetic waveforms and moment tensors used for waveform modelling. For the geometry of the synthetic source models we choose  $\mathbf{s} = (1,0,0)$ ,  $\mathbf{n} = (0,1,0)$  for shear faulting (vertical strike-slip faulting, source type 1, see Fig. 3.1 for the coordinate system) and  $\mathbf{s} = (1,0.1,0)$ ,  $\mathbf{n} = (0,1,0)$  for tensile faulting (source type 2). We also study effects that are related to the degree of anisotropy. The elastic properties are therefore described by the same generic transversely isotropic media with 1% (medium M2) and with 10% anisotropy (medium M3), respectively (see Table 3.1). Making use of its symmetry properties we systematically rotate the elastic tensor about the  $\mathbf{x}_1$ -axis within  $0^\circ \leq \beta \leq 180^\circ$  and the  $\mathbf{x}_2$ -axis within  $-90^\circ \leq \gamma \leq 90^\circ$ , respectively, in intervals of  $10^\circ$ . For no rotation ( $\beta = \gamma = 0^\circ$ ) the symmetry axis is parallel to  $\mathbf{x}_3$ . Using each set of stiffness parameters and source model we analyse properties of the moment tensor.

#### 3.4.1 Properties of generated moment tensors

Characteristics of moment tensors modelled by Eq. (3.1) for both fault types are presented in Figures 3.5 and 3.6. There, systematic dependencies between the orientation of the elastic tensor with respect to the fault and the modelled moment tensors can be found. In our Figs. 3.5-3.10 "no rotation" refers to the point (0,0). Pure shear in the medium M2 (see Fig. 3.5a) produces significant apparent non-double-couple components over a wide range of orientations of the elastic tensor. They can be related to the apparent slip inclination  $\alpha$ . Both, apparent opening ( $\alpha < 90^\circ$ ) or closure ( $\alpha > 90^\circ$ ) of the fault are comprised in the moment tensors due to the effect of anisotropy in the near source area. Not surprisingly, these effects further increase for stronger anisotropy (medium M3, see Fig. 3.6a). The distribution of  $\alpha$  is similar to that of the CLVD than to that of the ISO because only the deviatoric moment tensor is used for determination. The seismic moment  $M_0$  is also influenced. For 10% anisotropy variations of up to 20% occur. They depend on the orientation of the elastic tensor. Similar effects can be observed for the tensile source in the media M2 and M3 (see Figs. 3.5b, 3.6b). After rotation of the elastic tensor the components of the forward-modelled moment tensors vary with the orientation of the medium parameters. The isotropic components (ISO) are either increased or decreased compare with "no rotation" but remain positive. In contrast, from the apparent slip inclinations we find that fracture opening is completely hidden in the moment tensor for some orientations ( $\alpha \approx 90^\circ$ ). It can even be over-compensated within a small range of orientations ( $\alpha \geq 90^\circ$ ), i.e. the moment tensor of this tensile source that exhibits fracture opening comprises the apparent character of fracture closing. Notice that also for this source model the behaviour of the CLVD and the  $\alpha$  are well correlated.

#### 3.4.2 Properties of retrieved moment tensors

Next, we compare moment tensors used for the generation of synthetic waveforms with moment tensors retrieved from the synthetic waveforms under assumption of isotropy (see Figs. 3.7-3.10). To study the different effects related to anisotropy in

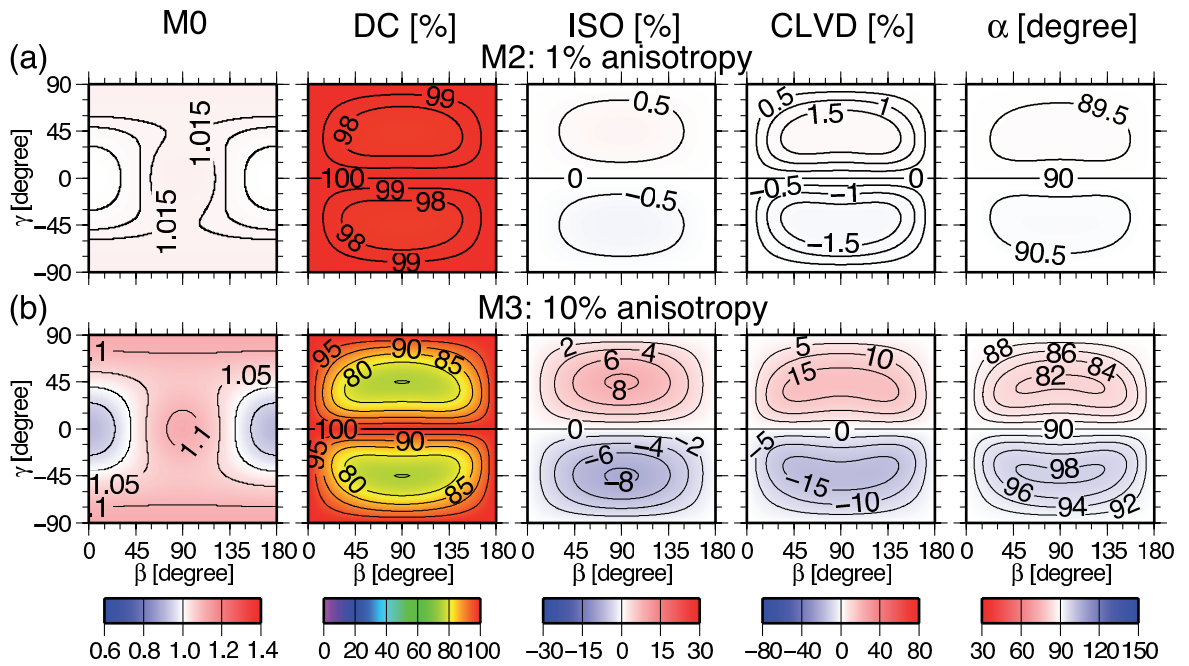


Figure 3.5: Seismic moment, moment-tensor components and apparent slip inclination  $\alpha$  for different orientations of the anisotropic elastic tensor and synthetic shear faulting. Source:  $\mathbf{s} = (1,0,0)$ ,  $\mathbf{n} = (0,1,0)$ . The anisotropic elastic source medium is transversely isotropic with (a) 1% and (b) 10% anisotropy. The elastic tensor was systematically rotated by the angles  $\beta$  and  $\gamma$  about the  $\mathbf{x}_1$ - and the  $\mathbf{x}_2$ -axes, respectively. In (a) and (b)  $M_0$  is normalised by  $3.2 * 10^{10}$ .

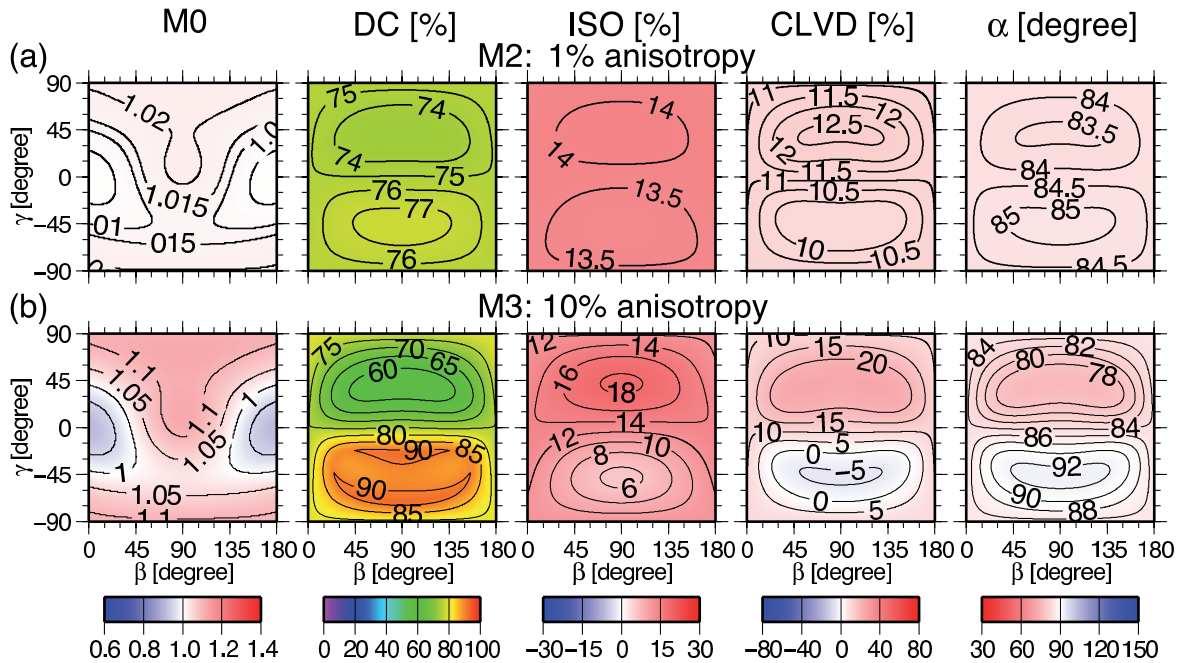


Figure 3.6: Seismic moment, moment-tensor components and apparent slip inclination  $\alpha$  for different orientations of the anisotropic elastic tensor and synthetic tensile faulting. Source:  $\mathbf{s} = (1,0,1,0)$ ,  $\mathbf{n} = (0,1,0)$ . Otherwise as in Fig. 3.5.

the source region and along the ray path waveforms are modelled for sources of type 1 and 2 in the homogeneous and inhomogeneous anisotropic media M2 and M3, respectively (see Table 3.1). Again, inhomogeneous means that the source-related quantities that form (3.11) are determined assuming anisotropic material properties, whereas the medium along the ray path is isotropic. For the inhomogeneous model we invert the vertical component of the P waves for the moment tensors. For the homogeneous model we first invert the vertical component of the qP waves. Then, we additionally invert the transverse component of the qS waves. These 2 options are often used in routine source retrieval. As in our synthetic example before, results of inversions are referred to as P\*, P, or P+S in Figs. 3.7-3.10.

For shear faulting in the weakly anisotropic medium M2 (1% anisotropy) the features of retrieved moment tensors are presented in Fig. 3.7. We find that the effects of weak anisotropy in the source region and along the ray path on apparent volumetric components in the retrieved moment tensors are small ( $ISO \rightarrow 0$ ,  $CLVD \rightarrow 0$ ). From the inversion of P and qP waves (referred to as P\* and P in Fig. 3.7a, b) we obtain moment tensors that comprise almost 100% double-couple components and only small apparent volumetric components. The distribution of these features is, however, similar to the synthetic moment tensors in Fig. 3.5a.  $M_0$  is nearly equal for all orientations of the elastic tensor. The effects of anisotropy on the retrieved moment tensor characteristics increase when additionally involving qS waves (Fig. 3.7c). We especially find enhanced dependency of the seismic moment and the characteristic features of moment tensor on the orientation of the elastic tensor. Effects related to the inversion of qS waves can be attributed to the modulated amplitude spectrum of the 2 split qS waves compared with that of the single S wave in isotropic media.

In the next example we assume medium M3 (10% anisotropy) for the modelling of synthetic waveforms. Inverting the P and qP waves, fault-plane solutions can be correctly determined (Fig. 3.8). Inaccuracies in determination of strike and rake occur when additionally using qS waves. Stronger anisotropy (10%, medium M3) near the source and along the raypath causes larger effects on the retrieved moment tensors (see Figs. 3.9a-c) than in the case of medium M2. For the inhomogeneous model properties of retrieved moment tensors follow the characteristics of the moment tensors used for waveform modelling, i.e. we observe the same orientation-dependent separation (compare Figs. 3.5b and 3.9a). However, non-double-couple components are smaller and the effect of source anisotropy appears less pronounced in the retrieved moment tensors. In the case of the homogeneous anisotropic model synthetic and retrieved moment tensors deviate significantly (compare Figs. 3.5b and 3.9b). This fact must be attributed to effects of anisotropy along the ray path. Non-double-couple components are about two times larger than in the inhomogeneous model. If qS waves are additionally included in the inversion the features of the inverted moment-tensor components are similarly distributed as for inversions based on qP waves only. The size of the retrieved seismic moment behaves similar to inversions of sources in the medium M2 but the orientation-dependent differences are larger. However, for some orientations of the elastic tensor strong amplifications of retrieved moment-tensor components and slip inclinations occur, e.g. for  $\beta \approx 40^\circ, \gamma \approx 30^\circ$  and  $\beta \approx 140^\circ, \gamma \approx -20^\circ$ . For different starting models we obtain very different moment tensors during inversion that may equally explain the fitted spectra. The corresponding fault-plane solutions strongly deviate from the true source models (see Fig. 3.8).

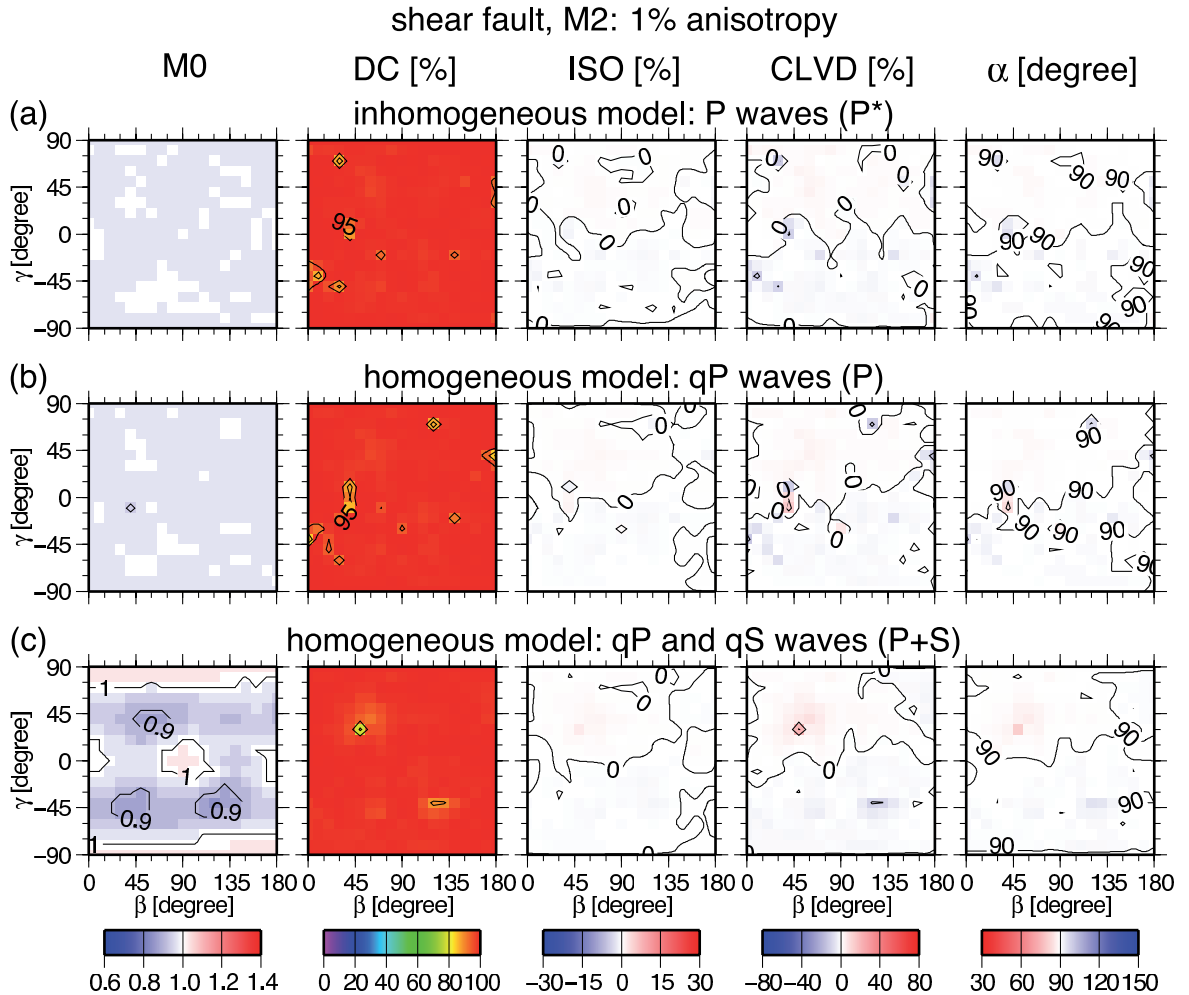


Figure 3.7: Characteristics of retrieved moment tensors for shear faulting (source as in Fig. 3.5) in the homogeneous, transversely isotropic medium M2 (1% anisotropy, see Table 3.1). (a) The source medium is anisotropic; the ray-along medium is isotropic. Inversions are based on the vertical component of the P wave. (b) The complete medium is homogeneous and anisotropic. Inversions are based on the vertical component of the qP wave. (c) Model as in (b) but the inversions are performed using the vertical component of the qP wave and the transverse component of the qS wave. As in Fig. 3.5 the elastic tensor was systematically rotated by the angles  $\beta$  and  $\gamma$  about the  $\mathbf{x}_1$ - and the  $\mathbf{x}_2$ -axes, respectively. In (a)-(c)  $M_0$  is normalised by  $3.2 * 10^{10}$ .

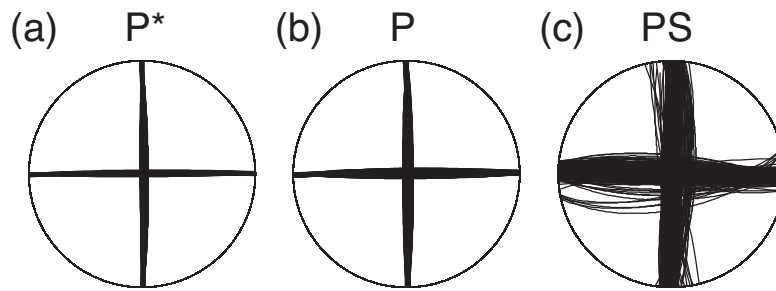


Figure 3.8: Fault-plane solutions retrieved from synthetic waveforms modelled for the vertical strike-slip shear source. For modelling of waveforms rotation is applied to the elastic tensor (medium M3, 10% anisotropy, see Table 3.1). Each solution corresponds to one inversion of synthetic waveforms that were generated after applying a different rotation to the elastic tensor. The symmetry axis is rotated about the  $\mathbf{x}_1$ - and the  $\mathbf{x}_2$ -axes, by the angles  $\beta$  and  $\gamma$ , respectively). Notations as in Fig. 3.7.

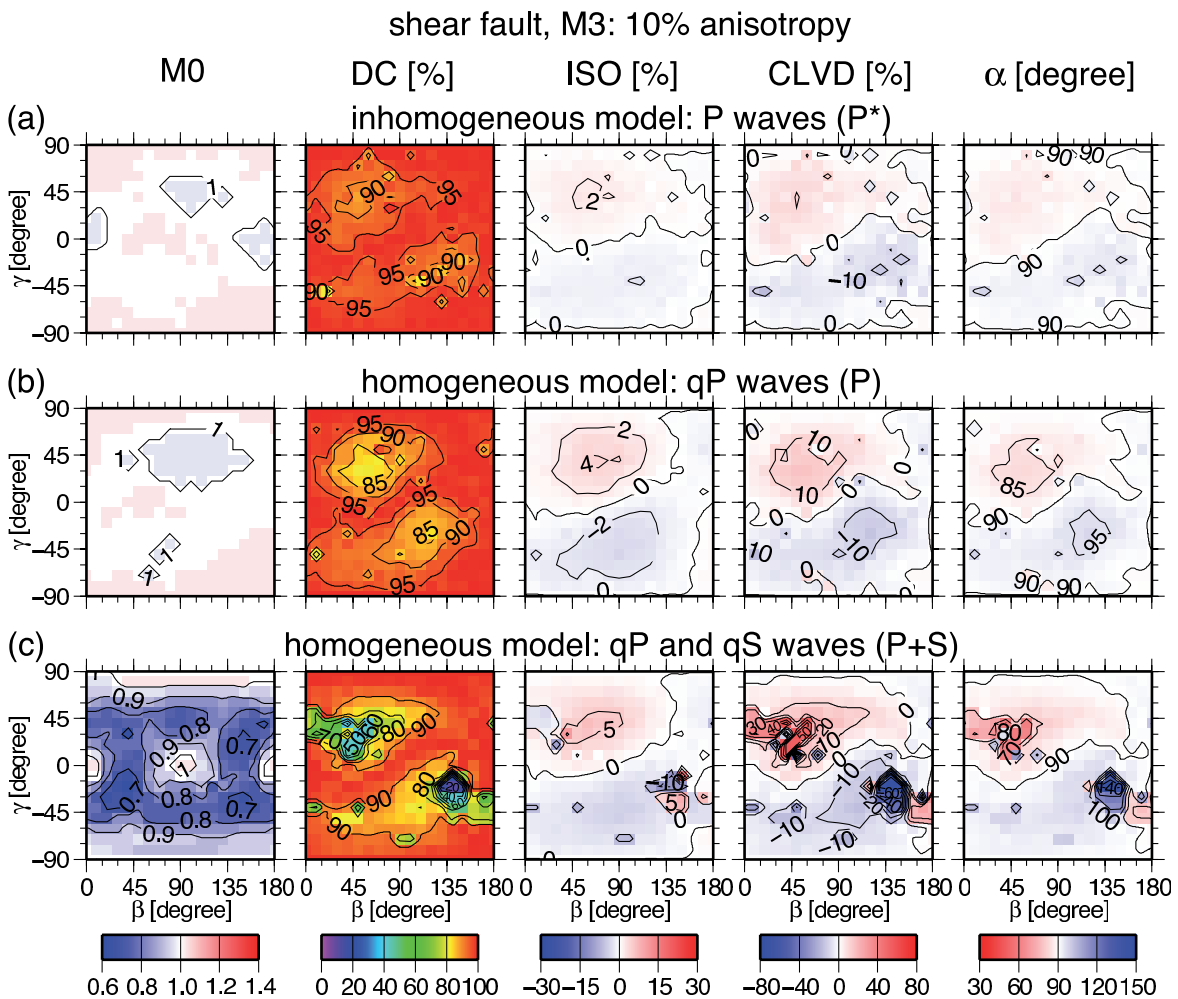


Figure 3.9: Characteristics of retrieved moment tensors of shear faulting (compare Fig. 3.8) in the homogeneous, transversely isotropic medium M3 (10% anisotropy, see Table 3.1). Otherwise as in Fig. 3.7.

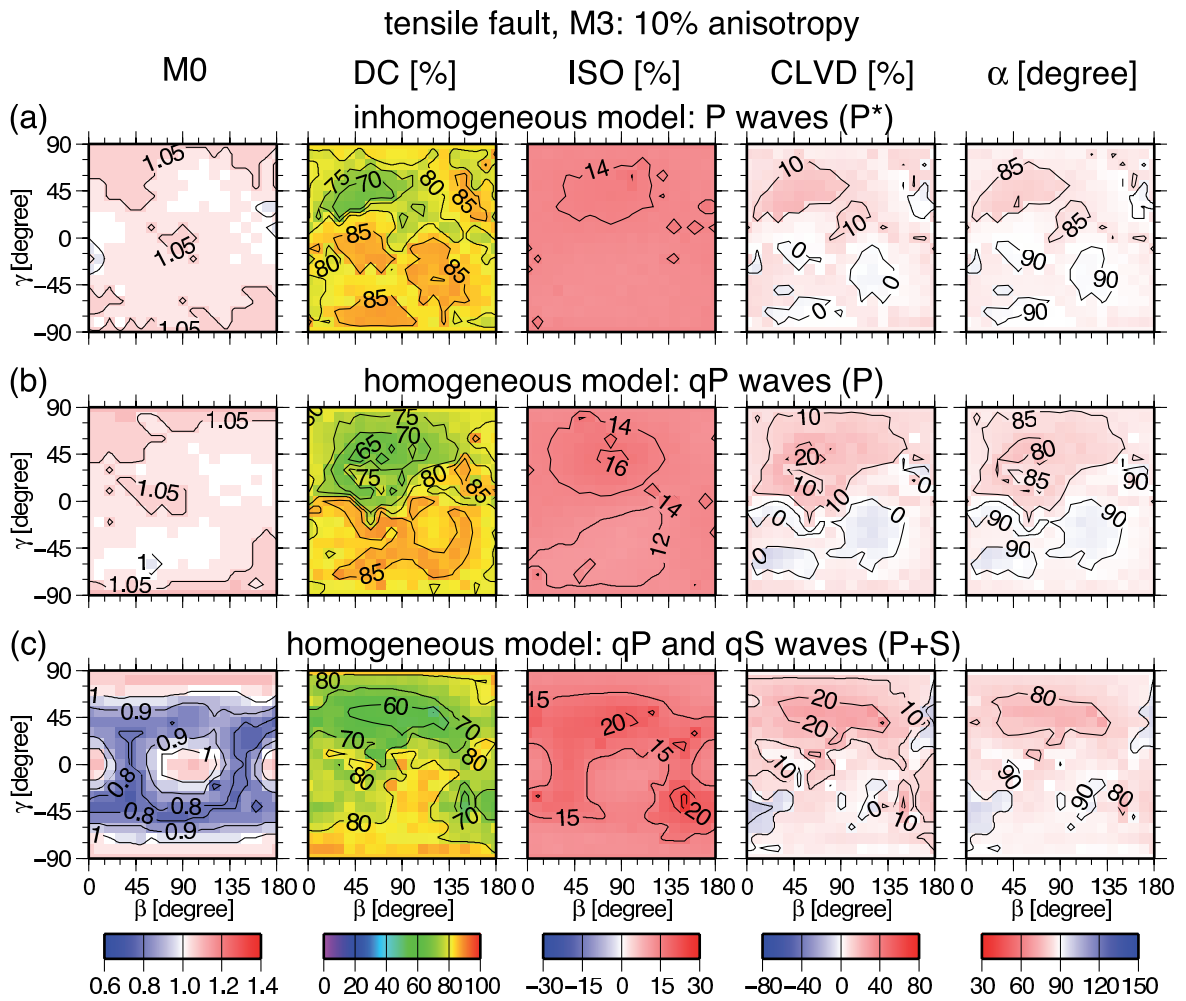


Figure 3.10: As in Fig. 3.9 but for tensile faulting (source as in Fig. 3.6).

Next, we consider the tensile source (source type 2) in the medium M3. Similar to the forward-modelled moment tensors, sources retrieved from P waves in the inhomogeneous model show high positive volumetric components (ISO) for all orientations of the elastic tensor (Fig. 3.10a). As in the case of the shear source they are, however, weakened in retrieved moment tensors. CLVD components and apparent slip inclinations show stronger fluctuations than the isotropic components. Indicated by  $\alpha < 90^\circ$  most resulting source models show opening of the fault. For some cases  $\alpha > 90^\circ$  corresponding to a closure of the fault plane is observed. The latter effect is much less pronounced here than in the moment tensors used for the forward modelling of waveforms. Therefore, in the retrieved moment tensors the real tensile component of the source is visible. It dominates the effects due to source anisotropy. In the homogeneous anisotropic model the variations in the non-double-couple components increase (Fig. 3.10b) when inverting qP waves. As an effect of anisotropy along the ray path the percentage of the DC decreases and the non-double-couple components increase. The dependence of the determined  $M_0$  on the orientation of the elastic tensor is weak. As regards complexity and seismic moment, results of joint inversions of qP and qS waves (Fig. 3.10c) allow for similar interpretation as for the pure shear source in the medium M3 in Fig. 3.9c.

### 3.5 Interpretation of moment tensors for events at the KTB borehole

In the previous sections we have shown that anisotropy influences the double-couple and non-double-couple components of moment tensors. Considering the full elastic tensor is therefore desired for the interpretation of tensile source components of earthquakes in anisotropic rocks. We now give an example for an interpretation of moment tensors retrieved for two earthquake induced during a fluid injection experiment at the KTB deep drilling site, FR Germany in 1996. A detailed description of the injection experiment, induced seismicity, and the carried out source determination can be found in *Jost et al. (1998)*. After fluid injection in the KTB main borehole about 400 earthquakes were triggered between 8 and 9 km depth in an otherwise seismically sparsely active region. The observed events were grouped into 10 clusters (*Jost et al., 1998*). For 10 events of cluster 1 and 4, at 8.9 km depth and at 8.6 km depth, respectively, *Jost et al. (1998)* determined the full moment tensors applying the relative moment tensor inversion technique by *Dahm (1996)*. Anisotropy along the ray-path and near the source was not considered during inversion. However, depth-dependent anisotropy near the borehole was reported by *Rabbel et al. (2004)* and *Okaya et al. (2004)*. We assume that effects of weak anisotropy along the ray-path on the retrieved moment tensor are small due to the applied inversion technique (*Dahm, 1996*).

At depths between 7.9 and 8.2 km *Rabbel et al. (2004)* give elastic constants assuming transverse isotropy due to the dipping rock foliation and fractured layers (medium M4, Table 3.1). Notice, that the events of cluster 1 and 4 occurred slightly below this interval. The symmetry axis of the elastic tensor (strike  $\approx$  N60°E, dip  $\approx$  45°) points normal to the foliation plane (*Rabbel et al., 2004*). Availability of reliably determined moment tensors and the knowledge of the elastic near-source medium properties allow us to re-interpret the moment tensors in terms of possible volume changes at the source during rupturing. For this purpose we choose the medium M4 and the moment tensors determined for events 47 and 111 of cluster 1 and cluster 4, respectively (*Jost et al. (1998)*, see Fig. 3.11a, c). The chosen events are representative for the two clusters. Decomposing the moment tensors (Eqs. 3.6-3.8) we find large non-double-couple components for event 47 (DC = 45%, ISO = -10%, CLVD = 44%) indicating tensile rupturing and small non-double-couple components for event 111 (DC = 88%, ISO = 0%, CLVD = -12%), respectively. It should be noted that the negative volumetric component of event 47 is in contradiction with hydro-fracturing where we expect positive volumetric changes.

We re-write the moment tensor (3.1) in terms of the elastic parameters  $c_{ijkl}$  near the source and the source tensor  $D_{kl}$  that describes the geometry of the source

$$M_{jk} = c_{ijkl}D_{kl}, \quad (3.13)$$

where  $D_{kl} = sA_0/2(s_k n_l + s_l n_k)$ . Replacing  $M_{jk}$  and  $D_{kl}$  by two 6-element vectors we solve (3.13) for the elements of  $D_{kl}$ . The eigenvalues of  $D_{kl}$  are  $\nu_1 = sA_0/2(s_i n_i + 1)$ ,  $\nu_2 = 0$ ,  $\nu_3 = sA_0/2(s_i n_i - 1)$  (compare *Vavryčuk, 2005*). Assuming a dislocation point source we calculate the slip inclination  $\delta$  from  $\nu_1$  and  $\nu_3$  as the angle between the slip direction and the fault normal

$$\cos(\delta) = \frac{\nu_1 + \nu_3}{\nu_1 - \nu_3}. \quad (3.14)$$

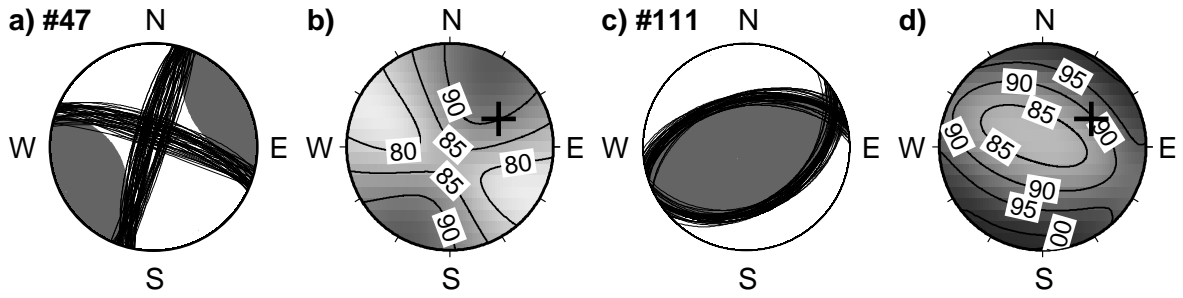


Figure 3.11: a) Moment tensor solution of event 47 in *Jost et al.* (1998) and fault-plane solutions obtained from retrieved source tensors  $D_{kl}$  in (3.13). b) Slip inclination (Eq. 3.14) for event 47 and different orientations of the axis of symmetry of the medium M4 (Table 3.3) in lower-hemisphere projection. The cross indicates the orientation of the symmetry axis of the elastic tensor given in (*Rabbel et al.*, 2004). c) and d) as a) and b), respectively, but for event 111.

The angle  $\delta$  in Eq. 3.14 expresses volumetric changes that occur during faulting. For shear faulting  $\delta = 90^\circ$  and for tensile earthquakes  $\delta \neq 90^\circ$  can be expected. We vary the orientation of the axis of symmetry of the elastic tensor (medium M4), determine  $D_{kl}$ , and calculate the slip inclination using (3.14).

Here, considering the elastic properties near the source affects the interpretation of the moment tensor. We find that for both events the slip inclination varies with the orientation of the symmetry axis (Fig. 3.11b, d). Both earthquakes show  $\delta \approx 90^\circ$  for a rotation of the symmetry axis of the elastic tensor in the same direction as observed by *Rabbel et al.* (2004). Therefore, the source mechanisms of the events 47 and 111 are consistently close to shear faulting in our interpretation and the apparent contradiction between the two earthquakes can be disproved although their moment tensors comprise different non-double-couple components.

### 3.6 Inversion for elastic constants in the source area

For pure shear sources the previous results indicate that the source orientation can be retrieved from good quality qP wave data even when anisotropy is neglected during the moment tensor inversion. Where anisotropy is limited to the source area and the medium along the ray path is isotropic (inhomogeneous models) features of synthetic and inverted moment tensors show similar patterns depending on the orientation of the elastic tensor (compare Figs. 3.5a, 3.7a and 3.5b, 3.9a). If these conditions apply it seems feasible to invert for the elastic constants in the source area directly from retrieved moment tensors and fault-plane solutions.

Assuming shear faulting the slip direction  $s_p$  and fault normal  $n_q$  can be derived from the retrieved fault-plane solutions. Using one set of elastic constants for the source area  $c_{pqjk}$  we model the moment tensor  $M_{jk}^{(sym)}$  in Eq. (3.1) for the retrieved sources. Modelled and retrieved moment tensor of  $I$  events are compared by the *residual*:

$$residual = \sqrt{\frac{\sum_{i=1}^I \sum_{j=1}^3 \sum_{k=1}^3 \left( M_{jk}^{(i,ret)} - M_{jk}^{(i,syn)} \right)^2}{M_{jk}^{(i,ret)} M_{jk}^{(i,ret)}}}. \quad (3.15)$$

However, due to direct coupling of  $c_{ijkl}$  and  $sA_0$  in (3.1) it is necessary to constrain two



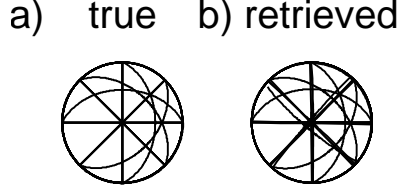


Figure 3.12: Fault plane solutions for sources used to model synthetic waveforms (a) and for source retrieved from inversion of the synthetic waveforms (b).

elastic constants (see also *Vavryčuk*, 2004). A similar approach that we follow here is a normalisation of  $M_{jk}^{(syn)}$  and  $M_{jk}^{(ret)}$  based on  $M_0$  (Eq. 3.5). Pure shearing in isotropic media always produces moment tensors with 100% DC. Therefore, for shear sources in anisotropic media the residual in (3.15) will be strongly biased towards isotropic elastic properties if normalisation is applied. Furthermore, retrieved CLVD are often poorly constrained (*Sipkin*, 1986a). For these reasons, we compare the isotropic moment-tensor components:

$$residual = \sqrt{\frac{\sum_{i=1}^I \left( \text{Tr}(\mathbf{M}^{(i,ret)}) - \text{Tr}(\mathbf{M}^{(i,syn)}) \right)^2}{\text{Tr}(\mathbf{M}^{(i,ret)})\text{Tr}(\mathbf{M}^{(i,ret)})}}. \quad (3.16)$$

By variation of the elastic tensor Eq. (3.16) may be used to determine the elastic parameters in the vicinity of the seismic source from the minimum of the residual function. This will be demonstrated by the following example. Hereby, we suppose 12 synthetic shear events seated in the same anisotropic source region. To guarantee an overdetermined system of equations (3.16) these events have different source mechanisms.

We compute synthetic waveforms assuming anisotropic stiffness parameters in the vicinity of the source (10% anisotropy, transversely isotropic medium M3, see Tab. 3.1) and isotropy along the ray path ( $v_p = 6000 \text{ ms}^{-1}$ ,  $v_s = v_p/\sqrt{3}$ ,  $\rho = 2650 \text{ kg/m}^3$ ). We choose a rotation of the elastic tensor by  $\beta = \gamma = 60^\circ$  about the  $\mathbf{x}_1$ - and  $\mathbf{x}_2$ -axis, respectively. Therefore, the moment tensors of these sources may comprise apparent volumetric components (see Tab. 3.3). The P-wave spectra of these events are inverted for the moment tensors  $M_{jk}^{(ret)}$  and the fault-plane solutions (see Fig. 3.12). The fault-plane solutions of true and retrieved sources are in good agreement.

Table 3.3: Percentage of isotropic components [%] of (true) moment tensors for sources in the anisotropic source medium M3 used for modelling of waveforms and moment tensors retrieved from modelled waveforms assuming isotropy (compare Fig. 3.12).

event no.	#1	#2	#3	#4	#5	#6	#7	#8	#9	#10	#11	#12
true	6.3	7.0	3.8	4.8	4.5	1.6	-4.8	-6.1	-4.0	-6.3	5.9	2.2
retrieved	1.9	2.7	1.6	0.3	0.1	0.5	-0.3	-0.7	-1.8	-2.0	2.3	1.0

To find the elastic parameters from retrieved sources in Fig. 3.12 we compute  $M_{jk}^{(syn)}$ . Hereby, we calculate  $c_{ijkl}$  assuming simple forms of transverse isotropy defined by the reference isotropic velocities  $v_p$  and  $v_s$  and density (*Rümpker* and *Kendall*, 2002). We

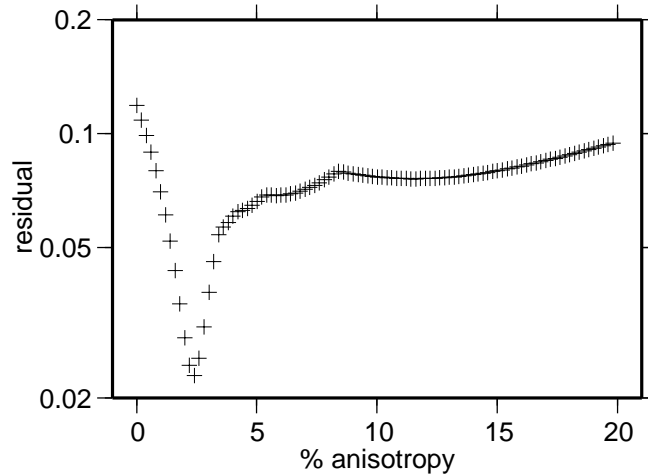


Figure 3.13: Residual function of isotropic moment tensor (*rms*, see Eq. 3.16) for variation of the degree of anisotropy (0-20%). For each degree of anisotropy we apply systematic rotation to the elastic tensor about the  $\mathbf{x}_1$ - and  $\mathbf{x}_2$ -axes in intervals of  $5^\circ$ . From these solutions the smallest residual is plotted. We assume transverse isotropy.

vary the degree of anisotropy from 0-20% in steps of 0.1%. The orientation of the axis of symmetry is defined by systematic rotation of the elastic tensor about the the  $\mathbf{x}_1$ - and  $\mathbf{x}_2$ -axes (compare Fig. 3.1) within  $180^\circ$  in intervals of  $5^\circ$ .

The calculated residual function is presented in Figs. 3.13 and 3.14 showing uniquely the dependence of the residual on the degree of anisotropy and the orientation of the elastic tensor. Only one global minimum but no other local minima exists. From modelling in the previous section we found that retrieved apparent isotropic components for sources in anisotropic media are underestimated compared to the true source which can be also observed in this example (Tab. 3.3). This affects the degree of anisotropy: applying Eq. (3.16) we find a minimum residual at 2.4% anisotropy thus a smaller value than in the true model (Fig. 3.13). From the residual plot as a function of rotation of the elastic tensor about the  $\mathbf{x}_1$ - and the  $\mathbf{x}_2$ -axis (Fig. 3.14) we find a global minimum at  $60^\circ$  for rotation about  $\mathbf{x}_1$  (true value:  $60^\circ$ ) and at  $40^\circ$  for rotation about  $\mathbf{x}_2$  (true value:  $60^\circ$ ). Thus, orientations of true and retrieved elastic tensor are equal for rotation about  $\mathbf{x}_1$  and similar for rotation about  $\mathbf{x}_2$ . Here, the residual function is more sensitive to variations of rotation about  $\mathbf{x}_2$  then about  $\mathbf{x}_1$ .

We have also carried out tests to determine the elastic properties in the vicinity of the source from moment tensors that were retrieved from noisy synthetics. In accordance with our previous results we found that the retrieved orientation of the elastic tensor is stable. However, random noise added to the synthetic waveforms is comparable to introducing an explosive type of source when inverting amplitude spectra. Therefore, retrieved moment tensors comprised larger isotropic components leading to higher percentage of anisotropy for retrieved elastic parameters.

Due to the observed ambiguities of non-double-couple moment tensors components retrieved for sources in anisotropic media it can be difficult to distinguish between the effect of anisotropy and tensile faulting. This issue might be resolved, e.g. by inverting a large number of events with different source orientations for the elastic properties at

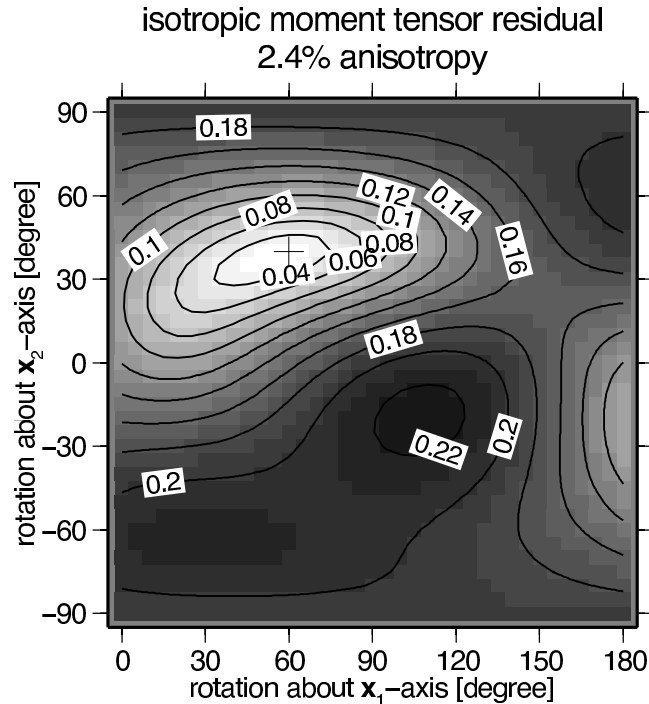


Figure 3.14: Residual function of isotropic moment tensor for variations of the orientation of the elastic tensor and 2.4% anisotropy (minimum residual in Fig. 3.13). The orientation of the elastic tensor is determined by its rotation about the  $\mathbf{x}_1$ - and  $\mathbf{x}_2$ -axes (compare Fig. 3.13). The smallest residual at point (60,40) is marked by a cross.

the source. For shear events in the same focal volume (that is homogeneous within this volume) the residual function (3.16) should show one distinct minimum. If no unique minimum exists the behaviour of the residual function may be indicative for real volumetric source changes.

Three conditions have to be met to apply this method:

- 1) the seismic source contains no real volumetric changes, observed non-double-couple components are an effect of anisotropy,
- 2) the medium along the ray path is approximately isotropic,
- 3) retrieved moment tensors are accurate, they show different source mechanisms, and the source orientation is confidently derived.

The first condition states a limitation for events where pure shearing cannot be assumed a priori. Travel-path effects on inverted moment tensors can be avoided by applying inversion methods that are independent of the accuracy of the Green's functions, e.g. relative methods (see, e.g., *Dahm, 1996; Dahm et al., 2000*).

### 3.7 Discussion

Based on synthetic and real events we have studied effects of anisotropy on moment tensors in anisotropic media. We conclude that

- 1) based on a frequency-domain moment tensor inversion algorithm (*Dahm et al.*, 1999; *Krüger and Dahm*, 2002) the source orientation can be determined with confidence from anisotropic qP waves even if anisotropic material properties are neglected. This agrees with findings of *Šílený and Vavryčuk* (2000) who utilised a different approach in the time domain additionally including inversion of qS waves. However, different fault-plane solutions may explain the amplitude spectra of waveforms for sources in anisotropic media similarly well. In this case the moment tensor inversion can be stabilised and the correct fault-plane solution can be found by first demanding  $\text{Tr}(\mathbf{M}) = 0$  to constrain the source orientation before inverting for the full moment tensor.
- 2) If anisotropy is restricted to the source area characteristic features of inverted moment tensors and moment tensors used for waveform modelling are similar. However, the strength of real and apparent non-double-couple components may be underestimated in retrieved moment tensors.
- 3) If the medium along the ray path is also anisotropic, one can expect more complex moment tensors.
- 4) Retrieved moment tensors may be difficult to interpret in terms of volumetric changes at the source without further knowledge regarding the elastic constants. Accounting for near-source anisotropy, we find shear faulting for two events induced at the KTB borehole although non-double-couple moment-tensor components are observed.
- 5) If the medium along the ray path is isotropic it is possible to determine elastic properties in the source region directly from retrieved moment tensors.

In our observations non-double couple components of retrieved moment tensors are generally smaller than in moment tensors used for modelling of waveforms. Since we apply no damping during inversion we attribute this fact to an averaging over the radiation pattern of the source. When inverting recorded seismograms we discretely sample the radiation pattern. As an effect of anisotropy we observe increased or decreased amplitudes compared to amplitudes in an isotropic reference medium. Depending on the discrete distribution of stations this effect is averaged and partially suppressed during inversion. We have inverted noise-free synthetic waveforms for the moment tensors. Additional noise will add equally to the amplitude spectra of the seismograms introducing additional spectral energy comparable to an explosive-type source. Therefore, for noisy data apparent volumetric source components will be enlarged.

A method is introduced to determine the elastic properties in the source area directly from moment tensors. Commonly applied algorithms analyse travel time information of qP and qS waves to interpret direction-dependent velocities and shear wave splitting in terms of anisotropy (see, e.g., *Vavryčuk*, 1993; *Hiramatsu and Masataka*, 1996; *Šílený and Plomerová*, 1996; *Růžek et al.*, 2003). Other authors have used polarities to determine the elastic parameters at the receiver (*Gomes et al.*, 2004). Therefore, they sample properties along the ray path but do not directly infer on the near-source region. Possible applications of the introduced method can be seen where the determination of the orientation of the elastic tensor in the source area is of interest to derive

constraints on rock deformation or stress field or where interpretation of isotropic moment tensor is desired. The procedure was not repeated for the events at the KTB due to insufficient coverage of source mechanisms. However, the new interpretation of the mechanism of the two earthquakes in terms of shear faulting indicates that in this case a consistent near-source anisotropy model can be found.

In our inversions of synthetic waveforms for the moment tensor the non-double couple components are underestimated. As a result the degree of anisotropy determined from retrieved non-double-couple components for the properties near the source is also lowered. An interesting example using a different approach is given in *Vavryčuk (2004)*. There, the CLVD determined by the USGS and Harvard University are exploited to derive anisotropic properties near the foci of earthquake in the Tonga subduction zone. From our findings we suspect that the degree of anisotropy may be even at a lower limit.

## Acknowledgments

We would like to thank E. Sanger, R. Wang, and I. Pšenčik for help concerning computational aspects, J. Šileny and L. Rivera for carefully reviewing the manuscript, and G. Richter and V. Vavryčuk for encouraging discussions. We used Seismic Handler by K. Stammler for seismogram processing and GMT by P. Wessel for plotting of figures. This work was supported by the German Science Foundation (DFG), grants KR 1935/1-1 and KR 1935/1-3.

## 4 Retrieval of source parameters of an event of the West Bohemia earthquake swarm in 2000 assuming anisotropy

Dirk Rößler<sup>1\*</sup>, Frank Krüger<sup>1</sup>, I. Pšenčík<sup>2</sup>, Georg Rümpker<sup>3</sup>

<sup>1</sup>Department of Earthsciences, University of Potsdam, K.-Liebknecht-Str. 24, 14476 Golm, FR Germany

<sup>2</sup>Geophysical Institute AS CR, Czech Republic, Boční II/1401, 14131 Prague 4, Czech Republic

<sup>3</sup>Department of Meteorology and Geophysics, University of Frankfurt/Main, Feldbergstr. 47, 60323 Frankfurt/Main, FR Germany

\*corresponding author

**Submitted for publication in *Studia Geophysica et Geodaetica***

### Abstract

Moment tensors retrieved from seismic waves generated by point sources in anisotropic media may be biased if anisotropy is neglected during inversion. Apparent volumetric components may be obtained for shear sources and falsely interpreted in terms of tensile earthquakes. Similarly, real volumetric components due to tensile faulting may not be visible in retrieved moment tensors.

Therefore, we propose an inversion scheme to retrieve characteristics of seismic point sources, which, in contrast to previous, does not neglect, but takes into account anisotropy. Instead of the moment tensor, the geometry of the source is retrieved directly in our inversion. This allows direct interpretation of the source geometry in terms of shear and tensile faulting, and to identify volumetric source changes that occur during rupturing. The source geometry is defined by the orientation of the slip vector and the fault normal as well as the strength of the event given by the size of the slip and the area of the fault. The source geometry may be used to calculate the moment tensor.

We apply the described algorithm to one event of the year 2000 earthquake swarm episode in the Vogtland/West Bohemia (Central Europe). For inversion we use information of the direct P waves. The structure is approximated by three different models determined from travel time observations. The models are inhomogeneous isotropic, inhomogeneous anisotropic, and homogeneous anisotropic. For these models we observe seismic moment  $M_T = 3.2 - 3.8 * 10^{14}$  Nm and left-lateral near-vertical oblique normal faulting on a N-S trending rupture surface. This is consistent with fault-plane solutions of earlier studies and with the spatial distribution of hypocentres. The event seems to be accompanied by a small amount of crack opening. The amount of crack opening is slightly reduced when the inhomogeneous anisotropic model is assumed but it persists. This seems to indicate a role of fluids on the triggering of events during this swarm.

*Keywords: seismic source, tensile earthquake, anisotropy, West Bohemia*

## 4.1 Introduction

Seismic moment tensors are retrieved from waveforms to describe the orientation and the strength of point sources. They are routinely determined under the assumption that the medium around the source and along the ray-path is isotropic. Anisotropic material properties are usually neglected during the inversion. However, the radiation pattern of seismic sources may be affected by anisotropy (see e.g. *Kawasaki and Tanimoto, 1981; Gajewski, 1993; Pšenčík and Teles, 1996; Rößler et al., 2004*). This may lead to the occurrence of apparent non-double-couple moment-tensor components (see e.g. *Rößler et al., 2004; Vavryčuk, 2005; Rößler et al., 2006*). On the contrary, true volumetric components may become invisible in moment tensors. The effect of anisotropy on moment tensors depends on the strength of anisotropy and on the orientation of the anisotropic elastic tensor with respect to the geometry of the source.

Moment tensors can be decomposed into the double-couple component (DC) quantifying the amount of shear faulting, the compensated-linear-vector-dipole component (CLVD), and the isotropic component (ISO) providing information on possible volumetric source changes that occur during faulting (*Jost and Herrmann, 1989; Aki and Richards, 2002*). Faulting events that comprise volumetric source changes are also called tensile earthquakes.

In practice, non-double-couple components are frequently observed and interpreted in terms of tensile faulting (see e.g. *Sykes, 1967; Solomon and Julian, 1974; Julian et al., 1997; Horálek et al., 2000b; Dahm et al., 2000; Vavryčuk, 2002; Foulger et al., 2004; Vavryčuk, 2004*). Observed volumetric components may be indicative of the role of fluids during rupturing and mineral phase changes at greater depth or may image existing pathways enabling fluid migration in carbonhydrate production fields. In these cases accurate and indisputable determination of tensile components is of primary interest. Without knowledge of anisotropy at the source, the reliability of interpretations of the moment tensor in terms of volumetric source changes must be questioned (*Vavryčuk, 2005; Rößler et al., 2006*). We therefore propose an inversion scheme for point sources in inhomogeneous anisotropic media. For such sources, we directly invert observed seismograms for the direction of slip and the fault normal.

We apply the inversion algorithm to one event that occurred during earthquake swarm in West Bohemia in 2000.

## 4.2 Inversion scheme

For seismic waves travelling in anisotropic media the  $i$ -th component  $u_i$  of the far-field complex-valued displacement at a location  $\mathbf{x}$  due to a moment point source at  $\mathbf{x}_0$  is given in the ray-theoretical high-frequency approximation (*Pšenčík and Teles, 1996*):

$$u_i(\mathbf{x}, t) = g_i(\mathbf{x}) \left[ \frac{\rho(\mathbf{x}_0)c(\mathbf{x}_0)}{\rho(\mathbf{x})c(\mathbf{x})} \right]^{1/2} \frac{Df^{(A)}(t - \tau(\mathbf{x}))}{|\Omega_M(\mathbf{x})|^{1/2}} \exp \left[ i\frac{\pi}{2}k_s - i\frac{\pi}{2}k(\mathbf{x}_0, \mathbf{x}) \right]. \quad (4.1)$$

Actual seismograms are given by the real part of the displacement  $\text{Re}(u_i(\mathbf{x}, t))$ . The quantity  $D$  in (4.1) denotes the directivity given by

$$D(\mathbf{x}_0, \theta, \phi) = \frac{g_j(\mathbf{x}_0)M_{jk}p_k(\mathbf{x}_0)}{4\pi\rho(\mathbf{x}_0)c(\mathbf{x}_0)}. \quad (4.2)$$

The directivity (4.2) represents a spreading-free amplitude at the source. It should not be confused with the directional dependence of amplitudes due to source finiteness. It depends on the moment tensor  $M_{jk}$ , the polarisation and the slowness vectors  $g_j$  and  $p_k$ , respectively, as well as the phase velocity  $c$  and the density  $\rho$  at the source. The slowness vector  $p_k$  at the source is specified by the angles  $\theta$  and  $\phi$ .

In (4.1),  $\Omega_M$  is related to the relative geometrical spreading  $|\Omega_M|$ ,  $g_i(\mathbf{x})$  is the polarisation vector at  $\mathbf{x}$ , and  $f^{(A)}$  is the analytical signal corresponding to the source time function. The integer quantities  $k$  and  $k_s$  are the indices of the trajectory and of the source, respectively (see *Pšenčík and Teles, 1996*, for a detailed description). Note that we are referring to a right-handed coordinate system: N,E,Z  $\rightarrow x_1, x_2, x_3$  but observed seismograms are recorded in the coordinate system: N,E,Z with Z pointing positive up.

For dislocation point sources, the source geometry is described by the unit slip vector  $s_p$ , the unit normal  $n_q$  to the fault plane, and the product of the size of the slip  $s$  and the fault area  $A_0$ . Elastic moduli  $c_{j k p q}$ , that describe medium properties in the vicinity of the source, and source geometry define the moment tensor  $M_{jk}$  (*Aki and Richards, 2002*):

$$M_{jk} = c_{j k p q} s_p n_q s A_0. \quad (4.3)$$

From (4.3), we can see that different properties of the moment tensor arise from sources in isotropic and anisotropic media. For example, shear faulting in anisotropic media may produce moment tensors which correspond to tensile earthquakes in isotropic media, i.e. shear faulting accompanied by some amount of opening or closing of the fault during rupturing (see e.g. *Rößler et al., 2004; Vavryčuk, 2005*).

We can also express the moment tensor in (4.3) in terms of the source tensor  $D_{pq}$ :

$$M_{jk} = c_{j k p q} D_{pq}, \quad (4.4)$$

where  $D_{pq}$  is formed by the dyadic product of the slip and the fault normal

$$D_{pq} = \frac{1}{2} s A_0 \begin{pmatrix} 2s_1n_1 & s_1n_2 + s_2n_1 & s_1n_3 + s_3n_1 \\ s_1n_2 + s_2n_1 & 2s_2n_2 & s_2n_3 + s_3n_2 \\ s_1n_3 + s_3n_1 & s_2n_3 + s_3n_2 & 2s_3n_3 \end{pmatrix}. \quad (4.5)$$

Elements of the source tensor  $D_{pq}$  make up 6 elementary sources  $\sigma_i$ , which are components of the vector  $\boldsymbol{\sigma}$

$$\boldsymbol{\sigma}^T = s A_0 (s_1n_1, s_1n_2 + s_2n_1, s_1n_3 + s_3n_1, s_2n_2, s_2n_3 + s_3n_2, s_3n_3). \quad (4.6)$$

Inserting (4.2), (4.3), and (4.6) into (4.1), we can express the seismograms in terms of the elementary sources  $\sigma_l$

$$\text{Re}(u_i(\mathbf{x}, t)) = \text{Re} \left( Y_{il} f(t - \tau(\mathbf{x})) \exp \left[ i \frac{\pi}{2} k_s - i \frac{\pi}{2} k(\mathbf{x}_0, \mathbf{x}) \right] \right) \sigma_l. \quad (4.7)$$



For  $Y_{il}$  see Appendix 4.5.1.

The left-hand side of (4.7) is determined from observations. All quantities except of  $\sigma_l$  of the right-hand side are determined numerically. The system of equations (4.7) corresponding to observations at different receivers is then solved for  $\sigma_i$  by minimising the misfit  $\epsilon_j$  between the left-hand side and right-hand side of (4.7) in a least-square sense. The residual  $R$  is formed by normalisation of the misfit

$$R = \frac{\epsilon_j \epsilon_j}{\text{Re}(u_i) \text{Re}(u_i)}. \quad (4.8)$$

In this way, residuals for events of different size are comparable.

A singular value decomposition of  $D_{pq}$  in (4.5) yields the eigenvalues  $\nu_1 = sA_0/2(s_i n_i + 1)$ ,  $\nu_2 = 0$ ,  $\nu_3 = sA_0/2(s_i n_i - 1)$  (compare *Vavryčuk*, 2005). The corresponding (normalised) eigenvectors are  $\mathbf{e}_1 = (\mathbf{s} + \mathbf{n})/|\mathbf{s} + \mathbf{n}|$ ,  $\mathbf{e}_2 = (\mathbf{s} \times \mathbf{n})/|\mathbf{s} \times \mathbf{n}|$ , and  $\mathbf{e}_3 = (\mathbf{s} - \mathbf{n})/|\mathbf{s} - \mathbf{n}|$ , where  $\times$  denotes the vectorial cross product. In the following we calculate the slip inclination  $\delta$ , i.e. the angle between the direction of the slip and the fault normal,  $\cos(\delta) = |s_i n_i|$ , from the retrieved  $\sigma_l$  forming  $D_{pq}$

$$\cos(\delta) = \frac{\nu_1 + \nu_3}{\nu_1 - \nu_3}. \quad (4.9)$$

For pure shear faulting,  $\delta = 90^\circ$ , but  $\delta \gtrless 90^\circ$  for tensile earthquakes (volumetric source changes, see Appendix 4.5.2). However, for sources other than dislocation point sources, e.g. explosions or faultings on non-planar fault surfaces, inversions using (4.7) will yield  $\nu_2 \neq 0$ . Occurrence of  $\nu_2 \neq 0$  may be an indication of an inadequate description of the seismic source by (4.3) or insufficient modelling of ray-path effects by  $Y_{il}$ . From a combination of the eigenvalues and the eigenvectors of  $D_{pq}$  we get  $s_i$ ,  $n_i$ , and  $A_0 s$  (see Appendix 4.5.2). In fact, we obtain two vectors but we cannot uniquely identify from observations of seismograms which is  $s_i$  and which is  $n_i$ . We get two conjugate fault planes that are perpendicular to  $s_i$  or  $n_i$ . These two planes are associated with the rupture plane and the auxiliary plane. They can form any angle. For shear faulting both planes are perpendicular. As in other source inversions, the rupture plane must be identified from additional information such as aftershock distribution or known fault-zone geometry. The area of the fault  $A_0$  and the length of the slip  $s$  cannot be separated. From inversion we can only get their product  $A_0 s$ .

Given the retrieved source geometry, the moment tensor, which is usually sought in seismological practice, may be immediately computed from (4.3). We decompose the moment tensor into its double-couple (DC) and non-double-couple components, i.e. the compensated-linear-vector-dipole (CLVD) and the isotropic component (ISO). Several different decompositions of  $M_{ij}$  have been proposed (see e.g. *Silver and Jordan*, 1982; *Jost and Herrmann*, 1989; *Vavryčuk*, 2002). Herein, we use equations of *Vavryčuk* (2002) that relate the moment-tensor components to the complete moment tensor. The (real or apparent) non-double-couple components have often been interpreted in terms of volumetric source changes connected to the faulting process. In anisotropic media, this interpretation might not be correct because the (apparent) non-double-couple moment-tensor components may be a consequence of neglected anisotropy (*Rößler et al.*, 2004; *Vavryčuk*, 2005; *Rößler et al.*, 2006). If, however, anisotropy is taken into account and the slip inclination  $\delta$  differs from  $90^\circ$ , this is a more reliable indication of real volumetric source changes. The slip inclination is therefore considered as an important parameter during inversion. Possible conclusions made from the

slip inclination and from the standard non-double-couple components may be later compared.

As a measure of strength of the event, we calculate the seismic moment  $M_T$  from the moment tensor (*Silver and Jordan, 1982*):

$$M_T = \sqrt{\sum_{ij} M_{ij}^2} / 2. \quad (4.10)$$

We seek the source vector  $\sigma_i$  by inversion of observed body wave seismograms. The inversion is carried out in the time domain. We use the least square approach to minimise the squared misfit between observations and predicted seismograms given by the left and the right hand side of Eq. (4.7), respectively (see *Menke, 1989*). The synthetic seismograms  $\text{Re}(u(\mathbf{x}, t))$  corresponding to the 6 elementary sources  $\sigma_i$  are computed for inhomogeneous anisotropic media using the software package ANRAY (*Pšenčík, 1998*).

Misalignment of observed data and synthetic seismograms often occurs due to inaccurate phase picking. For time-domain inversion this may cause spurious non-shear components in retrieved source geometries. Phase alignment is therefore carried out in 3 steps prior to inversion:

- 1) Observed phases are manually picked. A time window for inversion is defined.
- 2) Within the time window the phases are manually aligned with the computed synthetic seismograms.
- 3) Automatic cross-correlation is applied. A threshold based on the correlation coefficient may be used to define if data are to be included in inversion.

The efficiency of the algorithm is demonstrated by inversion of seismograms generated by synthetic sources in *Rößler et al. (2005)*.

### 4.3 Source retrieval for an earthquake from West Bohemia

Studies of source mechanisms for West Bohemia swarm episode in 1997 revealed evidence for tensile faulting, i.e. shear faulting that is accompanied by volumetric source changes during faulting. Such volume changes were found from interpretation of the non-double-couple components of retrieved moment tensors (*Vavryčuk, 2002*). However, seismic anisotropy observed in this region (*Vavryčuk, 1993; Růžek et al., 2003; Málek et al., 2005*) was neither accounted for during interpretations nor during inversions for moment tensors.

We apply our inversion algorithm to one earthquake that occurred during the year 2000 earthquake swarm episode in Vogtland/West Bohemia. This earthquake swarm represents the most recent period of intense seismic activity in the region. It started on August 28, 2000 and lasted for 4 months. The events occurred on a fault, oriented in N-S direction at depths between 8 and 11 km. Accurate hypocentre locations are provided by *Boušková (2005)*. The swarm has been subdivided into nine separate phases. The selected event forms the onset of the fifth phase. Hypocentre parameters are 50.2085° N, 12.4576° E, 9.243 km depth, source time is October 15, 2000, 16:36:48 (*Fischer, pers. comm.*). Till now, a detailed study of source mechanisms of the year 2000 earthquake swarm has not yet been performed but indications of fluid related earthquake triggering have been found, e.g. by *Fischer and Horálek (2005); Hainzl and Ogata (2005)* and *Parotidis et al. (2005)*. Observations by *Hainzl and Ogata (2005)* indicate that changes

in pore pressure by high-pressure crustal fluids may be important for the triggering of events at the beginning and also during the fifth phase of the swarm.

In addition to the permanent stations in the region, temporary stations were installed by the University of Potsdam, the WEBNET group, the Central Seismological Observatory and the GeoForschungsZentrum Potsdam at different periods during the swarm (see Tab. 4.5, Fig. 4.1, and *Klinge et al.*, 2003). The selected event occurred at a time of maximum station coverage. Note that although many stations were available, ray coverage was non-uniform. For example, only one station in SE direction can be used.

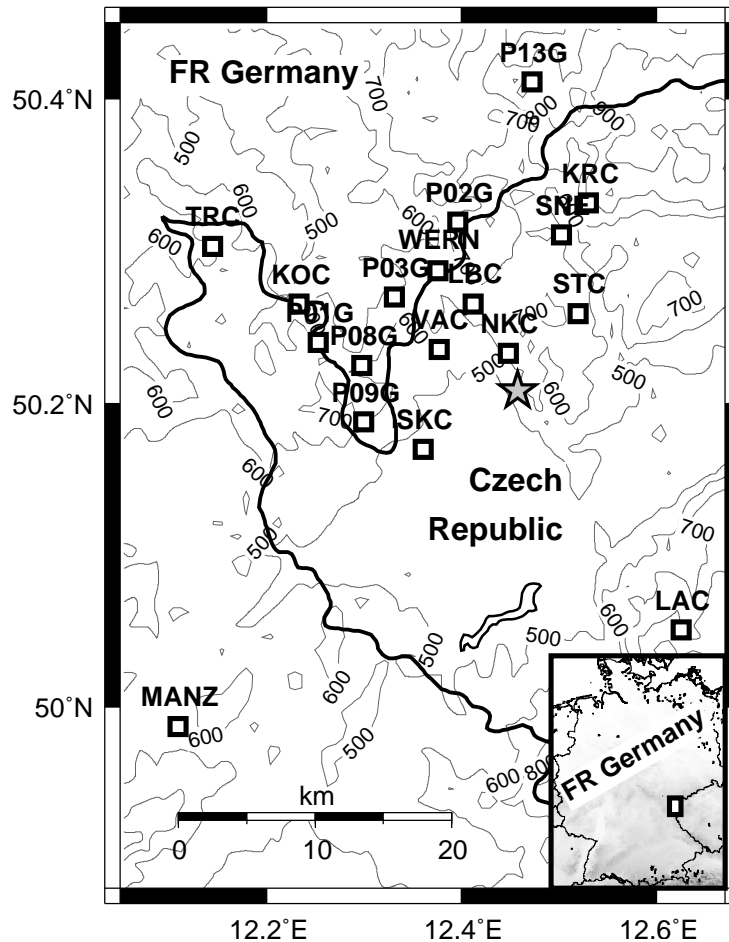


Figure 4.1: Map of West Bohemia. Star: epicentre at  $50.2085^{\circ}\text{N}$ ,  $12.4576^{\circ}\text{E}$ , 9.243 km depth, source time: October 15, 2000, 16:36:48. Squares: stations used for inversion of waveforms.

Several homogeneous and inhomogeneous isotropic velocity models were published for the focal area in West Bohemia (see e.g. *Novotný*, 1996; *Málek et al.*, 2004). Three anisotropic/isotropic models used in this study and referred to as models I-III, see Fig. 4.2, Tables 4.1-4.3, were derived by *Málek et al.* (2005) and *Vavryčuk* (1993).

**Model I** is a vertically inhomogeneous isotropic model derived by *Málek et al.* (2005), see Fig. 4.2 and Table 4.1.

**Model II** is a vertically inhomogeneous, weak anisotropy model also derived by *Málek et al.* (2005), see Fig. 4.2 and Table 4.2. The model has been derived from P waves only.

**Model III** is homogeneous and transversely isotropic. See Fig. 4.2 for averaged

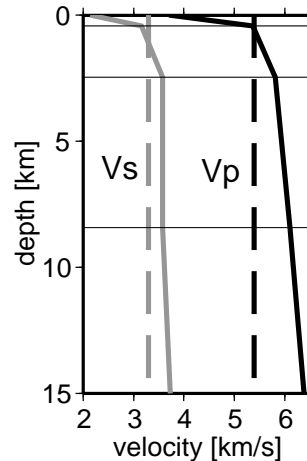


Figure 4.2: P-wave (black) and S-wave (grey) velocities for West Bohemia (compare Tab. 4.1). Solid line: vertically inhomogeneous model I (reference velocities for model II) derived by *Málek et al. (2005)*. Dashed line: homogeneous transversely isotropic model III characterised by  $v_p = \sqrt{(A_{11} + A_{22} + A_{33})/3}$ ,  $v_s = \sqrt{(A_{44} + A_{55} + A_{66})/3}$  (*Vavryčuk, 1993*).

isotropic velocities and Tab. 4.3 for the elastic moduli. It has been derived from S-wave splitting and S-P travel time differences using effective medium theory (*Vavryčuk, 1993*).

Table 4.1: Model I. P- ( $v_p$ ) and S-wave ( $v_s$ ) velocity as functions of depth (*Málek et al., 2005*). Cubic-spline interpolation is used.  $v_s$  at 32.00 km depth is determined from  $v_p$  assuming  $v_p/v_s = \sqrt{3}$ , density:  $\rho = 2650 \text{ kgm}^{-3}$ .

depth [km]	0.00	0.41	2.46	8.41	32.00
$v_p$ [kms <sup>-1</sup> ]	3.70	5.37	5.81	6.10	7.20
$v_s$ [kms <sup>-1</sup> ]	2.18	3.16	3.57	3.58	4.16

Table 4.2: Model II: weak anisotropy (WA) parameters (see *Pšenčík and Gajewski, 1998*) used to specify the model (*Málek et al., 2005*). The WA parameters and reference P-wave velocities taken from model I are used to determine depth distribution of P-wave related parameters. Remaining parameters are determined from S-wave velocities of model I.

WA par.	$\epsilon_x$	$\epsilon_y$	$\epsilon_z$	$\delta_x$	$\delta_y$	$\delta_z$	$\chi_x$	$\chi_y$	$\chi_z$	$\epsilon_{15}$	$\epsilon_{16}$	$\epsilon_{24}$	$\epsilon_{26}$	$\epsilon_{34}$	$\epsilon_{35}$
$\times 10^{-3}$	-12	7	11	-4	6	-5	9	-4	1	2	7	3	7	-7	-5

We invert three-component displacement seismograms of the P waves recorded at 18 stations, for which the amplitude transfer functions are accurately known (see Fig. 4.1 for their locations and Tab. 4.5 for their coordinates). Stations with unknown amplitude characteristics are not included. Seismograms are uniformly resampled to 0.01 s sampling interval. A time window of 0.4 s around the P wavelet is used for inversion. The similarity between the shape of observed and modelled waveforms is expressed by the cross-correlation coefficient. The cross-correlation coefficient for most traces is above 0.9. We exclude seismograms with complicated P wavelets that have cross-correlation coefficients below 0.6. Observed P waves are generally characterised by high

Table 4.3: Model III. Density normalised elastic parameters  $A_{ij}$  in Voigt notation ( $A_{ij} = C_{ij}/\rho$ ) that describe a homogeneous anisotropic model for West Bohemia.

	$A_{11}$	$A_{12}$	$A_{13}$	$A_{22}$	$A_{23}$	$A_{33}$	$A_{44}$	$A_{55}$	$A_{66}$
$\times 10^6 \text{ m}^2 \text{ s}^{-2}$	23.5	7.8	7.8	31.9	9.9	31.9	11.0	10.8	10.8

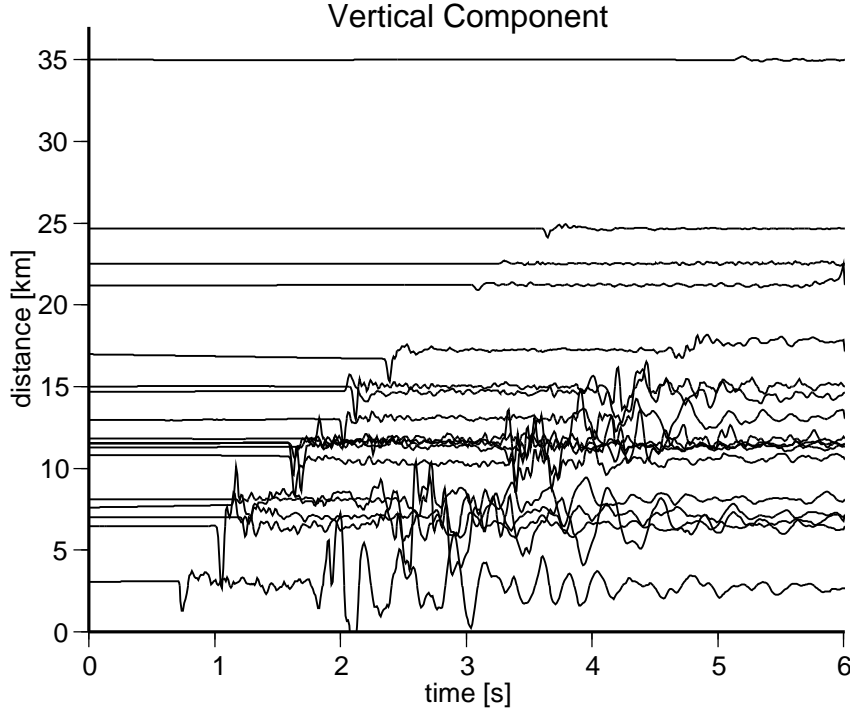


Figure 4.3: Vertical-component seismograms (displacement) at stations and for event in Fig. 4.1. Seismograms are unfiltered and sorted by epicentral distance. Positive amplitudes refer to upwards directed displacement. Source time corresponds to -1 s in the seismograms.

signal-to-noise ratios and clear onsets (Fig. 4.3). The corner frequency of the studied event is around 10 Hz (Fig. 4.4). To guarantee that the inversion is independent of the source-time function of the event, we low-pass filter data and synthetic seismograms at 10 Hz.

Using the models I-III similar fault-plane solutions are obtained (see Fig. 4.5 and Tab. 4.4) and the residuals are similarly reduced. Wavelets match well at all stations except the station LBC (Fig. 4.6, trace 9). The plane oriented in N-S direction is identified as the rupture plane. It can be associated with the map of the fault zone obtained from located earthquake foci (*Fischer*, 2003). The event is therefore characterised by left-lateral oblique normal faulting on a N-S oriented fault plane dipping steeply towards the West. This orientation is similar to results obtained by *Fischer* and *Horálek* (2005) using the FOCMEC algorithm (*Snoke*, 2003). The retrieved dip-slip component is increased for model III as compared to the models I and II. The seismic moment varies in the range  $3.2 - 3.8 \times 10^{14}$  Nm.

Retrieved sources comprise a small amount of tensile component (crack opening) indicated by  $\delta < 90^\circ$  for all three models (see Tab. 4.4). The deviation from pure shear faulting (tensile character) is smallest for the inhomogeneous anisotropic model II. Here, the slip vector deviates off the fault plane by  $3.2^\circ$  (Tab. 4.4). A small in-

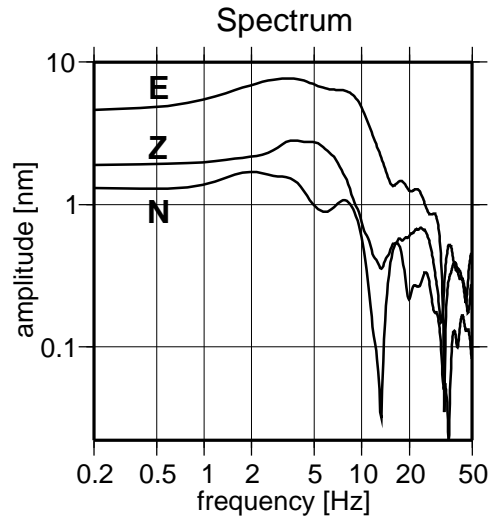


Figure 4.4: Three-component displacement spectra of the P wave at NKC, the station closest to the epicentre.

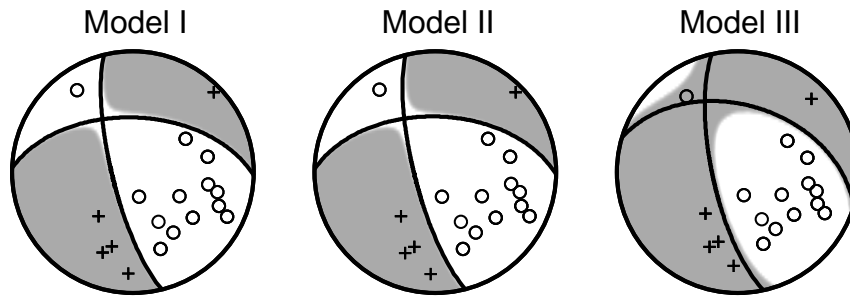


Figure 4.5: Fault-plane solutions and P-wave radiation patterns for models I, II, and III. Take-off directions of the P waves (lower-hemisphere projection) from the source (star) to the stations (squares) in Fig. 4.1. First motion of the P waves is compression (grey area, crosses) or dilatation (white area, circles).

Table 4.4: Residual, slip inclination  $\delta$ , orientation of the rupture plane, seismic moment  $M_T$  ( $M_T = M * 10^{14}$  Nm), and moment-tensor components retrieved by using initial conditions and velocity models I-III. (★) – inversion without station LBC. Mean slip inclinations  $\bar{\delta}$  and standard deviations  $\sigma(\delta)$  obtained from bootstrap tests are also given.

model	res.	slip inclination [°]			rupture plane [°]			moment tensor [%]			
		$\delta$	$\bar{\delta}$	$\sigma(\delta)$	strike	dip	rake	M	DC	ISO	CLVD
I	0.06	86.5	86.7	1.2	166	76	-39	3.4	81.0	+4.9	+14.1
I (★)	0.06	87.6	87.8	1.1	168	75	-42	3.5	90.0	+7.8	+2.2
II	0.06	86.8	86.9	1.2	166	76	-40	3.6	82.0	+4.9	+13.1
II (★)	0.06	88.0	87.2	1.2	168	75	-42	3.8	91.5	+8.2	-0.4
III	0.08	83.9	84.1	1.1	168	73	-51	3.2	71.5	+12.7	+15.8
III (★)	0.08	84.3	84.4	1.3	169	73	-52	3.3	74.8	+17.1	+8.2

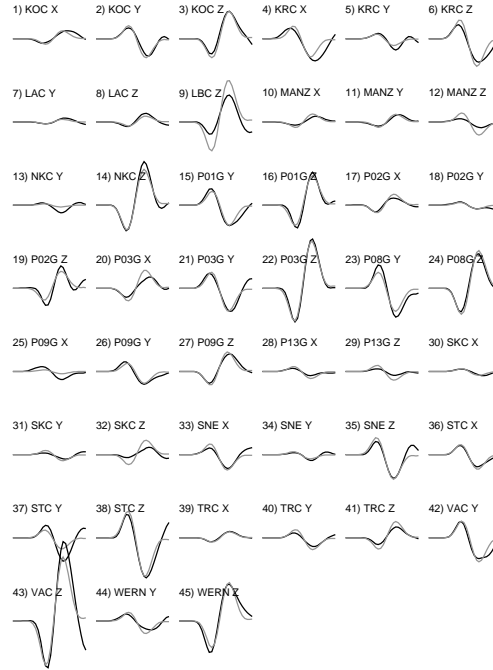


Figure 4.6: Observed data (black) used during inversion vs. modelled synthetic seismograms (grey) for stations in Fig. 4.1, 1-10 Hz band-pass filtered. Length of seismograms: 0.4 s, maximum amplitude: 6516 nm at VAC (trace 43). Trace number, station name and component are given above the seismograms. Notation of components: X-North, Y-East, Z-vertical, positive upwards. Note that some components are excluded from inversion due to low correlation between data and synthetics.

crease in the tensile character is observed for the inhomogeneous isotropic model I. The non-double-couple components of the resulting moment tensors are also small and nearly equal for models I and II (Tab. 4.4). The largest tensile components and largest non-double-couple moment-tensor components are retrieved for the homogeneous anisotropic model III. For all velocity models I-III, the eigenvalues of retrieved  $D_{pq}$  in (4.5) are  $\nu_1 \gg \nu_2$  and  $\nu_3 \gg \nu_2$ . This indicates that the determined source mechanisms are in accordance with the model for dislocation point sources assumed in (4.3)-(4.5) and (4.9). The differences in solution resulting from models I/II and III can be explained by the structural differences causing differently modulated amplitudes in the modelled wavefield and different ray take-off angles at the source (Fig. 4.7). Take-off directions are indistinguishable for rays in the models I and II. Therefore, the small differences in source geometry for models I and II most probably result from anisotropy.

In our data example it seems that the retrieved source mechanism is more similar to a shear source when assuming more structural complexity including vertical inhomogeneity and P-wave anisotropy. Adding information on anisotropy from observations of S waves to the inhomogeneous anisotropic model II could intensify this effect. However, accounting for structural inhomogeneity takes the largest effects on retrieved source parameters. Similar observations were made by *Ramos-Martínez* and *McMechan* (2001) using a finite-difference approach.

Only the inhomogeneous anisotropic model II contains information on structural complexity and anisotropy. This model is therefore used to test the sensitivity of the inversion to variations of the station distribution and of the weight given to the data

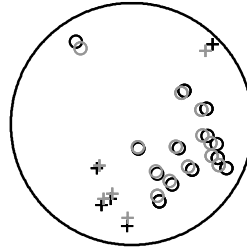


Figure 4.7: Comparison of take-off directions of the P waves in Fig. 4.5 (lower-hemisphere projection) for the models II (black), and III (grey). Take-off directions for P waves in model I from Fig. 4.5 are not plotted. They are indistinguishable from take-off directions in model II. First motion is compression (crosses) or dilatation (circles).

of a station. First we perform jackknife tests, i.e. we randomly omit 10% or 25% of all traces available from all stations. The procedure is repeated 200 times (see Fig. 4.8 for results of jackknife tests). We find that fault orientation, slip inclination, and components of moment tensors are well constrained if the number of traces is randomly reduced by 10% (Fig. 4.8a). For most realisations the slip inclination varies between  $85^\circ$  and  $89^\circ$ . The retrieved double-couple and isotropic components are in the range of 75-90% and 0-10%, respectively. When reducing the number of traces by 25% (Fig. 4.8b), fault planes show a wider range of variability. Slip inclinations are in the same range as for the 10%-jackknife test. The distribution of double-couple and isotropic components is broadened and a greater number with small DC occur. For most realisations, isotropic components are positive. We can therefore rule out that the observed tensile source component is an artefact of the station distribution.

Next we carry out bootstrap tests, i.e. we modify the weight of one single station during inversion by feeding the data of this station 1, 2, 5, 10, 20, 50 or 100 times into the system of equations (4.7), see Fig. 4.9. The procedure is repeated for every station while the weights of the remaining stations are kept equal. For a station with high weight factor the inversion aims to fit the amplitudes of this station preferentially. If rays to one station are of special importance for the inversion, e.g. for isolated station location, the solution can be stabilised by increasing the weight for this station. However, inversions may become unstable if amplitudes are inappropriately modelled at the station that is weighted higher. This can be the case for unknown near-station structure.

Retrieved fault-plane solutions show only minor variability for all bootstrap tests (Fig. 4.9a). Except for station LBC the variations of the slip inclination, the moment-tensor components, and the residuals are close to each other (see Fig. 4.9b). The mean values of the slip inclinations are slightly larger than values for unchanged initial conditions (see Tab. 4.4). However, small standard deviations indicate that the tensile components are significant. Increasing weight for station LBC causes deviation of all quantities. Observed  $DC < 70\%$  in Fig. 4.9 is caused by overweighting station LBC. The influence of LBC cannot be explained by the station location because it is situated in a direction of dense ray coverage (compare Fig. 4.1). Therefore, it must be caused by the mismodelling of the P-wave amplitude (Fig. 4.6). Omitting LBC during inversion leads to increase in shear character ( $\delta = 88^\circ$  for otherwise unchanged initial conditions and model II) and to an increase in the double-couple component of the moment tensor as well as a slight rotation of the fault orientation (see Tab. 4.4). However, a small



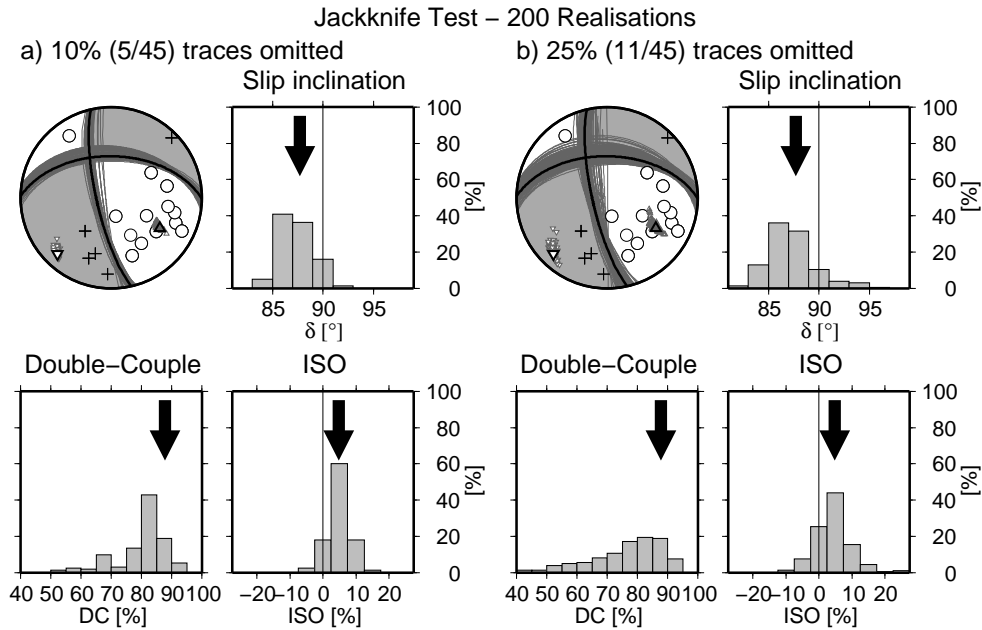


Figure 4.8: Jackknife tests for event (star) and stations (squares) in Fig. 4.1 using model II. In 200 realisations, a) 10% (left) and b) 25% (right) of all available traces are randomly omitted for inversion. Fault-plane solutions with P and T axes (grey triangles and grey inverted triangles, respectively) are plotted for each realisation (grey lines) as well as the distribution of corresponding slip inclinations ( $\delta$ ) and moment-tensor components (DC, ISO). For unmodified conditions, fault-plane solutions and the P and T axes are plotted in black, the radiation pattern due to the retrieved source is underlying the fault-plane solutions (grey area: compression, white area: dilatation), and corresponding quantities are indicated by arrows.

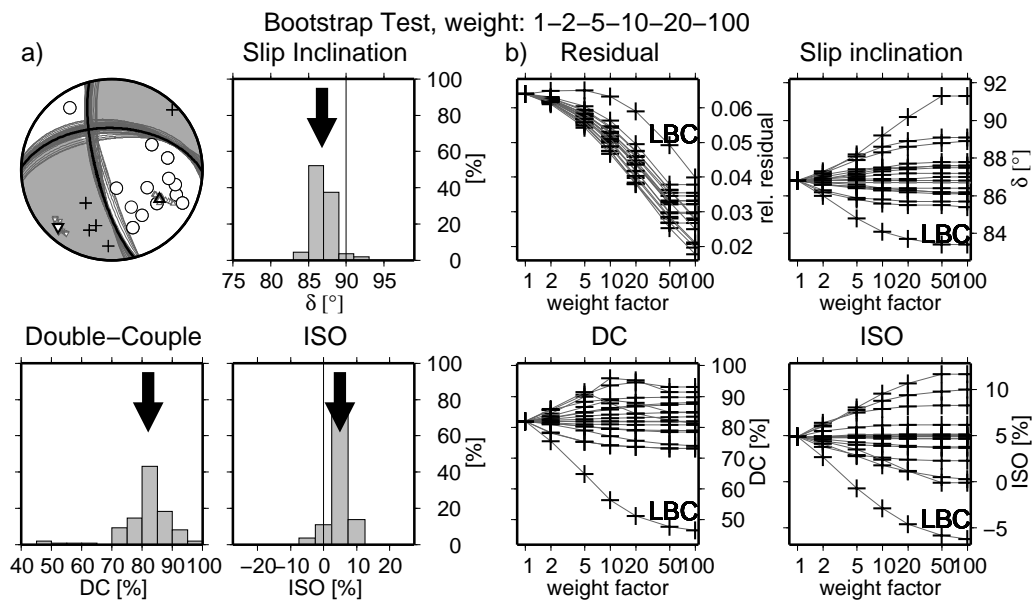


Figure 4.9: Bootstrap tests for event (star) and stations (squares) in Fig. 4.1 using model II. During every realisation the weight of each station is varied (weight factors: 1, 2, 5, 10, 20, 50, 100) while the weight of remaining stations is one. The procedure is repeated for each station. a) Fault-plane solutions and source parameters retrieved by bootstrapping. See Fig. 4.8 for more details. b) Results for bootstrapping of individual stations (one curve - one station). Along every curve the weight of another station is varied while the weight of the remaining stations is kept constant, equal one. Note outliers for bootstrapping of station LBC.

amount of non-shear component remains. A similar trend is also found for the models I and III (see Tab. 4.4). Therefore, the observed tensile component does not seem to be an artefact of mismodelled structure along a ray to a particular station.

The principle directions of the local stress field (P and T axes) are stable during testing (see Figs. 4.8, 4.9). They indicate compression in SE–NW direction and extension in SW–NE which is similar to the stress field observed before in West Bohemia and Central Europe (*Wirth et al.*, 2000; *Hinzen*, 2003; *Plenefisch and Klinge*, 2003)

We have also carried out computations to evaluate the influence of mismodelled source depth. For the calculations of synthetic seismograms we considered all three velocity models and put sources between 6 km and 14 km depth with a step of 500 m. Note that the depth uncertainty due to the localisation algorithm is about 100 m (*Fischer, pers. comm.*). Additional errors in source locations may occur due to ignored anisotropy in the localisation algorithm (*Málek et al.*, 2005).

Residuals as well as retrieved slip inclinations and seismic moment tensors show sensitivity to source depth in all three models I-III (Figs. 4.10-4.12). The fault orientation is rotated towards a larger strike slip component for shallower event depths.

Assuming the inhomogeneous isotropic model I a minimum residual is reached at 2 km above the localisation depth (Fig. 4.10). Here, the slip inclination  $\delta$  indicates almost pure shear faulting. A maximum of the DC moment-tensor component is reached for a source depth below 8 km. The seismic moment and the size of the isotropic moment-tensor component increase whereas the slip inclination decreases monotonously with the assumed source depth.

Similar observations are made for the inhomogeneous anisotropic model II. In contrast to model I, the smallest residuals are observed for source depths between 8 and 9 km, thus closer to the localisation depth, which is 9.24 km. Retrieved seismic moments are slightly increased. In contrast to model I, therefore as an effect of anisotropy, the minimum of the residual function and the CLVD coincide with the maximum of the DC.

For the homogeneous anisotropic model III, the residual function shows a broader minimum at 11-12.3 km source depth, thus significantly below the localised source depth. Seismic moments are slightly larger than for the models I and II. No extremum is observed for the deviatoric moment-tensor components in the considered depth range. The fault plane solutions contain an increased dip-slip component. The different behaviour of the residual function and the source orientation as compared to the models I and II can be partly explained by increased angles of incident waves at the surface. Models I and II contain a near-surface low-velocity zone that is missing in model III. Therefore, angles of incident waves are steeper in models I and II than in model III. Consequently, for sources in model III greater hypocentre depths are required to obtain the same incidence angles at the surface. This explains why the smallest residuals in model III can be found at greater depth than in models I and II. As a result, different take-off angles in models I/II and III lead to a rotation of the retrieved source mechanisms.

## 4.4 Discussion and conclusions

We have introduced an algorithm to retrieve the geometry of point sources in anisotropic media. Decoupling the source geometry from the elastic properties of the

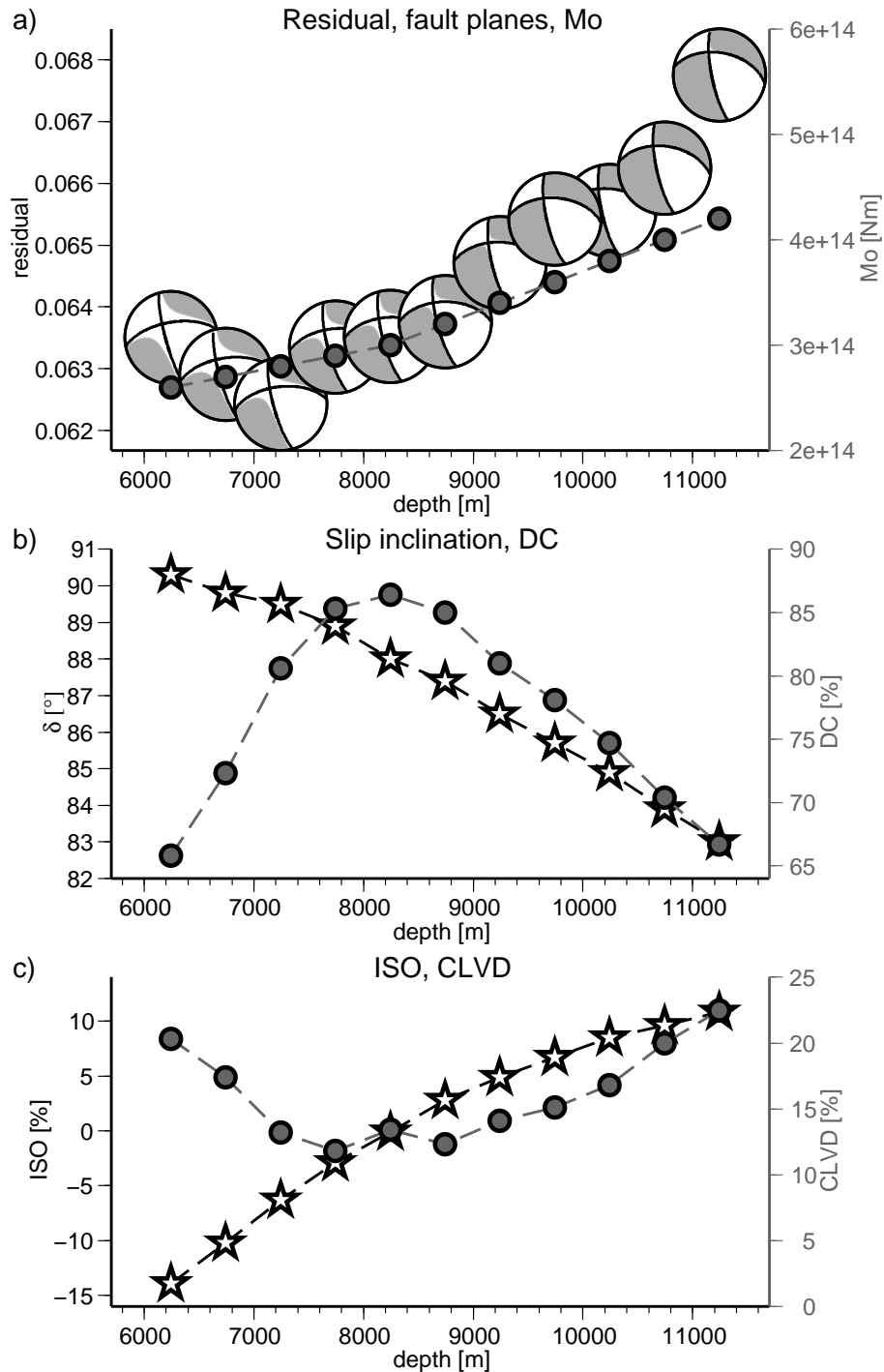


Figure 4.10: Source parameters as a function of varying depth obtained from inversions assuming model I, epicentre position and stations in Fig. 4.1 but different source depths. Localised source depth: 9.243 km. a) Fault-plane solutions positioned at residual values  $R$  and seismic moments  $M_T$  (circles). b) Slip inclinations  $\delta$  (stars) and double-couple moment-tensor components DC (circles). c) Isotropic moment-tensor components ISO (stars) and compensated linear vector dipole components CLVD (circles).

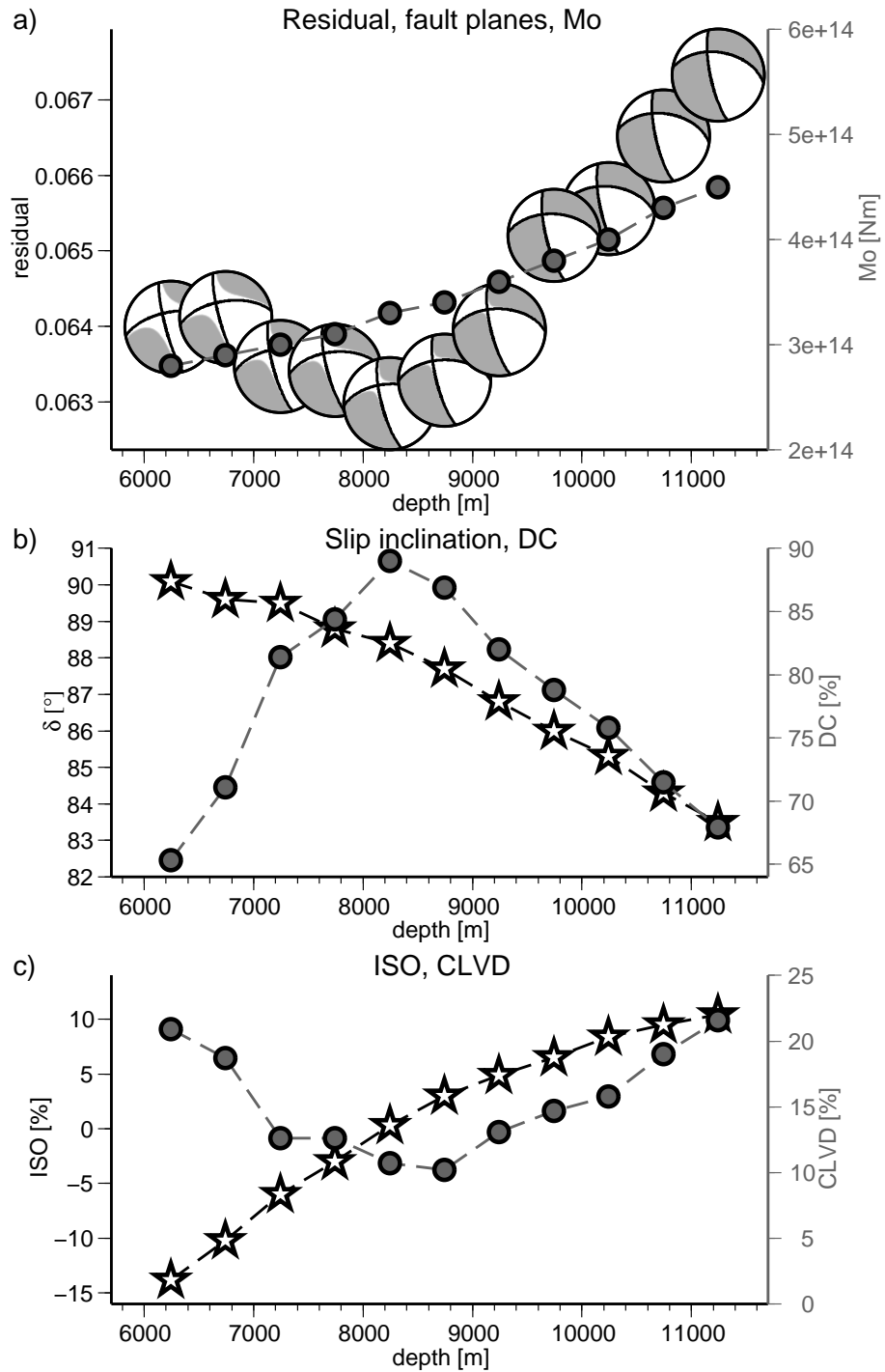


Figure 4.11: As in Fig. 4.10 but for model II.

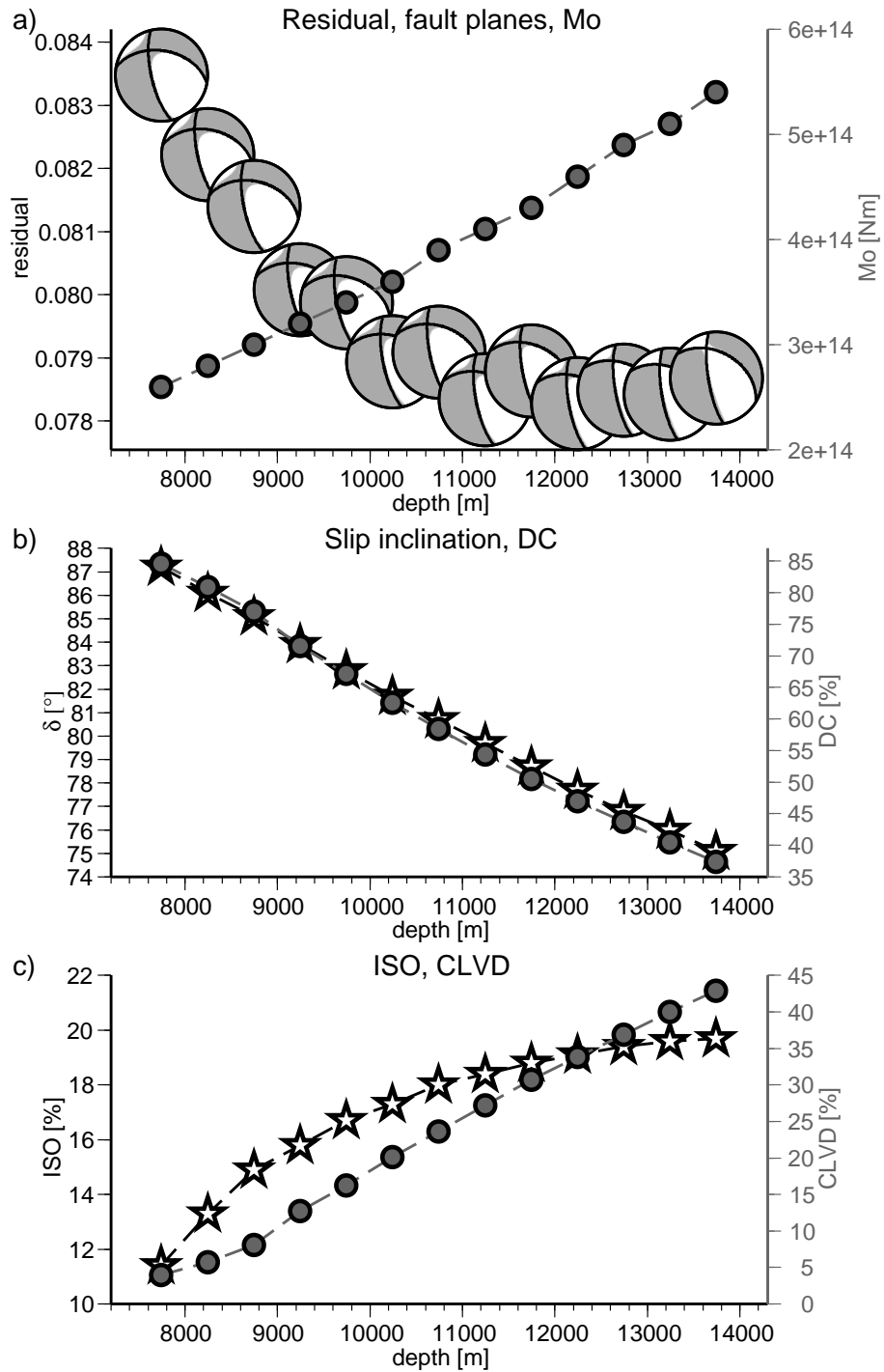


Figure 4.12: As in Fig. 4.10 but for model III.

medium surrounding the source allows direct interpretation of the retrieved source mechanism in terms of possible volumetric source changes. For interpretation we assume dislocation point sources characterised by the normal to the fault plane, the direction of the slip, the fault area, and the size of the slip. Fault normal and slip vector may be arbitrarily oriented. Thus, we allow shear faulting as well as tensile faulting. Deviations from the dislocation model may be found by an eigenvalue analysis of the source tensor  $D_{pq}$ . The inversion scheme is based on fitting of synthetic seismograms to observed ones. For computation of synthetic seismograms we apply ray methods for isotropic or anisotropic media, which represent a basis of the ANRAY software package (Pšenčík, 1998). The algorithm is therefore time-effective and applicable in standard data processing. The success of the proposed inversion scheme depends on the accuracy of the used structural model.

The inversion algorithm was applied to one earthquake of the earthquake swarm that occurred in West Bohemia in the year 2000. We observe  $M_T \approx 3.4 * 10^{14}$  Nm and left-lateral strike oblique normal faulting. The source mechanism retrieved for this event is in agreement with the model for dislocation point sources. A small amount of crack opening is indicated. Although it is only slight, this feature seems to be generally stable and significant for different structural models, different assumptions about source depth and for changing station coverage. The local stress field obtained from the retrieved source mechanisms is in agreement with other observations in West Bohemia and Central Europe. The results of inversion are constrained by jackknife and bootstrap tests. Accounting for structural 1D inhomogeneity has a significant effect on the solution. Taking into account anisotropy in the inhomogeneous model II leads to a slight decrease in the tensile component of the obtained source mechanism. In model II anisotropy is derived from information of P waves only. Changes in anisotropy caused by considering S waves are expected to further influence the results. Effects due to more complicated source-time functions are diminished by excluding frequencies above the corner frequency of the event. The influence of intrinsic attenuation, near-source inhomogeneity, e.g., crack induced changes in near-source anisotropy, and source finiteness are not considered here.

Future applications of the introduced inversion algorithm can be seen where accurate determination of source mechanisms is of superior interest and where well-defined anisotropic velocity models exist, e.g. in borehole vicinity or in carbonhydrate production fields.

## Acknowledgements

Support of the German Science Foundation (DFG, grants KR1935/1-1 and KR1935/1-3), of the Charles University, Prague through the MAGMA project, of the Geophysical Institute, Acad. Sci. of the CR, and of the consortium project SW3D is appreciated. We thank the following people for data provision: T. Fischer (Geophysical Institute, Acad. Sci. of the CR), Th. Plenefisch (SZGRF), S. Funke (University of Leipzig), J. Wassermann (University of Munich) as well as colleagues and students from the University of Potsdam.

## 4.5 Appendix

### 4.5.1 Equations for source retrieval

Equations (4.7) can be derived from Eqs. (4.1), (4.2), (4.3), and (4.6) in the following way:

$$\begin{aligned} u_i(\mathbf{x}, t) &= g_i(\mathbf{x}) \left[ \frac{\rho(\mathbf{x}_0)c(\mathbf{x}_0)}{\rho(\mathbf{x})c(\mathbf{x})} \right]^{1/2} \frac{Df^{(A)}(t - \tau(\mathbf{x}))}{|\Omega_M(\mathbf{x})|^{1/2}} \exp \left[ i\frac{\pi}{2}k_s - i\frac{\pi}{2}k(\mathbf{x}_0, \mathbf{x}) \right] \\ &= A_i B_{jk} s_p n_q c_{pqjk} s A_0 f(t - \tau(\mathbf{x})) \exp \left[ i\frac{\pi}{2}k_s - i\frac{\pi}{2}k(\mathbf{x}_0, \mathbf{x}) \right]. \end{aligned} \quad (4.11)$$

From (4.11), we obtain Eq. (4.7)

$$\operatorname{Re}(u_i(\mathbf{x}, t)) = \operatorname{Re} \left( Y_{il} f(t - \tau(\mathbf{x})) \exp \left[ i\frac{\pi}{2}k_s - i\frac{\pi}{2}k(\mathbf{x}_0, \mathbf{x}) \right] \right) \sigma_l.$$

In (4.11) we use the following notations:

$$A_i = \frac{g_i(\mathbf{x})}{(\rho(\mathbf{x})c(\mathbf{x}))^{1/2}} \frac{1}{|\Omega_M(\mathbf{x})|}, \quad (4.12)$$

$$B_{jk} = \frac{g_j(\mathbf{x}_0)p_k(\mathbf{x}_0)}{4\pi (\rho(\mathbf{x}_0)c(\mathbf{x}_0))^{1/2}}, \quad (4.13)$$

$$\begin{aligned} Y_{i1} &= X_{i1}c_{1111} + X_{i2}c_{1112} + X_{i3}c_{1113} + X_{i4}c_{1122} + X_{i5}c_{1123} + X_{i6}c_{1133}, \\ Y_{i2} &= X_{i1}c_{1211} + X_{i2}c_{1212} + X_{i3}c_{1213} + X_{i4}c_{1222} + X_{i5}c_{1223} + X_{i6}c_{1233}, \\ Y_{i3} &= X_{i1}c_{1311} + X_{i2}c_{1312} + X_{i3}c_{1313} + X_{i4}c_{1322} + X_{i5}c_{1323} + X_{i6}c_{1333}, \\ Y_{i4} &= X_{i1}c_{2211} + X_{i2}c_{2212} + X_{i3}c_{2213} + X_{i4}c_{2222} + X_{i5}c_{2223} + X_{i6}c_{2233}, \\ Y_{i5} &= X_{i1}c_{2311} + X_{i2}c_{2312} + X_{i3}c_{2313} + X_{i4}c_{2322} + X_{i5}c_{2323} + X_{i6}c_{2333}, \\ Y_{i6} &= X_{i1}c_{3311} + X_{i2}c_{3312} + X_{i3}c_{3313} + X_{i4}c_{3322} + X_{i5}c_{3323} + X_{i6}c_{3333}, \end{aligned} \quad (4.14)$$

where

$$\begin{aligned} X_{i1} &= A_i B_{11}, \\ X_{i2} &= A_i (B_{12} + B_{21}), \\ X_{i3} &= A_i (B_{13} + B_{31}), \\ X_{i4} &= A_i B_{22}, \\ X_{i5} &= A_i (B_{23} + B_{32}), \\ X_{i6} &= A_i B_{33}. \end{aligned} \quad (4.15)$$

### 4.5.2 Slip and fault normal from the source tensor

The orientation of the slip  $s_i$ , the fault normal  $n_i$ , and the product of fault area  $A_0$  and the length of the slip  $s$  are determined from the eigenvalues  $\nu_i$  and the corresponding eigenvectors  $\mathbf{e}_i$  of the source tensor  $D_{ij}$ . The eigenvalues of  $D_{ij}$  are (compare Vavryčuk, 2005)

$$\nu_1 = \frac{sA_0}{2} (s_i n_i + 1), \quad \nu_2 = 0, \quad \nu_3 = \frac{sA_0}{2} (s_i n_i - 1). \quad (4.16)$$

They can be also written as

$$\nu_1 = \frac{sA_0}{4}(\mathbf{s} + \mathbf{n}) \cdot (\mathbf{s} + \mathbf{n}), \quad \nu_2 = 0, \quad \nu_3 = \frac{sA_0}{4}(\mathbf{s} - \mathbf{n}) \cdot (\mathbf{s} - \mathbf{n}). \quad (4.17)$$

The corresponding (normalised) eigenvectors are

$$\mathbf{e}_1 = (\mathbf{s} + \mathbf{n})/|\mathbf{s} + \mathbf{n}|, \quad \mathbf{e}_2 = (\mathbf{s} \times \mathbf{n})/|\mathbf{s} \times \mathbf{n}|, \quad \mathbf{e}_3 = (\mathbf{s} - \mathbf{n})/|\mathbf{s} - \mathbf{n}|, \quad (4.18)$$

where  $\times$  denotes the vectorial cross product. Then,  $s_i$ ,  $n_i$ , and  $A_0s$  are determined from (4.17) and (4.18)

$$\mathbf{s} = \frac{\mathbf{e}_1\sqrt{\nu_1} + \mathbf{e}_3\sqrt{|\nu_3|}}{|\mathbf{e}_1\sqrt{\nu_1} + \mathbf{e}_3\sqrt{|\nu_3|}|}, \quad \mathbf{n} = \frac{\mathbf{e}_1\sqrt{\nu_1} - \mathbf{e}_3\sqrt{|\nu_3|}}{|\mathbf{e}_1\sqrt{\nu_1} - \mathbf{e}_3\sqrt{|\nu_3|}|}, \quad sA_0 = \nu_1 - \nu_3. \quad (4.19)$$

### 4.5.3 Parameters of seismic stations in West Bohemia in 2000

Table 4.5: Coordinates of stations used for source retrieval (see Figure 4.1).

station	lat. [° North]	lon. [° East]	height [m]	s.r. [Hz]	sensor	institution
KOC	50.26521	12.23352	575	250	SM-3	WEBNET
KRC	50.33159	12.53028	760	250	SM-3	WEBNET
LAC	50.05075	12.62495	838	250	SM-3	WEBNET
LBC	50.26555	12.41218	638	250	SM-3	WEBNET
MANZ	49.98710	12.10950	553	250	STS2	U. Munich
NKC	50.23312	12.44786	564	250	SM-3	WEBNET
P01G	50.240	12.253	750	250	LE-3D/5s	U. Potsdam
P02G	50.319	12.396	630	250	LE-3D/5s	U. Potsdam
P03G	50.270	12.331	800	250	LE-3D/5s	U. Potsdam
P08G	50.225	12.298	710	250	LE-3D/5s	U. Potsdam
P09G	50.188	12.300	720	250	LE-3D/5s	U. Potsdam
P13G	50.411	12.472	480	250	LE-3D/5s	U. Potsdam
SKC	50.16980	12.36103	455	250	LE-3D	WEBNET
SNE	50.31072	12.50273	702	250	SM-3	WEBNET
STC	50.25914	12.51965	666	250	SM-3	WEBNET
TRC	50.30321	12.14452	566	250	LE-3D	WEBNET
VAC	50.23540	12.37710	535	250	SM-3	WEBNET
WERN	50.2874	12.3761	630	250	STS2	U. Leipzig

s.r.=sampling rate, U.=University of, lat./lon.=geographic coordinates



## 5 Source parameters for swarm earthquakes in West Bohemia in 2000

Motivated by the geoscientific observations described earlier in Section 1 and the findings about the influence of anisotropy on moment tensors introduced in Sections 1-3, I challenge the question for the occurrence, reliability, and the origin of possible tensile components of earthquakes in West Bohemia. Using the inversion algorithm that was first presented in Section 4, source parameters are determined for events of the swarm episode in 2000.

### 5.1 Data selection

To date, no detailed source investigations including studies of tensile components for the swarm events in the Vogtland in 2000 have been performed. *Hainzl and Ogata* (2005) observe high and intermediate influence of fluids on the triggering of earthquakes during the swarm phases 1-3 and 4-7, respectively, but a lowered role of fluids towards the end of the swarm (see also Section 1.4.5). If over-pressurised fluids cause hydrofracturing (opening of cracks during faulting) in the focal area, tensile components with different size should thus be observable for events of the phases 1-7 between August 28, 2000 and October 30, 2000. In addition, the existing networks of permanent and temporary seismic stations were supplemented by instruments of the University of Potsdam from September 11, 2000 until October 24, 2000 (see Fig. 1.9 and Tab. C.1 for information on seismic stations). For these reasons, the source mechanisms of earthquakes that occurred during the swarm phases 1-7 are studied. This section focuses on the results.

To guarantee that data show high signal-to-noise ratio and that events are recorded at most available stations, 112 out of totally 128 major events with  $M_L \geq 1.7$  that occurred within this period were selected for source determination. Precise source coordinates and times as well as preliminary local magnitudes (1.28) were obtained from *Fischer* (pers. comm.) who used a relative method for source location. Source coordinates have estimated uncertainties in depth and laterally of  $\approx 100$  m (*Fischer*, pers. comm.). They are given in Table C.2 (see also Figs. 1.11, 1.12, and 5.7 for their spatial and temporal distribution).

Waveform data were purchased for the selected events at the universities of Leipzig, Munich, and Potsdam, the Seismological Central Observatory in Erlangen (SZGRF), and the Geophys. Inst., Acad. Sci. of the CR (WEBNET). Data of the local networks operated by the Masaryk University, Brno, Czech Republic, and the GeoForschungsZentrum Potsdam (GFZ) were also obtained from the SZGRF. However, seismograms of stations run by the GFZ, the KRASNET, and the SZGRF could not be used herein (see Fig. 1.9 and Tab. C.1). The corner frequencies of the KRASNET stations are high (well above 1 Hz) and only insufficiently known (*Špáček*, pers. comm.). Tests on a shaking table have shown that they vary significantly between the single components of a station and also between stations (*Horálek*, pers. comm.). Stations of the SZGRF had partially low sampling rates and/or technical problems that could not be safely recovered (*Brunner and Klinge*, pers. comm.). GFZ stations were not used because true amplitudes could not be successfully obtained. However, only 3 events are concerned by this obstacle (events 110-112 in Tab. C.2).

## 5.2 Data preparation

The original signal of an incoming wavefield is modified by the characteristic transfer function, the sensitivity of the sensor (seismometer), and the gain of the data logger (*Aki and Richards, 2002; Scherbaum, 2001; Bormann, 2002*). Using its poles and zeroes the shape of the transfer function is described by a polynomial expansion. The electromagnetic seismometers utilised in this study (see Tab. C.1) are sensitive to the velocity of the particle motion in the wavefield (*Bormann, 2002*). They have constant amplification for frequencies in the pass band above the corner frequency of the sensor (see Tab. C.1 for the corner frequencies). Below this frequency, the amplification is proportional to the square of the circular frequency of the incoming velocity field ( $amplitude(\omega) \sim \omega^2$ ). However, for some stations in West Bohemia poles and zeroes are not accurately known. Their amplitudes in the low-frequency wavefield could not be safely recovered. The recorded raw data were therefore corrected only for sensitivity and gain. Hereby, the amplitudes of the velocity field were recovered for frequencies above the corner frequency of the sensor.

Depending on the station raw data have different sampling rates (see Tab. C.1 for sampling rates). Later inversion by matching of waveforms in the time domain requires equal sampling of data and of synthetic seismograms. Therefore, all seismograms are resampled with 10 ms sampling interval (Nyquist frequency: 50 Hz, *Gubbins, 2004*). Thereafter, the resampled, amplitude-corrected data were integrated to obtain the high-frequency displacement field. The integration of seismograms in the time domain corresponds to a division by frequency in the frequency domain (*Gubbins, 2004*). Thus, it leads to an amplification of the low-frequency content of the wavefield. To stabilise integration and to suppress amplitudes below the corner frequencies of the sensor a casual 5<sup>th</sup>-order 1 Hz Butterworth high-pass filter is applied to the data.

The P wavelets of the chosen events (compare Fig. 1.13) show corner frequencies above 10 Hz (Fig. 4.4). Independence of inversions from the source-time functions of the events is guaranteed by additional filtering of the integrated data with a casual 5<sup>th</sup>-order 10 Hz low-pass Butterworth filter.

## 5.3 Computation of synthetic seismograms

As in Section 4, the software package ANRAY (*Pšenčík, 1998*) is utilised to calculate the synthetic waveforms required for inversion. Again, the inhomogeneous isotropic model I, the inhomogeneous anisotropic model II, and the homogeneous anisotropic model III are used to specify elastic medium properties (see Appendix for model specifications). Inversion tests using synthetic waveforms and real-world data have shown the stability and applicability of the algorithm (see Section 4 and *Rößler et al., 2005*). During modelling of synthetic seismograms a source duration of  $\approx 100$  ms with the shape of a Brüstle-Müller signal, Equation (1.63), is uniformly assumed for all events. This simplification is justified because P waveforms are very similar (see Section 1.4.5 and Fig. 1.13). Equal sampling and filtering is applied to synthetic seismograms and data.

A first estimate about the goodness of the velocity models is obtained by comparing the differences between travel times for the synthetic seismograms in the velocity models I, II, and III (see Fig. 5.1 for travel-time differences) and observed travel times.

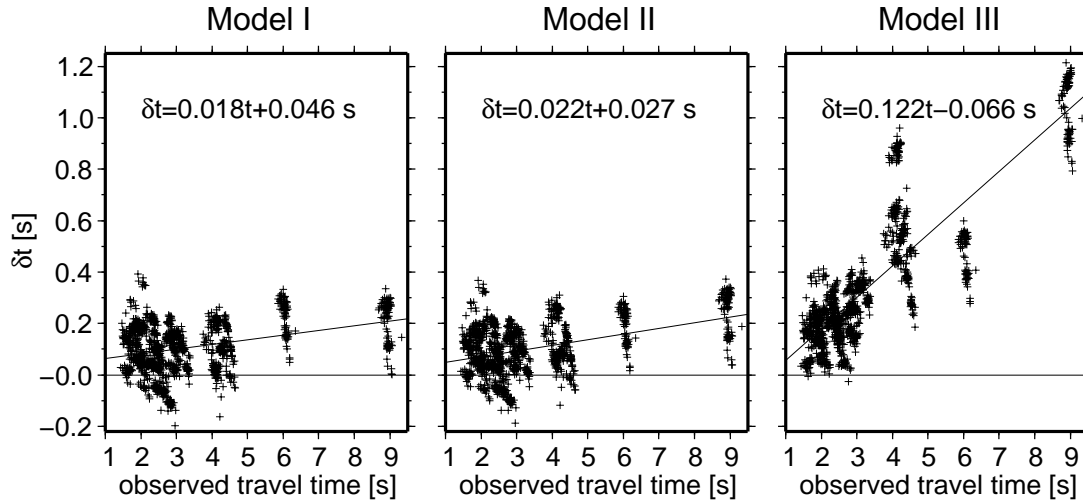


Figure 5.1: Travel-time differences  $\delta t$  vs. observed travel times  $t$  for velocity models I, II, and III and P waves of events in Tab. C.2 with confidence class 1 or 2.  $\delta t = t^{theo} - t$ , where  $t^{theo}$  are theoretical travel times. Mean absolute differences are  $\delta t = 0.122 \text{ s}$ ,  $0.120 \text{ s}$ , and  $0.351 \text{ s}$  for models I, II, and III, respectively. Functions of linear regressions are also given.

The latter are calculated as the difference between source time and picked P-wave onsets. Travel times of modelled waves are on average larger than observed travel times. The dependence of travel-time differences  $\delta t$  on observed travel times  $t$  (thus, epicentral distance) is smaller for the models I and II than for model III. Mean values of absolute differences for models I, II, and III are  $0.122 \text{ s}$ ,  $0.120 \text{ s}$ , and  $0.351 \text{ s}$ , respectively. A linear approximation of the dependence  $\delta t = \delta t(t)$  by  $\delta t(t) = mt + n$  yields  $(m,n)=(0.018,0.046 \text{ s})$ ,  $(m,n)=(0.022,0.027 \text{ s})$ , and  $(m,n)=(0.122,-0.066 \text{ s})$  for models I, II, and III, respectively. Therefore, models I and II provide a better estimate of travel times than model III. Assuming isotropic P-wave velocities with  $v_p = 6100 \text{ m/s}$  at  $8410 \text{ m}$  depth (compare model I, Appendix B.4), the constants  $n = 0.046 \text{ s}$  and  $n = 0.022 \text{ s}$  correspond to uncertainties in event depth of  $280 \text{ m}$  and  $134 \text{ m}$ , respectively. These values are larger than those estimated by Fischer (pers. comm.) but they are similar to those by Málek et al. (2005). Uncertainties in focal depth and model-dependent differences are also indicated by inversions assuming different source depths (compare Section 4.3).

## 5.4 Retrieved source parameters

The signals of the P waves of all 112 events are used to retrieve seismic source parameters such as size of an event, source geometry, fault-plane solutions, as well as possible volumetric changes and moment tensor components. For inversion, a time window of  $0.3 \text{ s}$  around the P wavelets is defined. The same procedure as in Section 4, including phase alignment, is applied. Based on the model for dislocation sources, the amount of tensile faulting (opening or closing of the crack) is quantified by the slip inclination  $\delta$  that refers to the angle between the slip direction and the normal to the fault (see Section 1.2.2). S waves are not included in inversions because their waveforms are more complicated than those of P waves (see Fig. 1.10). They may be affected by S-wave splitting (anisotropy) and by effects due to overcritical incidence at the earth's surface (Aki and Richards, 2002). These effects are strongly dependent

on the ratio of  $v_p/v_s$  and difficult to control. In addition, the inhomogeneous isotropic model I and the inhomogeneous anisotropic model II contain no information that are derived from S wave propagation in anisotropic media (see Sections 4 and B). Although S-wave splitting is observed in the Vogtland (see Section 1.4.4 and Fig. 1.10), it cannot be modelled with these two models.

By time-shifting and merging the split qS1 and qS2 waves, Šílený and Vavryčuk (2002) succeeded to retrieve fault-plane solutions for events in anisotropic media assuming isotropy. However, this method comes with the cost of loosing resolution of tensile source components.

During inversion only those stations are used for which true displacement amplitudes can be recovered. Stations with unknown sensitivity and gain are excluded from the inversions (see Fig. 1.9). The length and the shape of the source-time functions of the events are assumed as a constant. Anelastic attenuation for P waves, as described by the quality factor  $Q_P$ , is not considered for waveform modelling because no detailed attenuation model exists so far. However, studies of earlier events in West Bohemia indicate low attenuation below frequencies of 5 Hz (Fischer, 1993) and values in the range of  $198 \pm 72 \leq Q_P \leq 231 \pm 135$  (Kolář, 2003). Observations at the nearby KTB borehole report on much larger attenuation and  $14 \leq Q_P \leq 32$  (Pujol *et al.*, 1998) or  $Q_P \approx 40$  for frequencies between 10 and 20 Hz (Trela, 2003).

The filtered displacement-proportional seismograms and synthetic waveforms are manually time-aligned and finally shifted using automatic cross-correlation to match the waveforms before inversion. Only those seismograms for which phase alignment was successful are used for source retrieval. Dissimilar traces with low cross-correlation coefficients below 0.6 are excluded. However, most traces show high cross-correlation and cross-correlation coefficients  $\geq 0.9$ . Many consecutive swarm events have short interevent times that may lead to a contamination of their phases with phases of earlier events (see Fig. 1.14 for seismogram examples). When two or more earthquakes occurred close in time, phase picking was complicated or even non-unique. Low correlation and unsafe phase identification can be further caused by noise, multiple events, and complicated source-time functions. Traces with visually complicated signal or traces with unacceptable uncertainty in phase picking are also not used for inversion.

The P-wave signals of all 112 events in Tab. C.2 are inverted for the six elements of the source vector (1.18). As in Section 4, bootstrap and jackknife tests are carried out to test the reliability of the inversions. Based on inversions using the velocity models I or II, results are classified by their confidence and stability during testing. Three confidence classes are defined:

**Confidence class 1:** The fault planes and the slip inclination  $\delta$  are uniquely derived and can be interpreted. Only minor variations of these quantities occur during testing. They do not lead to differing interpretations. Residuals are low. Polarities and amplitudes of most waveforms are well fitted.

**Confidence class 2:** Fault planes are uniquely derived and can be interpreted. If data from station NKC, the station nearest to the hypocentres, are missing and/or ray coverage is low, this did not lead to instabilities of the source orientation during testing. However, during testing instabilities are found for retrieved  $\delta$ .

**Confidence class 3:** Neither the fault-plane solutions nor the slip inclination are uniquely derived. They are unstable during testing. Resulting source mechanisms cannot be interpreted. Additional criteria are unsafe phase picking due to high noise level,

short inter-event times with phase contamination, and clear observations of multiple events.

Based on these criteria, a total number of 72, 30, and 10 events are found to meet conditions for the confidence classes 1, 2, and 3, respectively. Events 2, 12, 39, 41, 43, 44, 85, 102, 103, and 111 are associated with class 3 (see Table C.2). To conclude on determined source orientations, only events with confidence class 1 or 2 and for interpretation of tensile source components only events with confidence class 1 are considered.

In theory, exploiting the P and S waves at only one station is sufficient to determine a source mechanism (*Dreger and Helmberger, 1993*). As in other techniques for determination of source parameters, good azimuthal coverage improves the stability of the solutions (see e.g. *Dahm, 1993; Dufumier and Cara, 1995*). The gap criterion is a common measure of station coverage. It is defined as the largest occurring azimuthal distance between two neighbouring stations for one event.

In West Bohemia the distribution of stations used for inversion is rather non-uniform (see Fig. 1.9). Only one station (LAC) provides observations in southeast direction. For source retrieval of events with confidence class 1 or 2 at least 7 stations and 16 traces could be used. The gap varies between  $68^\circ$  and  $161^\circ$  (see Tab. C.2). If only few observations and no seismograms from station LAC are available, gap is large and the stability of inversion is generally reduced.

The stability of the inversion results are assessed by jackknife and bootstrap tests, as well as mutual comparison. Standard deviations obtained from these tests are used as a measure of the uncertainty for the determined parameters. Results of the inversions using the velocity models I, II and III are summarised for all events in the Figs. 5.2-5.6. Detailed information on solutions for single events, statistic parameters, and confidence classes can be found in Appendix C, Figures C.1-C.24 and Tables C.3-C.6.

#### 5.4.1 Misfit reduction

Remaining residuals between synthetic and observed data are on average 0.07 for inversions using the models I and II and 0.08 for model III (see Tab. C.4). Therefore, the misfit can be significantly reduced during source retrieval. Using the three velocity models the retrieved mechanisms can explain observed P-wave amplitudes in a similar way. Observed P-wave polarities can be matched for most events independent of the model used here (see examples in Section 4.3 and in Figs. 5.10, 5.11 or Figs. C.1-C.7 for an overview). However, using model III a larger number of mismatches occurs than for the models I and II.

#### 5.4.2 Size of events

For events with confidence class 1 or 2, seismic moments between  $8.9 \cdot 10^{12}$  Nm and  $4.6 \cdot 10^{14}$  Nm are observed (see Fig. 5.2b and Tab. C.3 for more details). For the considered events, most moment release occurs in depths between 8500 m and 9500 m, see Fig. 5.2b. In addition, peak moment release also occurs at depths of about 8100 m and 9900 m. Accordingly, local magnitudes  $M_L$ , Eq. (1.28), are in the range  $1.6 \leq M_L \leq 3.2$  (see Fig. 5.2a and Tab. C.3 for a list of  $M_L$ ). On average they are larger by 0.2 than the local magnitudes of *Boušková (2005)* but similar to those determined by *Tittel and Wendt (2003)*, compare magnitudes in Figure 5.2. For the single events,

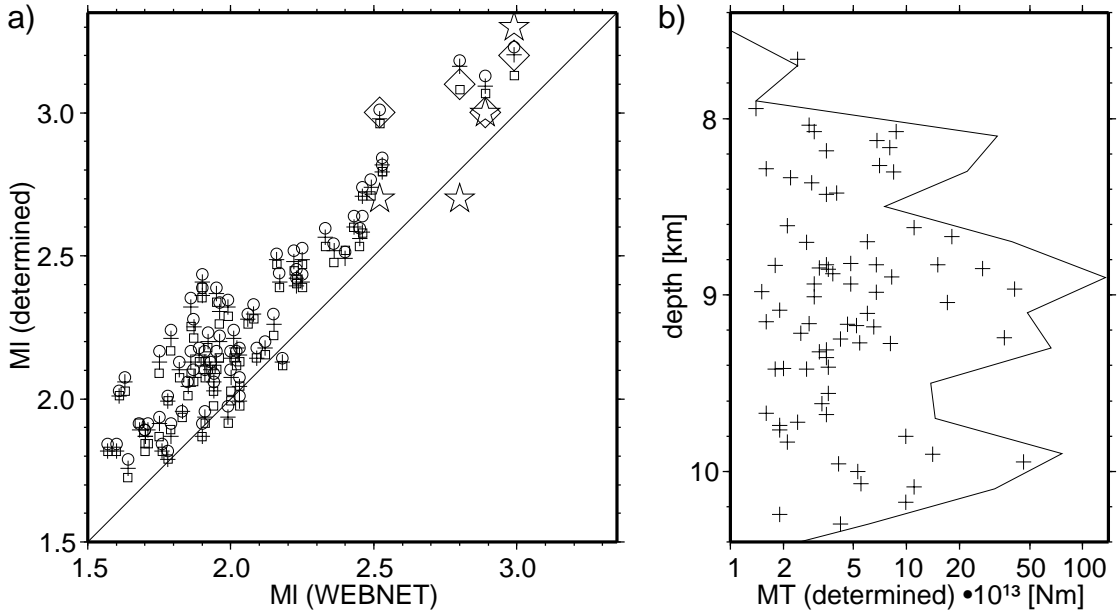


Figure 5.2: Local magnitudes and seismic moment for events with confidence class I in Tab. C.2. a)  $M_L$  determined from inversions vs.  $M_L$  by WEBNET (*Fischer*, pers. comm.). Magnitudes are calculated using relation (1.28) and velocity models I (crosses), II (circles), or III (squares). Large symbols at  $M_L > 2.5$  represent local magnitudes determined by *Tittel* and *Wendt* (2003) at station WERN (stars) or the GRSN station CLL (diamonds). b) Source depth vs. seismic moment  $M_T$  determined for model II. The solid line represents the cumulative seismic moment that is released within depth intervals of 200 m.

the mean differences in magnitudes that result from inversions using the models I, II, or III are less than 0.1. Determined potencies, Eq. (1.22), vary between  $472 \text{ m}^3$  and  $25110 \text{ m}^3$  (see Tab. C.3). Assuming circular fault planes, a uniform stress drop of  $\Delta\sigma = 1.7 \text{ MPa}$  for each event during faulting (*Hainzl* and *Fischer*, 2002), and relation (1.29) estimates for the radii  $r$  of the rupture planes, with  $114 \text{ m} \leq r \leq 450 \text{ m}$ , are found (compare Fig. 5.3). For intraplate earthquakes, the stress drop assumed here is at a lower limit (*Scholz*, 2002). Hence, the calculated radii might be overestimated. Using the definition of the potency,  $sA_0$ , with  $A_0 = \pi r^2$ , the size of the slip  $s$  is in the range  $0.01 \text{ m} \leq s \leq 0.05 \text{ m}$ .

### 5.4.3 Fault-plane solutions

Fault-plane solutions were determined using the three velocity models I, II, and III, see Fig. 5.4a for fault-plane solutions. They are similar for most events and approximately described by faulting on steeply dipping N–S oriented or shallowly dipping E–W oriented planes. Variability in strike and dip is largest for model III and reduced for the models I and II (see Fig. 5.4a and Tabs. C.4 for more details). Because the event foci are situated along a NNW striking fault zone (see Figs. 1.11 and 5.3) the roughly N–S oriented fault-planes are identified as the rupture plane with sinistral sense of shear. Associated strike directions are  $\Phi_1^s \leq 21^\circ$ ,  $\Phi_1^s \geq 348^\circ$ , and  $148^\circ \leq \Phi_1^s \leq 189^\circ$  (see Fig. 5.4 and Tab. C.4). Oblique reverse and oblique normal faulting is observed (see figures in Appendix C.3 for source mechanisms determined for each event). However, oblique reverse faulting on almost vertical fault planes is mainly found for events

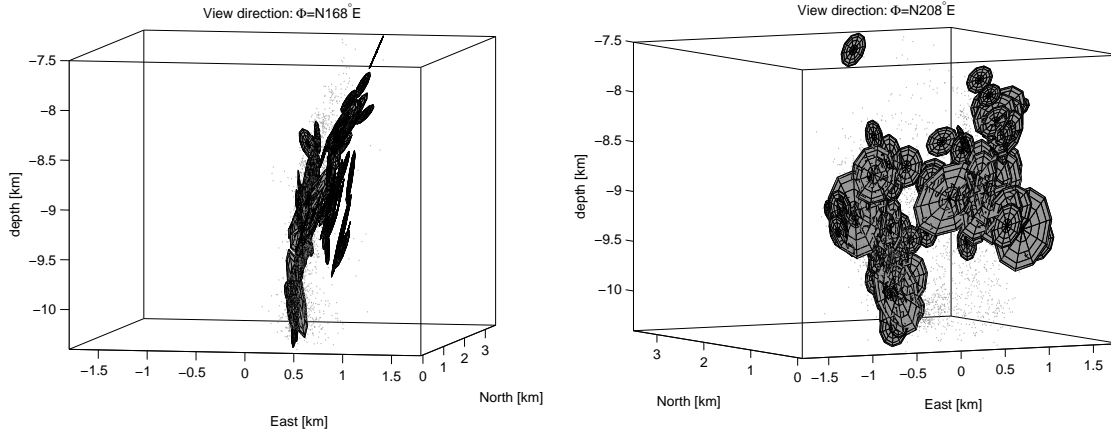


Figure 5.3: Three-dimensional view on determined rupture planes (meshed circles) and over 4,000 foci (dots) of swarm earthquakes in 2000 projected into the focal zone. Rupture planes are obtained for the velocity model II. They are centred at source position. Assuming circular rupture planes, Eq. (1.29), and constant stress drop of  $\Delta\sigma = 1.7\text{MPa}$  (Hainzl and Fischer, 2002) their radii  $r$  are approximated. Left: fault-parallel view along the rupture zone from  $N168^\circ\text{E}$ , right: view from  $N208^\circ\text{E}$ . Changes in dip of the rupture planes coincide with bending of the fault zone near 8.5 and 9.5 km depth. Origin point is at  $(50.2059^\circ\text{N}, 12.4449^\circ\text{E}, 0\text{ km})$ .

until September 10, 2000. During the later swarm phases 5, 6, and 7 oblique reverse faulting is rare (compare mechanism of single events in Figs. C.1-C.7). These events also coincide with observations of positive first P-wave motion at station NKC. From the 3D-projection of the retrieved rupture planes onto their epicentres in Fig. 5.3 the 2D-character of the fault zone becomes visible. Most rupture planes are aligned with this zone. Some exceptions occur for events between 8 and 9 km.

The dip angles of the rupture planes  $\delta_1^s$  are in the range of  $51^\circ \leq \delta_1^s \leq 90^\circ$  (see Fig. 5.4b and Tab. C.4). Although some variations occur, a general trend towards steeper dip angles at greater depth is observed. Average dip increases from relatively low angles ( $\delta_1^s \approx 55^\circ$ ) above 8400 m to steep angles ( $\delta_1^s \geq 75^\circ$ ) below 8400 m with only few exceptions. The focal depths where changes in dip angle are observed also coincide with bending of the fault zone as described by the earthquake foci (see Figs. 5.3, 5.4b). At great depth, deeper than 9500 m, overturning of the fault planes occurs. It is indicated by steep dip angles and strike directions of  $\Phi_1^s \geq 345^\circ$  or  $\Phi_1^s \leq 21^\circ$  (compare Figs. 5.3, 5.4a, and Tab. C.4). The latter events also coincide with earthquakes for which oblique reverse faulting is observed. Since the swarm phases are separated in space and time this indicates altering stress conditions in the progress of the swarm.

Fault-plane solutions are also confirmed by inversions using MTINVERS by T. Dahm and F. Krüger, see Appendix C.9.

#### 5.4.4 Tensile source components

Tensile components are observed for most events. Regardless of the velocity model used during inversion the slip inclinations  $\delta$  vary in the range  $77^\circ \leq \delta \leq 95^\circ$  (see Fig. 5.4c,d and Tab. C.4 for more details and for standard deviations).

During testing of inversion results it was found that slip inclinations determined for single events using different ray coverage (jackknife tests) may vary within  $\pm 2^\circ$ . This value is regarded as an approximation of the absolute uncertainty of  $\delta$  and valid for

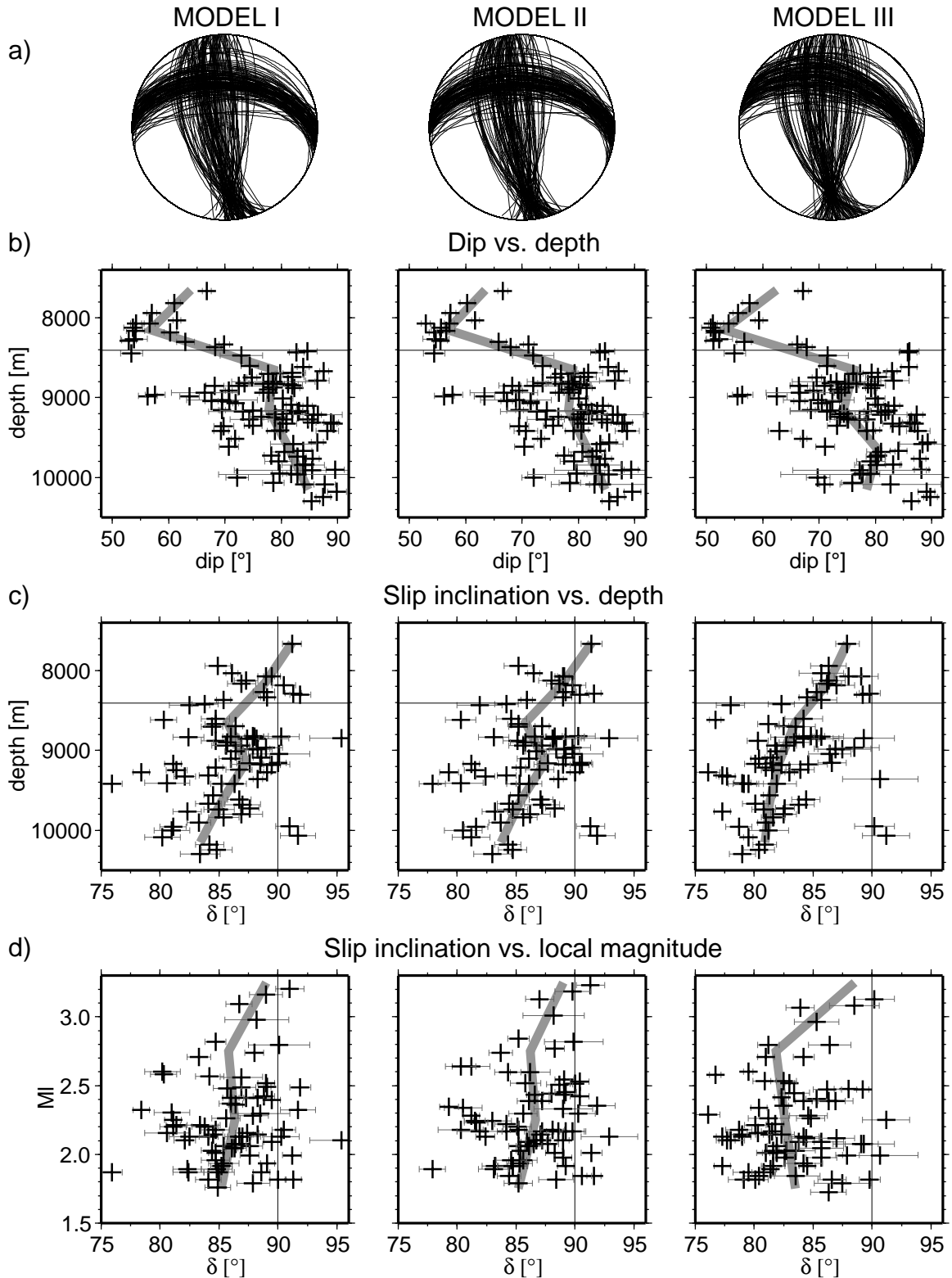


Figure 5.4: Fault-plane solutions (FPS) (a) and source parameters (b-d) retrieved for events in Tab. C.2 using the velocity models I-III. Events with confidence class 1 or 2 are used for plotting the FPS and the dip angles. Slip inclinations are displayed for events with confidence class 1 (compare Tab. C.4). Error bars represent intervals of two standard deviation obtained from bootstrap tests (compare Tabs. C.4-C.6, and Figs. C.10-C.19). Solid grey lines: interpolated median values determined for intervals of 500 m depth or  $0.5 M_L$ . The internal layer boundary in model I and II at 8.41 km depth is indicated.



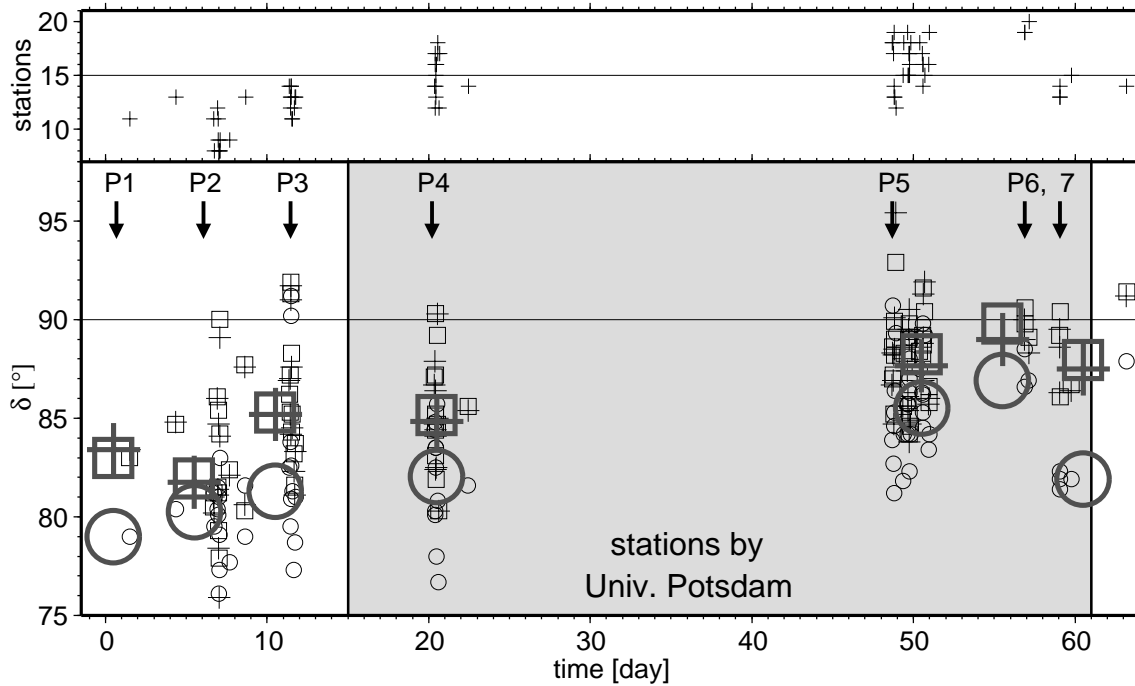


Figure 5.5: Temporal distribution of slip inclinations  $\delta$  determined for events in Tab. C.2 using the velocity model I (crosses), II (squares), and III (circles) and events with confidence class 1 (see Tab. C.4). See also Fig. 5.7 for their spatial distribution. Enlarged grey symbols: median values formed for intervals of 5 days. The station coverage is increased by seismic stations that were installed by the University of Potsdam (grey shaded area). The number of stations used for inversion are plotted on the top (compare Tab. C.2). See Fig. 1.12 for the event-time distribution during the entire swarm. Time = 0 corresponds to August 28, 2000, 00:00:00.

most events. Therefore, events with  $\delta = 90 \pm 2^\circ$  are considered to be shear sources. Results of detailed testing are later described in Sec. 5.5.

The majority of the events show  $\delta \leq 90^\circ$  indicating pure shear or crack opening (positive volume changes), see Figs. 5.4c,d and 5.5. From all 72 events with confidence class 1, positive volume changes are found for 45 events (63%) using model II, 51 events (71%) using model I, and 65 events (90%) using model III. One event with  $\delta > 92^\circ$  ( $\delta = 92.9^\circ$  for model II) and the character of crack closure (negative volume change) is observed for the models I and II but none for model III.

The amount of tensile faulting depends on the velocity model used during inversion (see Fig. 5.5). Using the inhomogeneous anisotropic model II, slip inclinations are on average slightly increased compared to the inhomogeneous isotropic model I. For the homogeneous anisotropic model III most events show decreased values  $\delta$  indicating larger positive volume changes as compared to the models I and II.

The difference in determined tensile components for the velocity models I and II is expressed by the difference in the model-dependent deviation of the event from pure shear ( $|\delta - 90^\circ|$ ):

$$\Delta\delta = |\delta(\text{model II}) - 90^\circ| - |\delta(\text{model I}) - 90^\circ|. \quad (5.1)$$

Differences  $\Delta\delta < 0^\circ$  are found for most events (see Fig. 5.6). This means that the retrieved source mechanisms are more similar to shear faulting and tensile components

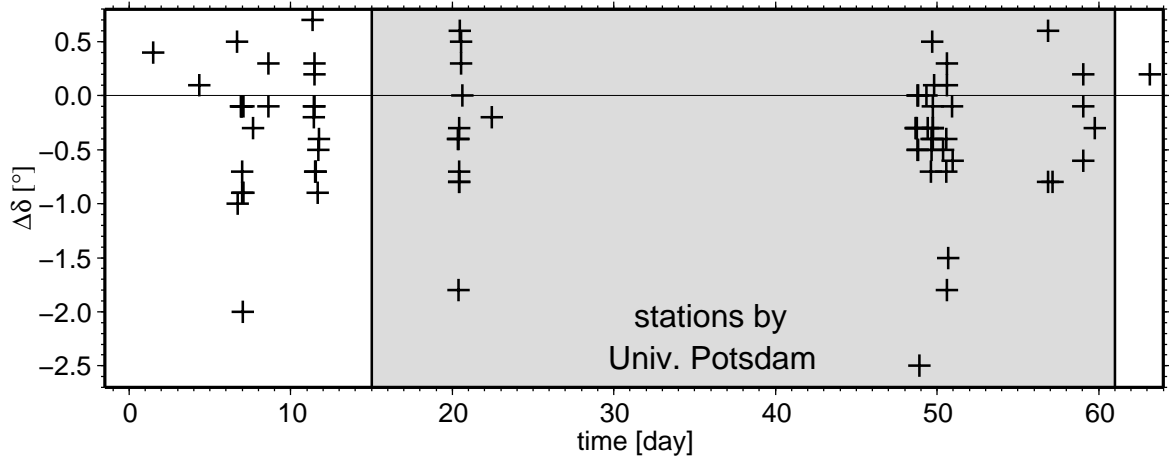


Figure 5.6: Differences in the deviation of retrieved source from pure shear ( $\Delta\delta$  in Eq. 5.1) using the models I and II. Negative values indicate that when using the model II the obtained source mechanism is more similar to pure shear than when using the model I. Events and notations as in Fig. 5.5.

are reduced when using the model II in comparison to inversions for model I. However, the tensile components remain also significant for the inhomogeneous anisotropic model II. The fact that tensile components are on average smallest when using model II during inversion is also valid for the majority of events at different times in the course of the swarm (see Figs. 5.5, 5.6).

Depth-dependence of the slip inclination  $\delta$  is visible in Fig. 5.4c for the three velocity models and in Fig. 5.7. Deep events comprise on average larger tensile components than shallow events. This is indicated by the median curves formed from values of the slip inclination  $\delta$  in depth intervals of 500 m (grey lines in Fig. 5.4c). Tensile components increase with greater depth for the three velocity models used during inversions. The observations might suggest that changes in slip inclination may be an artefact of increasing structural uncertainty at increasing depth. However, this concern may be ruled out because shearing and tensile sources are observed at comparable depths (see Figs. 5.4c, 5.7). The fact that, independent of the velocity model, the largest tensile components can be found for events located at the bottom tip of the hypocentres may be an indicator that they are related to the influence of over-pressurised fluids rising up from a deep-seated reservoir.

Tensile components are mainly observed for small events with  $M_L \leq 2.8$  (Fig. 5.4d). Using model I or II, the largest events are pure shear sources.

In addition to the increase in slip inclination with depth, clear temporal variation in  $\delta$  is observed (see Figs. 5.5 and 5.7). As expressed by the median of  $\delta$ , the majority of events that occurred early during the swarm in phases 1-4 comprise large tensile components with the character of crack opening ( $\delta \leq 86^\circ$ ). In contrast, more shear events and less tensile earthquakes are found during the swarm phases 5-7. Median values of  $\delta$  indicate that events are closer to shear faulting during the phases 5-7 than during the phases 1-4 (see Fig. 5.5).

The spatio-temporal distribution of the events and observed slip inclinations (Fig. 5.7) again demonstrates that events with the largest tensile components are confined to the swarm phases 1-4 and to depths below 8400 m.

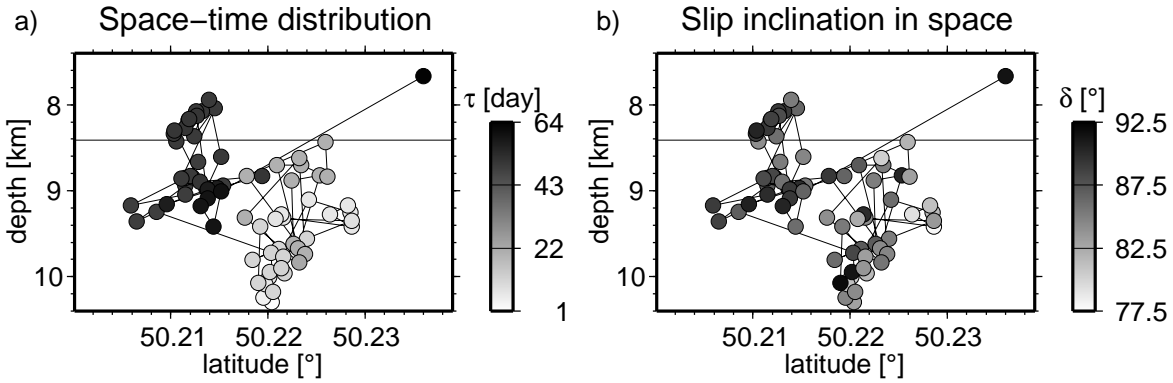


Figure 5.7: Spatial distribution (depth vs. latitude) of events in Tab. C.2 with confidence class 1 along a N-S oriented vertical section. Consecutive events are connected by lines. The layer boundary at a depth of 8.41 km is indicated. a) Source times  $\tau$  are colour-coded,  $\tau = 0$  corresponds to August 28, 2000, 00:00:00. b) Slip inclinations  $\delta$  retrieved using model II are colour-coded.

### 5.4.5 Properties of determined moment tensors

The moment tensor components corresponding to the retrieved source geometries were calculated. They are similar for the models I and II but they comprise on average larger non-double-couple components when using model III (compare results in Fig. 5.8, see also Figures and Tables in Appendix C.6 for a more detailed summary).

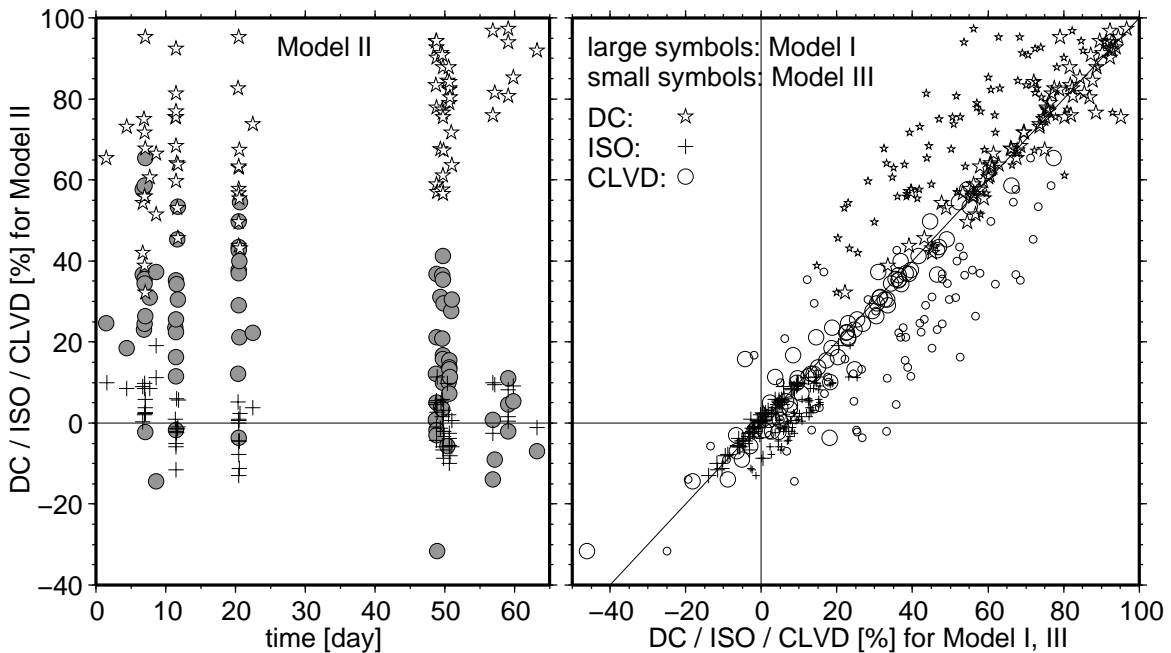


Figure 5.8: Distribution of moment-tensor components determined for events in Tab. C.2 with confidence class 1. Left: Temporal distribution of DC (stars), ISO (crosses), and CLVD (circles) determined using the velocity model II. Time = 0 corresponds to August 28, 2000, 00:00:00. See Fig. C.9 for more details on inversions for models I, II, and III. Right: Moment-tensor components obtained using model I or III vs. results for model II.

Double-couple and CLVD components show clear dependence on source time in the progression of the swarm (see Fig. 5.8). Using the velocity model II during inversion,

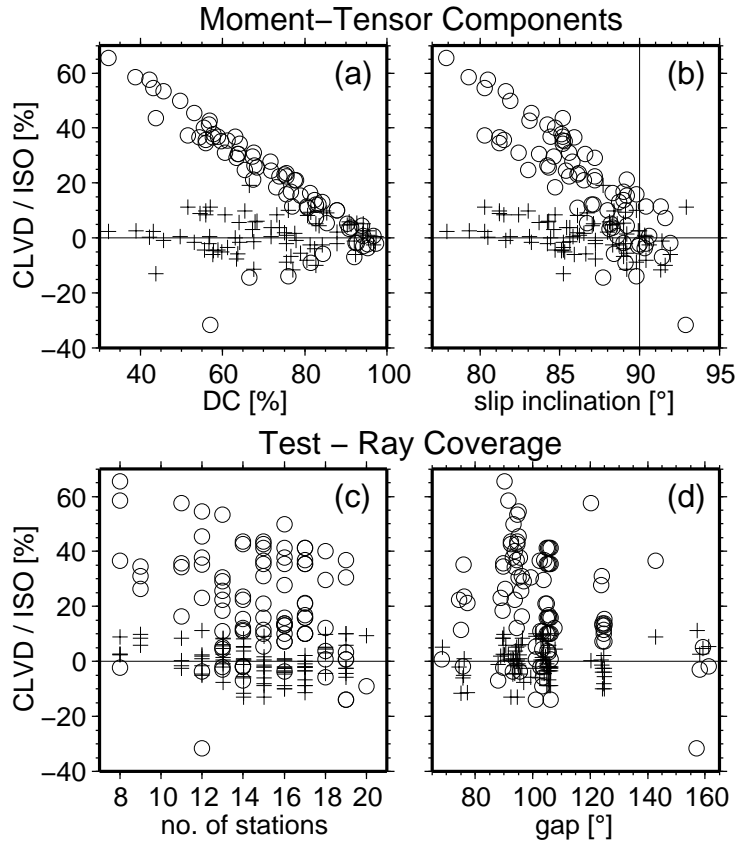


Figure 5.9: Moment-tensor components for events in Tab. C.2 with confidence class 1 using the velocity model II during inversion (compare Fig. 5.8). Crosses: ISO, circles: CLVD. a) ISO and CLVD vs. DC, b) ISO and CLVD vs. slip inclination  $\delta$ . Pure shear occurs for  $\delta = 0^\circ$ . c) Test of ISO and CLVD against the number of stations used during inversion, d) Test of ISO and CLVD against gap (the largest azimuthal distance of neighbouring stations). Compare Fig. 5.8 for the temporal distribution.

exceptionally large CLVD of up to 65% are observed during the phases 1-4 of the swarm. They are significantly smaller during phases 5 (CLVD  $\leq 41\%$ ) and 6 or 7 (CLVD  $\leq |15|\%$ ), compare also Appendix C.6, Fig. C.9. In contrast, the ISO vary almost uniformly between -15% and +20% in the course of the swarm. No direct correlation between ISO and CLVD can be found. Due to the observed independence of the ISO and because the isotropic components are relatively small, variations in CLVD are directly connected to changes in DC. Large CLVD are observed for decreased DC (see Fig. 5.9a). Similarly, the slip inclinations  $\delta$  indicate large tensile components for small DC (anti-correlation between  $\delta$  and CLVD, see Fig. 5.9b).

The largest CLVD component is observed for the event with the lowest number of observations (Fig. 5.9c) which occurred at the beginning of the swarm (see also Appendix C.6, Fig. C.9). However, many events with large CLVD can also be found during the swarm phase 4 where they are constrained by a large number of observations (see Fig. 5.8). No clear relation between the number of seismogram observations and observed CLVD components can thus be found (Fig. 5.9c) and the clear temporal dependence, reported before, dominates the distribution of non-DC components. A direct connection between non-DC components and gap can also be rejected for most events (see Fig. 5.9d). Since the non-DC components are of comparable size for the isotropic model I and the anisotropic model II, they are considered to be real instead of apparent.

#### 5.4.6 Interpretation of source parameters

In accordance with the relations between  $\delta$  and CLVD, the largest CLVD are observed for events at early times during the considered swarm period, at great depths, and for events with small  $M_L$ . Therefore, the large CLVD found together with small ISO and observations of  $\delta \leq 90^\circ$  express significant tensile source components for many events with spatio-temporal variations.

For microearthquakes and also larger events at Long Valley Caldera, USA, *Julian* (1983), *Douglas et al.* (2000), and *Foulger et al.* (2004) found important volumetric source changes. They reported on large CLVD but small isotropic components thus similar to the observations in West Bohemia. Interestingly, *Nettles and Ekström* (1998) explained considerable CLVD components of earthquakes in volcanic areas on Iceland by motion on several segments that form ring faults due to a magma chamber inflation. Near Tori Shima, Japan, *Kanamori et al.* (1993) found an  $m_b = 5.5$  earthquake with dominating CLVD but also negligible ISO. The observations were explained by fluid injection from a deeper source and crack opening (*Kanamori et al.*, 1993) and, alternatively, by ring-fault structures (*Ekström*, 1994).

According to *Foulger and Long* (1984), compensation of isotropic components during tensile faulting may occur due to fluid flow into tensile cracks in response to pressure drop by crack opening. The effects on moment tensor components depend on the compressibility of the fluid. They are smaller for highly compressible fluids such as steam than for less compressible fluids such as water or magma.

Such effects may also account for the observations in West Bohemia. During modelling of moment tensors for synthetic shear and tensile sources in isotropic or anisotropic media (see Section 1.2.3, Tab. 1.1 and Section 3) large CLVD components are usually connected to large isotropic components. This is somewhat dissimilar to the observations in West Bohemia (events with small ISO but large CLVD). In comparison, moment tensors comprising large CLVD but small ISO were found for a synthetic tensile source in an isotropic medium with low  $v_p/v_s$  ratio ( $v_p/v_s = \sqrt{2.5}$ , #2 in Tab. 1.1). The ratio  $v_p/v_s = \sqrt{2.5}$  is, however, low and unexpected for fluid-filled basement rocks at a depth of about 10 km (*Schön*, 1996). In contrast, fluids usually lead to an increase in  $v_p$  and  $v_p/v_s > \sqrt{3}$ . Similar moment-tensor components were also obtained for two composite sources, one source consisting of a tensile and a compensating implosional component (#7 in Tab. 1.1) and another source comprising two synthetic shear sources on different fault planes (#5 in Tab. 1.1).

The two models, complex fault geometry or fluid driven tensile earthquakes, may provide competing or complementary explanations for the large CLVD components mainly observed for events during the swarm phases 1-4. However, examples of synthetic tensile sources with a compensating isotropic component as well as moment tensors and their interpretations found by *Kanamori et al.* (1993) and *Foulger et al.* (2004) resemble the observations in West Bohemia.

Therefore, the significant tensile source parameters found for many events in West Bohemia suggest that positive volumetric source changes due to changes in the fluid system are important during earthquake faulting. This finding is most developed for events of the swarm phases 1-4 and for deep events. It is proposed herein that fluids, released from a deeper source, migrated up where they were observed eight weeks later at the surface (*Bräuer et al.*, 2005) triggering earthquakes on their way and/or being

released through pathways formed by crack opening. The swarm phases 1-4 span a time period of 3 weeks. During this time, fluids passed a vertical distance of about 2 km which is estimated from the hypocentre depths in Fig. 5.7. Then, it took them another 5 weeks to arrive at the surface. Later events were triggered by self-organisation of the swarm (Hainzl and Ogata, 2005). The influence of fluid injection on swarm initiation and earthquake triggering near the onset of the swarm is also supported by a number of other observations such as analyses of  $b$ -values and the spatiotemporal evolution of the swarm as well as of pore-pressure diffusion and direct observations of fluids on the surface (see Section 1.4). These findings seem comparable with observations of an aftershock sequence near Colfiorito, Italy, showing that pore-pressure changes due to fluid migration were largest near a presumed fluid reservoir below the earthquake foci (Miller, 2004).

Approximations of net-volume changes at the source due to tensile faulting depend on the crack shape, the elastic parameters at the source, and the representing equivalent force system (Müller, 1973; Julian, 1983; Müller, 2001; Richards and Kim, 2005). However, a first and rough estimate is provided by simply taking obtained potencies, slip inclinations, uniform stress drop of  $\Delta\sigma = 1.7$  MPa (Hainzl and Fischer, 2002), and Eq. (1.29). This neither accounts for fault complexity nor for composite sources. Then, the largest amount found for crack opening (thickness of a crack) is almost 1 cm. Such small amounts are unlikely to be linked with magma intrusions, demanding for water or steam instead. In addition, no such magma body was observed by gravity modelling in the upper crust (Hofmann *et al.*, 2003). Typical values of about 100 m<sup>3</sup> are obtained for the volume of intruded liquid. Similar quantities can also be found using equation (1.33). However, these values have to be treated with care. In comparison, Foulger *et al.* (2004) reported on maximum values for crack thicknesses and volumes of 8.5 cm and 600 m<sup>3</sup>, respectively, for microearthquakes at Long Valley Caldera, USA. This appears to be intriguingly similar to the observations in West Bohemia.

## 5.5 Reliability of determined source parameters

Assessing the reliability of determined source parameters is crucial to deduce their significance. Quantities, such as mean value, standard deviation, co-variance etc. describe their confidence intervals and uncertainties. They may be obtained immediately during the solution of Eq. (4.7) (Press *et al.*, 1992; Vogel, 1995). However, they have only limited significance because additional errors in the solutions may result from uncertainties in the velocity model that determines the synthetic seismograms in Eq. (4.7). In previous studies the problem was approached by a systematic perturbation of isotropic velocity models within a certain confidence interval during inversion and a statistical description of the solutions (see e.g. Šílený, 1998; Šílený and Hofstetter, 2002; Šílený, 2004). However, for the velocity models I, II, and III no confidence intervals on elastic parameters are provided. This fact limits the meaning of such tests. These models represent the 1-D structure of the Vogtland whereas the geology is, to a certain degree, clearly 3-dimensional. Estimates of confidences should therefore also account for errors resulting from this simplification. Observations of anisotropy further complicate error estimation. In anisotropic media uncertainties for 21 independent elastic moduli need to be considered at all points that define a model instead of 2 parameters for isotropic media. In the previous Sections 5.4.1-5.4.5 the discussions of the influence

of models parameters were therefore confined to the mutual comparison of solutions obtained using the velocity models I-III.

### 5.5.1 Jackknife and bootstrap tests

Alternatively, the stability of the solutions can be assessed by jackknife and bootstrap tests where the initial conditions of the inversion are modified (see e.g. *Bruhn*, 2003). These two methods were introduced before in Section 4. By jackknife testing the influence of varying ray coverage due to modified station distribution and lack of stations, thus the missing of information, is tested. By bootstrapping, the influence of single stations, thus of single rays passing through geological structures on their way to the stations, is examined. Instead of removing information, data observed at a certain station are overweighted and their importance for inversion is increased. Therefore, bootstrap tests are considered to be more meaningful and preferred to jackknife tests to conclude on the stability of the inversions. They are carried out for all 112 events assuming the velocity models I, II, and III. Fault-plane solutions resulting from these tests can be found in Appendix C.7, Figs. C.10-C.19. From the distribution of source parameters determined during bootstrapping the standard deviations are calculated (see Tab. C.6). They describe the solution variability due to different station weights.

For detailed testing, jackknife tests are additionally performed for event 1 of August 29, 2000, 12:13:15 and event 17 of September 4, 2000, 01:18:06 using the inhomogeneous anisotropic model II (see Figs. 5.10, 5.11 and Tab. 5.1 for results of tests). The same procedure is applied as in Section 4.3 for event 59 of October 15, 2000, 16:36:48.

Table 5.1: Mean values of the slip inclination  $\bar{\delta}$  as well as standard deviations of slip inclinations ( $\sigma(\delta)$ ) and of fault parameters: strike  $\sigma(\Phi_1^s)$ , dip  $\sigma(\delta_1^s)$ , and rake  $\sigma(\lambda_1^s)$  for events 1 and 17 in Tab. C.2. For completeness, details of event 59 are also given (compare Table 4.4). Solutions are obtained from jackknife and bootstrap testing using the velocity model II (compare Figs. 4.9, 5.10, and 5.11 for fault-plane solutions and source components). Values of  $\delta$  refer to solutions with unmodified conditions (all seismograms are used with equal weight).

#	$\delta$ [°]	jackknife test					bootstrap test				
		$\bar{\delta}$ [°]	$\sigma(\delta)$	$\sigma(\Phi_1^s)$	$\sigma(\delta_1^s)$	$\sigma(\lambda_1^s)$	$\bar{\delta}$ [°]	$\sigma(\delta)$	$\sigma(\Phi_1^s)$	$\sigma(\delta_1^s)$	$\sigma(\lambda_1^s)$
1	83.0	82.9	0.9	2.5	2.6	5.4	83.0	1.6	3.8	1.3	2.5
17	77.9	79.0	2.7	14.7	23.7	20.6	77.6	1.1	1.6	2.1	1.6
59	86.8	87.3	1.5	1.7	1.8	3.0	86.9	1.2	1.4	2.1	3.3

Source mechanisms of both events comprise large tensile components. Event 1 is of special interest because it is the first large event and marks the onset of the swarm in 2000. Using the velocity models I and II, event 17 comprises the largest component of crack opening among all determined source mechanisms and extremely low double-couple moment-tensor components. Furthermore, P-wave polarity at station NKC is upwards whereas observations show negative first motion polarities at NKC for most other events (see also Fig. 1.13 for an overview on polarities at station NKC).

Obviously, for both events variations in fault-plane solutions occur during testing. With the exception of only 5 solutions obtained by bootstrapping, fault orientations are within a narrow range for event 1 (Fig. 5.10). By jackknife tests, larger variations, mainly in rake, occur. However, standard deviations are low (Tab. 5.1). For event 17, standard deviations are high from the jackknife test but also low from bootstrapping

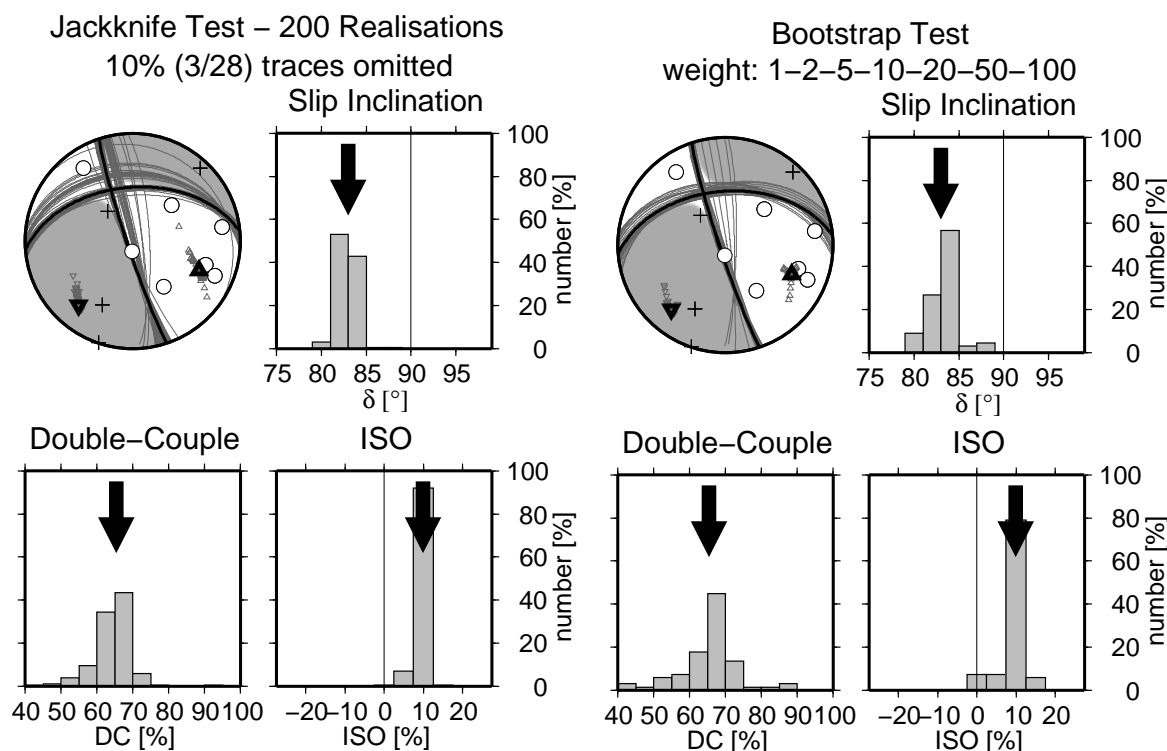


Figure 5.10: Fault-plane solutions (grey), slip inclination  $\delta$ , and moment-tensor components obtained from jackknife (left) and bootstrap tests (right) for event 1 in Tab. C.2 (source time: August 29, 2000, 12:13:15) using the inhomogeneous, anisotropic model II. Determined principle stress axes are plotted on top of the FPS. The  $\sigma_1$  and  $\sigma_3$  axes are marked by grey inverted triangles and grey triangles, respectively. For jackknife tests, 200 realizations were carried out by randomly omitting 10% of the seismograms during inversion. The bootstrap tests were performed by successively varying the weight of every station (weights: 1, 2, 5, 10, 20, 50, 100). Arrows,  $\sigma_1$  and  $\sigma_3$  axes in black, and underlying radiation patterns mark results of inversions with unmodified conditions (11 stations, 28 traces, equal station weight).

(Tab. 5.1). This can be attributed to the non-uniform ray-coverage that is only provided by station LAC in south and southeast direction (compare ray directions given by P-wave polarities in Figs. 5.10, 5.11). Station coverage is even lowered for this event during jackknife testing. However, during bootstrap tests fault-plane solutions and source components are well defined. For both events, mean values  $\bar{\delta}$  of the slip inclination  $\delta$  are similar to the solutions with unmodified conditions (all stations are used with equal weight). The standard deviations  $\sigma(\delta)$  are low.

The tensile components that indicate crack opening are therefore confirmed and found to be significant. Similarly, moment-tensor components are stable during testing (compare Figs. 5.10, 5.11, and Tab. C.6). Complex source properties of event 17 are also indicated by the great variability of solutions during iterative inversion of amplitude spectra by means of MTINVERS (see Appendix. C.9). Note that the source mechanism of event 59 which is similar to other events of the swarm phases 5-7 is similarly constrained using MTINVERS (see Appendix. C.9).

Standard deviations of the source parameters obtained from bootstrap testing of events 1, 17, and 59 in Section 4 are representative for the remaining events with confidence class 1 or 2 that are processed in this work (compare Tabs. 5.1, C.4, and C.6).





By using inappropriately high frequencies for source retrieval of large earthquakes the point source approximation is violated. Effects resulting from source finiteness are mapped into increasing CLVD components of determined moment tensors (*Bruhn*, 2003). This artefact can be ruled out in this study, because the slip inclinations and CLVD are smallest for the largest events (highest  $M_L$ ) being another validation of the assumed point source approximation.

Similarly to the slip inclination, variations in size of the CLVD can also not be explained by different ray (station) coverage and gap during the swarm (compare Figs. 5.6 and 5.9c,d). Only few events with very large CLVD and confidence class 1 coincide with very large gap (events 64, 69, 71, and 72, gap  $> 150^\circ$  but 12-17 stations) or low number of stations (8 stations but smaller gap), see Tabs. C.2 and C.5. However, small tensile components are found for other events with similar ray coverage and gap.

Moreover, velocity gradients in the medium surrounding a source cause asymmetry in the radiation pattern (*Ben-Menahem et al.*, 1991). During source retrieval vertically inhomogeneous isotropic or anisotropic models are assumed but lateral variations are not accounted for. Studies of the velocity structure and the gravity field show that epicentres are located in 3D complex structures near the eastern part of the Fichtelgebirge pluton (see Section 1.4). Resulting uncertainties in the mismodelling of the structure are projected into the standard deviations obtained from bootstrap testing (see Sec. 5.5.1).

As seen before in Sections 2 and 3 anisotropy complicates the interpretation of moment tensor components. However, the different models I-III used during inversion reveal similar results. Variation in near-source anisotropy that may be a source for errors in source retrieval is not assumed in this study. Distinct anisotropic properties with decreased velocities and increased degree of anisotropy can be expected within fault zones by long-term rock deformation that may cause remineralisation, fracturing and changes in the crack system (see *Rabbel et al.*, 2004; *Rümpker et al.*, 2003, for examples). Because shear and tensile sources are both observed at similar locations such effects are considered to be small. Although some effects due to near-source anisotropy can be expected, the principle difference between the events should persist.

For more detailed testing, the inversions are repeated for events 1, 17, and 59 assuming two different generic transversely isotropic media near the source during waveform modelling. See App. B.3 for a description of such media. Isotropic reference values are  $v_p = 6000 \text{ ms}^{-1}$  being slightly reduced compared to the models I and II at focal depth and  $v_p/v_s = \sqrt{3}$  for both near-source media. The axes of symmetry point horizontally in E-W direction, thus almost perpendicular to the fault zone. For testing, stronger anisotropy of 10% or 20% is assumed near the source. Such type of anisotropy may be caused by the formation of fault-parallel fractures. The near source anisotropic model forms an inclusion in the model II of about 2 km in all three dimensions.

The inversions show that retrieved source parameters also depend on the near-source elastic model (compare Tab. 5.2). Whereas the slip inclinations do not change for events 1 and 17, pure shearing is obtained for event 59 when 20% anisotropy near the source is assumed. The non-DC component are reduced for the three events when increasing the degree of anisotropy. However, the principle differences between the events remain. The assumed properties of the inclusion are unconstrained by direct observations. Therefore, different effects can be expected for other types of parameterisation.

Table 5.2: Source parameters (slip inclination  $\delta$  and moment-tensor components) for events 1, 17, and 59 in Tab. C.2. During a first inversion the inhomogeneous anisotropic model II was used. For testing, the medium near the source was replaced by 2 generic transversely isotropic models with different degrees of anisotropy,  $v_p = 6000 \text{ ms}^{-1}$ ,  $v_p/v_s = \sqrt{3}$ , and  $a_0 = -1$  (see Appendix B.3 for a description of generic transversely isotropic media). The axis of symmetry points E-W (similar to the normal to the fault zone). Degree of anisotropy near the source: 10%,  $a_1 = 0.1$  (model: II-ti10%) or 20%,  $a_1 = 0.2$  (model: II-ti20%).

event	model	$\delta$ [°]	DC [%]	ISO [%]	CLVD [%]
1	II	83.0	65.4	9.9	24.7
	II-ti10%	82.3	69.5	9.1	21.3
	II-ti20%	82.3	76.1	7.1	16.9
17	II	77.9	32.2	2.4	65.4
	II-ti10%	78.1	42.9	0.7	56.4
	II-ti20%	78.1	52.5	0.0	47.5
59	II	86.9	83.4	4.5	12.1
	II-ti10%	87.9	91.6	2.3	6.2
	II-ti20%	89.1	94.4	-3.3	-2.3

## 5.6 Principle directions of the local stress field

The principle directions of the local stress field are given by the P, B, and T axis (see Sec. 1.2.3). They are calculated for all events using the velocity model II and presented in Fig. 5.12. More complete Figures including results for models I and III can be found in Appendix C.10, Figs. C.22, C.23, and C.24. The variations in strike are small for the P and T axes (within  $\approx 20^\circ$ ) but larger for the B axis (within  $\approx 60^\circ$ ), see Fig. 5.12a. Strike directions of the P and T axes are thus almost uniform along the fault zone. Mean strike directions (azimuth) of the P, B, and T axes for all events with confidence class 1 are  $124^\circ$ ,  $25^\circ$ , and  $227^\circ$ , respectively (see Tab. 5.3). They are also in agreement with other studies in West Bohemia (*Havřr*, 2000; *Wirth et al.*, 2000; *Plenefisch and Klinge*, 2003) and with the overall stress regime in Central Europe (*Hinzen*, 2003).

Table 5.3: Mean values for strike and plunge angles of P and T axes in different depth ranges (compare Fig. 5.12). Results are obtained from inversions using velocity model II.

depth range [m]	P axis		T axis	
	strike[N°E]	plunge [°]	strike[N°E]	plunge [°]
full range	124	37	227	19
< 8400	130	50	226	8
8400 – 9400	120	39	228	21
> 9400	126	26	228	23

In contrast, the plunge angles observed for the P and T axes change with depth (see Fig. 5.12b). Three depth ranges, above 8400 m, 8400-9400 m, and below 9400 m with different characteristics can be distinguished (see Fig. 5.12b and Tab. 5.3). The plunge of the P axes decreases gradually towards greater depths. The T axes lie almost horizontally above 8400 m and are inclined below. For both, the P and the T axes,

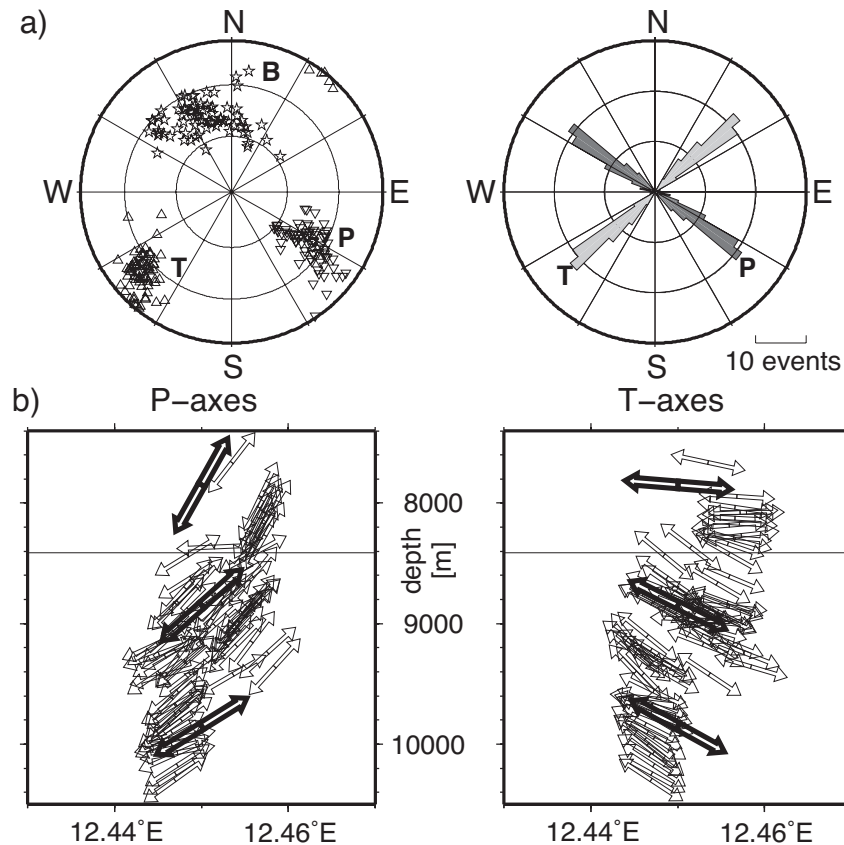


Figure 5.12: Principle directions of the stress field (P, B, and T axes) obtained for events with confidence class 1 in Tab. C.2 using the velocity model II. a) Directions of P, B, and T axes in lower hemisphere projection (left) and rose histogram of the strike directions of the P and T axes (right). b) Projection of the P and T axes on a vertical section in E-W direction. Centres of arrows are at source position. Enlarged arrows represent mean values for depth intervals of 1000 m. The internal layer boundary of model I and II at 8.41 km depth is indicated. Note stability of the strike directions and variability of the plunge with depth. See Tab. 5.3 and Figs. C.22, C.23, and C.24 for more details and results from models I and III.

determined plunge angles are uniform above 8400 m and below 9600 m depth. At a depth between 8400-9400 m, shallow and steep plunge angles are observed. Horizontal T axes above 8400 m coincide with observations of shallow dipping rupture planes and decreased tensile components (compare Fig. 5.4b,c).

Interestingly, the change in plunge of the T axes at a depth of about 8.4 km occurs at a layer boundary in model II (and I) (compare Fig. 4.2 and Sec. B.4 for model specification). Changes in the stress field are similarly found when using the inhomogeneous isotropic model I or the homogeneous anisotropic model III (see Figs. C.22, C.24). Therefore, it cannot be explained as a simple artefact of model specification.

By interpretation of the gravity field, *Hofmann et al.* (2003) locates the transition to the Saxothuringian crust and the contact of Saxothuringian to Avalonian crust at depths of  $\approx 8.5$  km and  $\approx 9.5$  km, respectively. These depths where changes in rock density and geological boundaries take place also seem to coincide with the observed changes in the directions of the principle stress axes.

## 6 Discussion and conclusions

Although the mechanisms of many large earthquakes are routinely determined today, accurate and indisputable resolution of non-shear source components is still an important and ambitious issue. In addition to difficulties that may arise from the lack of models describing small-scale structural features, anisotropy introduces non-uniqueness in the interpretation of moment tensors. Detailed source studies make an important contribution to explain physical processes that control the nucleation of earthquakes and the evolution of faults. They also help to assess the seismic hazard for humans living in seismoactive regions.

In this work, effects of anisotropy on moment tensors, radiation patterns due to dislocation point sources, and source retrieval were investigated. The possible role of anisotropy on non-shear source components in West Bohemia in 1997 (*Horálek et al.*, 2000b) was studied. Moment tensor determined for events at the KTB borehole, FR Germany (*Jost et al.*, 1998), were re-interpreted assuming anisotropy (*Rabbel et al.*, 2004). It was shown that anisotropy may be important for the interpretation of real or apparent non-shear moment tensors and should be considered during inversions. Therefore, a new algorithm was developed to determine source parameters for point sources in anisotropic media. The algorithm has been successfully applied to swarm earthquakes that occurred in the Vogtland/West Bohemia in 2000.

### 6.1 Source components in anisotropic media

Results of this work about source parameters in anisotropic media are summarised in the following.

- 1) Moment tensors are influenced by anisotropy near the source. The influence increases with the degree of anisotropy. For dislocation sources, the seismic moment shows sensitivity to the orientation of the source. This is in contrast to sources in isotropic media. Moment-tensor components of shear sources may comprise significant apparent non-double-couple components due to near-source anisotropy. Similarly, non-double-couple components of tensile earthquakes may be obscured such that their corresponding moment tensors have characteristics usually assumed for shear sources in isotropic media.
- 2) Anisotropy near the source and in the medium along the ray causes pronounced distortions of the radiation patterns of P and S waves. The radiation patterns of P waves generated in homogeneous anisotropic media are similar to the radiation patterns in media where anisotropy is restricted to the near-source region and the medium along the ray path is isotropic. This indicates that little information on the extent of the source region can be gained from P waves. S-wave radiation patterns are influenced by anisotropy along the ray. As a consequence, they may be strongly deformed due to effects of modified geometrical spreading and S-wave splitting.
- 3) Moment tensors are modelled for sources that are typical for two types of swarm events in West Bohemia in 1997. Large non-double-couple components, observed earlier by *Horálek et al.* (2000b), can only partly be attributed to effects of reasonable models of anisotropy in the medium near the source or along the ray.

- 4) In the presence of anisotropy, fault-plane solutions can be determined with sufficient accuracy by inversion of the spectra of P waves even if isotropic material properties are assumed. Using constraints during iterative inversion of amplitude spectra by suppressing the isotropic moment-tensor component helps to identify the correct solution.
- 5) If the medium is anisotropic near the source but isotropic along the ray path, moment tensors retrieved by inversion of P waves provide a good image of the forces acting at the source. Because smoothing of the observed radiation pattern occurs due to discrete and imperfect sampling of the wavefield, the non-double-couple moment-tensor components may be underestimated during inversion.
- 6) Greater difficulties in the interpretation of moment tensors arise from more general conditions where the medium along the ray path is also anisotropic, especially when the spectra of split S waves are used during inversion but isotropy is assumed.
- 7) Near-source anisotropic elastic parameters may be retrieved from the non-double-couple components of observed moment tensors. The determined degree of anisotropy may be lowered due to a potential underestimation of the size of the non-double moment-tensor components.
- 8) Accounting for local anisotropy in the vicinity of the KTB borehole, FR Germany (*Rabbel et al.*, 2004), the moment tensors of 2 earthquakes (*Jost et al.*, 1998) are re-interpreted assuming a dislocation source. These events are representative for 2 clusters of earthquakes that were induced during a fluid-injection experiment at a depth of about 8.8 km. Although their moment tensors suggest opening (hydro-fracturing) or closure of fault planes, they can be consistently explained by two shear sources on different fault planes.
- 9) A new algorithm is developed and coded to invert for source parameters of dislocation point sources in general isotropic or anisotropic media. Hereby, the geometry of the source is determined together with the moment tensor. The source geometry is defined by the normal to the fault, the slip direction, and the potency, a measure of the size of the event. The slip inclination, i.e. the angle between slip and fault normal, is obtained as an important parameter to quantify tensile components of an earthquake. The interpretation of the source geometry is restricted to sources with dislocation on single faults. The efficiency of this method depends on the accuracy of source location and structural model.

## 6.2 Implications from swarm earthquakes in West Bohemia

Source parameters of 112 major swarm earthquakes that occurred in West Bohemia between August 28, 2000 and October 30, 2000 at depths between 7.7 and 10.3 km were determined by means of the new inversion algorithm. Results of inversions, characteristic features of the studied events, and conclusions are summarised as follows.

- 1) Three different homogeneous or vertically inhomogeneous, isotropic or anisotropic models are assumed during source retrieval. By comparison of travel-time residuals for the three models as well as results of source retrieval assuming different

source depths, the vertically inhomogeneous anisotropic model seems to be most appropriate to describe the 1D-structure in West-Bohemia. The differences between observed and theoretical travel times computed for sources in the inhomogeneous isotropic and anisotropic velocity models are small. They may be partly explained by source mislocation of 100-200 m.

Studies of the velocity structure (Novotný, 1996; Málek *et al.*, 2004; Hrubcová *et al.*, 2005) and the gravity field (Hofmann *et al.*, 2003) show that epicentres are situated in a region with lateral variations, at the eastern part of the Fichtelgebirge pluton. Lateral velocity gradients or discontinuities are not accounted for during inversion. This may introduce additional uncertainties during source retrieval. Resulting possible ambiguities are ruled out by detailed testing of single events and because variations of tensile source components with time occur for similar ray coverage.

- 2) Observed seismic moments are in the range of  $8.9 \cdot 10^{12} \leq M_L \leq 4.6 \cdot 10^{14}$  Nm, corresponding to local magnitudes of  $1.6 \leq M_L \leq 3.2$ . For the studied swarm phases, moment release is concentrated between depth of 8400 m and 9400 m. Further maxima occur at depths of around 8100 m and 9900 m. Local magnitudes are similar to those observed by other authors (Fischer, pers. comm. and Tittel and Wendt, 2003). Potencies vary between  $472 \text{ m}^3$  and  $25110 \text{ m}^3$ .
- 3) Making assumptions on stress drop and source geometry, obtained source extents confirm point source approximation. The influence of source finiteness on possible CLVD components is rejected by the observation that non-double-couple components are small for the largest events.
- 4) Fault-plane solutions show left-lateral movement on a N-S striking fault with oblique normal or oblique reverse faulting. They are similar to solutions obtained by Fischer and Horálek (2005) who, however, inverted for the fault-plane solutions but neither for the complete source geometries nor the moment tensors. In contrast, earthquake mechanisms that are dominated by strike-slip faulting were found by Plenefisch *et al.* (2003) using the method of relative moment-tensor inversion (Dahm, 1996). The orientations of the fault-planes vary with source time and depth. Significant changes in dip of the rupture planes are found at source depths of around 8400 and 9400 m.
- 5) More than 60% of the studied events show non-DC components. Temporal and spatial variations of tensile components are observed. Largest tensile components are found for events between August 28 and September 17, 2000 and at depths below 8400 m. By comparing results for three different isotropic or anisotropic structural models as well as jackknife and bootstrap tests, it can be ruled out that this observation is a simple artefact of inappropriate model specification or varying data availability.
- 6) Observed tensile source components persist even if anisotropic models are assumed during inversion. The differences in results obtained for the inhomogeneous isotropic model and the inhomogeneous anisotropic model are, however, small. Greater effects can be expected by accounting for anisotropic models that also contain detailed information on S-wave propagation.

- 7) Observed tensile components are large for the swarm phases 1-4 but significantly smaller or insignificant during the phases 5-7. The clear maximum at the beginning of the swarm coincides on average with the deepest events considered here. Possible explanations for the large tensile components include faulting on complex fault geometries or tensile faulting due to the injection of over-pressurised fluids. Whereas the first inference cannot be safely rejected, the influence of migrating fluids on the triggering of the swarm events in West Bohemia is suggested and supported by many other independent observations. Some of these observations are discussed below. The latter also suggests that high pore pressures are most important for the creation of tensile components during phases 1-4 of the swarm and at the bottom of the focal area. Typical amounts of crack thicknesses and net-volume changes are about 1 cm and 100 m<sup>3</sup>, respectively.

**By this work, spatial and temporal variations of tensile source components and of the local stress field are reported for the first time for swarm earthquakes in West Bohemia in 2000.**

Volumetric source changes caused by injection of fluids or by pressurisation of fluid-saturated faults due to magmatic heating have also been described in other volcanically active areas (*Kanamori et al.*, 1993; *Douglas et al.*, 2000; *Foulger et al.*, 2004).

In comparison, *Hainzl and Fischer* (2002) found large *b*-values that document the pronounced swarm character of events near the beginning of the swarm. They decrease during later swarm phases for which smaller tensile components are reported in this work. These temporal changes in determined source mechanisms also coincide with findings of *Hainzl and Ogata* (2005) who reported on indications that pore-pressure changes due to fluid intrusion are important for the initiation of the swarm but play a reduced role during later times. They are also supported by *Parotidis et al.* (2005) who found that pore-pressure diffusion is significant for earthquake triggering during the swarm in 2000 and by investigations of the space-time relation of consecutive events (*Fischer and Horálek*, 2005).

Recent geochemical studies show that those gases emanating on the surface in the Vogtland have their origin in the upper mantle. They seem to rise up from a deep-seated source below the earthquake foci (*Weinlich et al.*, 1993, 1999; *Weise et al.*, 2001; *Bräuer et al.*, 2003, 2004, 2005). Temporal changes in the gas flux and content are correlated with earthquake activity (*Bräuer et al.*, 2003). The scenario that fluids rising up from a reservoir below the epicentres are responsible for the triggering of earthquakes in West Bohemia resembles observations for another earthquake sequence near Colfiorito, Italy. There, *Miller* (2004) found that pore-pressure changes due to upwards directed fluid migration from a deep-seated reservoir are largest near the deepest events but reduced towards shallower depths. In West Bohemia, large and small tensile source components for great and shallow source depths respectively, coincide in principle with the distribution of the modelled pore-pressure changes in Italy.

Moment tensors of clearly non-DC sources in West Bohemia comprise large CLVD up to 40% but relatively small ISO. These observation resembles findings in vol-



canic areas (*Kanamori et al.*, 1993; *Foulger et al.*, 2004). There, the compensation of isotropic components were explained by immediate fluid injection into the crack after faulting.

- 8) The principle directions of the local stress field are determined. Strike directions of the P and T axes point in NW and SW direction, respectively. They confirm earlier observations that the stress field in West Bohemia is determined by the more regional stress field in Central Europe (*Havříř*, 2000; *Wirth et al.*, 2000; *Hinzen*, 2003; *Plenefisch and Klinge*, 2003). However, indications for depth-dependence of the plunge are found. The plunge of the P axes decreases gradually with increasing depth from  $\approx 50^\circ$  to  $\approx 26^\circ$ . Observed T axes lie almost horizontally at depths above 8400 m (plunge  $\approx 8^\circ$ ) but they plunge  $\approx 21^\circ$  below. The near-horizontal direction of the T axes above 8400 m depth is also close to the direction of the symmetry axis of the anisotropic elastic tensor that was found from observations of shear-wave splitting in the upper crust (*Vavryčuk*, 1993). Rapid vertical changes in the stress field also indicate a different role of pore-pressure changes due to fluid migration below 8400 m depth.
- 9) The depths of changes in stress field, namely in the plunge of the T axes, and the depths of changes in slip inclinations coincide with geological boundaries found from gravity modelling (*Hofmann et al.*, 2003). Therefore, observations of changes in source parameters and in the stress field might be an indicator for boundaries that controls the extent of fluid migration.
- 10) Constraints on volumetric source changes that occur during earthquake rupturing and that vary with time, as well as changes in the local stress field provide additional hints that changes in the fluid regime are in causal connection to the triggering of events in the Vogtland.

### 6.3 Outlook

In future work, events with lower magnitudes and also at later phases of the swarm will be investigated in detail to obtain a complete image of the seismic activity during the swarm episode in West Bohemia in 2000. For more precise quantification of tensile source components in West Bohemia source retrieval can be enhanced by a number of advances in waveform modelling such as:

- 3D-tomographic imaging of the velocity structure,
- accounting of the influence of amplitude damping,
- inhomogeneous anisotropic models containing detailed information on S-wave propagation,
- considering near-source inhomogeneity by determination of elastic properties, including possible temporal changes in anisotropy
- assumptions on more complex source-time functions,
- comparison of source parameters for earthquakes from different focal zones.

In addition, the role of possible complex source geometries or secondary faulting, (i.e. mode I fracturing conjugate to the main rupture plane, *Scholz, 2002*), for volumetric source components is another field for valuable research. Studies of the time-dependence of the elastic properties in the focal region may further provide insight into changes in crack density prior, during, and after swarm occurrence.

## Acknowledgements

This work was clearly only possible by the great coincidence of the experiences of many scientists who are also engaged in this subject. These people gave me incredible support, inspiration and motivation.

I owe Dr. Frank Krüger and Prof. Dr. Georg Rümpker, who also initiated this project, much gratitude for supervision during the time this thesis developed. I thank them for teaching, very inspiring discussions, detailed questions, and uncounted hints.

I am grateful to Dr. Ivan Pšenčík for intensive and very fruitful collaboration, many valuable details I could learn about wave propagation in anisotropic media, and his interest in discussing many topics.

Dr. Erik Säger and Dr. Ronjiang Wang are appreciated for cooperation to validate programs that I developed to compute waveforms in anisotropic media.

Waveform data from earthquakes in West Bohemia were provided by the Geophysical Institute, Acad. Sci. of the CR, GFZ, KRASNET, SZGRF, and the universities of Leipzig, Munich, and Potsdam. For data provision I acknowledge Dr. Tomáš Fischer, Dr. Thomas Plenefisch, Siegfried Funke, and Dr. Joachim Wassermann. Dr. Tomáš Fischer also provided accurate hypocentre parameters.

Conny Hammer and Alexander Rohrmann helped me with data preparation and inversion. Birgit Fabian found tricks for post-processing of some figures in this work. I thank them for their motivated aid.

Colleagues and students at the Department of Geosciences of the University of Potsdam, the GeoForschungsZentrum Potsdam, and the Geophysical Institute of the Academy of Sciences of the Czech Republic in Prague are appreciated for the friendly and very productive work atmosphere. I enjoyed discussing hottest geophysics, solving computer problems, and chatting at tea or coffee with Dr. Tadashi Kito, Dietrich Lange, and Andreas Köhler who shared their office with me as well as many other colleagues and friends.

I thank all who contributed to this manuscript by carefully reading, spell-checking, and their helpful comments.

Financial support of the German Science Foundation (DFG, grant KR1935), of the Charles University, Prague, through the MAGMA project, of the Geophysical Institute, Acad. Sci. of the CR, and of the consortium project SW3D is appreciated.

Many processing steps were carried out using the software package SEISMIC HANDLER by *Stammler* (1992). For plotting of figures GMT by P. Wessel, Gnuplot by T. Williams, and Matlab by The MathWorks, Inc. were used.

Last but not least, everything was possible with support of Claudia.

## References

- Aki, K. and Richards, P. (2002). *Quantitative seismology*, University Science Books.
- Babuška, V. and Cara, M. (1991). *Seismic anisotropy in the earth*, Kluwer Academic Publishers, London.
- Babuška, V. and Plomerová, J. (2001). Subcrustal lithosphere around the Saxothuringian-Moldaunbian suture zone - a model derived from anisotropy of seismic wave velocities, *Tectonophysics*, **332**, 185–199.
- Babuška, V., Plomerová, J. and the BOHEMA working group (2003). Seismic experiment searches for active magmatic source in deep lithosphere, Central Europe, *EOS, Transactions*, **84**, 409.
- Babuška, V., Plomerová, J., Vecesey, L., U., A. and the BOHEMA working group (2004). Deep seismic structure around the Eger rift in the Bohemian Massif – initial results of the BOHEMA project, in *European Seismological Commission XXIX General Assembly, Abstract and Papers*.
- Bankwitz, P., Kämpf, H., Störr, M. and Schneider, G. (2002). Shear faults in Tertiary clay formation of the Eger Basin (Czech Republic) and their role for the degassing of the uppermost mantle, *Mitt. naturwiss. Ver. Steiermark*, **132**, 31–34.
- Bankwitz, P. and Schneider, G. (2000). Seismic and aseismic movements in the western Bohemia/Vogtland area, *Stud. Geophys. Geod.*, **44**, 611–613.
- Bankwitz, P., Schneider, G., Kämpf, H. and Bankwitz, E. (2003). Structural characteristics of epicentral areas in Central Europe: study case Cheb Basin (Czech Republic), *J. Geodynamics*, **35**, 5–32.
- Ben-Menahem, A., Gibson Jr, R. and Sena, A. (1991). Green's tensor and radiation pattern of point sources in general anisotropic inhomogeneous elastic media, *Geophys. J. Int.*, **107**, 297–308.
- Ben-Menahem, A. and Singh, S. (1981). *Seismic Waves and Sources*, Springer-Verlag New York Inc.
- Ben-Zion, Y. (2001). A note on quantification of the earthquake source, *Seis. Res. Lett.*, **72**, 151–152.
- Bormann, P. (Ed.) (2002). *IASPEI new manual of seismological observatory practice (NMSOP)*, GeoForschungszentrum Potsdam.
- Bos, L., Gibson, P., Kotchetov, M. and Slawinski, M. (2004). Classes of anisotropic media: a tutorial, *Stud. Geophys. Geod.*, **48**, 265–287.
- Boušková, A. (2005). Catalogue of seismic events, Report, Academy of Sciences of the Czech Republic. Online at <http://www.ig.cas.cz/seismo/Webnet/>.

- Bräuer, K., Kämpf, H., Faber, E., Koch, U., Nitzsche, H.-M. and Strauch, G. (2005). Seismically triggered microbial methane production relating to the Vogtland–NW-Bohemia earthquake swarm period 2000, Central Europe, *Geochem. J.*, **39**, 441–450.
- Bräuer, K., Kämpf, H., Niedermann, S., Strauch, G. and Weise, S. (2004). Evidence for nitrogen flux directly derived from European subcontinental mantle in the Western Eger Rift, Central Europe, *Geochim. Cosmochim. Acta*, **68**, 4935–4947. doi:10.1016/j.gca.2004.05.032.
- Bräuer, K., Kämpf, H., Strauch, G. and Weise, S. (2003). Isotopic evidence ( $^3\text{He}/^4\text{He}$ ,  $^{13}\text{C}_{\text{CO}_2}$ ) of fluid-triggered intraplate seismicity, *J. Geophys. Res.*, **108**. doi:10.1029/2002JB002077.
- Bruhn, C. (2003). Momententensoren hochfrequenter Ereignisse in Südchile, dissertation, Mathematisch-Naturwissenschaftliche Fakultät der Universität Potsdam.
- Brürtle, W. and Müller, G. (1983). Moment and duration of shallow earthquakes from Love-wave modelling for regional distances, *Phys. Earth Planet. Inter.*, **32**, 312–324.
- Červený, V. (2001). *Seismic ray theory*, Cambridge University Press.
- Červený, V., Molotkov, I. and Pšenčík, I. (1977). *Ray Method in Seismology*, Univerzita Karlova, Praha.
- Chlupáčová, M., Skácelova, Z. and Nehybka, V. (2003). P-wave anisotropy of rocks from the seismic area in Western Bohemia, *J. Geodynamics*, **35**, 45–57.
- Crampin, S. (1994). The fracture criticality of crustal rocks, *Geophys. J. Int.*, **118**, 428–438.
- Dahm, T. (1993). Relativmethoden zur Bestimmung der Abstrahlcharakteristik von seismischen Quellen, dissertation, Fakultät für Physik der Universität Karlsruhe (TH).
- Dahm, T. (1996). Relative moment tensor inversion based on ray theory: theory and synthetic tests, *Geophys. J. Int.*, **124**, 245–257.
- Dahm, T., Horálek, J. and Šílený (2000). Comparison of absolute and relative moment tensor solutions for the January 1997 West Bohemia earthquake swarm, *Stud. Geophys. Geod.*, **44**, 233–250.
- Dahm, T., Manthei, G. and Eisenblätter, J. (1999). Automated moment tensor inversion to estimate source mechanisms of hydraulically induced micro-seismicity in salt rock, *Tectonophysics*, **306**, 1–17. doi:10.1016/S0040-1951(99)00041-4.
- DEKORP Research Group (1988). Results of the DEKORP 4/KTB Oberpfalz deep seismic reflection investigation, *J. Geophys.*, **62**, 69–101.
- DEKORP Research Group (1994). DEKORP 3/MVE90(West)– preliminary geological interpretation of a deep near-vertical reflection profile between the Rhenish and the Bohemian Massifs, Germany, *Z. geol. Wiss.*, **22**, 771–801.

- Douglas, S. and Dreger, D., Tkalčić, H. and Johnston, M. (2000). Dilational processes accompanying earthquakes in the Long Valley Caldera, *Science*, **288**, 122–125. DOI:10.1126/science.288.5463.122.
- Dreger, D. and Helmberger, D. (1993). Determination of source parameters at regional distances with three-component sparse network data, *J. Geophys. Res.*, **98**, 8107–8125.
- Dufumier, H. and Cara, M. (1995). On the limits of linear moment tensor inversion of surface wave spectra, *PAGEOPH*, **145**, 235–257.
- Dufumier, H. and Rivera, L. (1997). On the resolution of the isotropic component in moment tensor inversion, *Geophys. J. Int.*, **131**, 595–606.
- Dziak, R., Cowen, J., Baker, E., Bohnenstiehl, D., Resing, J. and Enbley, R. (2006). Detecting volcanic events in the northeast Pacific, *EOS, Transactions*, **87**.
- Eckhardt, C. (2004). Kohärenzuntersuchungen an Sg- und Codawellen von Ereignissen des Erdbebenschwarms im Jahr 2000 in NW-Böhmen, diploma thesis, Fakultät für Physik und Geowissenschaften, Universität Leipzig.
- Ekström, G. (1994). Anomalous earthquakes on volcano ring-fault structures, *Earth Planet. Sci. Lett.*, **128**, 707–712.
- Ellenberg, J. (1992). Recent fault tectonics and their relationship to the seismicity of East Germany, *Tectonophysics*, **202**, 117–121.
- Enderle, U., Schuster, K., Prodehl, C., Schulze, A. and Bribach, J. (1998). The refraction seismic experiment GRANU95 in the Saxothuringian belt, southeastern Germany, *Geophys. J. Int.*, **133**, 245–259.
- Fischer, T. (1993). Attenuation parameters and site amplification derived from quarry blasts recordings, in *Proceedings of the seventeenth regional european seminar on earthquake engineering*, published by A. Rutenberg, p. 93–99.
- Fischer, T. (2003). The August–December 2000 earthquake swarm in NW Bohemia: the first results based on automatic processing of seismograms, *J. Geodynamics*, **35**, 59–81.
- Fischer, T. (2005). Modelling of multiple-events using empirical Greens functions: method, application to swarm earthquakes and implications for their rupture propagation., *Geophys. J. Int.*, **163**, 991–1005. doi:10.1111/j.1365-246X.2005.02739.x.
- Fischer, T. and Horálek, J. (2000). Refined locations of the swarm earthquakes in the Nový Kostel Focal Zone and spatial distribution of the January 1997 swarm in Western Bohemia, Czech Republic, *Stud. Geophys. Geod.*, **44**, 210–226.
- Fischer, T. and Horálek, J. (2005). Slip-generated patterns of swarm microearthquakes from West Bohemia/Vogtland (Central Europe): Evidence of their triggering mechanism?, *J. Geophys. Res.*, **110**. doi:10.1029/2004JB003363.

- Foulger, G. and Long, R. (1984). Anomalous focal mechanisms; tensile crack formation on an accreting plate boundary, *Nature*, **310**, 43–45.
- Foulger, G. R., Julian, B. R., Hill, D. P., Pitt, A. M., Malin, P. E. and Shalev, E. (2004). Non-double-couple microearthquakes at Long Valley caldera, California, provide evidence for hydraulic fracturing, *J. Volcanol. Geotherm. Res.*, **132**, 45–71. doi:10.1016/S0377-0273(03)00420-7.
- Franke, W., Haak, V., Oncken, O. and Tanner, D. (Ed.) (2000). *Orogenic processes: quantification and modelling in the Variscan Belt*, Vol. 179, The Geological Society, London, Special Publication.
- Franke, W. and Stein, E. (2000). Exhumation of high-grade rocks in the Saxo-Thuringian belt: geological constraints and geodynamic concepts, in *Orogenic Processes: Quantification and Modelling in the Variscan Belt*, published by W. Franke, V. Haak, O. Oncken and D. Tanner, Geological Society, London, Special Publication, Vol. 179, p. 337–354.
- Franke, W. and Żelaźniewicz, A. (2000). The eastern termination of the Variscides: terrane correlation and kinematic evolution, in *Orogenic Processes: Quantification and Modelling in the Variscan Belt*, published by W. Franke, V. Haak, O. Oncken and D. Tanner, Geological Society, London, Special Publication, Vol. 179, p. 63–86.
- Gajewski, D. (1993). Radiation from a point source in general anisotropic media, *Geophys. J. Int.*, **113**, 299–317.
- Gajewski, D. and Pšenčík, I. (1987). Computation of high-frequency seismic wavefields in 3-D laterally inhomogeneous media, *Geophys. J. R. astr. Soc.*, **91**, 383–411.
- Geissler, W. (2005). Seismic and petrological investigations of the lithosphere in the swarm-earthquake and CO<sub>2</sub> degassing region Vogtland/NW-Bohemia, dissertation, Freie Universität Berlin.
- Geissler, W., Kämpf, H., Kind, R., Bräuer, K., Klinge, K., Plenefisch, T., Horálek, J., Zedník, J. and Nehybka, V. (2005). Seismic structure and location of a CO<sub>2</sub> source in the upper mantle of the western Eger (Ohře) rift, Central Europe, *Tectonics*, **24**. doi:10.1029/2004TC001672.
- Gomes, E., Zheng, X., Pšenčík, Horne, S. and Leaney, S. (2004). Local determination of weak anisotropy parameters from walkaway VSP qP-wave data in the Java Sea region, *Stud. Geophys. Geod.*, **48**, 188–194.
- Grünthal, G., Schenk, V., Zeman, A. and Schenkova, Z. (1990). Seismotectonic model for the earthquake swarm of 1985–1986 in the Vogtland/West Bohemia focal area, *Tectonophysics*, **174**, 369–383.
- Gubbins, D. (2004). *Time Series Analysis and Inverse Theory for Geophysicists*, Cambridge University Press.
- Gutenberg, B. and Richter, C. (1956). Earthquake magnitude, intensity, energy and acceleration, *Bull. Seismol. Soc. Am.*, **46**, 105–145.

- Hainzl, S. and Fischer, T. (2002). Indications for a successively triggered rupture growth underlying the 2000 earthquake swarm in Vogtland/NW Bohemia, *J. Geophys. Res.*, **107**. doi:10.1029/2002JB001865.
- Hainzl, S. and Ogata, Y. (2005). Detecting fluid signals in seismicity data through statistical earthquake modeling, *J. Geophys. Res.*, **110**. doi:10.1029/2004JB003247.
- HAMPL, F., FISCHER, T., HORÁLEK, J., BOUŠKOVÁ, A., JEDLIČKA, P., JÍRA, T. and BROŽ, M. (1995). Local West Bohemian Seismological Network (WEBNET)., in *Proceedings and Activity Report 1992 - 1994, XXIV General Assembly of the European Seismological Commission*, Univ. of Athens, Vol. II, p. 789–794.
- Havří, J. (2000). Stress analysis in the epicentral area of Nový Kostel (Western Bohemia), *Stud. Geophys. Geod.*, **44**, 522–536.
- Heuer, B., Kind, R., Kämpf and BOHEMA working group (2006). Seismic evidence for asthenospheric updoming beneath the western Bohemian Massif, central Europe, *Geophys. Res. Lett.*. Accepted.
- Hinzen, K. (2003). Stress field in the Northern Rhine area, Central Europe, from earthquake fault plane solutions, *Tectonophysics*, **377**, 325–356.
- Hiramatsu, Y. and Masataka, A. (1996). Seismic anisotropy near source region in subduction zones around Japan, *Phys. Earth Planet. Inter.*, **95**, 237–250.
- Hirschmann, G. (1993). Zur Geologie der KTB-Lokation Oberpfalz, *Z. geol. Wiss.*, **21**, 105–116.
- Hirschmann, G. (1995). The KTB location and models of the crustal structure, in *KTB Report 94-2*, Vol. 2, p. A35–A44.
- Hofmann, Y., Jahr, T. and Jentzsch, G. (2003). Three-dimensional gravimetric modelling to detect the deep structure of the region Vogtland/NW-Bohemia, *J. Geodynamics*, **35**, 209–220.
- Horálek, J., Fischer, T., Boušková, A. and Jedlička, P. (2000a). The western Bohemia region in the light of the WEBNET network, *Stud. Geophys. Geod.*, **44**, 107–125.
- Horálek, J., Šílený, J., Fischer, T., Slancová, A. and Boušková, A. (2000b). Scenario of the January 1997 West Bohemia earthquake swarm, *Stud. Geophys. Geod.*, **44**, 491–521.
- Hrubcová, P., Šroda, P., Špičák, A., Guterch, A., Grad, M., Keller, G., Bruekl, E. and Thybo, H. (2005). Crustal and uppermost mantle structure of the Bohemian Massif based on CELEBRATION 2000 data, *J. Geophys. Res.*, **110**(B11305). doi:10.1029/2004JB003080.
- Jost, M., Büßelberg, T., Jost, Ö. and Harijes, H.-P. (1998). Source parameters of injection-induced microearthquakes at 9 km depth at the KTB deep drilling site, Germany, *Bull. Seismol. Soc. Am.*, **88**, 815–832.



- Jost, M. and Herrmann, R. (1989). A student's guide to and review of moment tensors, *Seism. Res. Letters*, **60**, 37–57.
- Julian, B. (1983). Evidence for dyke intrusion earthquake mechanisms near Long Valley caldera, California, *Nature*, **303**, 323–325.
- Julian, B., Miller, A. and Foulger, G. (1997). Non-double-couple earthquake mechanisms at the Hengill-Grensdalur volcanic complex, Southwest Iceland, *Geophys. Res. Lett.*, **24**, 743–746.
- Julian, B., Miller, A. and Foulger, G. (1998). Non-double-couple earthquakes, 1. theory, *Rev. Geophys.*, **36**, 525–549.
- Kämpf, H., Bräuer, K., Strauch, G. and Weise, S. (1999). Indication for an active magma chamber in the upper mantle below the western Eger Graben, Czech Republic, in *EOS 1999 Spring Meeting*.
- Kanamori, H., Ekström, G., Dziewonski, A., Barker, J. and Sipkin, S. (1993). Seismic radiation by magma injection: An anomalous seismic event near Tori Shima, Japan, *J. Geophys. Res.*, **98**(B4), 6511–6522. doi:10.1029/92JB02867.
- Kawasaki, H. (1991). Insignificant isotropic component in the moment tensor of deep earthquakes, *Nature*, **351**, 50–53.
- Kawasaki, I. and Tanimoto, T. (1981). Radiation patterns of body waves due to the seismic dislocation occurring in an anisotropic source medium, *Bull. Seismol. Soc. Am.*, **71**, 37–50.
- Kendall, J.-M. (1991). Contributions to the Theory and Modelling of Seismic Waves in Anisotropic Inhomogeneous Media with Applications to Subduction-zones, dissertation, Department of Geological Sciences, Queen's University Kingston, Ontario, Canada.
- Kirby, S., Durham, W. and Stern, L. (1991). Mantle phase changes and deep-earthquake faulting in subducting lithosphere, *Science*, **252**, 216–225.
- Klinge, K., Plenefisch, T. and Stammer, K. (2003). The earthquake swarm 2000 in the region Vogtland/NW-Bohemia—earthquake recording at German stations and temporal distribution of events, *J. Geodynamics*, **35**, 83–96.
- Knopoff, L. and Randall, M. (1970). The compensated linear vector dipole: a possible mechanism for deep earthquakes, *J. Geophys. Res.*, **75**, 4957–4963.
- Kolář, P. (2003). Seismic source model from West Bohemia seismograms inversion - the method and preliminary results for  $M_L=2.0$ , Jan 17 1997 event, *Acta Montana*, **22**, 33–49.
- Kopecký, L. (1978). Neoidic taphrogenic evolution and young alkaline volcanism of the Bohemian Massif, *Sbor. Geol. Věd*, **31**, 91–107.
- Krüger, F. and Dahm, T. (2002). *Ten years of German Regional Seismic Network (GRSN)*, WILEY-VCH Verlag GmbH & Co. KGaA, Weinheim, chapter 6.3.

- Langston, C. A., Barker, J. S. and Palvin, G. B. (1982). Point-source inversion techniques, *PHYS. EARTH PLANET. IN.*, **30**, 228–241.
- Lay, T. and Wallace, T. (1995). *Modern global seismology*, Vol. 58 of *International Geophysics Series*, Academic Press.
- Linnemann, U., Gehmlich, M., Tichomirowa, M., Buschmann, B., Nasdala, L., Jonas, P., Lützner, H. and Bombach, K. (2000). From Cadomian subduction to early Palaeozoic rifting: the evolution of Saxo-Thuringia at the margin of Gondwana in the light of single zircon geochronology and basin development (Central European Varicides, Germany), in *Orogenic Processes: Quantification and Modelling in the Variscan Belt*, published by W. Franke, V. Haak, O. Oncken and D. Tanner, Geological Society, London, Special Publication, Vol. 179, p. 131–153.
- Málek, J., Horálek, J. and Janský (2005). One-dimensional qP-wave velocity model of the upper crust for the West Bohemia/Vogtland earthquake swarm region, *Stud. Geophys. Geod.*, **49**, 709–730.
- Málek, J., Janský, J. and Horálek, J. (2000). Layered velocity models of the western Bohemia region, *Stud. Geoph. Geod.*, **44**, 475–490.
- Málek, J., Janský, J., Novotný, O., Rößler, D. and the CELEBRATION 2000 working group (2004). Vertically inhomogeneous models of the upper crustal structure in the West-Bohemian seismoactive region inferred from the CELEBRATION 2000 refraction data, *Stud. Geophys. Geod.*, **48**. doi:10.1023/B:SGEG.0000045478.42945.6a.
- Martínková, M., Pros, Z. and Klíma, K. (2000). Experimentally determined P-wave velocity anisotropy for rocks related to the Western Bohemia seismoactive region, *Stud. Geophys. Geod.*, **44**(4), 581–589.
- Matte, P. (1998). Continental subduction and exhumation of HP rocks in Paleozoic orogenic belts: Uralides and Variscides, *GFF*, **120**, 209–222.
- Menke, W. (1989). *Geophysical data analysis: discrete inverse theory*, Vol. 45 of *International Geophysics Series*, Harcourt Brace Jovanovich.
- Miller, A., Foulger, G. and Julian, B. (1998). Non-double-couple earthquakes, 1. observations, *Rev. Geophys.*, **36**, 551–568.
- Miller, S. (2004). Aftershocks driven by a high-pressure CO<sub>2</sub> source at depth, *Nature*, **427**, 724–727.
- Mrlina, J. (2000). Vertical displacements in the Nový Kostel seismoactive area, *Stud. Geophys. Geod.*, **44**, 336–345.
- Müller, G. (1973). Seismic moment and long-period radiation of underground nuclear explosions, *Bull. Seismol. Soc. Am.*, **63**, 847–857.
- Müller, G. (2001). Volume change of seismic sources from moment tensors, *Bull. Seismol. Soc. Am.*, **91**, 880–884.
- Musgrave, M. (1970). *Crustal acoustics*, Holden-Day.

- Nabalek, J. (1984). Determination of earthquake source parameters from inversion of body waves, dissertation, Massachusetts Institute of Technology, Columbia University.
- Nettles, M. and Ekström, G. (1998). Faulting mechanism of anomalous earthquakes near Bárðarbunga Volcano, Iceland, *J. Geophys. Res.*, **103**, 17973–17983.
- Neunhöfer, H. (2000). The catalogue of the Vogtland/Western Bohemia earthquakes and VOCATUS as an auxiliary code, *Stud. Geophys. Geod.*, **44**, 549–555.
- Neunhöfer, H. and Güth, D. (1988). Mikrobeben seit 1962 im Vogtland, *Zeitschrift für geologische Wissenschaften*, **16**, 135–146.
- Neunhöfer, H. and Güth, D. (1989). Detailed investigation of the great earthquake swarm in Western Bohemia by the local Vogtland Network, in *Monitoring and analysis of the earthquake swarm 1985/86 in the region Vogtland/Western Bohemia*, published by P. Bormann, p. 124–164.
- Novotný, O. (1996). A preliminary seismic model for the region of the West-Bohemian earthquake swarms, *Stud. Geophys. Geod.*, **40**, 353–366.
- O’Brien, P. (2000). The fundamental Variscan problem: high-temperature metamorphism at different depths and high-pressure metamorphism at different temperatures, in *Orogenic Processes: Quantification and Modelling in the Variscan Belt*, published by W. Franke, V. Haak, O. Oncken and D. Tanner, Geological Society, London, Special Publication, Vol. 179, p. 369–386.
- O’Brien, P. and Carswell, D. (1993). Tectonometamorphic evolution of the Bohemian Massif: evidence from high pressure metamorphic rocks, *Geol. Rundsch.*, **82**, 531–555.
- Okaya, D., Rabbel, W., T., B. and Hasenclever, J. (2004). P wave material anisotropy of a tectono-metamorphic terrane: an active source seismic experiment at the KTB super-deep drill hole, Southeast Germany, *Geophys. Res. Lett.*, **31**. 10.1029/2004GL020855.
- Parotidis, M., Shapiro, S. and Rothert, E. (2005). Evidence for triggering of the Vogtland swarms 2000 by pore pressure diffusion, *J. Geophys. Res.*, **110**. doi:10.1029/2004JB003267.
- Peterek, A., Coyle, D., Haak, U., Hirschmann, S., Lich, S., Rauche, H., Rust, Schröder, B., Semmel, A., Stettner, G., Stöckhert, B., Umsonst, T., Wagner, G., Wemmer, K. and Zulauf, G. (1994). The late and post-variscan tectonic evolution of the KTB-drilling site area – a short workshop report, in *KTB report 94-2*, Vol. 2, p. A55–A62.
- Pinar, A., Kuge, K. and Honkura, Y. (2003). Moment tensor inversion of recent small to moderate sized earthquakes: implications for seismic hazard and active tectonics beneath the sea of Marmara, *Geophys. J. Int.*, **153**, 133–145.

- Plenefisch, T., Heuer, B. and Klinge, K. (2003). Source mechanisms and scaling relations for the earthquake swarm 2000 at Nový Kostel (Vogtland/NW-Bohemia), *EGS-AGU-EUG Joint Assembly, Nice, 06-11 April 2003, abstract #EAE03-A-11165*. Online at <http://www.cosis.net/abstracts/EAE03/11165/EAE03-A-11165.pdf>.
- Plenefisch, T. and Klinge, K. (2003). Temporal variations of focal mechanisms in the Nový Kostel focal zone (Vogtland/NW-Bohemia)–comparison of the swarms 1994, 1997 and 2000, *J. Geodynamics*, **35**, 145–156.
- Plenefisch, T., Klinge, K. and Kind, R. (2001). Upper mantle anisotropy at the transition zone of the Saxothuringicum and Moldanubicum in southeast Germany revealed by shear wave splitting, *Geophys. J. Int.*, **144**, 309–319.
- Plomerová, J., Achauer, U., Granet, M., Babuška, V. and the BOHEMA working group (2003). Passive seismic experiment to study lithosphere-asthenosphere system in the western part of the Bohemian Massif, *Stud. Geophys. Geod.*, **47**, 691–701.
- Plomerová, J., Babuška, V., Šílený and Horálek, J. (1998). Seismic anisotropy and velocity variations in the mantle beneath the Saxothuringian-Moldaunubian contact in Central Europe, *Pure apply. geophys.*, **151**, 365–394.
- Plomerová, J., Granet, M., Judenherc, S., Achauer, U., Babuška, V., Jedlička, D., Kouba, D. and Vecsey, L. (2000). Temporary array data for studying seismic anisotropy of Variscan Massif – the Armorican Massif, French Massif Central and Bohemian Massif, *Stud. Geophys. Geod.*, **44**, 195–209.
- Plomerová, J., Vecsey, L., Babuška, V., Granet, M. and Achauer, U. (2005). Passive seismic experiment MOSAIC - a pilot study of mantle lithosphere anisotropy of the Bohemian Massif, *Stud. Geophys. Geod.*, **49**, 541–560.
- Press, W., Teulosky, S., Vetterling, W. and Flannery, B. (1992). *Numerical recipes in C*, Cambridge University Press.
- Pšenčík, I. (1998). ANRAY package, version 4.10, Report, Dept. of Geophysics, Charles University, Prague. Online at <http://sw3d.mff.cuni.cz>.
- Pšenčík, I. and Dellinger, J. (2001). Quasi-shear waves in inhomogeneous weakly anisotropic media by the quasi-isotropic approach: a model study, *Geophysics*, **66**, 308–319.
- Pšenčík, I. and Gajewski, D. (1998). Polarization, phase velocity, and NMO velocity of *qP*-waves in arbitrary weakly anisotropic media, *Geophysics*, **63**, 1754–1766.
- Pšenčík, I. and Teles, T. (1996). Point source radiation in inhomogeneous anisotropic structures, *PAGEOPH*, **148**, 591–623.
- Pujol, J., Luschen, E. and Hu, Y. (1998). Seismic wave attenuation in metamorphic rocks from VSP data in Germany's continental super-deep borehole, *Geophysics*, **63**, 354–365.

- Rabbel, W., Beilecke, T., Bohlen, T., Fischer, D., Frank, A., Hasenclever, J., Borm, G., Kuck, J., Bram, K., Druivenga, G., Luschen, E., Gebrande, H., Pujol, J. and Smithson, S. (2004). Superdeep vertical seismic profiling at the KTB deep drill hole (Germany): seismic close-up view of a major thrust zone down to 8.5 km depth, *J. Geophys. Res.*, **B09309**. doi:10.1029/2004JB002975.
- Ramos-Martínez, J. and McMechan, G. A. (2001). Source-parameter estimation by full waveform inversion in 3D heterogeneous, viscoelastic, anisotropic media, *Bull. Seismol. Soc. Am.*, **91**, 276–291.
- Richards, P. and Kim, W.-Y. (2005). Equivalent volume sources for explosions at depth: theory and observations, *Bull. Seismol. Soc. Am.*, **95**, 401–407.
- Rößler, D., Krüger, F. and Rümpker, G. (2006). Inversion for seismic moment tensors in anisotropic media using standard techniques for isotropic media, *Geophys. J. Int.*. Submitted.
- Rößler, D., Pšenčík, I., Krüger, F. and Rümpker, G. (2005). Retrieval of source parameters for local earthquakes in anisotropic media, Report 15, pp. 333–344, Dept. of Geophysics, Charles University, Prague. Online at <http://sw3d.mff.cuni.cz>.
- Rößler, D., Rümpker, G. and Krüger, F. (2004). Ambiguous moment tensors and radiation patterns in anisotropic media with applications to the modeling of earthquake mechanisms in W-Bohemia, *Stud. Geophys. Geod.*, **48**, 233–250. doi:10.1023/B:SGEG.0000015594.11070.21.
- Rümpker, G. and Kendall, J. (2002). A Maslov-propagator seismogram for weakly anisotropic media, *Geophys. J. Int.*, **150**, 23–36.
- Rümpker, G., Ryberg, T., Bock, G. and Desert Seismology Group (2003). Boundary-layer mantle flow under the Dead Sea transform fault inferred from seismic anisotropy, *Nature*, **425**, 497–501.
- Růžek, B., Vavryčuk, V., Hrubcová, Zedník and the CELEBRATION Working Group (2003). Crustal anisotropy in the Bohemian Massif, Czech Republic: observations based on Central European lithospheric experiment based on refraction (CELEBRATION) 2000, *J. Geophys. Res.*, **108**. doi:10.1029/2002JB002242.
- Scherbaum, F. (2001). *Of Poles and Zeros: Fundamentals of Digital Seismology*, Kluwer Academic Publishers, second edition.
- Scholz, C. (1968). The frequency-magnitude relation of microfracturing in rock and its relation to earthquakes, *Bull. Seismol. Soc. Am.*, **58**, 399–415.
- Scholz, C. H. (2002). *The mechanics of earthquakes and faulting*, Cambridge University Press.
- Schön, J. (1996). *Physical properties of rocks*, Vol. 18 of *Handbook of geophysical seismic exploration*, Elsevier.
- Šílený, J. (1998). Earthquake source parameters and their confidence regions by a genetic algorithm with a 'memory', *Geophys. J. Int.*, p. 228–242.

- Šílený, J. (2004). Regional moment tensor uncertainty due to mismodeling of the crust, *Tectonophysics*, **383**, 133–147.
- Šílený, J. and Hofstetter, R. (2002). Moment tensor of the 1999 Dead Sea calibration shot: limitations in the isotropic source retrieval without a detailed earth model, *Tectonophysics*, **356**, 157–169.
- Šílený, J. and Plomerová, J. (1996). Inversion of shear-wave splitting parameters to retrieve three-dimensional orientation in continental lithosphere, *Phys. Earth Planet. Inter.*, **95**, 277–292.
- Šílený, J. and Vavryčuk, V. (2000). Approximate retrieval of the point source in anisotropic media: numerical modelling by indirect parametrization of the source, *Geophys. J. Int.*, **143**, 700–708.
- Šílený, J. and Vavryčuk, V. (2002). Can unbiased source be retrieved from anisotropic waveforms by using an isotropic model of the medium, *Tectonophysics*, **356**, 125–138.
- Silver, G. P. and Jordan, T. H. (1982). Optimal estimation of the scalar seismic moment, *Geophys. J. R. astr. Soc.*, **70**, 755–787.
- Sipkin, S. (1986a). Estimation of earthquake source parameters by the inversion of waveform data: global seismicity, 1981–1983, *Bull. Seismol. Soc. Am.*, **76**, 1515–1541.
- Sipkin, S. (1986b). Interpretation of non-double-couple earthquake mechanisms derived from moment tensor inversions, *J. geophys. Res.*, **91**, 531–547.
- Snoke, J. (2003). FOCMEC: FOcal MECHANism determinations, in *International Handbook of Earthquake and Engineering Seismology*, published by W. Lee, H. Kanamori, P. Jennings and C. Kisslinger, Academic Press, chapter 85.12.
- Solomon, S. C. and Julian, B. R. (1974). Seismic constraints on ocean-ridge mantle structure: anomalous fault plane solutions from first motions, *Geophys. J. R. astr. Soc.*, **38**, 265–285.
- Špičák, A., Horálek, J., Boušková, Tomek, Ā. and Vaneček, J. (1999). Magma intrusion and earthquake swarm occurrence in the Western part of the Bohemian Massif, *Stud. Geophys. Geod.*, **43**, 87–106.
- Špičáková, A., Uličný, D. and Koudelková (2000). Tectonosedimentary evolution of the Cheb Basin (NW-Bohemia, Czech Republic) between late oligocene and pliocene: a preliminary note, *Stud. Geophys. Geod.*, **44**, 556–580.
- Stammler, K. (1992). *Seismic Handler*, Seismological Central Observatory, BGR. Online at <http://www.szgrf.bgr.de>.
- Stickney, M. and Sprenke, K. (1993). Seismic events with implosional focal mechanisms in the Coeur d'Alene mining district, Northern Idaho, *J. Geophys. Res.*.
- Švancara, J., Gnojek, I., Hubatka, F. and Dědáček (2000). Geophysical field pattern in the West Bohemian geodynamic active area, *Stud. Geophys. Geod.*, **44**, 307–326.

- Sykes, L. R. (1967). Mechanism of earthquakes and nature of faulting on the mid-ocean ridges, *J. Geophys. Res.*, **72**, 5–27.
- Templeton, D. and Dreger, D. (2006). Non-double-couple earthquakes in the Long Valley volcanic region, *Bull. Seismol. Soc. Am.*, **96**, 69–79. doi:10.1785/0120040206.
- Tittel, B., Korn, B., Lange, W., Leydecker, G., Rappsilber, I. and Wendt, S. (2001). Der Gebirgsschlag in Teutschenthal bei Halle vom 11. September 1996 Makroseismische Auswertung, *Z. angew. Geol.*, **47**, 126–131.
- Tittel, B. and Wendt, S. (2003). Magnitudes and time distribution of the swarm earthquakes August–November 2000 in NW Bohemia, *J. Geodynamics*, **35**, 97–105.
- Tomek, C., Dvořáková, V. and Vrána, S. (1997). Geological interpretation of the 9HR and 503M profiles in Western Bohemia, in *Geological model of Western Bohemia related to the KTB borehole in Germany*, published by S. Vrána and Štětrá, Vol. 47 of *Sborn. Geol. Vd, Geologie*, chapter B.3., p. 43–50.
- Trela, C. (2003). Seismische Untersuchungen der kristallinen Kruste an der KTB-Lokation, dissertation, Christian-Albrechts-Universität zu Kiel.
- Ulrych, J., Lang, M., Balogh, K. and Kropáček (1999). Cenozoic intraplate volcanic rock series in the Bohemia Massif: A review, *Geolines*, **9**, 123–129.
- Ulrych, J., Lloyd, F. and Balogh, K. (2003). Age relations and geochemical constraints of Cenozoic alkaline volcanic series in W Bohemia: A review, *Geolines*, **15**, 168–180.
- Vavryčuk, V. (1993). Crustal anisotropy from local observations of shear-wave splitting in West Bohemia, Czech Republic, *Bull. Seismol. Soc. Am.*, **83**, 1420–1441.
- Vavryčuk, V. (2001). Inversion for parameters of tensile earthquakes, *J. Geophys. Res.*, **106**, 16339–16355.
- Vavryčuk, V. (2002). Non-double-couple earthquakes of 1997 January in West Bohemia, Czech Republic: evidence of tensile faulting, *Geophys. J. Int.*, **149**, 364–373.
- Vavryčuk, V. (2004). Inversion for anisotropy from non-double-couple components of moment tensors, *J. Geophys. Res.*, **109**. doi:10.1029/2003JB002926.
- Vavryčuk, V. (2005). Focal mechanisms in anisotropic media, *Geophys. J. Int.*, **161**. doi:10.1111/j.1365-246X.2005.02585.
- Vogel, H. (1995). *Gerthsen Physik*, Springer.
- Voigt, W. (1928). *Lehrbuch der Kristallphysik*, Teubner-Verlag, Leipzig.
- Vrána, S. and Štědra, V. (1998). Crustal structure of the western part of the Bohemian Massif, Czech Republic - a summary of the project "Geological model of Western Bohemia, related to the deep borehole KTB in Germany", *Episodes*, **21**.

- Vrána, S. and Štětrá (Ed.) (1997). *Geological model of Western Bohemia related to the KTB borehole in Germany*, Sborn. Geol. Vd, Geologie, Czech Geological Survey, Prague.
- Weinlich, F., Bräuer, K., Kämpf, H., Strauch, G., Tesař, J. and Weise, S. (1999). An active subcontinental mantle volatile system in the western Eger rift, Central Europe: gas flux, isotopic (He, C and N) and compositional fingerprints, *Geochim. Cosmochim. Acta*, **63**, 3653–3671.
- Weinlich, F., Bräuer, K., Kämpf, H., Strauch, G. and Weise, S. (1993). Mantel-Kruste Wechselwirkung im Bereich der Marienbader Störungszone, Teil 2: Gasgeochemische Untersuchungen an Mineralquellen entlang eines Profils über das Eger-Rift, *Z. geol. Wiss.*, **21**, 135–142.
- Weise, S., Bräuer, K., Kämpf, H., Strauch, G. and Koch, U. (2001). Transport of mantle volatiles through the crust traced by seismically released fluids: a natural experiment in the earthquake swarm area Vogtland/NW Bohemia, Central Europe, *Tectonophysics*, **336**, 137–150.
- Wielandt, E. (2001). Basics of the volume-source model and its application in volcano seismology, script, Institute of Geophysics, University of Stuttgart. Online at [ftp.geophys.uni-stuttgart.de/pub/ew/postscripts](http://ftp.geophys.uni-stuttgart.de/pub/ew/postscripts).
- Wirth, W., Plenefisch, T., Klinge, K., Stammler, K. and Seidl, D. (2000). Focal mechanisms and stress field in the region Vogtland/Western Bohemia, *Stud. Geophys. Geod.*, **44**, 126–141.





## A Glossary

Table A.1: List of abbreviations, operators, and symbols frequently used in this work.

### Abbreviations

abbreviations	description
FPS	fault-plane solution
GFZ	GeoForschungsZentrum Potsdam
GRSN	German Regional Seismic Network
KTB	Kontinentale Tiefbohrung (German Continental Deep Drilling Program) near Windischechenbach, FR Germany
MOHO	Mohorvičić discontinuity
SZGRF	Seismologisches Zentralobservatorium Gräfenberg (Seismological Central Observatory)
WEBNET	WEst Bohemia local seismic NETwork

### Operators

operator	description
*	convolution symbol
$\delta_{ij}$	Kronecker symbol
$\times$	vectorial cross product

### Symbols

quantity	unit	description
$a_{ijkl}$	$\text{m}^2\text{s}^{-2}$	density normalised elastic tensor
$A_{ij}$	$\text{m}^2\text{s}^{-2}$	density normalised elastic tensor in Voigt notation
$A_0$	$\text{m}^2$	area of the fault plane
$c$	$\text{ms}^{-1}$	phase velocity
$c_{ijkl}$	Pa	elastic tensor
$C_{ij}$	Pa	elastic tensor in Voigt notation
CLVD	%	strength of the compensated linear vector dipole
$D$	$\text{m}^3$	directivity (spreading-free amplitude at the source)
$D_{ij}$	$\text{m}^3$	source tensor
DC	%	strength of the double couple moment tensor
$\delta$	°	slip inclination derived from the source tensor $D_{ij}$
$\delta_1^s$	°	dip of the rupture plane
$f^{(A)}$	$\text{s}^{-1}$	analytical signal
$g_i$	★★	vector of polarisation
$G_{ij,k}$	$\text{N}^{-1}$	spatial derivatives of the Green's functions with respect to $x_k$
$\gamma_i$	★★	direction cosine
ISO	%	strength of the isotropic moment tensor
$\lambda$	Pa	Lamé parameter, bulk modulus
$\lambda_1^s$	°	rake of the rupture plane

continued on next page

continuation of Table A.1

$M_{ij}$	Nm	moment tensor
$M_0$	Nm	seismic moment
$M_T$	Nm	total seismic moment
$M_L$	★★	local magnitude
$M_w$	★★	moment magnitude
$\mu$	Pa	Lamé parameter, shear modulus
$n_i$	★★	normal vector to the fault plane (fault normal)
$\nu_i$	★	vector of eigenvalues
$\Omega_M$	$\text{m}^4\text{s}^{-2}$	geometric spreading
$p_i$	$\text{sm}^{-1}$	slowness vector
$\phi$	°	azimuth (directional angle)
$\Phi_1^s$	°	strike of the rupture plane
$\rho$	$\text{kgm}^{-3}$	density
$s_i$	★★	orientation of the slip
$s$	m	size of the slip vector (slip vector)
$s'_i$	m	slip vector ( $s'_i = ss_i$ )
$\sigma_i$	$\text{m}^3$	source vector
$t$	s	time
$\theta$	°	inclination (directional angle)
$u_i$	m	displacement vector, complex valued
$v_p$	$\text{ms}^{-1}$	velocity of the P wave in an isotropic medium
$v_s$	$\text{ms}^{-1}$	velocity of the S wave in an isotropic medium
$v$	$\text{ms}^{-1}$	group velocity
$\mathbf{x}$	m	spatial coordinate of the point of observation
$\mathbf{x}_0$	m	spatial coordinate of the source

★: unit depends on initial quantity, ★★ dimensionless

## B Elastic constants and model specifications

*Aki and Richards (2002)*: "A medium is said to be *elastic* if it possess a natural state (in which strains and stresses are zero) to which it will revert when applied forces are removed."

In elastic media stress and strain will change when loads are imposed to a body. The elastic tensor  $c_{ijkl}$  describes the linear relation between the elements of the stress tensor  $\tau_{ij}$  and the elements of the strain tensor  $\epsilon_{kl}$  (*Aki and Richards, 2002*)

$$\tau_{ij} = c_{ijkl}\epsilon_{kl}. \quad (\text{B.1})$$

Equation (B.1) is a generalisation of Hooke's law (stress is proportional to strain). Due to the symmetry properties  $\tau_{ij} = \tau_{ji}$  and  $\epsilon_{kl} = \epsilon_{lk}$  and thermodynamic arguments the following symmetry relations apply for  $c_{ijkl}$  (*Musgrave, 1970*):

$$c_{ijkl} = c_{jikl} = c_{ijlk} = c_{klij}. \quad (\text{B.2})$$

The elastic tensor is of fourth-order with 81 elements. However, because of the relations in (B.2) only 21 elements are mutually independent (see elastic tensor later in Eq. B.5).

Equation (B.1) can therefore be conveniently transformed by arranging  $\tau_{ij}$  and  $\epsilon_{kl}$  in the form of two 6-element vectors ( $\bar{\tau}_m$  and  $\bar{\epsilon}_n$ ) writing  $c_{ijkl}$  in the Voigt notation ( $C_{mn}$ ) attributed to *Voigt (1928)*. The transformation is formed by contracting pairs of indices to one single index ( $ij \leftrightarrow m$ ). The following relations apply (*Musgrave, 1970*):

$$11 \leftrightarrow 1, 22 \leftrightarrow 2, 33 \leftrightarrow 3, 23 \leftrightarrow 4, 13 \leftrightarrow 5, 12 \leftrightarrow 6. \quad (\text{B.3})$$

Then, (B.1) reads (*Musgrave, 1970; Bos et al., 2004*)

$$\bar{\tau}_m = C_{mn}\bar{\epsilon}_n, \quad (\text{B.4})$$

where  $\bar{\tau}^T = (\tau_{11}, \tau_{22}, \tau_{33}, 2\tau_{23}, 2\tau_{13}, 2\tau_{12})$  and  $\bar{\epsilon}^T = (\epsilon_{11}, \epsilon_{22}, \epsilon_{33}, 2\epsilon_{23}, 2\epsilon_{13}, 2\epsilon_{12})$ . The tensor of density normalised elastic parameters is accordingly referred to as  $a_{ijkl}$  or  $A_{ij}$  ( $a_{ijkl} = c_{ijkl}/\rho$  or  $A_{ij} = C_{ij}/\rho$ , where  $\rho$  is density).

The 21 elastic moduli describe seismic anisotropy of a medium. They determine the phase and group velocities, the slownesses and the polarisation of waves travelling in a medium. In the most general case, triclinic anisotropy represented by (B.5), medium properties are  $\pi$ -symmetric, i.e. a medium has the same features (velocities, wave polarisation, etc.) for rays in one direction as in the opposite direction. The number of independent elastic parameters reduces for higher symmetry to 9 independent elastic parameters for orthorhombic anisotropy or to 5 independent elastic parameters for transverse isotropy. The elastic properties and derived quantities in a transversely isotropic medium are symmetric about one single symmetry axis (see (B.9) for the elastic tensor of a transversely isotropic medium with vertical axis of symmetry). Only 2 independent elastic parameters (the Lamé parameters  $\lambda$  and  $\mu$ ) describe isotropy (see Equation (B.6) and *Musgrave, 1970; Babuška and Cara, 1991*). See Appendices B.1-B.5 for examples on elastic parameters that were also used in this work and Figs. B.1-B.4 therein for examples of slownesses, polarisations and velocities. See also *Musgrave (1970); Babuška and Cara (1991)* or *Bos et al. (2004)* for details on other symmetry groups.

From (B.2) and (B.3) it follows that the elastic tensor in Voigt notation is symmetric about the diagonal. Therefore, elements of the elastic tensor  $C_{ij}$  or the density-normalised elastic tensor  $A_{ij}$  below the diagonal are not shown explicitly in the following. Elastic tensors and Figures of corresponding slownesses, polarisations, and velocities are given in cartesian coordinates that are defined in the crystallographic coordinate system (*Babuška and Cara, 1991*).

Structure of the elastic tensor for a triclinic anisotropic medium:

$$C_{ij} = \begin{pmatrix} C_{11} & C_{12} & C_{13} & C_{14} & C_{15} & C_{16} \\ & C_{22} & C_{23} & C_{24} & C_{25} & C_{26} \\ & & C_{33} & C_{34} & C_{35} & C_{36} \\ & & & C_{44} & C_{45} & C_{46} \\ & & & & C_{55} & C_{56} \\ & & & & & C_{66} \end{pmatrix}. \quad (\text{B.5})$$

## B.1 Isotropic media

In an isotropic medium elastic properties and wave velocities are independent of the propagation direction of the seismic wave. The medium is described by only two Lamé parameter  $\lambda$  and  $\mu$  that form the elastic tensor

$$C_{ij} = \begin{pmatrix} \lambda & \lambda + 2\mu & \lambda + 2\mu & 0 & 0 & 0 \\ & \lambda & \lambda + 2\mu & 0 & 0 & 0 \\ & & \lambda & 0 & 0 & 0 \\ & & & \mu & 0 & 0 \\ & & & & \mu & 0 \\ & & & & & \mu \end{pmatrix}. \quad (\text{B.6})$$

The Lamé parameters and the density determine the P- and S-wave velocities  $v_p$  and  $v_s$ , respectively

$$v_p = \sqrt{\frac{\lambda + 2\mu}{\rho}}, \quad v_s = \sqrt{\frac{\mu}{\rho}}. \quad (\text{B.7})$$

In natural isotropic rocks  $\lambda \approx \mu$  (*Schön, 1996*). Therefore,  $v_p > v_s$  and  $v_p/v_s \approx \sqrt{3}$ . In difference to anisotropic media phase and group velocities are equal. Wavefronts are circular. The normal to the wavefront points radially away from the source in the direction of the ray. The particle motion of P and S waves in homogeneous isotropic media is only determined by the source. It is normal to the wavefront for P waves and it lies within the wavefront for the S wave.

## B.2 Description of weak-anisotropy parameters

The 15 density normalised elastic parameters  $A_{ij}$  that determine P-wave propagation in an anisotropic medium and the P-wave velocity ( $v_p$ ) of an isotropic reference medium can be used to describe elastic properties in terms of the weak-anisotropy

(WA) parameters (Pšenčík and Gajewski, 1998)

$$\begin{aligned}
 \epsilon_x &= \frac{A_{11} - v_p^2}{2v_p^2}, & \epsilon_y &= \frac{A_{22} - v_p^2}{2v_p^2}, & \epsilon_z &= \frac{A_{33} - v_p^2}{2v_p^2}, \\
 \delta_x &= \frac{A_{13} + 2A_{55} - v_p^2}{v_p^2}, & \delta_y &= \frac{A_{23} + 2A_{44} - v_p^2}{v_p^2}, & \delta_z &= \frac{A_{12} + 2A_{66} - v_p^2}{v_p^2}, \\
 \chi_x &= \frac{A_{14} + 2A_{56} - v_p^2}{v_p^2}, & \chi_y &= \frac{A_{25} + 2A_{46} - v_p^2}{v_p^2}, & \chi_z &= \frac{A_{36} + 2A_{45} - v_p^2}{v_p^2}, \\
 \epsilon_{15} &= \frac{A_{15}}{v_p^2}, & \epsilon_{16} &= \frac{A_{16}}{v_p^2}, & \epsilon_{24} &= \frac{A_{24}}{v_p^2}, & \epsilon_{26} &= \frac{A_{26}}{v_p^2}, & \epsilon_{34} &= \frac{A_{34}}{v_p^2}, & \epsilon_{35} &= \frac{A_{35}}{v_p^2}.
 \end{aligned} \tag{B.8}$$

This representation was utilised by Málek *et al.* (2005) to specify model II used in Sections 4 and 5. Note that by means of the WA parameters the calculation of phase velocities and polarisations is simplified for waves in weakly anisotropic media (Pšenčík and Gajewski, 1998).

### B.3 Generic transversely isotropic models

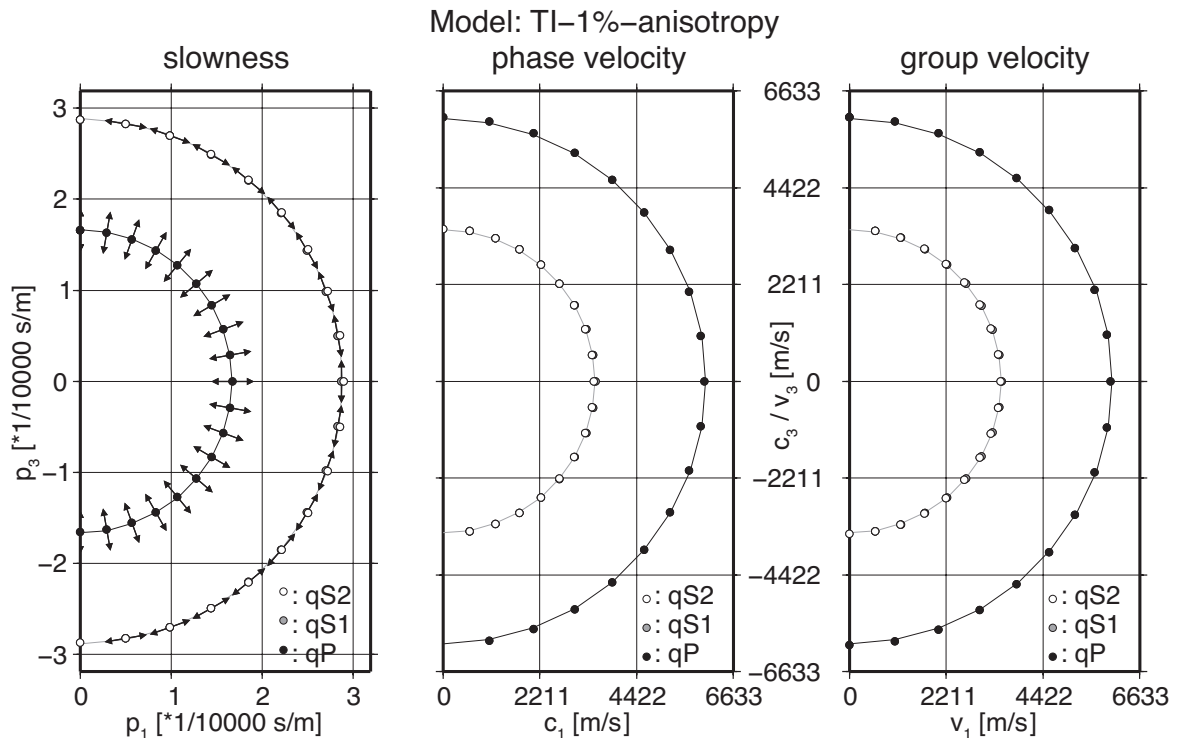


Figure B.1: Vertical sections in the  $x_1x_3$  plane of the slowness surfaces with polarisation vectors, phase velocities, and group velocities for the generic transversely anisotropic medium described by (B.9) and (B.10) with 1% anisotropy ( $v_p = 6000$  m/s,  $v_p/v_s = \sqrt{3}$ ,  $a_1 = 0.01$ ,  $a_0 = -1$ ). Note that the polarisation of the qS2 wave points perpendicular into this plane. Solid lines depict P- and S-wave quantities in the isotropic reference medium.

Transversely isotropic media are described by 5 independent elastic moduli (Musgrave, 1970). The elastic tensor  $C_{ij}$  for a general transversely isotropic medium

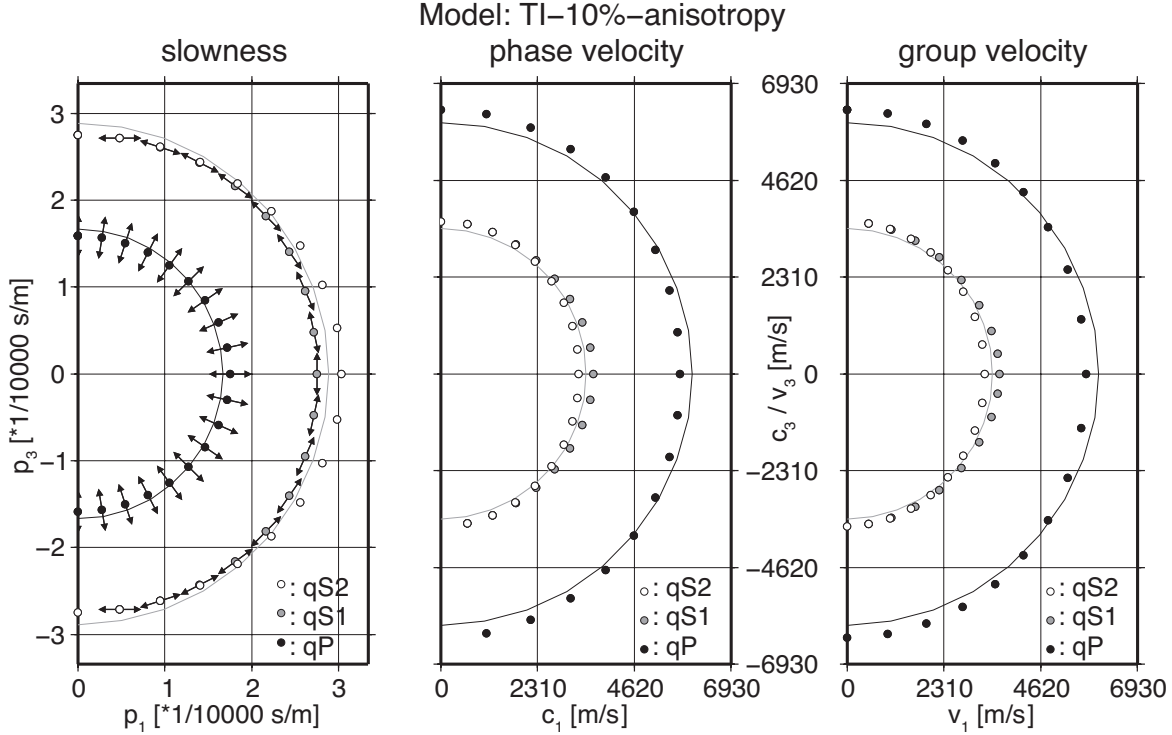


Figure B.2: As in Fig. B.1 but for the generic transversely anisotropic medium with 10% anisotropy ( $v_p = 6000$  m/s,  $v_p/v_s = \sqrt{3}$ ,  $a_1 = 0.1$ ,  $a_0 = -1$ ).

with a vertical axis of symmetry (parallel to the  $\mathbf{x}_3$ -direction) can be given by (*Musgrave, 1970*)

$$C_{ij} = \begin{pmatrix} C_{11} & C_{11} - 2C_{66} & C_{13} & 0 & 0 & 0 \\ & C_{11} & C_{13} & 0 & 0 & 0 \\ & & C_{33} & 0 & 0 & 0 \\ & & & C_{44} & 0 & 0 \\ & & & & C_{44} & 0 \\ & & & & & C_{66} \end{pmatrix}. \quad (\text{B.9})$$

The relation  $C_{11} - C_{12} - 2C_{66} = 0$  in (B.9) implies isotropy in the  $x_1x_2$  plane (*Musgrave, 1970*). Generic transversely isotropic models in the form of (B.9) can be formed by (*Rümpker and Kendall, 2002*)

$$\begin{aligned} C_{11} &= \left(v_p - \frac{a_1 v_p}{2}\right)^2, \quad C_{33} = \left(v_p + \frac{a_1 v_p}{2}\right)^2, \quad C_{13} = (1 + a_0 a_1)(v_p^2 - 2v_s^2), \\ C_{44} &= \left(v_s - \frac{a_1 v_s}{2}\right)^2, \quad C_{66} = \left(v_s + \frac{a_1 v_s}{2}\right)^2, \end{aligned} \quad (\text{B.10})$$

where  $v_p$  and  $v_s$  are P- and S-wave velocities, respectively, in the isotropic reference medium and  $a_0$  determines the Gaussian curvature of the slowness and group velocity (wave front) surfaces. In this work  $a_0 = -1$ , resulting in convex slowness surface sheets. The parameter  $a_1$  describes both the maximum variation of the P-wave (phase) velocity along different directions and the difference between fast and slow S-wave velocities. In the definition (B.10)  $C_{13} = (v_p^2 - 2v_s^2)$  in the isotropic limit ( $a_1 = 0$ ).

Relations (B.9) and (B.10) were used in Section 2 to form medium M2 (compare Tab. 3.1) and in Section 3 to form the media M2 and M3 with 1% and 10% anisotropy, respectively. Therein,  $v_p = 6000$  m/s,  $v_p/v_s = \sqrt{3}$ ,  $a_0 = -1$ , and  $a_1 = 0.01$  (1% anisotropy) and  $a_1 = 0.1$  (10% anisotropy) are assumed. Vertical sections of the slowness sheets, polarisation directions, as well as phase and group velocities are given in Figs. B.1, B.2 for models with 1% and 10% anisotropy, respectively.

## B.4 Models I and II for West Bohemia

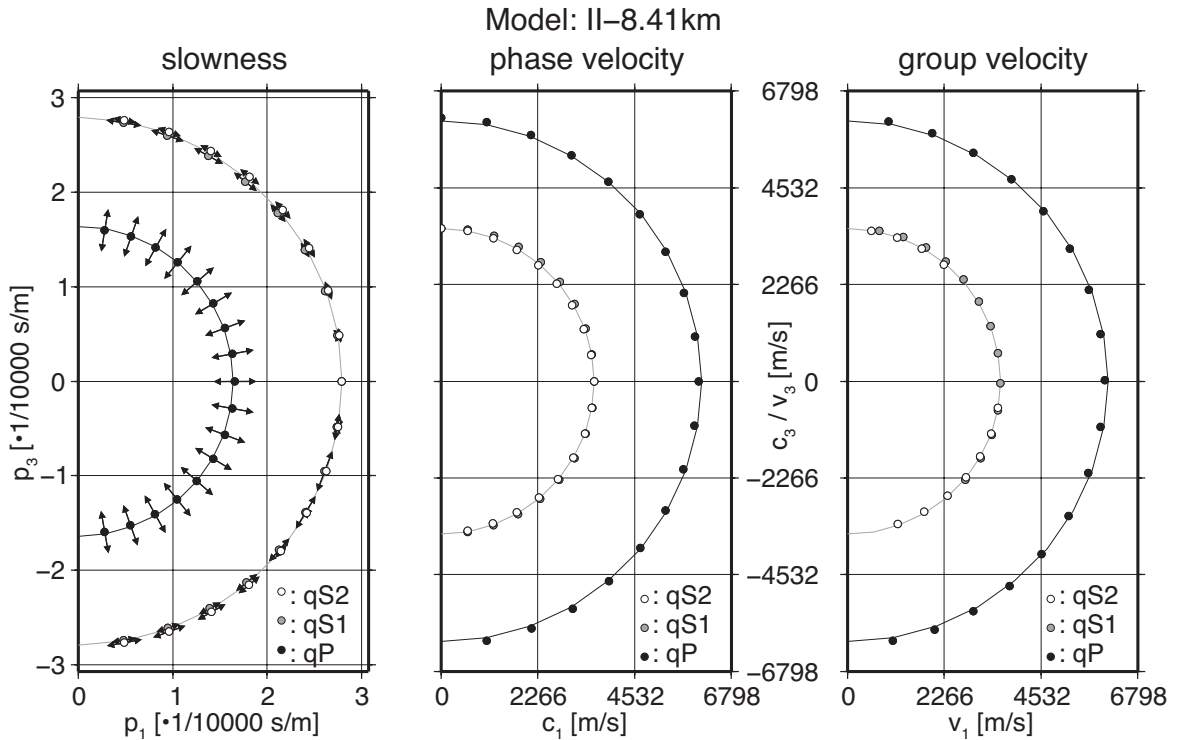


Figure B.3: Vertical sections in the  $x_1x_3$  plane of the slowness surfaces with projected polarisation vectors, phase velocities, and group velocities for the inhomogeneous anisotropic medium (model II) at 8.41 km depth given by the elastic constants in (B.14). Solid lines depict P- and S-wave quantities in the isotropic reference medium (model I). Because the medium shows triclinic anisotropy polarisation vectors of the qS1 and the qS2 waves are visible in the  $x_1x_3$  plane. For slownesses in the  $\mathbf{x}_1$  direction qS wave polarisations are almost perpendicular to this plane.

The vertically inhomogeneous velocity models I and II are used in Sections 4 and 5 to model waveforms due to sources in West Bohemia. Velocity models I and II are isotropic and anisotropic, respectively. Their properties are given at the surface and at depths of 0.41 km, 2.46 km, 8.41 km, and 32 km (*Málek et al.*, 2005). Velocities in between are obtained by spline interpolation. During waveform modelling in Sections 4 and 5  $\rho = 2650$  kgm $^{-3}$  is assumed for the crustal density. Properties of P and S waves in model I at a depth of 8.41 km are given in Table B.1 and in Figure B.3.

Model II is defined by the WA parameters (*Pšenčík*, 1998; *Málek et al.*, 2005) and by the isotropic reference velocities in Table B.1. The WA parameters are used to form the elastic tensors for each depth (compare Appendix B.2). The density normalised



Table B.1: Velocity-depth profile for P ( $v_p$ ) and S waves ( $v_s$ ) in the vertically inhomogeneous isotropic model I (*Málek et al.*, 2005) used in Sections 4 and 5. At a depth of 32 km  $v_p/v_s = \sqrt{3}$  is assumed.

depth [km]	0.00	0.41	2.46	8.41	32.00
$v_p$ [km/s]	3.70	5.37	5.81	6.10	7.20
$v_s$ [km/s]	2.18	3.16	3.57	3.58	4.16

elastic parameters  $A_{ij}$  for model II are given in Eqs. (B.11)-(B.15). Vertical cross-sections of the slowness sheets, phase and group velocities, and polarisation vectors are given in Fig. B.3 for 8.41 km depth. Medium II is shows triclinic symmetry.

Density normalised elastic parameters for model II at 0.00 km depth (surface):

$$A_{ij} = \begin{pmatrix} 13.361 & 4.495 & 4.509 & 0.123 & 0.027 & 0.096 \\ & 13.883 & 4.646 & 0.041 & -0.055 & 0.096 \\ & & 13.991 & -0.096 & -0.069 & 0.014 \\ & & & 4.563 & 0.000 & 0.000 \\ & & & & 4.563 & 0.000 \\ & & & & & 4.563 \end{pmatrix} 10^6 \text{ m}^2 \text{ s}^{-2}. \quad (\text{B.11})$$

Density normalised elastic parameters for model II at 0.41 km depth:

$$A_{ij} = \begin{pmatrix} 28.145 & 8.722 & 8.750 & 0.260 & 0.058 & 0.202 \\ & 29.241 & 9.039 & 0.087 & -0.115 & 0.202 \\ & & 29.471 & -0.202 & -0.144 & 0.029 \\ & & & 9.986 & 0.000 & 0.000 \\ & & & & 9.986 & 0.000 \\ & & & & & 9.986 \end{pmatrix} 10^6 \text{ m}^2 \text{ s}^{-2}. \quad (\text{B.12})$$

Density normalised elastic parameters for model II at 2.46 km depth:

$$A_{ij} = \begin{pmatrix} 32.955 & 8.106 & 8.140 & 0.304 & 0.068 & 0.236 \\ & 34.238 & 8.478 & 0.101 & -0.135 & 0.236 \\ & & 34.508 & -0.236 & -0.169 & 0.034 \\ & & & 12.745 & 0.000 & 0.000 \\ & & & & 12.745 & 0.000 \\ & & & & & 12.745 \end{pmatrix} 10^6 \text{ m}^2 \text{ s}^{-2} \quad (\text{B.13})$$

Density normalised elastic parameters for model II at 8.41 km depth (see Fig. B.3):

$$A_{ij} = \begin{pmatrix} 36.344 & 11.419 & 11.456 & 0.335 & 0.075 & 0.261 \\ & 37.759 & 11.829 & 0.112 & -0.149 & 0.261 \\ & & 38.057 & -0.261 & -0.186 & 0.037 \\ & & & 12.816 & 0.000 & 0.000 \\ & & & & 12.816 & 0.000 \\ & & & & & 12.816 \end{pmatrix} 10^6 \text{ m}^2 \text{ s}^{-2} \quad (\text{B.14})$$

Density normalised elastic parameters for model II at 32.0 km depth:

$$A_{ij} = \begin{pmatrix} 50.751 & 17.179 & 17.231 & 0.468 & 0.104 & 0.364 \\ & 52.727 & 17.751 & 0.156 & -0.208 & 0.364 \\ & & 53.143 & -0.364 & -0.26 & 0.052 \\ & & & 17.280 & 0.000 & 0.000 \\ & & & & 17.280 & 0.000 \\ & & & & & 17.280 \end{pmatrix} 10^6 \text{ m}^2 \text{ s}^{-2} \quad (\text{B.15})$$

## B.5 Model III for West Bohemia

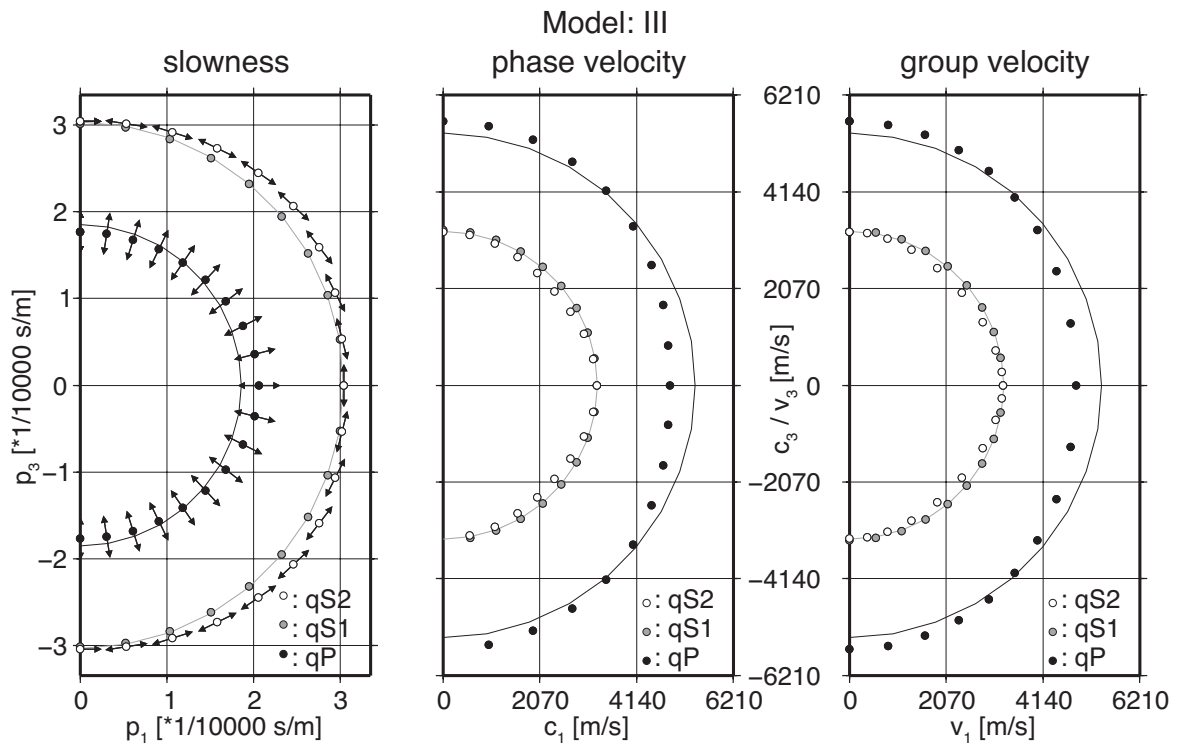


Figure B.4: Vertical sections in the  $x_1x_3$  plane of the slowness surfaces with polarisation vectors, phase velocities, and group velocities for model III. Note that the polarisation of the qS1 wave points perpendicular into this plane. Solid lines depict P- and S-wave quantities in the averaged isotropic reference medium  $v_p = \sqrt{(A_{11} + A_{22} + A_{33})/3}$ ,  $v_s = \sqrt{(A_{44} + A_{55} + A_{66})/3}$ .

Homogeneous anisotropic model used in Sections 2 (compare Tab. 3.1, medium M1), 3 (compare Tab. 3.1, medium M1), 4, and 5 (model III). This model was derived from shear-wave splitting times and S-P-wave travel-time differences for the Vogtland/West Bohemia by Vavryčuk (1993). The medium is transversely isotropic with about 6% anisotropy. In the crystallographic coordinate system the axis of symmetry of the elastic tensor points horizontally in the  $\mathbf{x}_1$ -direction (compare Fig. B.4). In situ strike direction of the symmetry axis in West Bohemia is approximately N31°E.

Density normalised elastic parameters for model III (compare Fig. B.4):

$$A_{ij} = \begin{pmatrix} 23.5 & 7.8 & 7.8 & 0.0 & 0.0 & 0.0 \\ & 31.9 & 9.9 & 0.0 & 0.0 & 0.0 \\ & & 31.9 & 0.0 & 0.0 & 0.0 \\ & & & 11.0 & 0.0 & 0.0 \\ & & & & 10.8 & 0.0 \\ & & & & & 10.8 \end{pmatrix} 10^6 \text{ m}^2 \text{ s}^{-2} \quad (\text{B.16})$$

## B.6 Anisotropy model at the KTB borehole

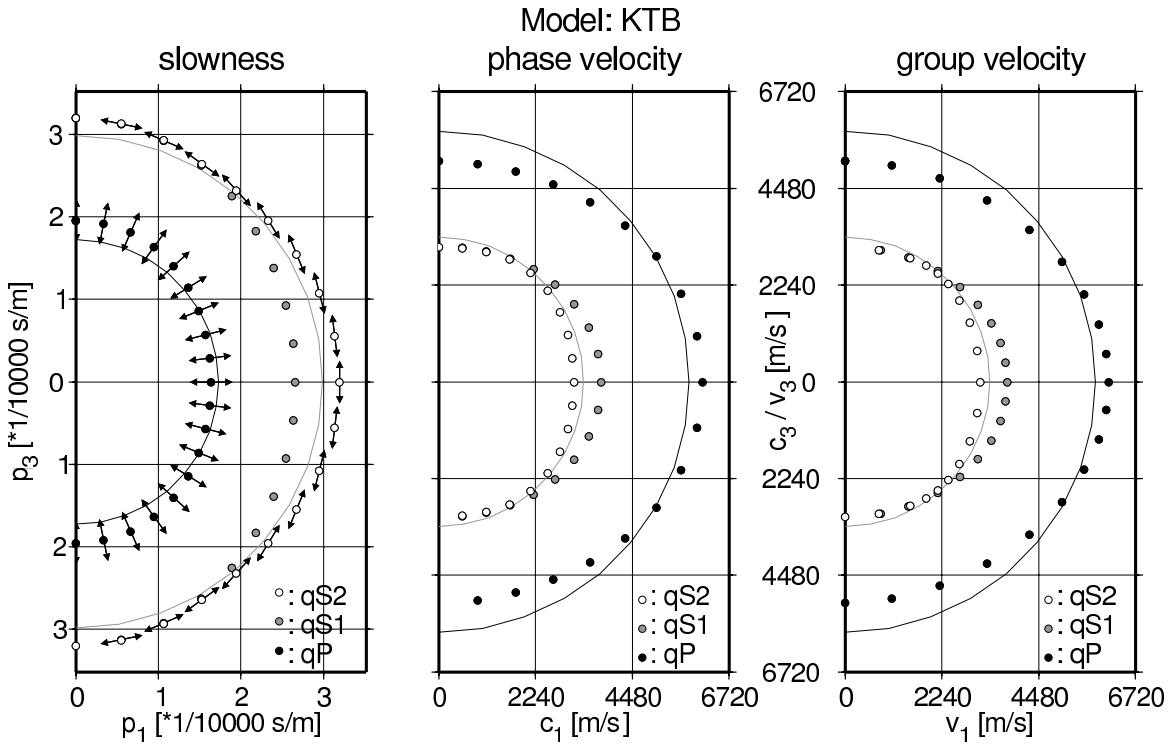


Figure B.5: Vertical sections in the  $x_1x_3$  plane of the slowness surfaces with polarisation vectors, phase velocities, and group velocities for the anisotropic model near the KTB borehole at depths of 7.9-8.2km. Note that the polarisation of the qS1 wave points perpendicular into this plane. Solid lines depict P- and S-wave quantities in the averaged isotropic reference medium  $v_p = \sqrt{(A_{11} + A_{22} + A_{33})/3}$ ,  $v_s = \sqrt{(A_{44} + A_{55} + A_{66})/3}$ .

Medium properties near the ICDP super-deep KTB borehole, FR Germany, at depths between 7.9 km and 8.2 km are described by a transversely isotropic model (Rabbel *et al.*, 2004). In the crystallographic coordinate system the elastic tensor has a vertical axis of symmetry (parallel to the  $x_3$  axis, see (B.17) and Fig. B.5). In situ orientation of the axis of symmetry at the KTB is strike  $\approx$  N60°E, plunge  $\approx$  45°. This model was used in Section 3.

Density normalised elastic parameters for the medium near the KTB borehole at

depth between 7.9 km and 8.2 km depth (compare Fig. B.5):

$$A_{ij} = \begin{pmatrix} 37.35 & 9.12 & 9.15 & 0.00 & 0.00 & 0.00 \\ & 37.35 & 9.15 & 0.00 & 0.00 & 0.00 \\ & & 26.15 & 0.00 & 0.00 & 0.00 \\ & & & 9.77 & 0.00 & 0.00 \\ & & & & 9.77 & 0.00 \\ & & & & & 14.12 \end{pmatrix} 10^6 \text{ m}^2 \text{ s}^{-2} \quad (\text{B.17})$$

## C Source retrieval in West Bohemia

The following Appendix provides Tables and Figures containing additional information on details of source retrieval in West Bohemia in Sections 4 and 5.

### C.1 Station information

Table C.1: List of permanent and temporary stations that were installed during the earthquake swarm 2000 in the Vogtland/W-Bohemia (compare Fig. 1.9). Note that stations with equal coordinates were renamed or operated by University of Potsdam or the GeoForschungsZentrum (GFZ) at different times. Corner frequencies of KRASNET stations are only approximately known. Tests on a shaking table have shown that they may vary significantly between different stations and also between single components (*Horálek, pers. comm.*).

station	latitude [° North]	longitude [° East]	height [m]	s.r. [Hz]	sensor	$T$ [s]	institution
BAC	50.0855	12.8396	570	62.5	TSJ10	10	SZGRF
BBRA	50.225	12.298	710	250	L-4C-3D	1	GFZ
BERN	50.2321	12.5117	646	125	WDS 200	< 0.5	KRASNET
BOH1	50.1866	12.7538	560	62.5	TSJ10	10	SZGRF
CAC	50.1814	12.4988	578	250	LE-3D	1	WEBNET
GUN	50.3635	12.3316	410	31.25	TSJ10	10	SZGRF
GRDH	50.240	12.253	750	250	L-4C-3D	1	GFZ
HRC	50.1926	12.5386	550	250	LE-3D	1	WEBNET
HOR	50.1834	12.4832	510	250	LE-3D	1	WEBNET
JIND	50.2621	12.6168	460	125	WDS 200	< 0.5	KRASNET
KAPB	50.188	12.300	720	250	L-4C-3D	1	GFZ
KLIN	50.3584	12.4616	640	31.25	L-4C-3D	1	SZGRF
KOC	50.2652	12.2335	575	250	SM-3	2	WEBNET
KRC	50.3316	12.5303	760	250	SM-3	2	WEBNET
KVE	50.2059	12.5151	550	250	LE-3D	1	WEBNET
LAC	50.0508	12.6250	838	250	SM-3	2	WEBNET
LDWT	50.270	12.331	800	250	L-4C-3D	1	GFZ
LBC	50.2656	12.4122	638	250	SM-3	1	WEBNET
LUBY	50.2602	12.3592	860	125	WDS 200	< 0.5	KRASNET
MANZ	49.9871	12.1095	553	250	STS-2	120	U. Munich
NALB	49.9812	12.4606	390	100	L-4C-3D	1	SZGRF
NKC	50.2331	12.4479	564	250	SM-3	2	WEBNET
OLV	50.2460	12.5650	950	250	LE-3D	1	WEBNET
P01G	50.240	12.253	750	250	LE-3D/5s	5	U. Potsdam
P02G	50.319	12.396	630	250	LE-3D/5s	5	U. Potsdam
P03G	50.270	12.331	800	250	LE-3D/5s	5	U. Potsdam
P04G	50.188	12.300	720	250	LE-3D/5s	5	U. Potsdam
P05G	50.235	12.312	800	250	LE-3D/5s	5	U. Potsdam
P06G	50.240	12.253	750	250	LE-3D/5s	5	U. Potsdam
P08G	50.225	12.298	710	250	LE-3D/5s	5	U. Potsdam
P09G	50.188	12.300	720	250	LE-3D/5s	5	U. Potsdam

continued on next page

continuation of Table C.1

P10G	50.225	12.298	710	250	LE-3D/5s	5	U. Potsdam
P11G	50.270	12.331	800	250	LE-3D/5s	5	U. Potsdam
P12G	50.411	12.472	480	250	LE-3D/5s	5	U. Potsdam
P13G	50.411	12.472	480	250	LE-3D/5s	5	U. Potsdam
POCA	50.3193	12.4346	750	125	WDS 200	< 0.5	KRASNET
ROTZ	49.7680	12.2080	505	250	STS-2	120	U. Munich
SBG	50.1817	12.3049	650	62.5	TSJ10	10	SZGRF
SELB	50.1542	12.1793	565	100	TSJ10	10	SZGRF
SKC	50.1698	12.3610	455	250	LE-3D	1	WEBNET
SNE	50.3107	12.5027	702	250	SM-3	2	WEBNET
STC	50.2591	12.5197	666	250	SM-3	2	WEBNET
TIS	50.3531	12.5086	650	250	LE-3D	1	WEBNET
TRC	50.3032	12.1445	566	250	LE-3D	1	WEBNET
VAC	50.2354	12.3771	535	250	SM-3	1	WEBNET
VACK	50.1414	12.4727	450	125	WDS 200	< 0.5	KRASNET
VIEL	50.1867	12.1044	602	250	STS-2	120	U. Munich
WERN	50.2874	12.3761	630	250	STS-2	120	U. Leipzig
WIGB	50.411	12.472	480	250	L-4C-3D	1	GFZ

latitude/longitude=geographic coordinates North/East, s.r.=sampling rate,  $T$ =period of the corner frequency  $\omega$  of the sensor:  $\omega = 2\pi/T$ , U.=University of

## C.2 Hypocentre parameters

Table C.2: Geographic coordinates of hypocentres, source depths and source times of the events for which source parameters are determined in this work. These events represent the largest swarm earthquakes that occurred between August 28, 2000 and October 30, 2000 in the Vogtland/West Bohemia. See Figures 1.9, 1.11 for location maps. Figure 1.12 shows their temporal distribution. Additionally, the confidence class (class) used for classification of retrieved parameters, the number of stations (stat.) and traces (trac.) used during inversion, and the station gap are given for each event. The station gap is the largest azimuthal distance between adjacent stations used during inversion of one event.

event no.	class	date <i>yyyymmdd</i>	time <i>hh:mm:ss</i>	latitude [° North]	longitude [° East]	depth [m]	stat.	trac.	gap [°]
1	1	20000829	12:13:15.67	50.2204	12.4469	10299	11	28	113
2	3	20000829	14:26:34.54	50.2192	12.4466	10264	4	11	127
3	1	20000901	08:37:53.10	50.2195	12.4470	10244	13	30	89
4	1	20000903	16:40:36.01	50.2201	12.4466	10002	11	26	120
5	1	20000903	17:11:03.19	50.2197	12.4468	10089	8	17	142
6	2	20000903	17:27:29.82	50.2177	12.4476	10087	10	24	120
7	2	20000903	18:23:50.88	50.2205	12.4465	9909	10	26	95
8	2	20000903	20:14:21.59	50.2201	12.4462	9960	10	24	120
9	1	20000903	22:07:54.18	50.2242	12.4465	9104	12	30	88
10	1	20000903	23:18:37.64	50.2285	12.4451	9250	11	27	89
11	1	20000903	23:38:12.45	50.2282	12.4449	9168	9	21	89
12	3	20000903	23:52:42.38	50.2271	12.4451	9048	6	14	86

continued on next page

continuation of Table C.2

13	2	20000903	23:58:38.36	50.2240	12.4469	9217	7	16	89
14	2	20000904	00:12:18.51	50.2275	12.4461	9202	9	21	90
15	1	20000904	00:16:35.17	50.2264	12.4458	9272	8	20	91
16	2	20000904	00:31:45.78	50.2264	12.4458	9214	9	21	91
17	1	20000904	01:18:06.14	50.2286	12.4460	9420	8	19	90
18	1	20000904	01:47:27.75	50.2216	12.4481	9312	9	23	90
19	1	20000904	01:51:43.66	50.2214	12.4473	9275	8	18	89
20	2	20000904	02:16:14.24	50.2282	12.4462	9516	9	22	87
21	1	20000904	16:18:12.58	50.2208	12.4482	9324	9	24	96
22	2	20000905	15:02:00.79	50.2288	12.4451	9408	8	21	140
23	2	20000905	15:03:34.71	50.2286	12.4451	9163	8	20	141
24	1	20000905	15:50:39.83	50.2286	12.4453	9350	13	32	89
25	1	20000908	09:14:01.05	50.2184	12.4477	9801	14	35	76
26	1	20000908	10:26:59.32	50.2211	12.4469	9677	13	33	74
27	2	20000908	10:27:08.58	50.2199	12.4474	9584	11	23	81
28	1	20000908	10:44:29.65	50.2192	12.4486	9416	12	27	75
29	1	20000908	11:36:08.52	50.2190	12.4472	10070	14	33	75
30	1	20000908	11:39:50.85	50.2202	12.4473	9947	14	32	74
31	1	20000908	12:00:15.34	50.2205	12.4472	10176	13	32	95
32	1	20000908	12:09:25.75	50.2203	12.4475	9723	11	27	96
33	1	20000908	13:41:15.68	50.2240	12.4472	9559	11	28	93
34	1	20000908	15:55:26.81	50.2216	12.4469	9766	12	29	95
35	1	20000908	17:21:07.59	50.2217	12.4463	9957	13	32	94
36	1	20000908	18:35:48.13	50.2214	12.4466	9902	13	32	95
37	2	20000910	17:03:19.44	50.2300	12.4450	9206	8	20	116
38	1	20000917	08:17:44.20	50.2226	12.4466	9616	14	34	94
39	3	20000917	08:31:34.22	50.2237	12.4470	9677	9	23	146
40	2	20000917	08:36:55.64	50.2206	12.4473	9847	11	24	127
41	3	20000917	08:57:17.61	50.2236	12.4472	9214	10	24	166
42	2	20000917	09:06:56.09	50.2232	12.4481	9326	8	22	146
43	3	20000917	09:37:21.00	50.2259	12.4464	8891	11	21	143
44	3	20000917	09:45:01.24	50.2190	12.4487	9005	16	32	97
45	1	20000917	09:45:51.51	50.2224	12.4485	8879	16	43	95
46	1	20000917	09:56:48.11	50.2253	12.4473	8820	12	30	93
47	1	20000917	09:59:05.41	50.2231	12.4471	9669	17	42	94
48	1	20000917	10:15:04.29	50.2209	12.4494	8698	13	32	96
49	1	20000917	10:33:56.95	50.2234	12.4481	8703	14	31	94
50	1	20000917	10:37:55.31	50.2261	12.4470	8833	15	29	92
51	2	20000917	11:00:32.58	50.2237	12.4482	8789	17	39	73
52	1	20000917	11:25:32.11	50.2259	12.4484	8431	16	41	93
53	1	20000917	12:53:19.20	50.2178	12.4507	8830	17	38	77
54	1	20000917	13:19:25.39	50.2238	12.4469	9739	18	42	93
55	1	20000917	14:52:33.29	50.2232	12.4488	8617	12	30	95
56	2	20000917	15:14:33.10	50.2249	12.4476	8803	15	35	120
57	1	20000917	16:12:24.33	50.2176	12.4499	9313	17	42	98

continued on next page

continuation of Table C.2

58	1	20000919	10:30:42.21	50.2232	12.4463	9835	14	35	93
59	1	20001015	16:36:47.82	50.2085	12.4576	9243	18	45	107
60	1	20001015	16:56:54.14	50.2065	12.4584	9356	18	44	68
61	1	20001015	18:20:21.30	50.2115	12.4549	8938	17	44	104
62	1	20001015	19:11:20.76	50.2128	12.4545	8668	19	48	104
63	2	20001015	19:15:05.77	50.2071	12.4586	9274	14	32	108
64	2	20001015	19:18:08.78	50.2067	12.4541	9029	15	37	161
65	1	20001015	19:24:14.34	50.2115	12.4557	8850	13	34	159
66	1	20001015	19:37:01.68	50.2059	12.4529	9172	14	37	161
67	2	20001015	19:58:51.33	50.2080	12.4535	9072	13	34	160
68	2	20001015	20:00:51.64	50.2109	12.4529	8743	10	27	158
69	2	20001015	20:01:43.22	50.2109	12.4518	8910	12	31	157
70	1	20001015	20:03:00.80	50.2115	12.4537	9044	13	34	158
71	2	20001015	20:14:47.29	50.2146	12.4531	8475	12	32	155
72	1	20001015	21:56:26.11	50.2122	12.4524	8846	12	32	157
73	2	20001016	08:52:18.22	50.2132	12.4555	8871	15	36	124
74	1	20001016	08:52:53.39	50.2154	12.4551	8938	15	38	124
75	1	20001016	09:46:39.37	50.2120	12.4557	8829	18	45	105
76	1	20001016	15:17:48.70	50.2111	12.4559	8856	19	48	105
77	1	20001016	15:39:13.81	50.2145	12.4566	8036	15	33	104
78	1	20001016	15:51:24.48	50.2124	12.4515	8366	15	38	102
79	2	20001016	16:02:59.69	50.2119	12.4578	8688	13	32	160
80	1	20001016	16:55:57.66	50.2132	12.4572	8075	17	44	105
81	1	20001016	17:56:10.93	50.2126	12.4579	8075	17	44	106
82	1	20001016	18:01:37.96	50.2118	12.4559	8184	16	42	105
83	2	20001016	18:01:47.24	50.2121	12.4598	8055	9	14	126
84	1	20001016	18:03:50.71	50.2106	12.4559	8423	17	43	105
85	3	20001016	18:03:57.83	50.2112	12.4550	8430	17	45	105
86	1	20001016	18:04:10.97	50.2139	12.4568	7942	15	27	104
87	2	20001016	19:57:08.44	50.2161	12.4536	8751	14	34	123
88	1	20001016	19:59:17.35	50.2152	12.4559	8606	18	46	103
89	1	20001017	09:09:44.36	50.2137	12.4543	8981	18	39	103
90	1	20001017	13:23:02.40	50.2127	12.4566	8126	17	44	124
91	1	20001017	14:05:19.45	50.2115	12.4573	8266	14	36	124
92	2	20001017	14:06:27.26	50.2170	12.4578	7813	16	36	125
93	1	20001017	14:22:31.99	50.2103	12.4558	8337	16	40	124
94	2	20001017	14:22:04.50	50.2099	12.4564	8286	17	39	124
95	1	20001017	14:26:14.17	50.2119	12.4571	8165	16	41	124
96	1	20001017	16:41:55.11	50.2104	12.4566	8301	15	37	124
97	1	20001017	22:45:32.53	50.2130	12.4546	8899	16	41	123
98	1	20001017	23:15:25.38	50.2194	12.4523	8829	19	47	99
99	1	20001023	21:22:01.71	50.2148	12.4512	8967	19	45	101
100	1	20001023	21:24:08.06	50.2096	12.4558	9153	19	40	106
101	2	20001023	21:24:38.82	50.2138	12.4549	8938	17	34	103
102	3	20001023	21:46:58.12	50.2185	12.4520	9028	20	51	99

continued on next page



continuation of Table C.2

103	3	20001024	01:35:41.21	50.2124	12.4542	9215	20	51	104
104	2	20001024	01:36:35.48	50.2132	12.4537	9161	15	36	157
105	1	20001024	03:19:55.31	50.2138	12.4542	8985	20	50	103
106	1	20001026	01:22:04.98	50.2138	12.4541	9087	13	31	103
107	1	20001026	01:35:52.76	50.2131	12.4540	9180	13	31	103
108	1	20001026	01:36:19.93	50.2144	12.4536	9419	14	29	102
109	1	20001026	18:48:21.32	50.2152	12.4515	9010	15	36	101
110	2	20001029	05:09:39.20	50.2195	12.4539	8446	13	31	85
111	3	20001029	05:10:46.87	50.2200	12.4539	8438	14	37	62
112	1	20001030	04:35:39.34	50.2360	12.4535	7665	14	31	87

stat.=number of stations, trac.=number of traces

### **C.3 Determined fault-plane solutions, principle stress axes, and matched polarities**

In this appendix fault-plane solutions and corresponding radiation patterns are given. They are retrieved for source in West Bohemia, see Tab. C.2, using the velocity models I-III, see Apps. B.4 and B.5. Note that conjugate fault planes can form any angle.

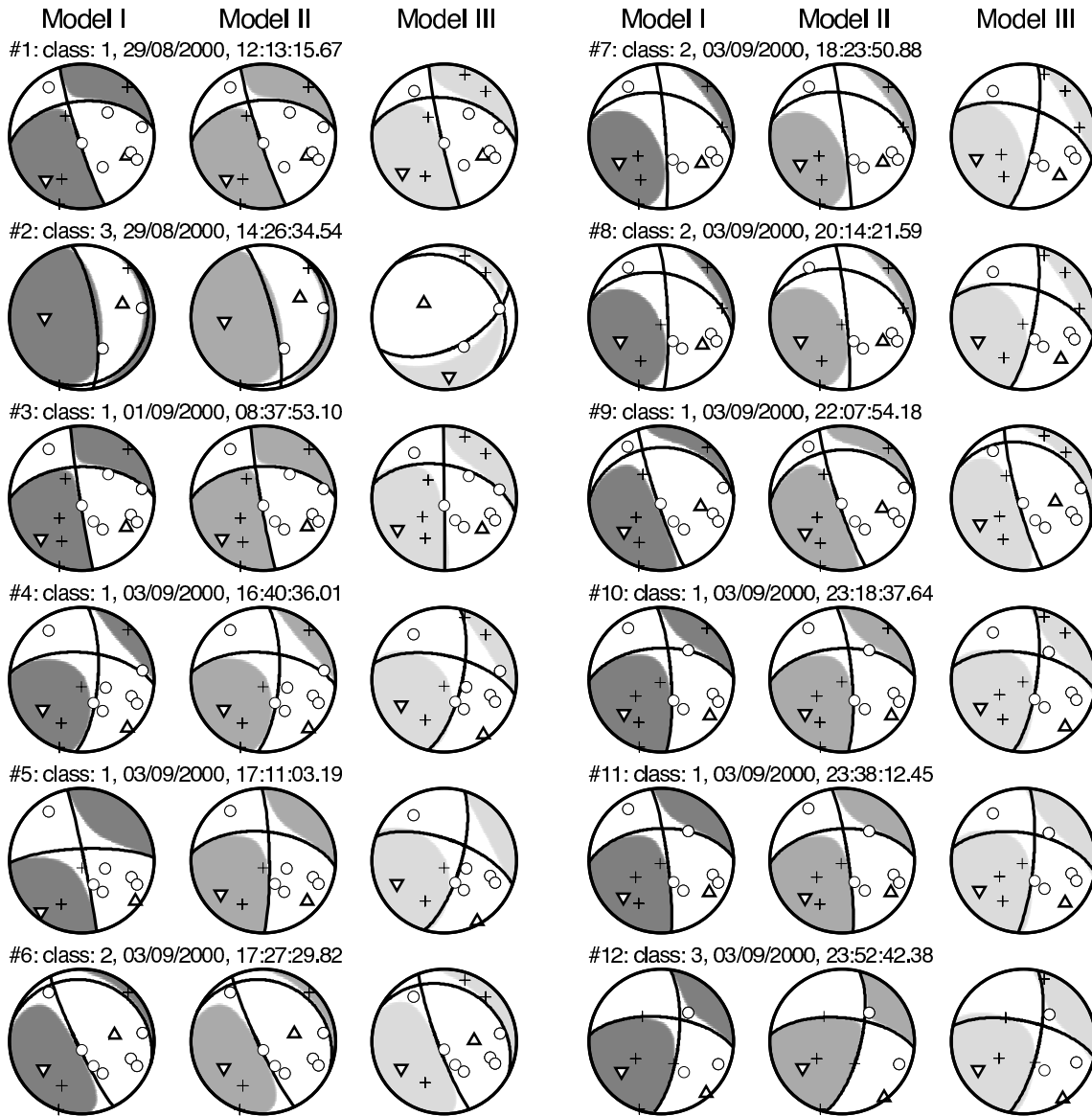


Figure C.1: Fault-plane solutions (FPS), P-wave radiation patterns (grey: compression, white: dilatation), and ray directions of P waves at the source (crosses/circles: observed first motion is up/down) determined for events 1-12 in Tab. C.2 using the velocity models I-III (lower hemisphere stereographic projection). The local stress field on the fault is illustrated by the directions of the P axes (triangles) and the T axis (inverted triangles). Depending on the used velocity model (I/II or III), different take-off directions arise for rays to station ROTZ: departure into the lower and upper hemisphere in the models I/II and in the model III, respectively. Projection of the corresponding ray: strike/plunge  $\approx 200^\circ/0^\circ$  (models I and II) and strike/plunge  $\approx 20^\circ/5^\circ$  (model III). Event numbers, confidence classes, and source times are given above the FPS. See Tabs. C.4, C.5 for details on source mechanisms, and C.2 station parameters.

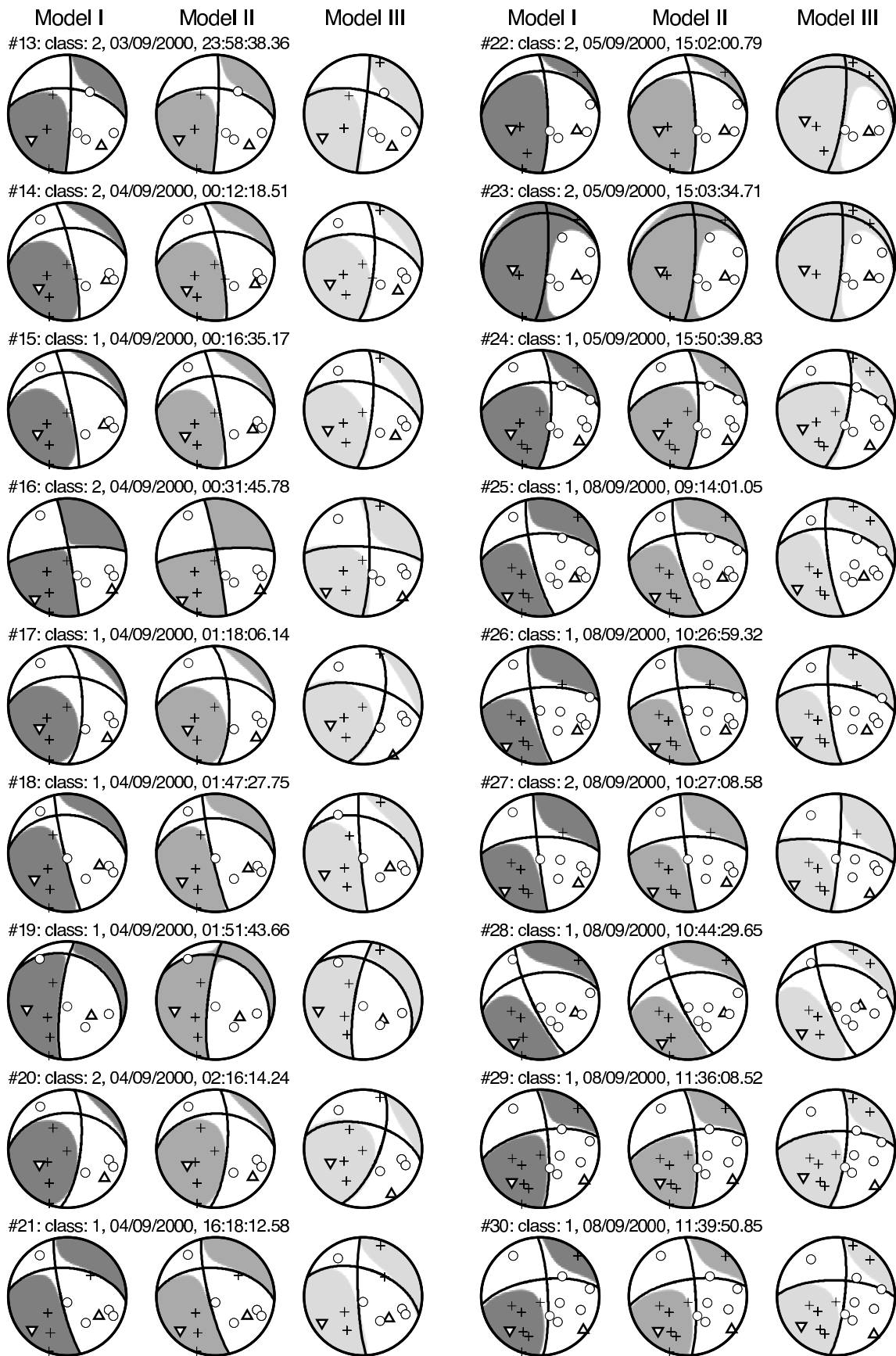


Figure C.2: As in Fig. C.1 but for events 13-30. Additional note to Figs. C.1-C.7:

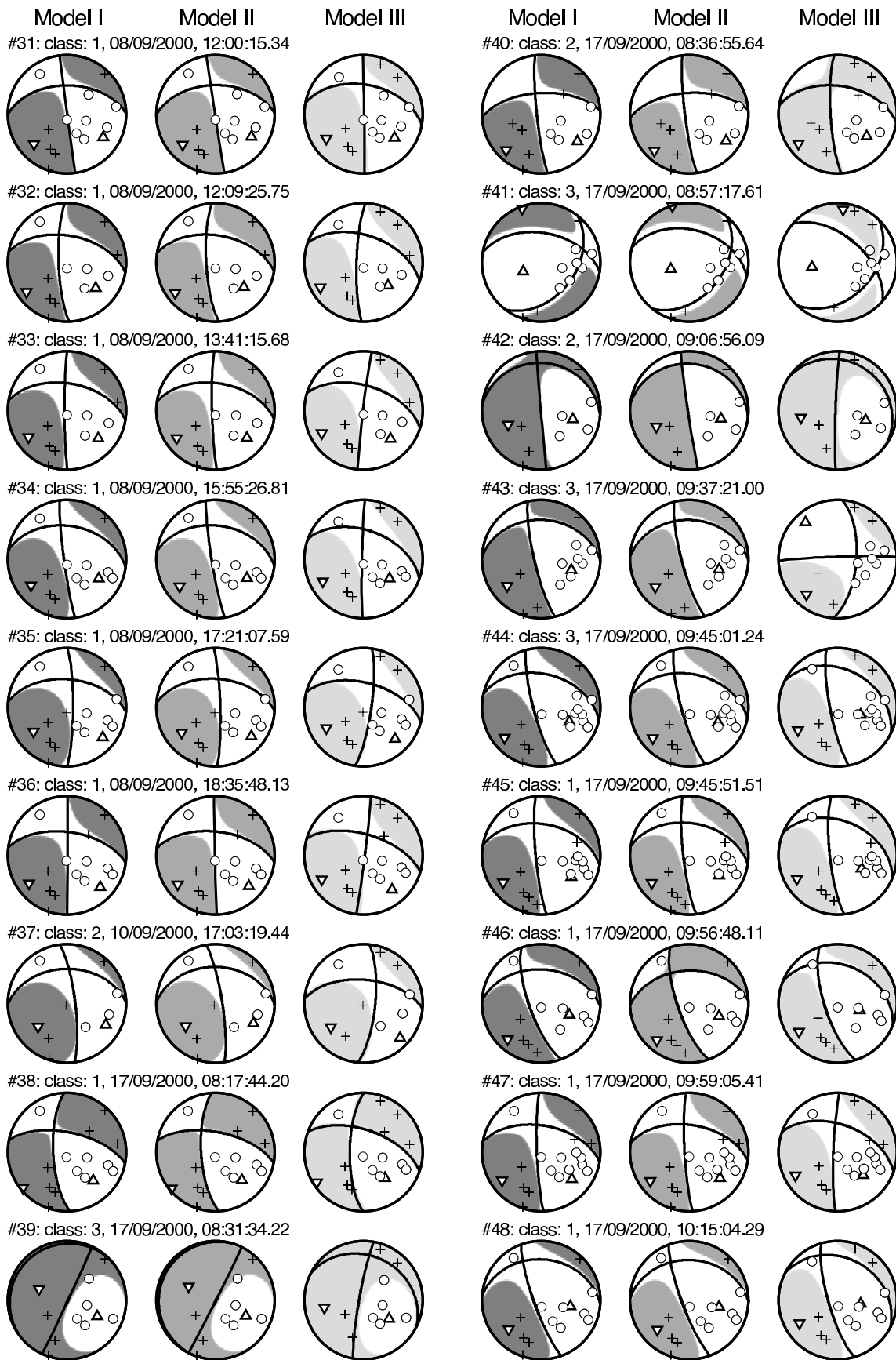


Figure C.3: As in Fig. C.1 but for events 31-48.

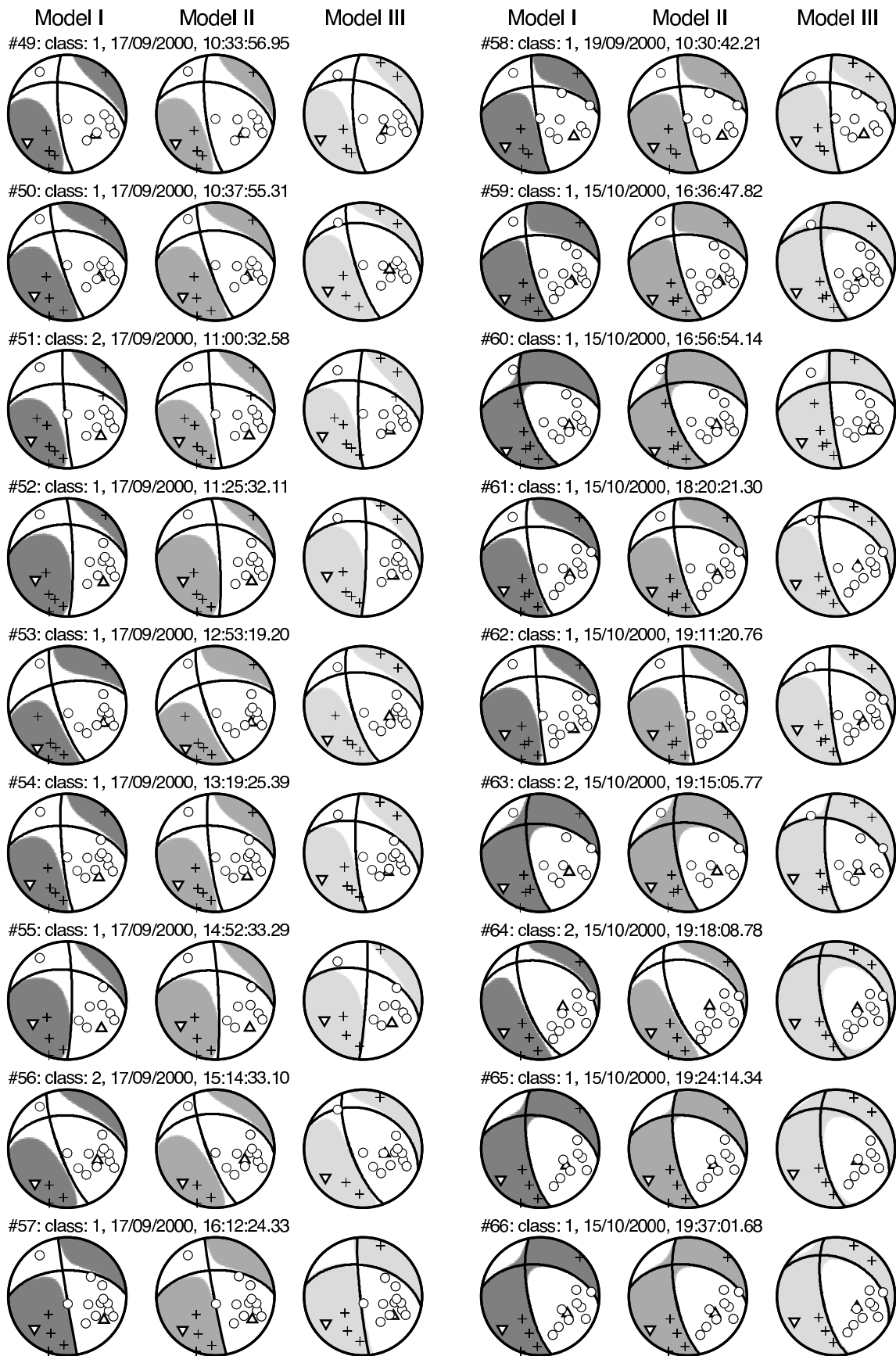


Figure C.4: As in Fig. C.1 but for events 49-66.

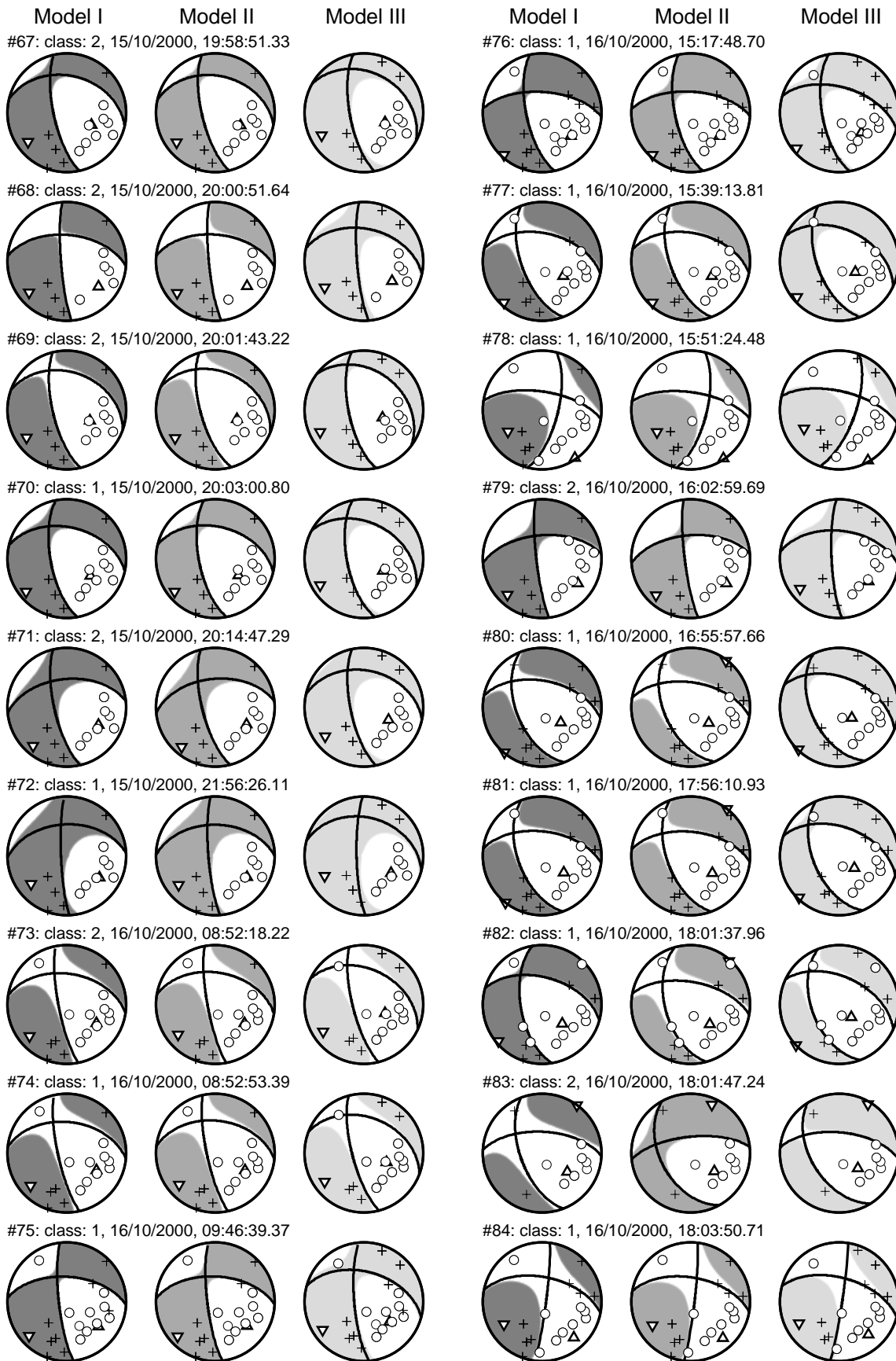


Figure C.5: As in Fig. C.1 but for events 67-84.

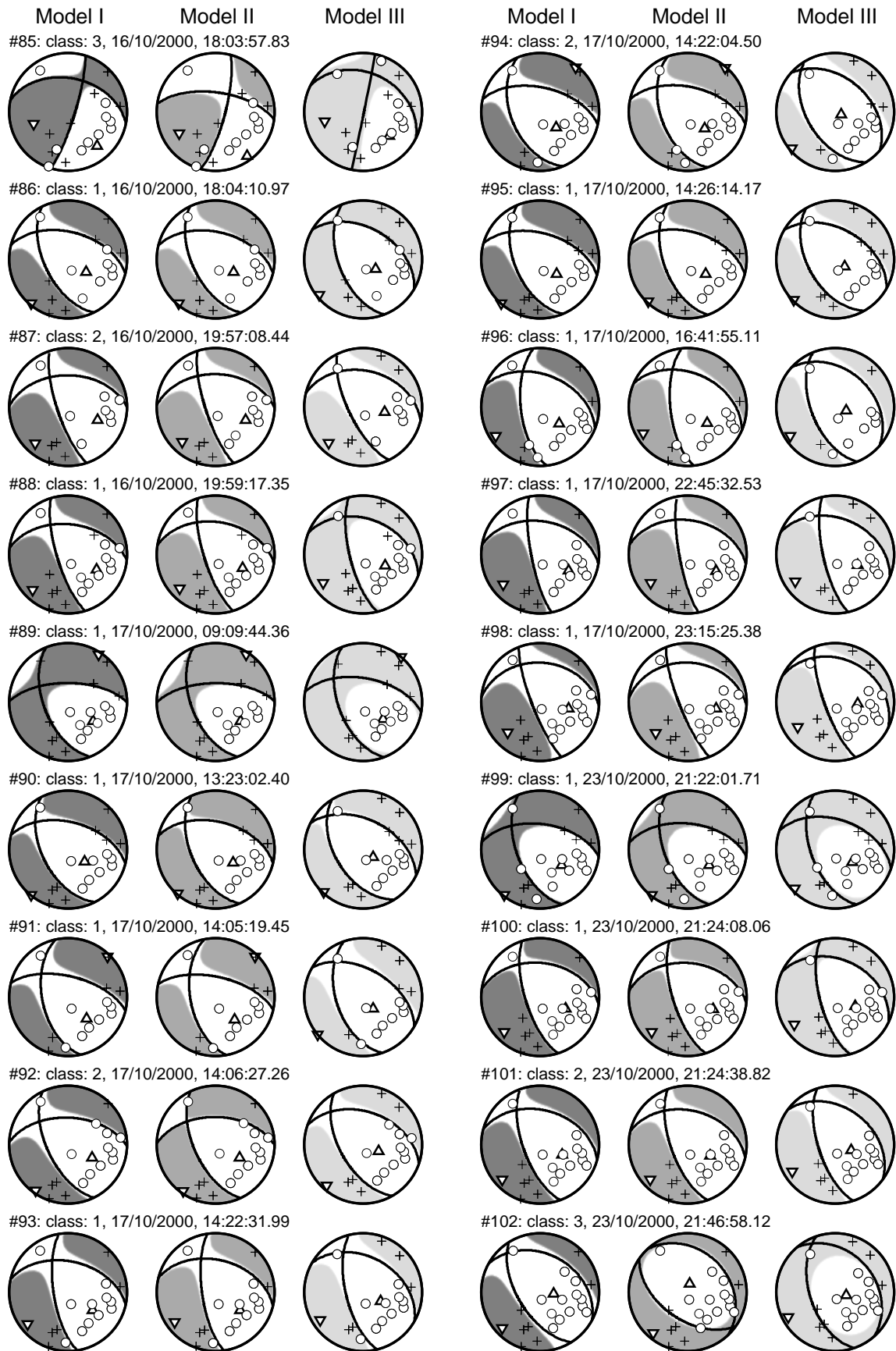


Figure C.6: As in Fig. C.1 but for events 86-102.



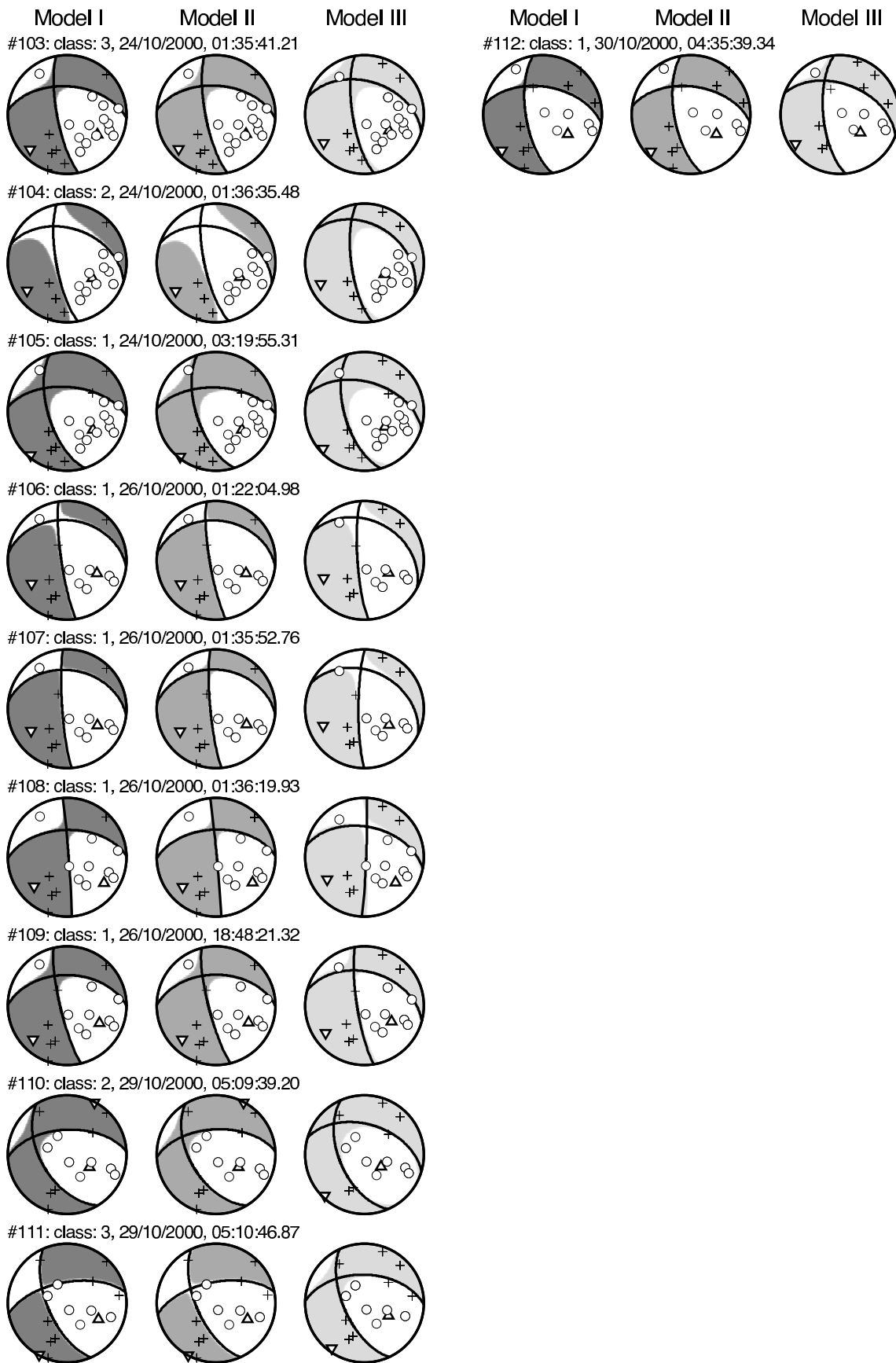


Figure C.7: As in Fig. C.1 but for events 103-112.

## C.4 Determined seismic moments, local magnitudes, and potencies

Table C.3: Seismic moment ( $M_T$ ), local magnitude ( $M_L$ ), and potency ( $sA_0$ ) determined for earthquakes in Tab. C.2 using the models I-III (compare Appendix B). The corresponding residuals, slip inclinations, source orientations, and moment-tensor components can be found in Tabs. C.4, C.5. Confidence classes are also given.

no.	class	Model I			Model II			Model III		
		$M_T$ [Nm]	$M_L$	$sA_s$ [m <sup>3</sup> ]	$M_T$ [Nm]	$M_L$	$sA_s$ [m <sup>3</sup> ]	$M_T$ [Nm]	$M_L$	$sA_s$ [m <sup>3</sup> ]
1	1	3.9e+13	2.2	2033	4.2e+13	2.2	2077	3.3e+13	2.1	2025
2	3	1.4e+17	5.6	6.3e06	2.1e+17	5.8	8.9e06	2.2e+17	5.8	1.1e07
3	1	1.8e+13	1.9	957	1.9e+13	1.9	953	1.6e+13	1.8	1022
4	1	4.9e+13	2.3	2510	5.3e+13	2.3	2559	4.4e+13	2.3	2815
5	1	1.0e+14	2.6	5289	1.1e+14	2.6	5383	1.0e+14	2.6	6643
6	2	2.3e+13	2.0	1238	2.8e+13	2.1	1652	1.9e+13	1.9	1137
7	2	4.7e+13	2.3	2301	5.0e+13	2.3	2273	4.4e+13	2.3	2693
8	2	3.9e+13	2.2	1900	4.3e+13	2.3	1952	3.2e+13	2.1	2008
9	1	5.7e+13	2.4	3081	6.0e+13	2.4	3057	5.3e+13	2.3	3314
10	1	3.9e+13	2.2	2067	4.2e+13	2.2	2051	3.5e+13	2.2	2289
11	1	4.3e+13	2.3	2274	4.6e+13	2.3	2265	3.9e+13	2.2	2481
12	3	4.3e+13	2.3	2318	4.8e+13	2.3	2428	4.3e+13	2.3	2805
13	2	2.4e+13	2.0	1287	2.5e+13	2.0	1253	2.4e+13	2.0	1549
14	2	2.9e+13	2.1	1487	3.1e+13	2.1	1498	2.6e+13	2.0	1587
15	1	5.1e+13	2.3	2593	5.4e+13	2.3	2607	4.7e+13	2.3	2860
16	2	4.2e+14	3.2	22390	4.6e+14	3.2	22920	3.6e+14	3.1	23830
17	1	1.7e+13	1.9	824	1.8e+13	1.9	834	1.5e+13	1.8	956
18	1	3.2e+13	2.1	1729	3.5e+13	2.2	1733	3.2e+13	2.1	1936
19	1	7.7e+13	2.5	4156	8.1e+13	2.5	4097	8.2e+13	2.5	5163
20	2	2.0e+13	1.9	1021	2.1e+13	2.0	1017	1.9e+13	1.9	1231
21	1	3.0e+13	2.1	1574	3.2e+13	2.1	1568	3.0e+13	2.1	1819
22	2	3.4e+13	2.2	1769	3.6e+13	2.2	1749	3.2e+13	2.1	1866
23	2	2.7e+13	2.1	1399	2.8e+13	2.1	1365	2.5e+13	2.0	1478
24	1	1.9e+13	1.9	1032	2.1e+13	2.0	1035	1.7e+13	1.9	1121
25	1	9.1e+13	2.6	4885	9.9e+13	2.6	4965	8.5e+13	2.5	5408
26	1	3.2e+13	2.1	1726	3.5e+13	2.2	1732	2.9e+13	2.1	1879
27	2	2.2e+13	2.0	1194	2.4e+13	2.0	1192	2.3e+13	2.0	1551
28	1	1.9e+13	1.9	1007	2.0e+13	1.9	1026	1.7e+13	1.9	1032
29	1	5.1e+13	2.3	2739	5.5e+13	2.4	2756	4.3e+13	2.3	2991
30	1	4.3e+14	3.2	22630	4.6e+14	3.2	22730	3.6e+14	3.1	25110
31	1	9.2e+13	2.6	4873	9.9e+13	2.6	4883	8.5e+13	2.5	5393
32	1	2.3e+13	2.0	1226	2.4e+13	2.0	1223	2.2e+13	2.0	1429
33	1	3.3e+13	2.1	1776	3.6e+13	2.2	1775	3.3e+13	2.1	2090
34	1	1.8e+13	1.9	959	1.9e+13	1.9	959	1.9e+13	1.9	1157
35	1	3.8e+13	2.2	1978	4.1e+13	2.2	1971	3.6e+13	2.2	2277
36	1	1.3e+14	2.7	6779	1.4e+14	2.7	6702	1.3e+14	2.7	8232

continued on next page

continuation of Table C.3

37	2	2.2e+13	2.0	1116	2.5e+13	2.0	1156	1.8e+13	1.9	1137
38	1	3.2e+13	2.1	1694	3.3e+13	2.1	1669	3.1e+13	2.1	1972
39	3	9.3e+13	2.6	4552	1.0e+14	2.6	4601	8.5e+13	2.5	5007
40	2	3.9e+13	2.2	2066	4.1e+13	2.2	2066	3.3e+13	2.1	2174
41	3	4.4e+13	2.3	2153	4.9e+13	2.3	2101	6.5e+13	2.4	3382
42	2	1.1e+14	2.6	5728	1.1e+14	2.6	5744	1.1e+14	2.6	6633
43	3	2.4e+13	2.0	1316	2.6e+13	2.0	1337	4.6e+13	2.3	3080
44	3	4.6e+13	2.3	2397	4.9e+13	2.3	2418	4.7e+13	2.3	2897
45	1	3.6e+13	2.2	1916	3.8e+13	2.2	1901	3.4e+13	2.2	2100
46	1	4.6e+13	2.3	2486	4.8e+13	2.3	2485	4.4e+13	2.3	2772
47	1	1.5e+13	1.8	800	1.6e+13	1.8	801	1.5e+13	1.8	921
48	1	5.6e+13	2.4	2993	6.0e+13	2.4	3028	5.5e+13	2.4	3419
49	1	2.5e+13	2.0	1320	2.7e+13	2.1	1313	2.5e+13	2.0	1609
50	1	1.7e+13	1.9	907	1.8e+13	1.9	913	1.6e+13	1.8	998
51	2	4.4e+13	2.3	2274	4.8e+13	2.3	2318	4.4e+13	2.3	2761
52	1	3.2e+13	2.1	1701	3.5e+13	2.2	1716	3.0e+13	2.1	1849
53	1	3.2e+13	2.1	1737	3.5e+13	2.2	1777	2.9e+13	2.1	1822
54	1	1.7e+13	1.9	924	1.9e+13	1.9	932	1.7e+13	1.9	1056
55	1	9.6e+13	2.6	5079	1.1e+14	2.6	5191	9.5e+13	2.6	5794
56	2	2.4e+14	3.0	12500	2.6e+14	3.0	12990	2.2e+14	2.9	13820
57	1	2.6e+13	2.0	1393	2.8e+13	2.1	1393	2.3e+13	2.0	1463
58	1	2.0e+13	1.9	1061	2.1e+13	2.0	1058	1.9e+13	1.9	1173
59	1	3.3e+14	3.1	17960	3.6e+14	3.1	18040	3.1e+14	3.1	19700
60	1	3.3e+13	2.1	1783	3.5e+13	2.2	1795	2.3e+13	2.0	1526
61	1	2.8e+13	2.1	1487	3.0e+13	2.1	1501	2.5e+13	2.0	1603
62	1	1.7e+14	2.8	9117	1.8e+14	2.8	9109	1.6e+14	2.8	9860
63	2	3.3e+13	2.1	1808	3.5e+13	2.2	1784	3.4e+13	2.2	2130
64	2	1.0e+14	2.6	5398	1.1e+14	2.6	5502	9.9e+13	2.6	6148
65	1	2.5e+14	3.0	13420	2.7e+14	3.0	13600	2.4e+14	3.0	15160
66	1	4.8e+13	2.3	2615	5.2e+13	2.3	2619	4.6e+13	2.3	2884
67	2	1.2e+14	2.7	6625	1.3e+14	2.7	6703	1.2e+14	2.7	7621
68	2	9.8e+13	2.6	5316	1.1e+14	2.6	5394	8.1e+13	2.5	5118
69	2	7.5e+13	2.5	4059	8.2e+13	2.5	4189	7.8e+13	2.5	4918
70	1	1.6e+14	2.8	8552	1.7e+14	2.8	8666	1.6e+14	2.8	9856
71	2	2.7e+13	2.1	1459	3.0e+13	2.1	1497	2.6e+13	2.0	1615
72	1	3.0e+13	2.1	1547	3.2e+13	2.1	1593	2.8e+13	2.1	1685
73	2	3.1e+13	2.1	1642	3.4e+13	2.2	1691	3.0e+13	2.1	1817
74	1	4.4e+13	2.3	2343	4.8e+13	2.3	2400	4.0e+13	2.2	2530
75	1	1.4e+14	2.7	7639	1.5e+14	2.8	7642	1.3e+14	2.7	8340
76	1	3.4e+13	2.2	1833	3.6e+13	2.2	1822	3.2e+13	2.1	1997
77	1	2.6e+13	2.0	1394	2.8e+13	2.1	1405	2.6e+13	2.0	1610
78	1	2.7e+13	2.1	1460	2.9e+13	2.1	1437	2.2e+13	2.0	1476
79	2	8.3e+13	2.5	4513	8.9e+13	2.6	4523	8.0e+13	2.5	5256
80	1	2.9e+13	2.1	1609	3.0e+13	2.1	1537	2.8e+13	2.1	1763
81	1	8.2e+13	2.5	4477	8.7e+13	2.5	4435	7.4e+13	2.5	4754

continued on next page

continuation of Table C.3

82	1	3.6e+13	2.2	1959	3.5e+13	2.2	1763	3.1e+13	2.1	1995
83	2	8.9e+12	1.6	472	1.0e+13	1.6	532	9.8e+12	1.6	623
84	1	3.8e+13	2.2	2013	4.0e+13	2.2	2015	3.3e+13	2.1	2138
85	3	1.5e+13	1.8	832	1.9e+13	1.9	960	1.5e+13	1.8	902
86	1	1.3e+13	1.8	696	1.4e+13	1.8	688	1.2e+13	1.7	789
87	2	2.7e+13	2.1	1479	3.0e+13	2.1	1532	2.4e+13	2.0	1481
88	1	2.1e+13	2.0	1137	2.1e+13	2.0	1081	2.0e+13	1.9	1270
89	1	1.4e+13	1.8	779	1.5e+13	1.8	774	1.4e+13	1.8	869
90	1	6.3e+13	2.4	3425	6.8e+13	2.4	3453	6.0e+13	2.4	3849
91	1	6.5e+13	2.4	3538	7.0e+13	2.5	3516	6.2e+13	2.4	3875
92	2	1.3e+13	1.8	683	1.4e+13	1.8	698	1.2e+13	1.7	748
93	1	2.0e+13	1.9	1093	2.2e+13	2.0	1133	1.9e+13	1.9	1232
94	2	1.5e+13	1.8	840	1.7e+13	1.9	841	1.5e+13	1.8	965
95	1	7.6e+13	2.5	4157	8.0e+13	2.5	4082	7.3e+13	2.5	4609
96	1	7.6e+13	2.5	4119	8.4e+13	2.5	4280	7.3e+13	2.5	4638
97	1	7.5e+13	2.5	4050	8.2e+13	2.5	4163	6.9e+13	2.4	4368
98	1	6.3e+13	2.4	3348	6.7e+13	2.4	3382	6.0e+13	2.4	3770
99	1	3.9e+14	3.2	20850	4.1e+14	3.2	20640	3.2e+14	3.1	19500
100	1	1.5e+13	1.8	797	1.6e+13	1.8	800	1.5e+13	1.8	948
101	2	1.3e+13	1.8	683	1.3e+13	1.8	680	1.4e+13	1.8	876
102	3	5.4e+13	2.3	2864	4.6e+13	2.3	2277	5.6e+13	2.4	3392
103	3	6.0e+13	2.4	3259	6.5e+13	2.4	3268	5.7e+13	2.4	3544
104	2	4.3e+13	2.3	2292	4.7e+13	2.3	2316	4.3e+13	2.3	2683
105	1	6.3e+13	2.4	3387	6.7e+13	2.4	3372	6.0e+13	2.4	3726
106	1	1.7e+13	1.9	942	1.9e+13	1.9	947	1.8e+13	1.9	1139
107	1	6.1e+13	2.4	3323	6.5e+13	2.4	3328	6.4e+13	2.4	4063
108	1	2.6e+13	2.0	1376	2.7e+13	2.1	1362	2.4e+13	2.0	1503
109	1	2.8e+13	2.1	1505	3.0e+13	2.1	1510	2.7e+13	2.1	1677
110	2	2.3e+13	2.0	1239	2.4e+13	2.0	1242	2.2e+13	2.0	1405
111	3	1.9e+14	2.9	10440	2.1e+14	2.9	10530	1.7e+14	2.8	10770
112	1	2.3e+13	2.0	1245	2.4e+13	2.0	1239	2.3e+13	2.0	1497

## C.5 Determined slip inclinations and rupture planes

Table C.4: Source parameters determined for events in Tab. C.2 using the velocity models I-III (see appendices B and C.7 for model parameters and results of Bootstrap tests): event number, confidence class, residual, slip inclination  $\delta$ , and orientation of the rupture plane given by strike  $\Phi_1^s$ , dip  $\delta_1^s$ , and rake  $\lambda_1^s$ . Mean residual values are also given. Standard deviations of the slip inclinations  $\sigma(\delta)$  obtained from bootstrap testing are given in brackets. Event sizes and moment-tensor components are given in Tabs. C.3 and C.5. For standard deviations of  $\Phi_1^s$ ,  $\delta_1^s$ ,  $\lambda_1^s$ , and moment-tensor components see Table C.6.

no.	class	Model I					Model II					Model III				
		res.	$\delta$ [°]	$\Phi_1^s$ [°]	$\delta_1^s$ [°]	$\lambda_1^s$ [°]	res.	$\delta$ [°]	$\Phi_1^s$ [°]	$\delta_1^s$ [°]	$\lambda_1^s$ [°]	res.	$\delta$ [°]	$\Phi_1^s$ [°]	$\delta_1^s$ [°]	$\lambda_1^s$ [°]
mean		0.07					0.07					0.08				
1	1	0.07	83.4 (1.7)	162.0	85.4	-40.6	0.07	83.0 (1.6)	161.7	85.5	-42.2	0.09	79.0 (1.1)	167.7	86.4	-45.7
2	3	0.07	66.2 (13.6)	351.6	74.8	98.1	0.07	69.1 (5.9)	346.0	78.4	99.2	0.08	116.6 (13.3)	317.7	23.2	-62.2
3	1	0.08	84.8 (1.3)	171.1	87.5	-36.2	0.08	84.7 (1.2)	170.2	87.0	-36.8	0.09	80.4 (1.3)	359.5	89.8	38.4
4	1	0.08	81.0 (1.5)	4.4	72.2	31.8	0.08	80.5 (1.6)	4.2	72.1	31.8	0.10	81.2 (1.7)	12.6	69.8	28.3
5	1	0.11	80.2 (1.5)	348.4	87.7	13.4	0.10	81.2 (1.6)	359.1	82.9	33.1	0.13	79.5 (0.4)	16.0	71.0	25.4
6	2	0.07	84.4 (0.5)	154.2	84.1	-78.1	0.09	82.8 (0.3)	154.6	84.2	-78.6	0.10	79.0 (0.3)	159.6	82.7	-73.4
7	2	0.06	75.8 (0.6)	355.9	85.5	50.1	0.07	76.3 (0.7)	353.0	87.7	51.3	0.08	76.8 (1.7)	11.3	77.2	33.2
8	2	0.07	75.5 (0.9)	357.9	82.9	51.8	0.07	75.1 (0.7)	354.5	85.4	56.4	0.10	79.0 (2.0)	10.5	77.6	34.6
9	1	0.07	86.0 (1.0)	161.4	84.7	-60.7	0.07	86.1 (1.0)	161.3	84.4	-57.7	0.08	80.4 (0.7)	164.6	83.4	-69.4
10	1	0.07	81.4 (0.9)	356.2	79.0	36.3	0.07	81.5 (0.9)	355.4	79.2	35.8	0.08	81.5 (0.9)	8.1	75.0	30.9
11	1	0.07	81.1 (0.7)	352.3	83.2	36.8	0.07	81.2 (0.7)	351.6	83.4	36.6	0.09	80.1 (0.9)	4.8	78.7	31.8
12	3	0.09	82.5 (1.2)	6.8	70.8	29.2	0.10	87.8 (1.3)	13.6	69.5	28.6	0.08	82.6 (0.1)	11.6	72.4	23.8
13	2	0.09	84.7 (0.6)	2.3	85.8	35.2	0.09	85.4 (0.4)	2.4	86.2	35.8	0.10	81.0 (0.3)	6.8	87.4	31.8
14	2	0.07	78.7 (0.8)	348.6	82.0	47.9	0.08	79.8 (1.0)	349.3	81.9	42.2	0.08	76.0 (0.9)	4.1	74.4	37.8
15	1	0.08	78.4 (0.7)	348.6	84.8	53.2	0.07	79.3 (0.8)	349.7	84.2	47.6	0.09	76.1 (1.0)	5.7	77.2	38.2
16	2	0.11	84.4 (0.8)	349.7	86.5	13.2	0.11	84.7 (0.9)	349.3	87.0	11.0	0.11	84.9 (1.1)	0.7	81.0	14.9

continued on next page

continuation of Table C.4

17	1	0.08	75.9 (0.9)	359.4	69.3	41.7	0.09	77.9 (1.1)	357.7	70.7	39.1	0.09	79.1 (1.3)	14.8	63.0	29.9
18	1	0.08	84.1 (0.8)	167.1	85.5	-55.1	0.08	84.2 (0.8)	167.4	85.1	-49.9	0.09	77.3 (0.5)	175.7	86.4	-52.5
19	1	0.08	89.1 (0.3)	186.6	80.3	-67.1	0.08	90.0 (0.4)	186.4	79.9	-65.2	0.10	83.0 (0.4)	189.1	78.4	-58.1
20	2	0.08	80.3 (1.0)	6.5	71.8	51.8	0.08	81.7 (1.1)	4.9	73.4	50.8	0.09	83.9 (1.5)	21.3	67.2	37.6
21	1	0.07	82.1 (0.9)	167.1	80.9	-41.5	0.07	82.4 (0.8)	166.3	80.9	-41.4	0.09	77.7 (0.7)	177.2	83.1	-40.3
22	2	0.08	80.6 (1.9)	358.5	79.8	61.9	0.08	80.3 (1.9)	356.4	80.6	59.9	0.09	79.0 (0.7)	8.4	79.6	68.5
23	2	0.08	87.6 (1.1)	4.9	80.3	71.6	0.08	87.7 (0.9)	3.6	80.6	68.9	0.07	81.6 (0.5)	5.0	82.3	69.2
24	1	0.07	83.6 (1.0)	1.8	75.0	39.0	0.07	83.4 (1.1)	0.4	75.5	38.5	0.07	83.0 (1.5)	11.1	73.2	37.5
25	1	0.07	86.9 (1.8)	166.2	79.5	-34.0	0.07	86.2 (1.7)	164.9	79.3	-34.2	0.08	82.5 (1.1)	172.0	79.2	-40.6
26	1	0.07	87.0 (1.5)	168.4	80.6	-24.8	0.07	87.2 (1.5)	167.8	80.8	-24.9	0.08	83.8 (1.3)	174.6	81.0	-28.5
27	2	0.11	85.6 (1.8)	173.1	87.3	-22.4	0.11	85.6 (1.8)	172.2	87.3	-22.5	0.11	83.6 (2.4)	4.8	85.8	15.0
28	1	0.08	85.2 (0.9)	154.6	78.9	-40.3	0.08	85.3 (1.1)	154.3	79.2	-39.4	0.09	79.5 (1.3)	159.6	78.5	-54.2
29	1	0.08	91.7 (1.5)	356.6	78.6	25.4	0.08	91.9 (1.5)	355.8	78.5	24.6	0.09	91.2 (2.0)	6.3	75.9	24.8
30	1	0.10	91.0 (1.2)	357.4	79.7	23.5	0.09	91.3 (1.2)	356.7	79.7	23.5	0.10	90.2 (1.7)	6.1	77.8	22.7
31	1	0.07	84.2 (1.2)	352.5	89.9	40.2	0.07	84.3 (1.1)	171.2	89.6	-40.6	0.08	80.9 (1.0)	359.3	89.1	41.7
32	1	0.08	87.6 (0.8)	177.9	78.2	-38.5	0.08	88.3 (0.8)	176.7	77.5	-39.0	0.09	82.6 (0.8)	181.8	80.5	-39.2
33	1	0.07	84.5 (0.8)	179.9	86.4	-38.4	0.06	85.2 (0.7)	178.6	85.5	-38.8	0.08	81.3 (0.5)	186.1	89.3	-35.1
34	1	0.07	82.3 (1.2)	172.5	85.6	-47.5	0.06	83.2 (1.1)	170.9	84.8	-48.0	0.08	77.3 (0.7)	181.2	87.9	-41.3
35	1	0.07	81.1 (1.1)	0.2	81.8	39.1	0.06	81.6 (1.0)	358.3	83.1	39.7	0.07	78.7 (1.1)	8.1	79.2	34.6
36	1	0.07	83.3 (1.0)	0.2	89.6	32.7	0.07	83.7 (1.0)	178.6	89.4	-33.2	0.08	81.0 (0.7)	7.1	88.2	29.5
37	2	0.09	77.4 (1.1)	353.0	78.9	49.7	0.08	76.5 (0.9)	351.3	80.4	52.7	0.11	82.0 (0.7)	5.7	73.8	34.2
38	1	0.06	86.7 (1.0)	177.3	70.7	-29.1	0.06	87.1 (1.0)	176.6	70.4	-29.6	0.07	84.4 (1.2)	180.6	71.1	-33.1
39	3	0.07	94.3 (1.2)	25.0	88.9	87.0	0.07	94.4 (1.3)	26.7	89.1	90.6	0.08	88.2 (1.7)	190.1	84.0	-65.1
40	2	0.08	90.3 (1.4)	174.0	83.9	-29.4	0.08	89.7 (1.6)	172.9	83.8	-29.5	0.09	87.4 (1.1)	176.6	80.3	-40.4
41	3	0.09	105.1 (10.2)	37.5	41.7	-123.9	0.09	109.5 (9.9)	38.6	42.6	-121.0	0.09	115.1 (4.2)	44.2	39.2	-130.9
42	2	0.07	86.6 (1.7)	175.0	89.3	-69.7	0.07	86.1 (1.5)	171.7	87.8	-68.7	0.08	83.9 (0.9)	181.9	87.0	-75.5
43	3	0.06	89.3 (5.1)	166.8	80.3	-56.9	0.06	89.2 (4.8)	165.1	79.1	-57.0	0.07	94.2 (2.2)	4.2	64.0	3.3
44	3	0.09	79.8 (1.8)	165.1	79.1	-50.7	0.09	80.3 (1.6)	164.5	78.8	-50.3	0.10	78.6 (1.7)	169.1	79.5	-60.4

continued on next page

continuation of Table C.4

45	1	0.06	84.7 (1.2)	174.7	82.3	-45.2	0.06	85.1 (1.2)	173.4	81.5	-46.7	0.07	80.3 (0.9)	173.7	79.3	-53.0
46	1	0.06	87.9 (1.3)	160.3	73.5	-51.6	0.07	90.3 (1.4)	160.9	73.7	-48.9	0.07	84.8 (1.2)	162.2	72.1	-63.1
47	1	0.05	84.1 (1.1)	177.8	83.9	-37.4	0.05	84.4 (1.0)	176.8	83.3	-38.2	0.07	80.1 (1.1)	182.1	84.1	-39.7
48	1	0.06	86.4 (0.6)	160.1	79.8	-60.9	0.06	87.2 (0.6)	159.6	79.4	-59.6	0.07	82.5 (0.4)	163.8	77.3	-68.6
49	1	0.06	84.4 (0.9)	174.0	77.7	-44.4	0.06	85.2 (0.8)	172.6	76.9	-45.7	0.08	83.5 (1.7)	176.8	76.1	-46.7
50	1	0.06	82.4 (1.3)	163.2	81.2	-45.2	0.06	83.1 (1.3)	161.9	80.4	-45.7	0.08	83.5 (2.1)	163.2	78.7	-57.9
51	2	0.06	84.2 (1.3)	175.2	86.4	-35.8	0.07	83.5 (1.3)	173.6	86.5	-35.6	0.07	82.0 (1.1)	179.5	83.3	-38.9
52	1	0.06	82.5 (1.7)	358.8	82.7	46.4	0.07	81.9 (1.9)	356.3	83.8	46.2	0.07	78.0 (1.2)	1.3	85.8	50.1
53	1	0.06	90.3 (1.5)	162.2	76.8	-33.3	0.07	89.2 (1.6)	160.8	77.0	-33.7	0.07	85.7 (1.9)	164.1	74.6	-48.9
54	1	0.06	85.0 (1.3)	174.5	82.9	-38.0	0.07	84.7 (1.3)	172.9	82.5	-38.5	0.07	80.8 (1.0)	176.5	80.1	-43.8
55	1	0.07	80.3 (1.1)	0.5	83.9	43.6	0.08	80.3 (1.3)	357.8	85.3	42.3	0.07	76.7 (0.5)	4.1	86.0	43.6
56	2	0.06	82.5 (1.9)	159.3	78.6	-49.8	0.06	82.4 (1.9)	159.0	78.8	-52.1	0.07	82.8 (1.1)	159.7	73.1	-64.2
57	1	0.06	83.8 (1.0)	170.9	88.9	-36.4	0.06	84.1 (0.8)	169.5	88.2	-36.8	0.07	81.1 (0.9)	174.1	86.2	-44.7
58	1	0.07	85.4 (1.3)	171.3	84.3	-38.8	0.07	85.6 (1.2)	170.0	83.8	-38.8	0.08	81.6 (1.0)	176.4	83.2	-43.4
59	1	0.05	86.7 (1.1)	167.0	76.5	-38.5	0.05	87.0 (1.2)	166.6	76.5	-39.3	0.07	83.9 (1.2)	168.7	73.7	-49.7
60	1	0.05	88.3 (0.4)	161.4	69.8	-40.9	0.05	88.6 (0.4)	160.5	69.5	-41.8	0.09	90.7 (3.2)	174.0	84.3	-38.1
61	1	0.05	86.9 (0.7)	168.1	76.8	-44.9	0.05	87.2 (0.7)	167.5	76.6	-44.9	0.08	82.7 (0.9)	166.1	73.5	-60.7
62	1	0.06	84.7 (0.9)	174.8	87.6	-40.4	0.06	85.2 (0.9)	174.1	87.2	-40.7	0.08	81.2 (0.9)	175.1	83.0	-49.7
63	2	0.07	90.0 (2.4)	169.7	74.3	-42.7	0.07	90.4 (2.2)	169.5	74.2	-44.3	0.09	83.8 (1.6)	175.9	75.2	-48.9
64	2	0.05	88.4 (1.7)	158.6	69.5	-63.1	0.06	88.2 (1.4)	157.0	68.9	-65.0	0.07	90.7 (1.7)	168.8	69.9	-68.0
65	1	0.07	88.2 (2.7)	170.2	72.5	-48.9	0.07	88.2 (2.6)	169.3	72.0	-49.4	0.09	85.3 (1.9)	170.7	71.0	-58.7
66	1	0.05	88.5 (2.5)	168.9	73.2	-47.1	0.05	89.0 (2.5)	168.4	72.7	-47.5	0.08	84.6 (1.6)	168.7	71.4	-61.2
67	2	0.07	89.7 (2.0)	167.6	71.9	-56.5	0.07	89.9 (2.0)	166.7	71.5	-56.3	0.09	87.5 (1.6)	169.7	70.5	-65.0
68	2	0.11	87.2 (2.1)	175.5	82.0	-37.3	0.11	86.8 (2.3)	174.4	81.0	-37.9	0.12	85.1 (2.0)	175.5	80.5	-47.2
69	2	0.07	87.8 (1.7)	166.6	70.7	-59.7	0.07	87.3 (1.4)	164.4	69.5	-62.6	0.09	84.6 (1.0)	168.2	69.0	-67.8
70	1	0.07	90.1 (2.6)	169.6	67.6	-48.4	0.07	89.9 (2.5)	168.9	67.3	-49.6	0.09	86.4 (1.8)	169.2	66.5	-59.4
71	2	0.06	95.1 (2.5)	166.9	72.9	-40.7	0.06	94.8 (2.4)	165.7	72.0	-41.2	0.08	90.7 (2.5)	168.5	71.5	-55.7
72	1	0.06	95.4 (2.7)	177.6	82.0	-44.3	0.06	92.9 (2.4)	175.4	80.4	-44.0	0.08	89.3 (2.6)	178.8	79.9	-55.9

continued on next page

continuation of Table C.4

73	2	0.05	83.9 (1.3)	169.1	78.6	-45.2	0.05	83.9 (1.3)	169.5	79.3	-46.9	0.09	78.8 (1.3)	165.8	74.6	-58.0
74	1	0.05	85.6 (1.2)	167.6	77.8	-45.5	0.05	85.6 (1.2)	167.8	78.3	-47.4	0.07	81.8 (0.7)	165.2	74.0	-57.3
75	1	0.06	88.0 (0.8)	173.5	79.1	-35.4	0.06	88.3 (0.8)	173.1	79.0	-35.8	0.08	84.2 (0.9)	175.1	76.7	-44.4
76	1	0.04	87.4 (1.0)	168.0	68.2	-31.4	0.05	88.1 (1.0)	168.2	68.3	-31.7	0.07	84.2 (1.3)	169.8	66.4	-40.9
77	1	0.06	86.1 (0.5)	159.4	61.5	-47.8	0.05	86.5 (0.5)	159.6	61.7	-47.6	0.08	85.7 (1.9)	159.5	59.3	-58.8
78	1	0.05	85.4 (0.6)	14.1	68.3	27.0	0.06	85.9 (0.5)	13.9	68.0	26.0	0.09	85.7 (1.3)	19.3	67.8	27.6
79	2	0.05	92.7 (1.2)	173.5	82.0	-32.6	0.06	92.2 (1.4)	172.9	81.8	-32.6	0.08	89.4 (1.6)	177.3	79.4	-39.5
80	1	0.04	89.5 (0.7)	157.9	54.2	-47.6	0.05	89.0 (0.5)	156.2	52.9	-45.5	0.07	89.1 (1.4)	154.4	51.1	-59.3
81	1	0.04	89.0 (0.7)	159.4	56.6	-42.1	0.04	89.1 (0.8)	159.6	57.1	-41.0	0.07	88.0 (1.2)	156.9	53.9	-54.9
82	1	0.05	90.5 (1.0)	170.4	60.3	-44.4	0.05	89.8 (1.1)	164.6	54.4	-39.4	0.08	87.0 (1.5)	159.2	51.6	-55.5
83	2	0.11	86.7 (1.7)	159.3	60.1	-35.3	0.11	89.5 (3.2)	151.2	47.8	-31.1	0.13	83.5 (2.9)	147.9	50.9	-41.4
84	1	0.05	83.8 (1.1)	7.4	84.7	34.3	0.05	84.2 (1.0)	6.6	84.8	33.6	0.08	82.3 (1.1)	8.6	86.1	33.3
85	3	0.12	86.8 (2.2)	17.0	80.7	48.2	0.12	90.2 (2.5)	14.7	76.9	27.8	0.12	80.7 (2.6)	11.5	88.9	56.6
86	1	0.07	84.9 (1.1)	154.0	57.0	-51.1	0.07	85.2 (1.2)	154.4	57.3	-50.4	0.10	86.3 (1.5)	158.9	55.6	-62.0
87	2	0.07	87.8 (1.1)	161.6	74.8	-47.2	0.06	87.5 (1.1)	162.0	75.9	-48.8	0.08	84.3 (0.7)	154.1	69.6	-60.0
88	1	0.07	84.7 (1.2)	163.2	74.4	-45.9	0.08	84.6 (1.3)	162.7	73.7	-50.0	0.08	84.2 (1.6)	166.0	71.4	-57.5
89	1	0.06	87.9 (1.4)	158.2	56.3	-32.7	0.06	88.4 (1.5)	158.1	56.2	-32.4	0.08	87.5 (2.4)	159.2	55.5	-42.8
90	1	0.06	87.3 (1.0)	153.1	53.7	-52.6	0.06	88.0 (1.1)	156.1	55.6	-50.9	0.07	86.3 (1.4)	148.1	50.8	-65.8
91	1	0.06	88.8 (0.9)	168.0	53.8	-37.1	0.06	89.2 (0.9)	169.3	54.7	-35.4	0.08	85.3 (0.9)	161.1	52.3	-57.1
92	2	0.06	88.5 (0.5)	154.2	61.0	-45.0	0.05	90.7 (0.6)	154.9	60.3	-45.5	0.08	87.1 (1.6)	150.3	57.7	-62.1
93	1	0.05	89.1 (0.6)	171.1	69.9	-47.1	0.05	89.0 (0.7)	172.0	71.2	-49.1	0.07	84.5 (0.7)	166.1	66.1	-60.7
94	2	0.04	90.4 (1.1)	157.2	49.0	-47.7	0.05	90.5 (0.9)	160.2	52.2	-46.2	0.07	89.1 (0.8)	148.6	50.4	-78.3
95	1	0.06	86.9 (1.2)	157.4	54.1	-49.5	0.06	88.7 (1.1)	160.0	56.5	-49.8	0.08	86.2 (1.2)	150.5	51.5	-66.7
96	1	0.06	91.9 (0.9)	173.7	63.0	-52.5	0.06	90.4 (0.8)	174.2	65.9	-54.5	0.09	89.2 (0.5)	158.1	56.7	-74.4
97	1	0.06	85.7 (1.2)	169.0	77.7	-49.4	0.06	85.8 (1.3)	169.6	78.4	-50.8	0.08	83.4 (1.3)	167.4	73.3	-57.9
98	1	0.05	86.0 (0.7)	158.7	78.5	-59.5	0.05	86.6 (0.7)	158.4	78.2	-59.5	0.06	84.2 (0.7)	159.8	75.3	-70.8
99	1	0.06	89.0 (1.4)	158.4	57.6	-44.1	0.06	89.8 (1.5)	158.5	57.7	-44.5	0.09	88.5 (2.1)	158.8	56.4	-54.7
100	1	0.05	90.0 (0.7)	162.4	69.5	-52.9	0.06	90.6 (0.8)	162.3	69.6	-52.4	0.07	86.6 (1.2)	165.5	68.6	-62.2

continued on next page



continuation of Table C.4

101	2	0.05	87.5 (0.8)	160.1	66.4	-56.6	0.05	88.0 (0.9)	160.3	66.8	-55.5	0.07	82.3 (1.0)	162.2	66.6	-67.8
102	3	0.11	88.8 (3.0)	148.1	59.3	-73.2	0.12	98.6 (4.4)	125.0	51.8	-95.2	0.11	94.9 (2.6)	161.5	54.7	-78.8
103	3	0.04	87.8 (0.9)	169.3	75.9	-40.7	0.04	88.1 (0.9)	169.0	75.8	-41.7	0.06	84.9 (1.3)	170.8	73.8	-50.6
104	2	0.05	83.3 (2.4)	169.6	75.0	-53.1	0.05	82.6 (2.2)	167.7	74.4	-54.4	0.07	83.5 (2.3)	172.2	72.0	-62.9
105	1	0.05	88.3 (1.2)	162.7	63.7	-39.0	0.05	89.1 (1.3)	161.7	63.3	-38.1	0.06	86.9 (1.5)	163.8	62.5	-49.5
106	1	0.06	88.6 (0.7)	171.6	81.8	-57.8	0.06	89.2 (0.7)	170.6	81.4	-57.4	0.08	81.4 (0.5)	176.1	80.5	-60.6
107	1	0.05	89.5 (0.7)	175.9	83.0	-55.4	0.05	90.4 (0.8)	174.5	82.4	-56.1	0.07	82.3 (0.6)	180.3	81.8	-56.4
108	1	0.07	86.3 (1.0)	355.6	88.2	38.1	0.07	86.1 (1.1)	354.6	88.7	38.4	0.08	81.9 (1.7)	2.3	87.6	43.1
109	1	0.06	86.4 (0.9)	166.5	80.3	-44.3	0.06	86.7 (0.9)	165.6	80.1	-44.8	0.07	81.9 (0.8)	170.9	80.0	-50.7
110	2	0.06	91.0 (1.1)	148.9	53.4	-44.1	0.06	91.1 (1.1)	149.2	54.4	-44.1	0.07	89.9 (1.6)	156.8	55.0	-55.2
111	3	0.12	92.1 (3.4)	156.2	62.9	-32.3	0.12	92.0 (3.5)	155.6	63.3	-32.3	0.13	90.1 (3.4)	155.4	61.6	-46.2
112	1	0.05	91.2 (0.8)	170.7	66.8	-42.3	0.05	91.4 (0.9)	169.8	66.6	-42.5	0.06	87.9 (1.0)	174.6	67.2	-47.8

## C.6 Determined moment-tensor components

In the following, details for moment-tensor components are given that were determined for events in West Bohemia during the swarm episode in 2000. See also Tab. C.2 for details on source locations and times, Table C.6 for standard deviations determined from bootstrap testing.

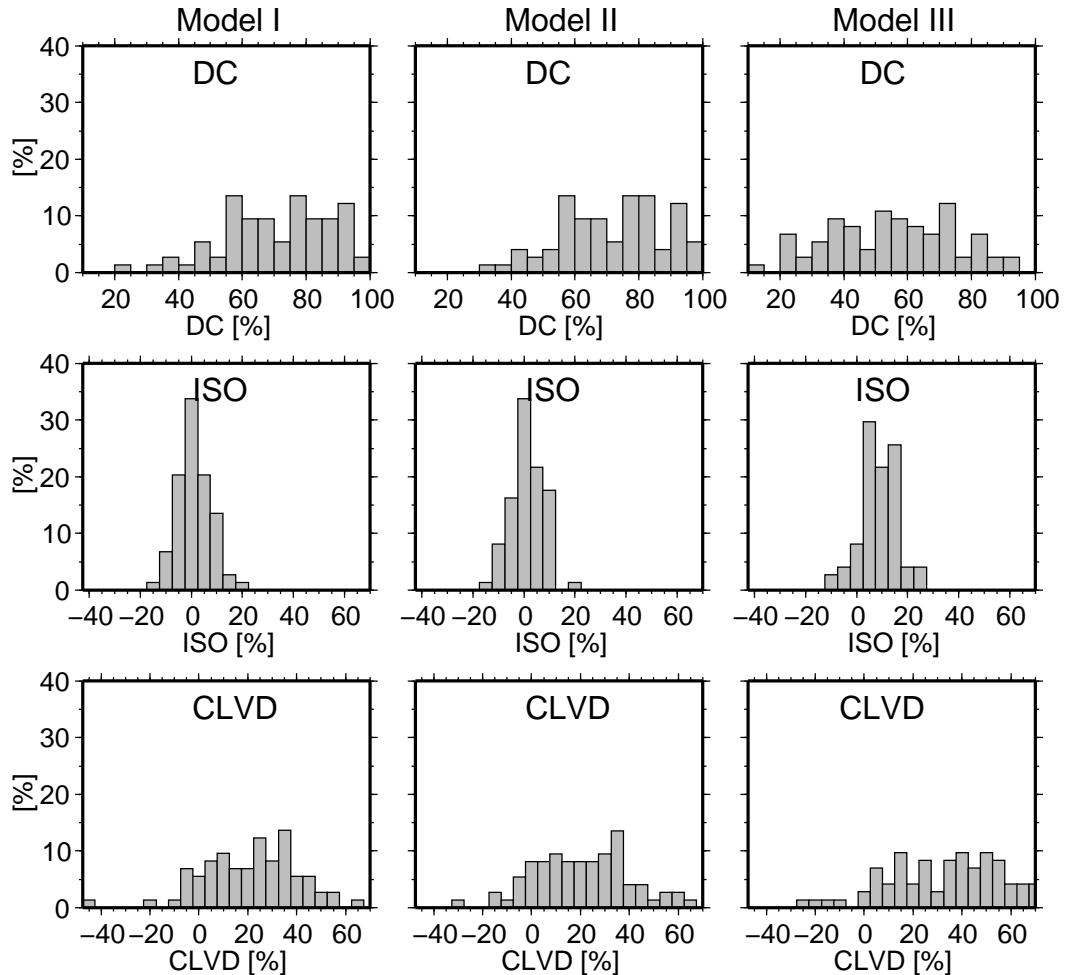


Figure C.8: Distribution of moment-tensor components in percent determined for events in Tab. C.2 with confidence class 1 or 2 (compare Tab. C.5 for details). During inversion the velocity models I, II, or III for West Bohemia were used. See Fig. C.9 for their temporal evolution and Appendices B.4 and B.5 for model descriptions.

Table C.5: Moment tensor components (DC, ISO, CLVD) retrieved for earthquakes in Tab. C.2 using the models I-III (compare Appendix B). Confidence classes are given. Corresponding event sizes, residuals, slip inclinations, and source orientations can be found in Tabs. C.3 and C.4. For standard deviations of the moment-tensor components see Table C.6.

no.	class	Model I			Model II			Model III		
		DC [%]	ISO [%]	CLVD [%]	DC [%]	ISO [%]	CLVD [%]	DC [%]	ISO [%]	CLVD [%]
1	1	67.6	9.5	23.0	65.4	9.9	24.7	43.8	14.2	42.0
2	3	19.7	25.6	54.6	23.4	23.8	52.9	16.0	-28.1	-55.9

continued on next page

continuation of Table C.5

3	1	73.6	7.8	18.5	73.1	8.5	18.4	41.9	13.0	45.1
4	1	45.1	-0.4	54.5	42.1	0.3	57.6	25.6	6.9	67.4
5	1	47.7	5.8	46.5	54.4	9.0	36.7	23.0	9.6	67.4
6	2	63.3	-0.5	36.2	55.9	0.7	43.4	43.1	8.4	48.5
7	2	14.2	-4.9	80.8	14.4	-4.7	80.9	11.3	5.8	82.9
8	2	15.8	-2.7	81.5	13.8	-1.4	84.8	20.9	6.9	72.2
9	1	74.6	0.7	24.7	75.0	2.0	23.0	47.0	6.5	46.6
10	1	56.1	8.4	35.5	55.9	8.5	35.6	38.4	13.8	47.8
11	1	56.0	9.7	34.3	55.9	9.8	34.4	36.1	14.6	49.3
12	3	61.5	7.8	30.7	84.5	4.4	11.1	41.6	14.6	43.7
13	2	69.3	3.8	26.9	71.8	3.7	24.5	39.2	12.9	47.9
14	2	39.8	4.9	55.3	46.5	7.1	46.4	16.9	10.8	72.3
15	1	33.5	0.3	66.2	38.8	2.5	58.6	14.7	8.6	76.7
16	2	72.2	8.9	18.9	73.3	9.6	17.1	50.7	12.1	37.2
17	1	22.2	0.4	77.4	32.2	2.4	65.4	20.0	8.8	71.2
18	1	66.0	3.6	30.4	67.8	5.9	26.3	32.5	10.8	56.7
19	1	94.4	1.1	4.5	95.3	2.5	-2.2	62.7	11.9	25.4
20	2	45.6	3.1	51.3	52.1	5.3	42.5	41.5	10.0	48.6
21	1	60.0	8.7	31.3	60.6	8.5	30.9	34.7	13.9	51.4
22	2	56.6	12.5	31.0	51.5	11.2	37.3	58.1	25.3	16.6
23	2	61.5	20.4	-18.2	66.5	19.1	-14.4	67.7	23.5	8.8
24	1	65.5	6.2	28.3	63.5	6.6	29.9	44.7	13.4	41.9
25	1	80.2	1.1	18.7	75.5	0.9	23.6	52.7	9.7	37.6
26	1	75.1	-2.3	22.6	75.5	-2.1	22.4	50.6	7.2	42.3
27	2	72.0	0.8	27.3	71.4	0.9	27.7	37.6	7.1	55.3
28	1	58.7	-4.9	36.4	59.7	-5.0	35.3	28.2	-3.3	68.5
29	1	92.6	-5.7	-1.7	92.4	-5.9	-1.7	72.5	2.3	25.2
30	1	76.0	-11.6	12.4	77.0	-11.5	11.5	58.1	-2.4	39.5
31	1	68.6	6.0	25.4	68.4	6.0	25.6	44.4	12.5	43.1
32	1	76.8	-3.1	20.2	81.3	-2.4	16.3	43.6	3.7	52.7
33	1	60.8	-2.1	37.1	64.2	-1.5	34.3	33.1	5.0	62.0
34	1	48.9	-2.0	49.1	53.1	-1.5	45.4	22.0	6.0	72.0
35	1	43.1	-1.8	55.2	45.6	-0.9	53.4	20.3	6.5	73.2
36	1	62.8	4.6	32.6	63.9	5.6	30.5	37.9	12.4	49.8
37	2	29.5	1.1	69.4	24.8	2.1	73.1	35.2	8.6	56.2
38	1	82.3	4.6	13.1	82.7	5.2	12.2	63.1	12.5	24.4
39	3	28.3	24.2	-47.4	28.7	24.0	-47.2	48.7	26.0	-25.4
40	2	89.6	-4.6	5.8	85.5	-4.6	9.9	78.0	10.3	11.7
41	3	43.8	-22.4	-33.8	30.8	-25.9	-43.2	16.2	-28.4	-55.3
42	2	86.0	10.1	4.0	77.8	7.3	14.9	76.0	21.8	-2.2
43	3	93.4	-0.6	6.1	89.1	-1.8	9.1	45.7	-19.6	34.8
44	3	41.2	1.6	57.2	43.4	2.4	54.2	34.5	4.8	60.7
45	1	55.2	-5.2	39.6	57.8	-4.5	37.7	39.7	4.5	55.8
46	1	79.1	-2.8	18.1	95.3	0.9	-3.7	68.4	4.8	26.7
47	1	61.1	-0.7	38.2	63.0	0.0	36.9	35.0	7.2	57.8

continued on next page

continuation of Table C.5

48	1	57.8	-8.8	33.4	63.3	-7.7	29.1	53.9	2.6	43.4
49	1	39.1	-13.9	47.0	43.7	-12.9	43.5	46.0	-1.5	52.5
50	1	53.3	-0.1	46.6	56.8	0.6	42.6	59.5	4.7	35.9
51	2	37.9	-14.1	47.9	33.2	-14.4	52.4	36.3	0.6	63.2
52	1	54.5	0.9	44.6	49.6	0.6	49.8	30.0	9.3	60.7
53	1	75.0	-10.4	14.6	67.5	-11.3	21.2	59.0	-2.8	38.2
54	1	58.9	-4.3	36.8	55.5	-4.4	40.0	41.3	6.9	51.7
55	1	45.1	2.6	52.3	43.1	2.4	54.5	23.4	10.1	66.6
56	2	40.6	-7.2	52.2	42.4	-5.3	52.3	59.1	6.2	34.8
57	1	67.2	6.5	26.3	68.1	6.7	25.3	52.7	15.8	31.5
58	1	73.6	3.9	22.5	73.8	3.8	22.3	51.0	12.6	36.4
59	1	81.8	4.4	13.8	83.4	4.5	12.1	70.1	15.1	14.8
60	1	92.7	5.2	2.0	94.2	5.1	0.7	90.8	4.1	5.0
61	1	75.4	-1.7	23.0	77.9	-1.0	21.1	57.1	6.0	36.9
62	1	56.2	-4.8	39.0	58.9	-4.3	36.8	45.0	7.2	47.8
63	2	86.2	5.3	-8.5	82.5	6.0	-11.4	65.3	12.5	22.2
64	2	74.3	-6.3	19.5	68.3	-8.1	23.7	58.6	15.8	-25.6
65	1	92.3	5.5	2.3	90.3	4.6	5.1	80.1	15.6	4.3
66	1	93.7	5.5	0.8	92.7	5.5	-1.8	73.9	12.8	13.3
67	2	92.6	3.5	-3.9	95.2	2.4	-2.3	76.3	15.5	-8.2
68	2	85.0	4.5	10.5	81.0	3.8	15.2	76.3	17.7	6.0
69	2	86.3	1.2	12.5	79.3	-0.6	20.1	73.8	11.2	14.9
70	1	89.5	3.8	-6.7	94.3	2.7	-3.0	84.7	13.2	2.1
71	2	59.1	3.8	-37.1	61.9	3.0	-35.1	62.8	14.8	-22.5
72	1	39.5	14.4	-46.1	57.0	11.3	-31.7	51.8	23.1	-25.0
73	2	60.3	-0.5	39.2	60.9	0.9	38.2	37.5	6.4	56.1
74	1	66.2	-2.4	31.4	67.6	-1.3	31.1	50.2	4.6	45.2
75	1	90.2	4.8	5.0	91.3	5.0	3.7	69.1	15.5	15.4
76	1	87.1	5.3	7.5	90.8	5.8	3.4	70.6	15.2	14.2
77	1	75.6	1.4	23.0	77.5	1.6	20.9	80.9	12.7	6.3
78	1	57.7	-5.9	36.4	57.6	-5.9	36.5	41.7	4.5	53.8
79	2	83.3	-1.3	-15.4	86.8	-1.8	-11.4	89.1	10.0	0.9
80	1	88.5	-3.2	8.4	76.6	-6.6	16.8	92.9	5.2	-1.9
81	1	88.7	-1.8	9.5	87.9	-2.1	10.0	89.1	5.9	5.0
82	1	95.2	0.5	-4.3	75.5	-8.7	15.8	77.8	0.1	22.1
83	2	52.5	-12.4	35.1	83.2	7.6	-9.2	68.1	9.7	22.3
84	1	56.1	-2.3	41.6	56.6	-2.1	41.3	38.5	8.1	53.4
85	3	85.1	7.7	7.2	85.3	-4.4	10.3	58.5	21.4	20.1
86	1	60.4	-3.3	36.4	61.2	-3.4	35.4	80.2	7.6	12.2
87	2	67.1	-7.9	25.0	68.0	-6.6	25.4	55.6	-2.8	41.6
88	1	67.7	1.7	30.6	67.3	3.1	29.6	72.3	13.7	14.0
89	1	87.6	9.5	-2.9	84.5	9.8	-5.7	67.8	18.7	-13.5
90	1	81.5	-0.2	18.3	87.9	2.1	10.1	78.2	3.9	17.8
91	1	76.3	-6.3	17.3	79.0	-5.6	15.4	57.0	-4.9	38.1
92	2	73.4	-6.7	19.9	96.6	-1.7	-1.7	75.8	-1.6	22.6

continued on next page

continuation of Table C.5

93	1	78.9	-6.0	15.1	82.4	-3.8	13.8	60.8	-0.4	38.8
94	2	79.8	-8.9	11.4	85.5	-6.6	8.0	63.6	-12.8	23.5
95	1	72.1	-3.3	24.6	84.2	-2.6	13.2	72.6	-0.8	26.6
96	1	86.8	-9.5	3.7	80.5	-8.1	11.4	74.2	-8.3	17.5
97	1	69.5	-1.1	29.4	71.7	0.6	27.7	61.9	7.8	30.3
98	1	60.5	-6.2	33.3	63.7	-5.8	30.5	66.4	5.4	28.2
99	1	81.9	9.4	-8.8	76.0	10.0	-13.9	61.8	18.9	-19.3
100	1	92.2	-2.9	4.9	96.8	-2.5	0.7	82.2	8.8	9.0
101	2	76.8	-2.6	20.6	80.3	-2.2	17.5	57.2	6.5	36.3
102	3	64.8	-11.5	23.7	56.0	-9.7	-34.2	42.4	14.4	-43.2
103	3	90.1	6.4	3.5	92.1	7.0	0.9	76.9	16.6	6.6
104	2	58.2	0.1	41.7	47.9	-2.3	49.8	71.6	16.3	12.2
105	1	85.4	9.5	-5.1	81.5	9.4	-9.1	72.5	18.3	-9.2
106	1	91.2	1.2	7.6	94.0	1.5	4.5	53.6	10.6	35.7
107	1	96.6	0.5	2.8	97.4	0.5	-2.1	56.2	10.7	33.2
108	1	82.5	8.0	9.6	80.7	8.2	11.1	51.6	15.1	33.3
109	1	84.3	9.2	6.5	85.4	9.2	5.4	60.0	15.6	24.5
110	2	83.4	3.9	-12.7	84.4	3.1	-12.5	71.0	12.1	-16.9
111	3	89.3	-4.0	-6.7	89.3	-4.6	-6.2	85.2	6.1	-8.6
112	1	92.7	-0.8	-6.5	92.0	-1.1	-6.9	85.1	8.2	6.7

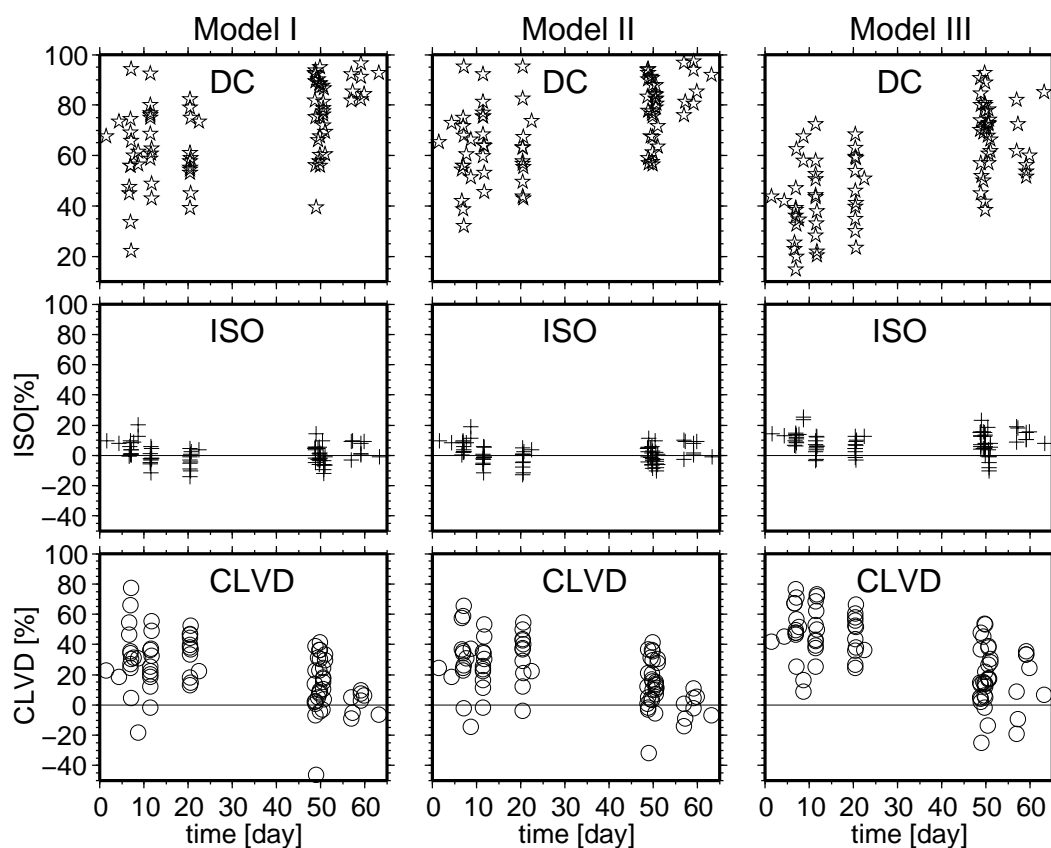


Figure C.9: Temporal distribution of moment-tensor components in percent determined for events in Tab. C.2 with confidence class 1 or 2 (compare Tab. C.5 for details). During inversion the velocity models I, II, or III for West Bohemia were used (see Appendices B.4 and B.5). Time = 0 corresponds to August 28, 2000, 00:00:00.

## C.7 Bootstrap tests for events in the West Bohemia

In order to test the stability of the inversions bootstrap tests are performed for every event using the models I, II, and III (see Figs. C.10-C.19, compare section 4). By bootstrapping the weight of every station is varied during inversion, i.e. seismograms recorded at one station are, in addition to the other seismograms, fed 1, 2, 5, 10, 20,50, or 100 times into the inversion routine during one realization. The procedure is repeated for every station. If the waveforms of one station cannot be modelled correctly, overweighting this station will significantly modify the solution. Grossly varying solutions obtained for one event are an indication for instabilities and low confidence in the inversion results.

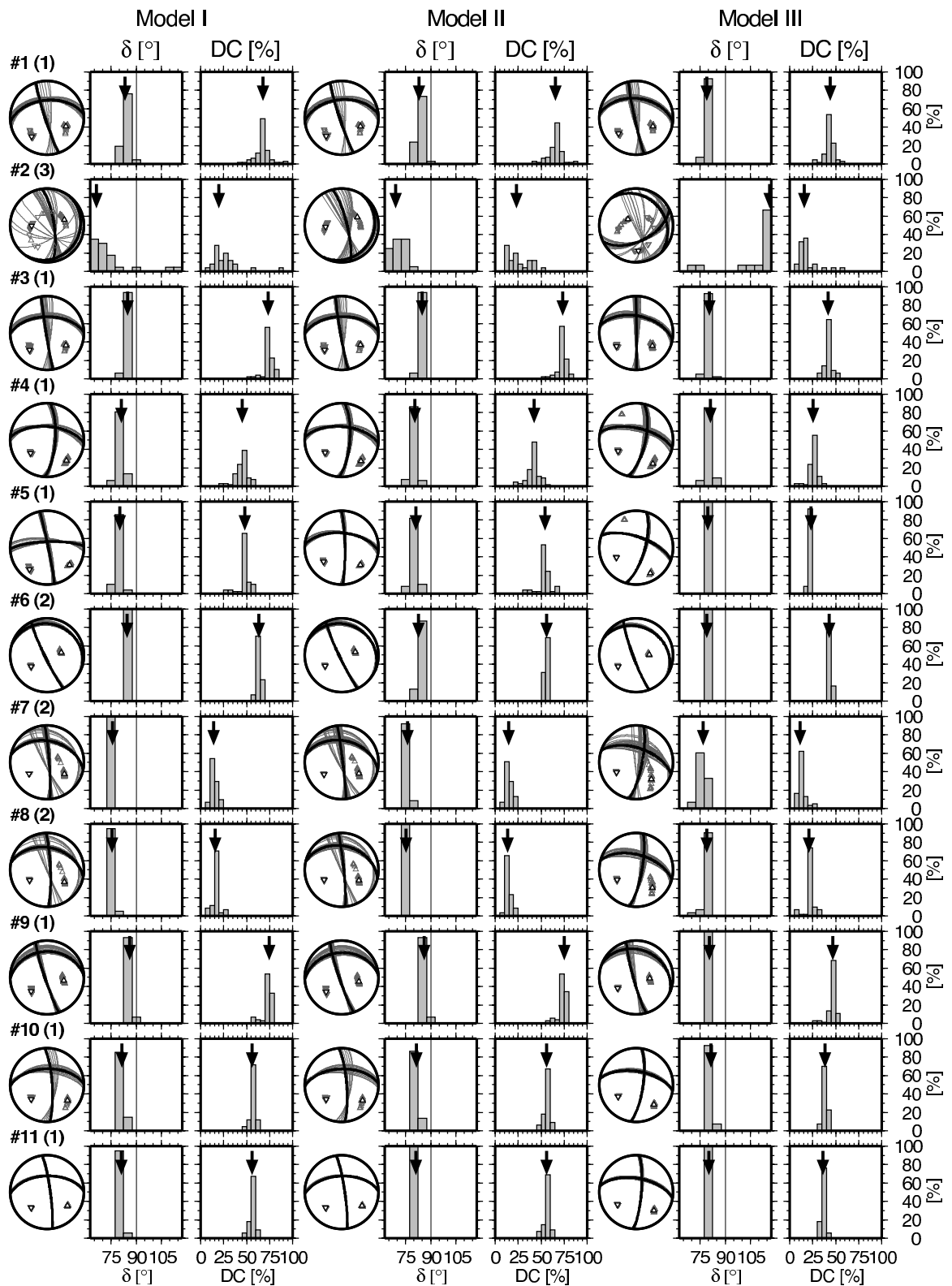


Figure C.10: Fault-plane solutions (grey), slip inclination  $\delta$  and DC obtained from bootstrap tests for events 1-11 in Tab. C.2 using the models I-III. Events are specified by their number (#) followed by their confidence class (in brackets). During inversion the station weight is varied (1, 2, 5, 10, 20, 50, or 100). The procedure is repeated for every station. Black FPS and arrows: solutions obtained with station weight 1 (see also Fig. 4.9).



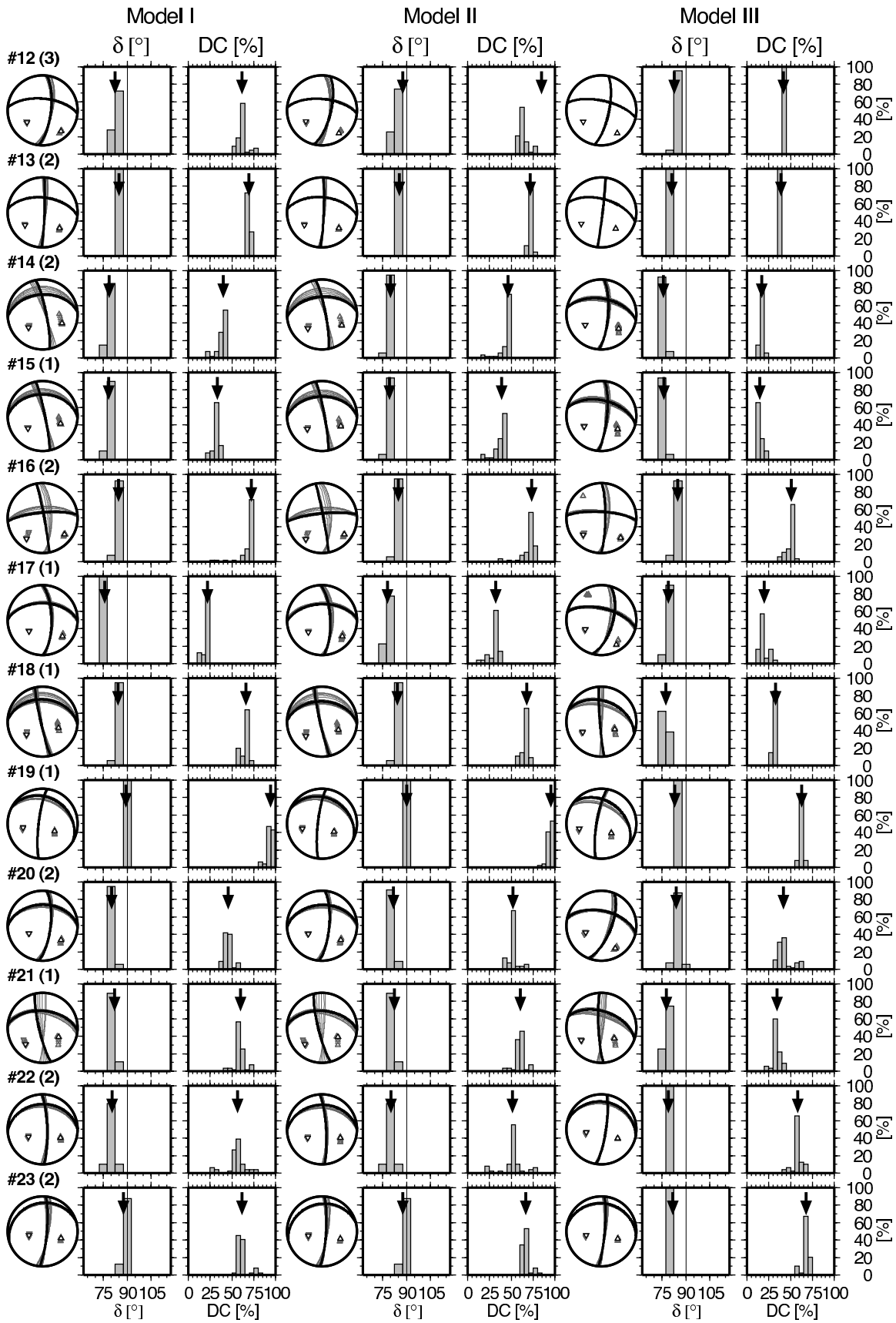


Figure C.11: As in Fig. C.10 but for events 12-23.

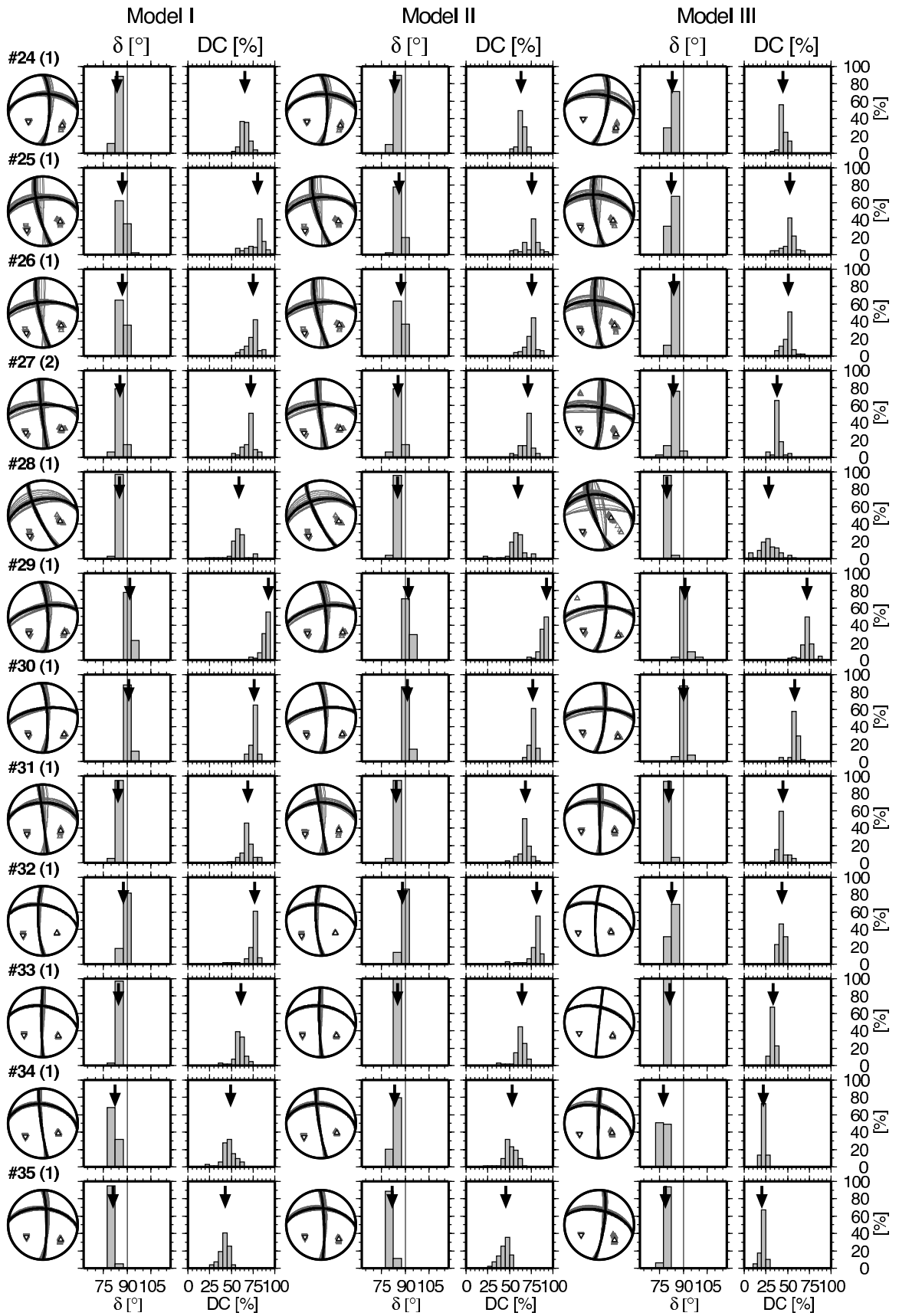


Figure C.12: As in Fig. C.10 but for events 24-35.

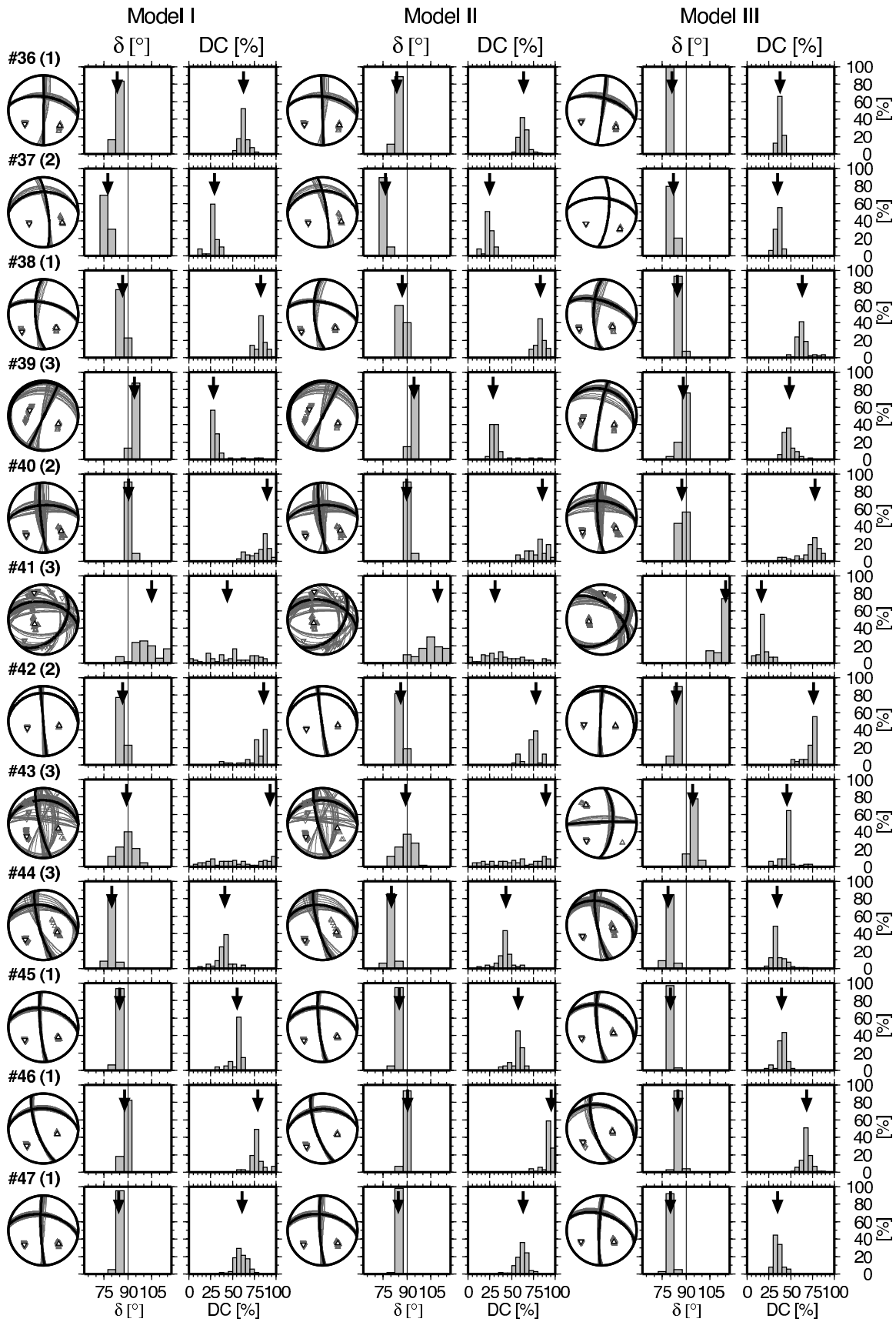


Figure C.13: As in Fig. C.10 but for events 36-47.

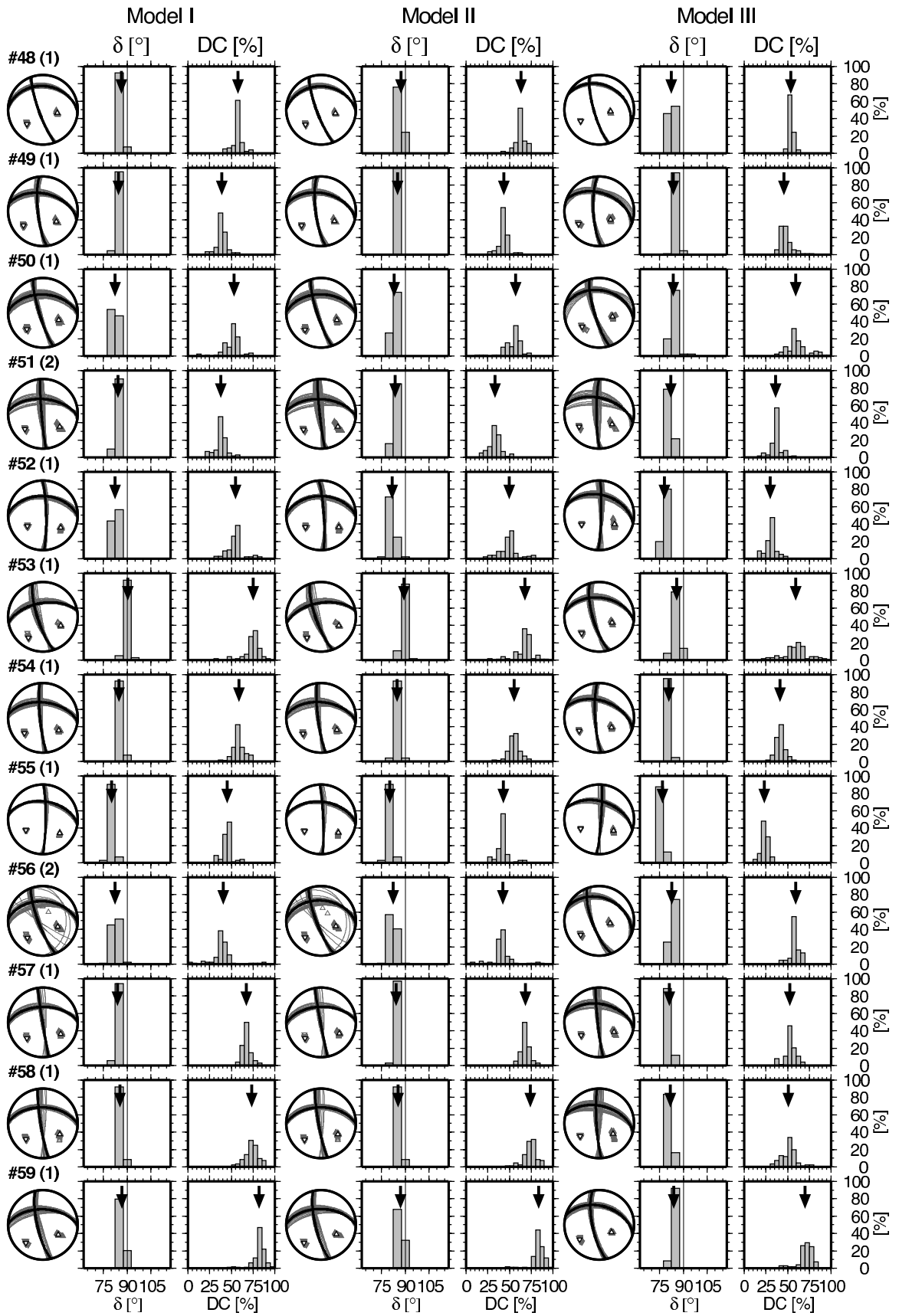


Figure C.14: As in Fig. C.10 but for events 48-59.

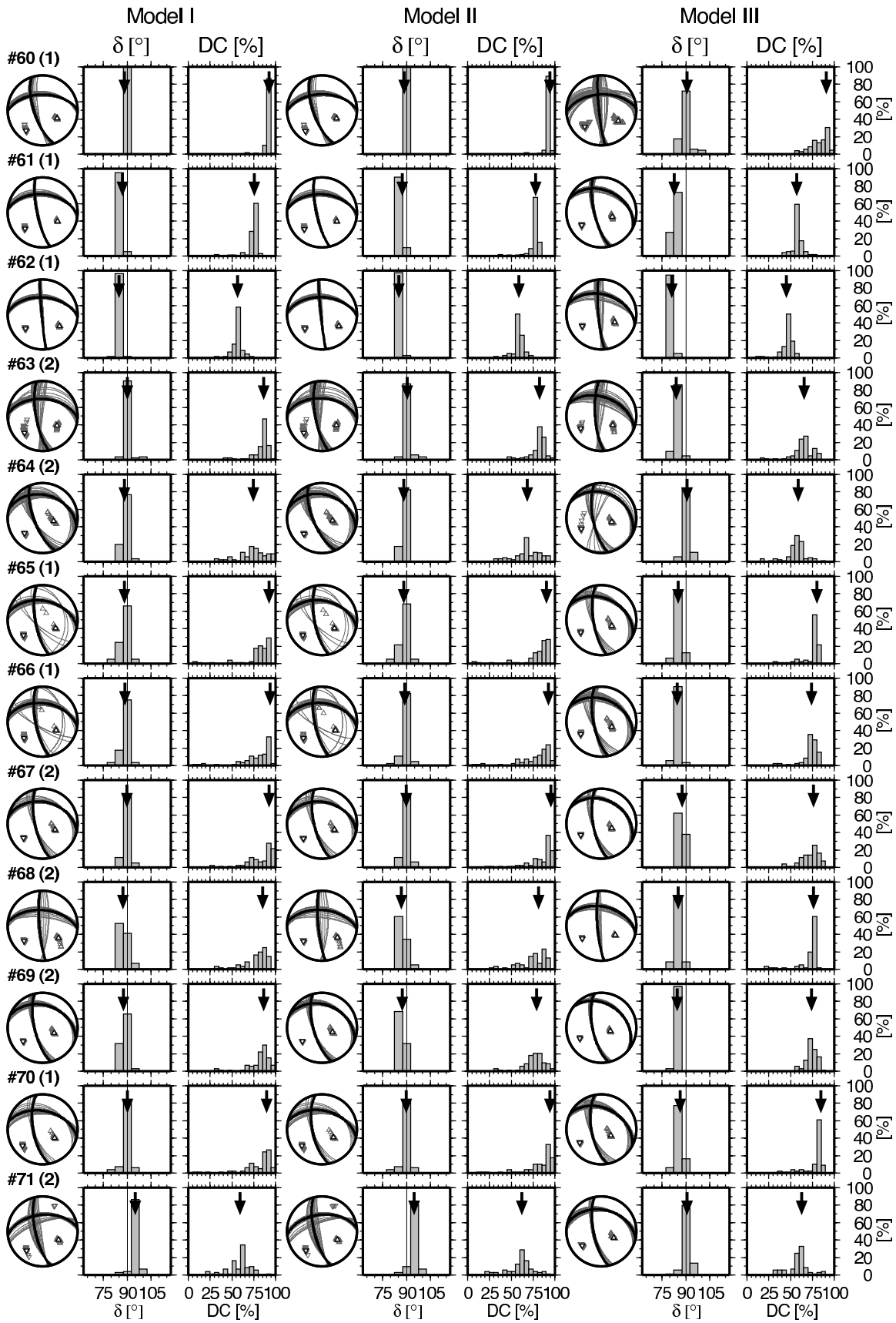


Figure C.15: As in Fig. C.10 but for events 60-71.

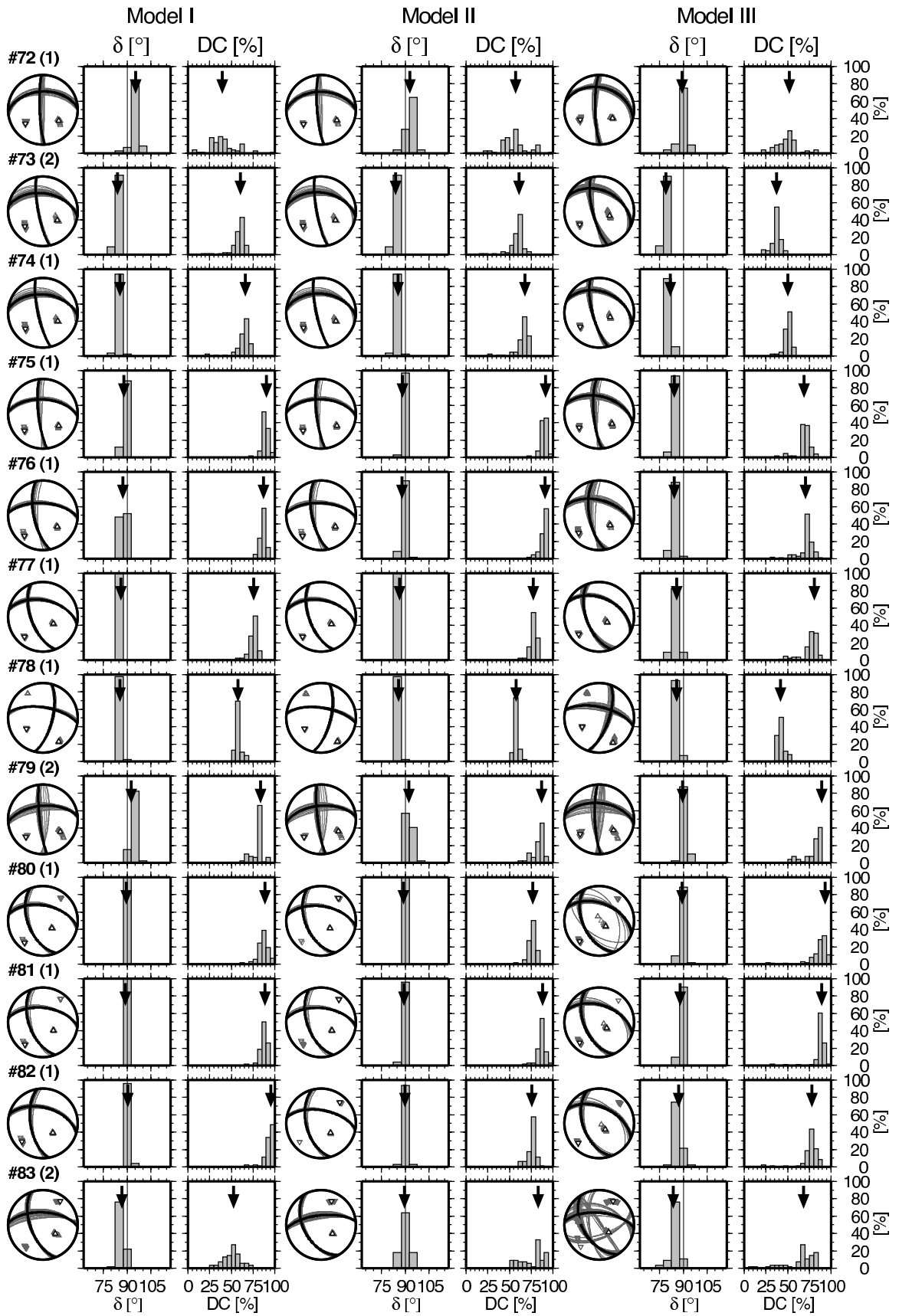


Figure C.16: As in Fig. C.10 but for events 72-83.

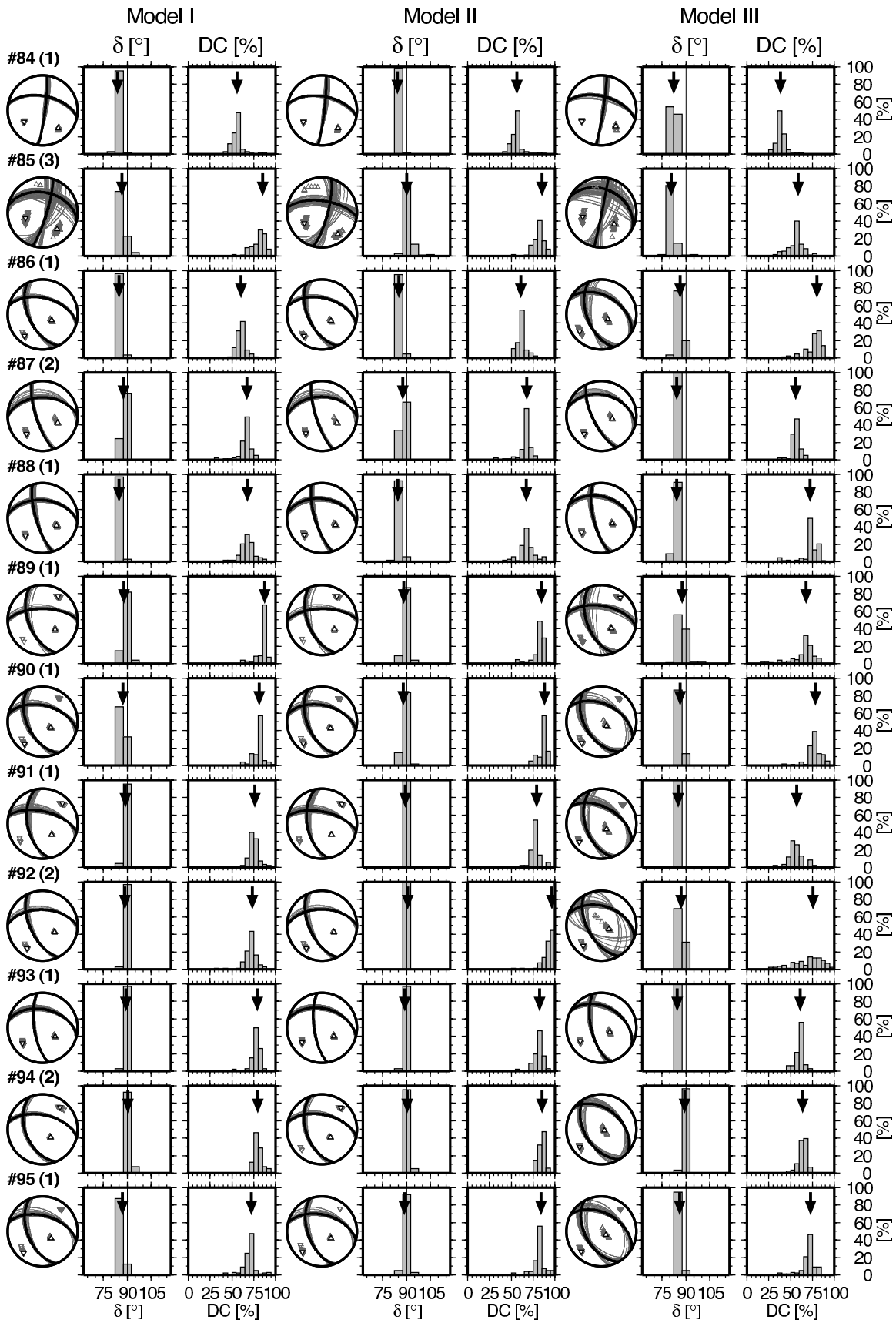


Figure C.17: As in Fig. C.10 but for events 84-95.

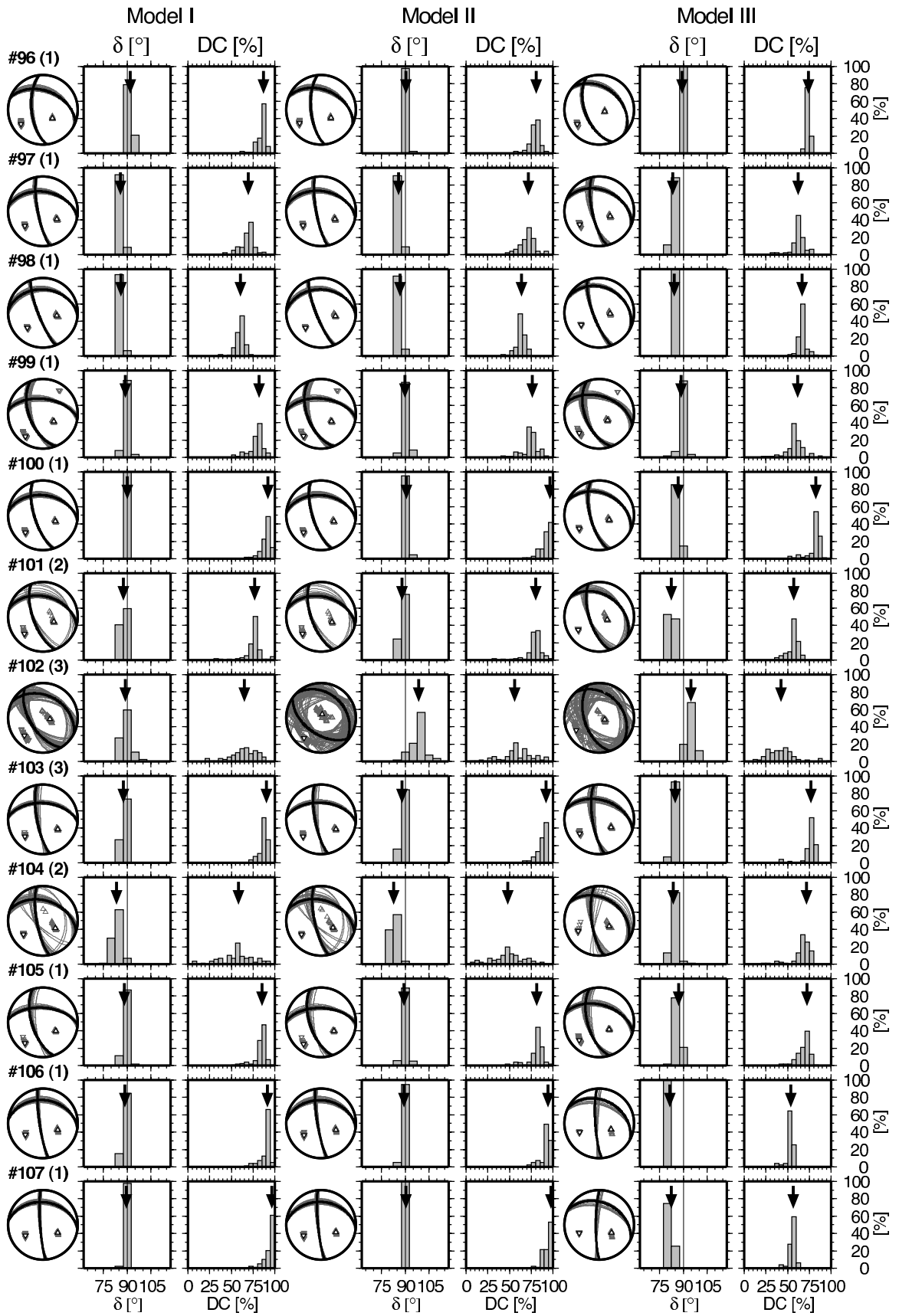


Figure C.18: As in Fig. C.10 but for events 96-107.



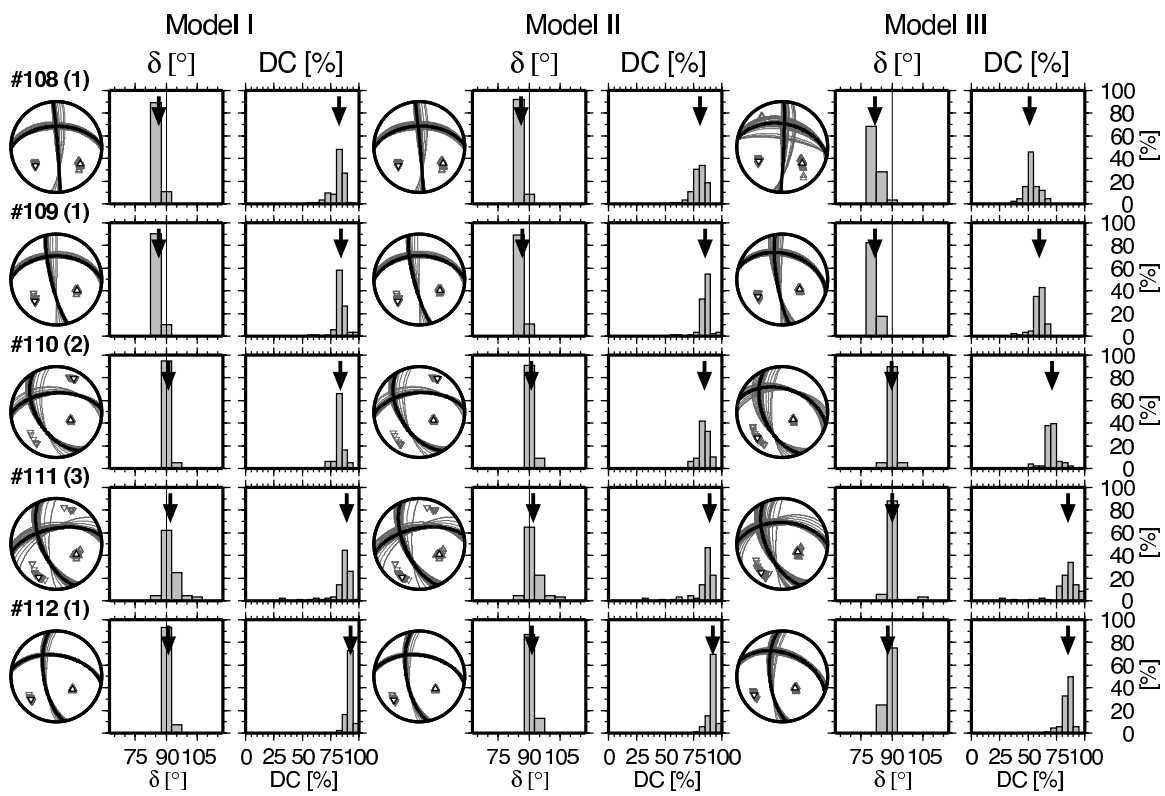


Figure C.19: As in Fig. C.10 but for events 108-112.

## C.8 Standard deviations for retrieved source parameters

Table C.6: Standard deviations of the orientations of the rupture planes given by strike ( $\sigma(\Phi_1^s)$ ), dip ( $\sigma(\delta_1^s)$ ), and rake ( $\sigma(\lambda_1^s)$ ) as well as of the corresponding moment tensor components given by DC ( $\sigma(\text{DC})$ ), ISO ( $\sigma(\text{ISO})$ ), and CLVD ( $\sigma(\text{CLVD})$ ) determined for events in Tab. C.2. The standard deviations are obtained from Bootstrag tests for each event using the velocity models I, II, and III. Bootstrap tests were performed by successively varying the weight of every station (weights: 1, 2, 5, 10, 20, 50, 100). All values are in units of degree.

event no.	class	Model I						Model II						Model III					
		$\sigma(\Phi_1^s)$	$\sigma(\delta_1^s)$	$\sigma(\lambda_1^s)$	$\sigma(\text{DC})$	$\sigma(\text{ISO})$	$\sigma(\text{CLVD})$	$\sigma(\Phi_1^s)$	$\sigma(\delta_1^s)$	$\sigma(\lambda_1^s)$	$\sigma(\text{DC})$	$\sigma(\text{ISO})$	$\sigma(\text{CLVD})$	$\sigma(\Phi_1^s)$	$\sigma(\delta_1^s)$	$\sigma(\lambda_1^s)$	$\sigma(\text{DC})$	$\sigma(\text{ISO})$	$\sigma(\text{CLVD})$
1	1	4.0	1.4	2.5	8.1	3.3	7.7	3.8	1.3	2.5	8.1	3.2	7.9	3.7	1.7	3.6	5.4	1.9	6.0
2	3	11.8	23.6	28.2	16.1	14.9	29.6	17.7	22.3	30.6	12.0	5.0	7.0	64.5	16.5	25.4	11.7	15.1	27.6
3	1	3.3	1.3	2.4	5.5	3.1	5.0	3.3	1.2	2.4	5.3	2.9	5.0	2.5	1.4	3.2	4.5	1.6	4.9
4	1	1.9	2.0	1.4	7.2	1.5	7.0	2.0	2.1	1.5	7.0	1.5	6.8	2.2	2.4	2.7	5.2	1.7	4.8
5	1	1.7	1.9	2.5	6.4	1.4	6.0	1.3	0.9	1.1	7.2	0.5	6.8	1.0	1.1	0.8	1.4	0.2	1.5
6	2	0.9	0.2	3.1	2.1	0.9	2.0	1.0	0.1	5.3	1.4	0.8	1.4	0.7	0.2	2.3	1.6	0.5	1.9
7	2	6.6	1.6	15.9	3.2	0.7	2.5	6.6	2.2	13.6	4.0	0.9	3.2	4.1	4.0	7.0	4.5	1.6	5.8
8	2	5.7	1.9	19.0	4.0	0.7	3.8	5.2	1.4	17.7	3.2	0.7	3.1	2.1	2.4	3.9	5.2	1.4	5.3
9	1	1.7	0.8	5.2	5.0	2.8	5.0	1.8	0.9	5.7	4.6	3.1	5.0	2.4	1.2	4.0	4.6	1.1	5.1
10	1	2.9	2.1	2.6	3.0	1.9	2.3	3.0	2.2	2.8	2.9	1.9	2.1	0.9	0.8	1.8	2.2	0.8	1.9
11	1	0.7	0.6	0.8	2.8	0.7	2.3	0.6	0.6	0.9	2.6	0.8	2.1	1.1	0.9	1.6	2.1	0.8	1.6
12	3	2.6	1.2	0.4	5.5	1.2	4.3	2.6	1.2	0.4	5.3	1.1	4.2	0.1	0.1	0.0	0.3	0.1	0.2
13	2	2.0	1.3	0.7	2.3	1.1	1.3	1.5	1.0	0.5	1.7	0.8	0.9	0.6	0.4	0.5	0.5	0.2	0.3
14	2	2.5	0.9	5.5	5.6	2.7	6.2	1.8	0.7	5.4	7.8	3.3	8.8	1.4	1.5	2.5	1.9	0.7	1.9
15	1	2.2	0.9	4.4	4.1	2.1	2.8	2.0	0.9	4.8	6.2	2.8	5.4	1.8	2.2	3.2	2.6	1.1	3.3
16	2	2.5	4.3	4.3	9.5	6.0	8.4	2.7	4.6	4.2	8.2	6.2	7.1	1.7	2.6	1.5	4.2	2.4	5.2
17	1	1.3	1.3	1.4	3.9	1.3	3.2	1.6	2.1	1.6	5.7	2.2	5.4	1.9	2.6	1.6	5.0	1.8	5.9

continued on next page

continuation of Table C.6

18	1	1.7	0.7	5.6	3.8	2.8	3.4	1.5	0.7	6.2	3.9	3.3	3.9	2.2	0.9	4.4	1.5	0.5	1.5
19	1	0.7	0.4	3.4	3.5	0.9	3.6	0.6	0.4	3.2	3.0	1.1	4.6	1.0	0.6	4.6	1.5	0.5	2.0
20	2	1.6	0.7	2.1	4.7	0.8	4.4	1.6	0.6	2.2	5.4	1.0	5.5	1.6	1.9	1.6	8.3	1.9	9.8
21	1	3.9	1.8	2.1	5.5	2.3	6.8	3.9	1.8	2.2	5.4	2.4	6.8	2.7	1.5	3.9	4.0	1.3	5.0
22	2	1.7	0.9	2.5	11.0	4.0	17.0	1.4	1.2	2.6	12.6	3.9	16.5	1.0	0.2	2.2	5.2	1.7	6.8
23	2	2.3	1.4	1.8	6.2	1.7	8.1	2.3	1.3	1.5	4.7	1.5	7.1	1.7	1.0	1.7	3.7	0.9	4.6
24	1	2.4	1.6	2.2	4.5	1.7	4.1	2.5	1.7	2.4	4.4	1.8	3.9	2.0	1.4	3.4	4.0	1.5	3.1
25	1	3.1	2.4	3.1	9.2	3.3	10.4	3.1	2.5	3.2	9.6	3.3	9.5	3.0	2.6	4.7	7.7	2.7	9.7
26	1	3.1	2.4	2.8	6.4	3.7	6.4	3.1	2.5	2.9	6.4	3.7	6.3	3.2	2.9	5.0	5.9	3.2	7.4
27	2	2.7	1.7	3.2	6.4	3.3	6.1	2.7	1.9	3.3	6.3	3.4	5.8	2.5	2.5	5.2	4.6	3.6	3.2
28	1	1.4	1.4	6.2	9.3	4.8	6.0	1.4	1.5	5.9	9.8	5.0	6.5	4.6	2.6	11.2	10.9	3.3	8.8
29	1	2.7	1.9	2.9	4.6	2.6	6.1	2.7	1.9	2.8	4.4	2.6	6.1	1.7	1.4	2.7	6.4	3.1	6.6
30	1	2.2	1.3	1.8	3.2	1.7	4.3	2.2	1.4	1.7	3.4	1.7	4.3	1.5	1.2	2.2	4.5	2.5	5.9
31	1	2.9	1.7	2.5	6.6	2.0	6.6	2.8	1.5	2.5	6.4	2.0	6.5	2.0	1.4	3.0	5.2	1.3	5.7
32	1	1.5	1.2	1.2	7.0	2.0	5.5	1.6	1.2	1.4	7.6	2.2	6.0	0.8	0.7	1.5	3.4	0.8	3.6
33	1	1.6	1.1	1.6	6.5	1.9	5.3	1.6	1.2	1.5	6.5	2.0	5.2	0.8	0.5	1.6	2.2	0.7	2.3
34	1	1.6	1.1	2.7	7.8	2.5	6.6	1.6	1.1	2.8	7.9	2.7	6.5	1.5	1.4	2.8	2.1	0.8	2.4
35	1	2.1	1.6	2.0	5.7	1.9	5.0	1.9	1.6	2.2	6.1	2.0	5.0	1.7	1.7	2.8	2.9	1.0	3.0
36	1	2.2	1.6	2.2	4.9	1.8	4.3	2.3	1.3	2.3	5.0	1.8	4.6	1.1	1.2	2.8	2.4	1.0	2.5
37	2	1.9	1.1	4.3	5.8	0.6	6.0	2.6	1.4	5.1	4.7	0.5	5.3	0.8	0.5	1.1	2.5	0.5	2.4
38	1	2.2	1.7	1.5	5.5	2.0	5.9	2.3	1.7	1.8	5.5	2.0	6.2	2.4	2.6	3.4	7.7	2.1	9.0
39	3	17.9	23.2	26.4	11.1	3.7	7.7	23.6	30.4	31.4	10.3	3.4	7.3	2.3	1.3	8.7	6.5	3.7	17.3
40	2	3.8	3.8	6.4	10.7	6.4	14.5	4.1	4.0	6.7	11.2	6.4	15.5	3.0	3.7	8.7	13.0	6.3	20.6
41	3	29.9	3.9	25.9	24.4	9.3	21.7	33.9	3.7	25.7	23.2	8.0	18.3	50.1	9.0	29.8	5.3	2.3	3.2
42	2	2.4	0.6	1.6	12.6	4.5	15.7	1.9	0.6	1.5	9.1	4.1	15.6	2.2	0.3	1.5	7.3	2.3	8.7
43	3	10.7	7.4	22.8	29.0	13.9	39.7	10.9	7.6	22.4	27.3	13.6	38.4	1.0	2.6	40.6	8.5	0.8	9.1
44	3	4.3	1.3	8.5	9.3	3.0	9.7	4.1	1.2	6.9	9.2	3.1	9.4	3.7	1.3	5.7	7.9	1.7	8.7
45	1	1.4	1.0	2.1	6.8	1.5	6.5	1.4	1.0	1.9	7.1	1.5	6.5	1.7	1.1	2.9	5.4	1.2	6.2

continued on next page

continuation of Table C.6

46	1	1.4	0.8	2.6	7.7	2.4	7.5	1.5	0.9	2.7	5.7	2.2	7.8	2.3	1.3	2.3	5.6	2.6	10.5
47	1	1.9	1.5	2.1	7.1	2.1	6.7	1.9	1.5	2.3	6.8	2.1	6.3	1.6	1.3	2.8	4.7	1.0	5.0
48	1	1.1	0.5	3.3	5.8	2.5	4.1	1.0	0.5	3.2	6.0	2.5	4.3	1.0	0.3	2.0	2.6	1.1	3.2
49	1	1.7	1.2	3.2	5.9	2.7	4.3	1.7	1.1	3.2	5.8	2.7	4.1	1.9	1.2	3.8	7.4	2.7	8.8
50	1	1.8	1.8	4.7	9.9	3.9	8.4	1.7	1.7	4.6	10.1	3.9	8.5	2.4	1.3	3.2	12.0	3.2	15.1
51	2	2.0	2.1	4.3	6.9	2.8	5.8	2.5	2.7	5.3	7.4	3.2	6.0	2.0	2.4	5.5	6.7	2.8	6.7
52	1	1.5	1.3	2.2	10.1	1.2	10.2	1.9	1.6	2.7	11.0	1.4	11.0	2.4	1.9	3.9	6.5	1.3	7.5
53	1	1.8	2.5	2.9	10.3	3.3	10.3	2.0	2.7	3.0	11.1	3.6	10.7	2.1	2.2	3.4	14.7	3.5	15.7
54	1	1.6	1.5	3.0	7.0	2.4	6.6	1.7	1.7	3.5	7.2	2.6	6.8	2.0	1.5	3.3	5.4	1.4	6.3
55	1	1.0	1.1	1.4	6.0	0.9	6.3	1.3	1.4	1.7	7.3	1.1	7.5	1.9	1.8	3.1	4.1	1.1	5.1
56	2	2.9	7.5	10.8	13.3	3.6	11.1	2.9	5.6	9.6	13.0	3.4	11.4	2.1	0.8	3.4	5.8	1.4	6.3
57	1	2.0	1.3	2.5	5.1	2.3	5.4	2.0	1.4	2.6	4.8	2.3	5.5	2.0	1.2	3.9	6.7	2.2	8.5
58	1	2.9	1.3	2.4	7.6	2.7	7.0	2.9	1.4	2.6	7.5	2.8	6.8	2.9	2.2	5.7	9.0	2.6	11.2
59	1	1.5	2.1	3.1	7.8	2.8	9.3	1.4	2.1	3.3	8.1	3.0	10.1	1.9	1.6	3.0	8.5	2.6	10.9
60	1	2.1	1.8	2.3	4.2	2.5	4.5	2.1	1.7	2.4	4.2	2.5	4.6	3.5	3.2	4.6	9.8	3.7	13.9
61	1	0.6	0.7	2.6	7.3	2.2	5.4	0.5	0.7	2.6	7.7	2.3	5.8	1.8	0.6	3.3	5.9	1.8	7.1
62	1	0.7	0.8	2.2	5.8	1.4	5.0	0.7	0.9	2.4	6.2	1.6	5.3	2.1	1.4	4.3	7.7	2.2	9.4
63	2	4.8	3.4	4.8	10.8	3.6	13.8	4.8	3.3	4.9	10.4	3.6	14.0	3.6	3.1	6.0	12.5	3.3	16.2
64	2	4.5	0.9	7.4	16.8	4.9	14.6	4.5	1.0	7.1	15.0	4.5	12.2	6.3	1.8	5.1	12.2	4.8	14.4
65	1	2.1	6.0	10.0	18.8	6.2	20.9	3.4	4.3	9.5	18.7	6.1	20.4	3.3	0.9	4.6	11.5	4.4	17.3
66	1	2.4	6.1	15.3	19.1	7.6	20.8	2.4	6.6	14.0	19.6	7.6	21.5	4.4	1.3	9.0	10.2	4.9	16.0
67	2	2.6	0.5	3.8	15.7	5.1	18.1	2.6	0.5	4.0	16.1	5.1	17.8	2.8	0.7	2.9	10.7	3.9	14.7
68	2	1.9	2.0	4.2	14.6	5.6	18.7	2.1	2.2	4.6	15.8	5.8	19.9	0.9	2.1	3.2	13.5	4.0	19.2
69	2	2.2	0.6	3.6	13.2	3.8	14.8	2.6	0.6	4.0	12.7	3.6	12.6	1.9	0.5	2.7	6.5	2.1	8.9
70	1	2.0	1.2	4.2	18.3	6.0	20.7	2.2	1.0	4.5	18.7	5.8	20.2	3.2	0.7	6.9	11.7	4.3	16.4
71	2	1.7	3.8	4.3	13.9	5.7	20.0	1.6	3.7	4.4	15.0	5.9	20.4	1.7	1.1	3.0	12.3	5.0	20.0
72	1	1.6	1.8	3.0	16.0	6.1	18.9	1.0	1.9	2.4	15.0	5.7	19.5	2.2	1.9	2.7	12.6	5.1	20.7
73	2	0.7	0.7	4.3	8.4	2.2	7.4	0.7	0.6	4.1	8.4	2.1	7.8	3.2	1.0	6.1	5.4	1.8	6.0

continued on next page

continuation of Table C.6

74	1	0.7	0.9	4.2	8.5	2.1	7.2	0.6	0.8	4.0	8.6	2.1	7.5	1.9	0.9	3.5	4.3	1.7	5.5
75	1	1.7	1.5	1.6	3.5	1.8	5.7	1.6	1.5	1.7	3.5	1.8	6.0	1.9	2.1	3.1	8.2	2.5	10.5
76	1	1.9	1.6	1.4	3.6	1.9	6.1	1.8	1.5	1.5	4.1	1.8	6.5	2.8	2.7	3.1	9.1	2.7	11.7
77	1	1.1	0.7	2.1	4.5	1.4	4.7	1.1	0.7	1.9	4.1	1.3	4.5	2.8	0.8	2.4	10.1	3.0	15.6
78	1	0.8	1.0	0.7	3.2	0.8	3.2	0.7	1.0	0.8	2.7	0.8	2.5	1.6	2.4	2.8	4.4	2.5	4.9
79	2	2.3	2.3	3.2	6.8	4.4	6.5	2.4	2.5	3.5	6.9	4.4	7.9	3.0	3.2	6.2	10.9	6.1	15.0
80	1	1.7	1.0	1.4	6.4	2.1	5.4	1.4	0.8	1.0	4.4	1.8	3.2	4.6	1.1	8.3	12.5	5.4	13.5
81	1	1.6	1.0	0.9	4.5	1.9	3.8	1.6	0.9	0.8	4.9	1.8	4.6	2.3	1.3	2.8	9.8	3.8	9.8
82	1	1.7	1.1	1.2	6.1	1.9	6.1	1.6	0.9	0.5	4.9	1.6	5.3	2.4	1.1	3.7	10.5	4.0	8.8
83	2	2.3	1.2	5.7	9.9	1.8	8.7	3.1	1.4	4.6	13.4	1.9	20.6	37.1	7.2	48.9	17.7	7.8	22.8
84	1	1.2	1.7	0.9	7.9	1.8	7.6	1.3	1.7	0.9	7.5	1.9	7.1	1.4	2.1	2.5	6.0	1.9	7.3
85	3	19.4	5.9	6.3	8.0	5.3	12.5	18.0	2.1	4.5	6.5	3.2	8.4	14.5	3.9	10.1	9.1	6.1	14.6
86	1	2.8	0.9	1.9	4.9	2.1	5.2	2.9	0.9	1.7	5.3	2.1	5.7	5.2	2.4	5.1	9.9	4.5	13.8
87	2	1.0	0.9	4.5	7.8	2.4	6.3	0.7	0.8	4.1	7.8	2.1	6.6	1.4	0.6	3.8	5.6	1.8	4.3
88	1	2.0	1.5	2.5	8.4	2.3	8.3	1.8	1.3	2.6	9.0	2.2	9.5	1.9	1.4	2.7	10.6	2.9	13.7
89	1	2.5	1.7	1.4	6.3	2.1	7.6	2.5	1.8	1.5	7.0	2.2	8.6	4.2	4.2	3.6	13.8	4.9	19.3
90	1	2.7	1.7	1.6	5.9	2.9	6.1	2.6	1.7	1.6	5.4	2.9	7.3	4.0	1.9	5.5	8.8	3.9	9.4
91	1	2.5	2.4	2.5	5.6	2.3	4.6	2.4	2.3	2.4	5.7	2.4	4.7	4.1	2.7	7.3	8.5	3.9	6.5
92	2	1.5	1.1	1.4	7.3	2.8	4.8	1.7	1.3	1.5	7.0	2.9	6.8	6.4	2.2	14.3	17.2	7.6	16.9
93	1	0.8	0.9	2.7	5.7	1.5	4.5	0.8	0.9	2.7	6.3	1.6	5.1	2.2	1.3	3.3	4.9	1.9	4.6
94	2	2.1	1.3	1.1	4.3	2.0	4.9	2.0	1.4	1.3	3.6	2.1	4.9	4.2	1.6	6.6	4.8	2.8	3.6
95	1	2.0	1.6	2.8	7.8	3.9	5.9	1.8	1.6	2.7	7.5	3.7	5.5	4.5	2.6	7.1	8.5	5.3	6.6
96	1	1.0	1.6	2.9	5.7	1.4	5.9	0.8	1.3	2.7	6.0	1.4	5.3	1.3	1.2	7.5	2.3	1.0	2.2
97	1	1.2	1.0	3.2	8.0	1.8	7.5	1.2	0.9	3.2	8.9	1.9	8.5	2.5	1.3	2.9	8.3	2.4	9.9
98	1	1.1	0.5	2.8	5.4	1.6	4.4	1.1	0.4	2.6	5.8	1.7	4.7	1.5	0.4	2.3	4.3	1.2	5.1
99	1	2.7	1.8	1.9	8.4	2.6	10.4	2.7	1.8	1.9	9.1	2.7	11.0	3.3	2.2	2.2	9.6	3.5	15.4
100	1	1.1	0.6	2.8	5.8	1.9	6.6	1.1	0.7	2.8	6.1	2.0	7.5	1.9	0.6	2.3	8.0	2.4	10.9
101	2	1.4	4.3	7.1	10.3	3.7	7.3	1.4	4.4	7.7	10.6	3.8	8.4	3.1	0.6	7.2	6.6	2.3	7.9

continued on next page

continuation of Table C.6

102	3	7.3	1.8	9.0	15.0	5.7	17.5	32.0	8.0	16.4	18.4	7.6	21.0	17.7	9.1	12.9	15.4	7.1	19.4
103	3	1.7	1.6	2.2	4.8	2.3	7.8	1.7	1.5	2.2	5.9	2.3	8.3	1.9	1.8	2.9	8.8	2.8	12.6
104	2	3.1	6.0	10.1	18.8	4.9	18.2	6.8	1.6	11.9	17.9	4.8	15.2	4.2	1.7	3.8	10.7	4.1	17.6
105	1	2.2	1.7	1.8	7.6	2.3	8.3	2.2	1.8	2.0	9.0	2.6	8.9	2.7	2.1	2.1	7.1	3.1	13.3
106	1	1.1	0.9	3.0	6.1	1.7	5.8	1.2	0.9	3.2	6.1	1.8	5.9	1.6	1.3	3.7	4.1	0.9	4.8
107	1	1.1	0.9	2.7	5.7	1.7	5.7	1.2	1.0	3.0	5.0	1.8	6.3	1.5	1.3	3.4	3.9	0.9	4.5
108	1	2.2	2.0	2.6	5.9	2.6	7.5	2.3	2.1	3.1	6.0	2.7	8.1	2.9	3.8	7.7	6.5	4.2	9.4
109	1	2.5	1.8	2.1	5.3	2.1	6.3	2.4	1.7	2.2	4.9	2.1	6.2	2.8	1.9	2.8	5.3	1.7	6.4
110	2	4.5	2.0	1.5	4.1	2.5	4.2	4.4	1.9	1.6	4.4	2.6	4.3	5.3	3.2	1.3	6.3	2.1	12.0
111	3	5.1	2.7	2.6	11.3	5.1	9.2	5.2	2.7	2.8	11.6	5.2	9.8	7.2	3.7	2.6	12.6	5.4	12.7
112	1	2.0	0.8	0.9	3.1	1.5	3.4	2.3	0.9	1.0	3.2	1.6	3.7	2.7	1.6	2.4	4.3	1.8	6.8

## C.9 Source parameters determined by means of MTINVERS

The Program MTINVERS by T. Dahm and F. Krüger is used (see also Section 3) to validate source parameters retrieved in Section 5 for events in West Bohemia. The program is well tested and has found a wide range of applications (*Dahm et al.*, 1999, 2000; *Krüger and Dahm*, 2002; *Bruhn*, 2003, see also Section 3). Because inversions are performed in an iterative scheme, many starting models are utilised and a large number of solutions are obtained. For roughness in the misfit function, different results may similarly fit the observations. Such results show similar residuals.

The velocity model used to compute the Green's functions for the events in West Bohemia consists of layers with constant velocities. It is adapted from the inhomogeneous anisotropic model I in Section B.4 (see Tab. C.7). To retrieve the six moment-tensor elements, the spectra of observed P and/or S waves were fitted here. During inversion of P and S waves, S waves are down-weighted. A time window of 0.5 is defined around the wave trains to compute the amplitude spectra. Frequencies in the range  $1 \text{ Hz} \leq f \leq 10 \text{ Hz}$  are used during inversion.

Table C.7: P- ( $v_p$ ) and S-wave ( $v_s$ ) velocity as functions of depth. The structure is described by a model of layers with constant velocities. The given velocities represent top-side velocities.

depth [km]	$v_p$ [m/s]	$v_s$ [m/s]
0.000	4535	2648
0.410	5590	3365
2.460	5956	3575
8.410	6156	3608
11.000	6652	3866

Although many other events were processed in this way, examples are given for events 17 (see Sec. 5.5.1) and 59 (see Sec. 4) in Tab. C.2.

Using only the vertical components of P waves during source retrieval for event 17, different solutions with similar residuals are found (see Fig. C.20). The solutions in Sec. 5 are not contained in the best-fitting inversion results. The great scatter of solutions indicates complicated misfit function. When using results from Sec. 5 as a starting model, fault-planes are rotated. However, the spectra of synthetic waveforms corresponding to solutions in Sec. 5 are also able to well-fit observed spectra. Additionally using the transverse components of S waves leads to a reduction in non-uniqueness (see Fig. C.20). The solution that is similar to results in Sec. 5 contains large non-DC components of about 50%. The interpretation of the volumetric components obtained from combined inversion of P and S waves may be difficult because no S waves are radiated from explosion-type source in isotropic media (*Julian et al.*, 1998).

For event 59 source-plane solutions found in Section 5 and from inversion using MTINVERS are similar (see Fig. C.21). However, larger non-double-couple moment-tensor components were found from inversion of P waves. When additionally using S waves they even appear enlarged.

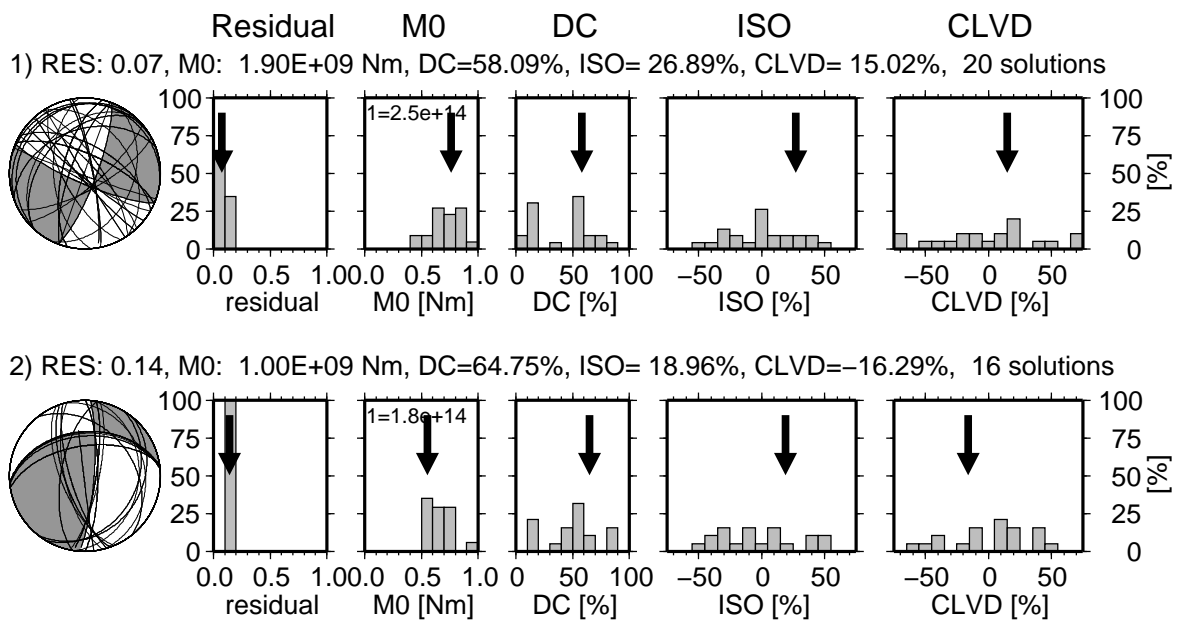


Figure C.20: Source parameters for event 17 (source time: September 4, 2000, 01:18:06) in Tab. C.2 using MTINVERS and the isotropic velocity model in Tab. C.7. All fault-plane solutions and the distribution of correspondig moment-tensor components are given for results with residuals  $\leq 0.2$ . 1) For inversion the vertical components of the P waves are used. Grey-shaded double-couple solutions and arrows depict radiation patterns and quantities, double-couple respectively, that the have smallest residual. 2) For inversion the vertical components of the P waves and the transvers components of the S waves are used. Grey-shaded double-couple solutions and arrows depict double-couple radiation patterns and quantities, respectively, for the solution that is similar to solutions for event 17 in Section 5, Fig. 5.11. Numerical values above the diagrams represent the highlighted solutions.

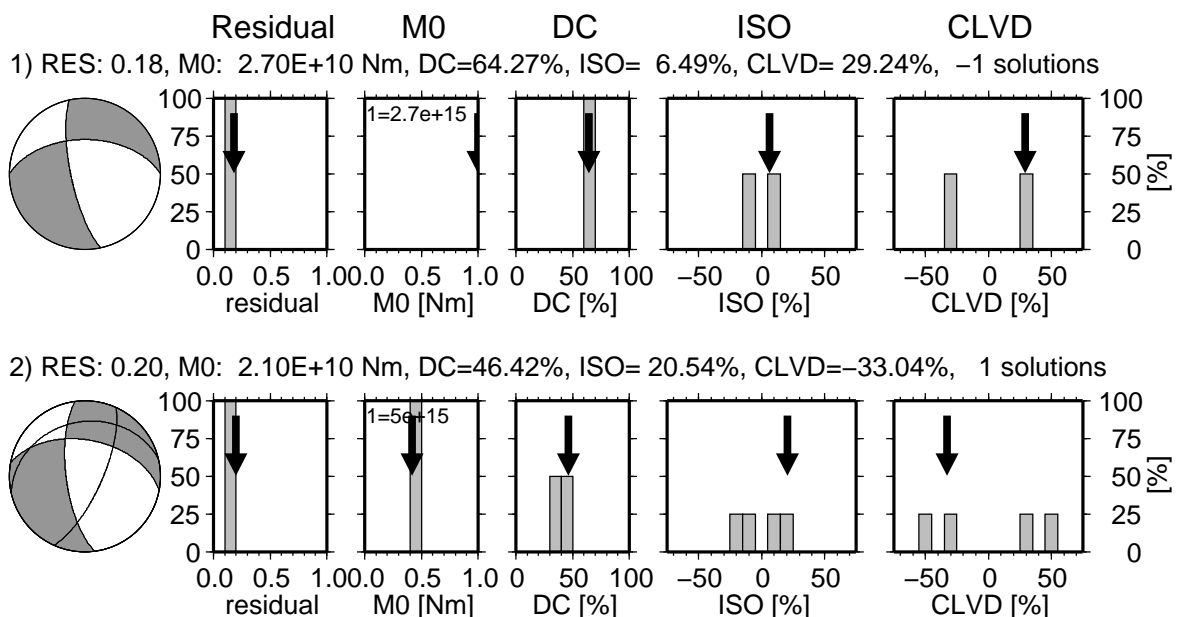


Figure C.21: As in Fig. C.20 but for event 59 (source time: October 15, 2000, 16:36:48) and solutions with residuals  $\leq 0.15$ .



**C.10 Principle stress axes in West Bohemia for models I, II, and III**

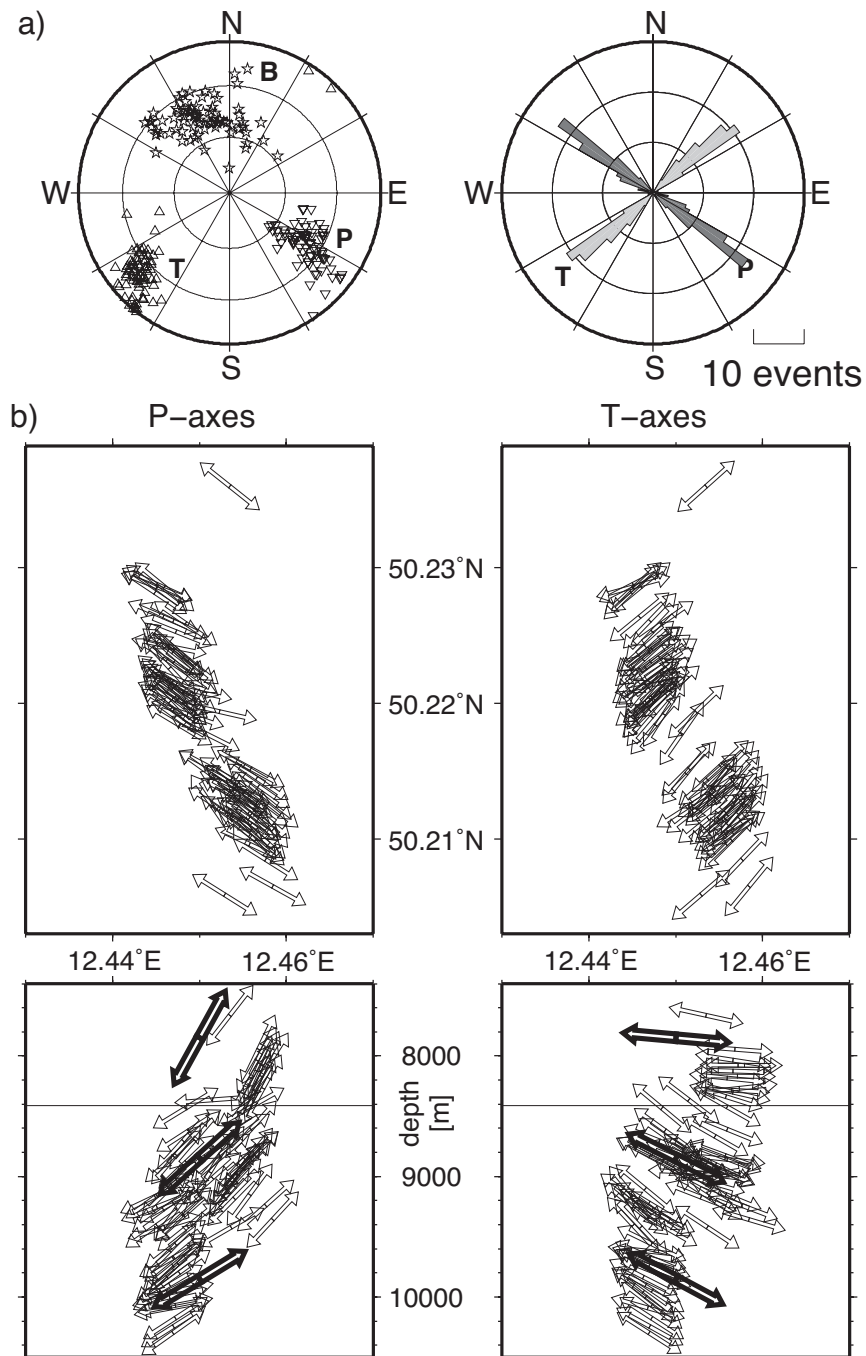


Figure C.22: Principle directions of the stress field (P, B, and T axes) obtained for events with confidence class 1 in Tab. C.2 using velocity model I (see also Section 5.6). a) Directions of P, B, and T axes in lower hemisphere projection (left) and rose histogram of the strike directions of the P and T axes (right). b) Projection of the P and T axes on the surface and on a vertical section in E-W direction. Centres of arrows are at source position. Enlarged arrows represent mean values for depth intervals of 1000 m. The internal layer boundary of model I and II at 8.41 km depth is indicated. Note stability of the strike directions and variability of the plunge with depth. Compare Figs. C.23 and C.24 for results using model II and III respectively. See Appendix B.4 for model specifications.

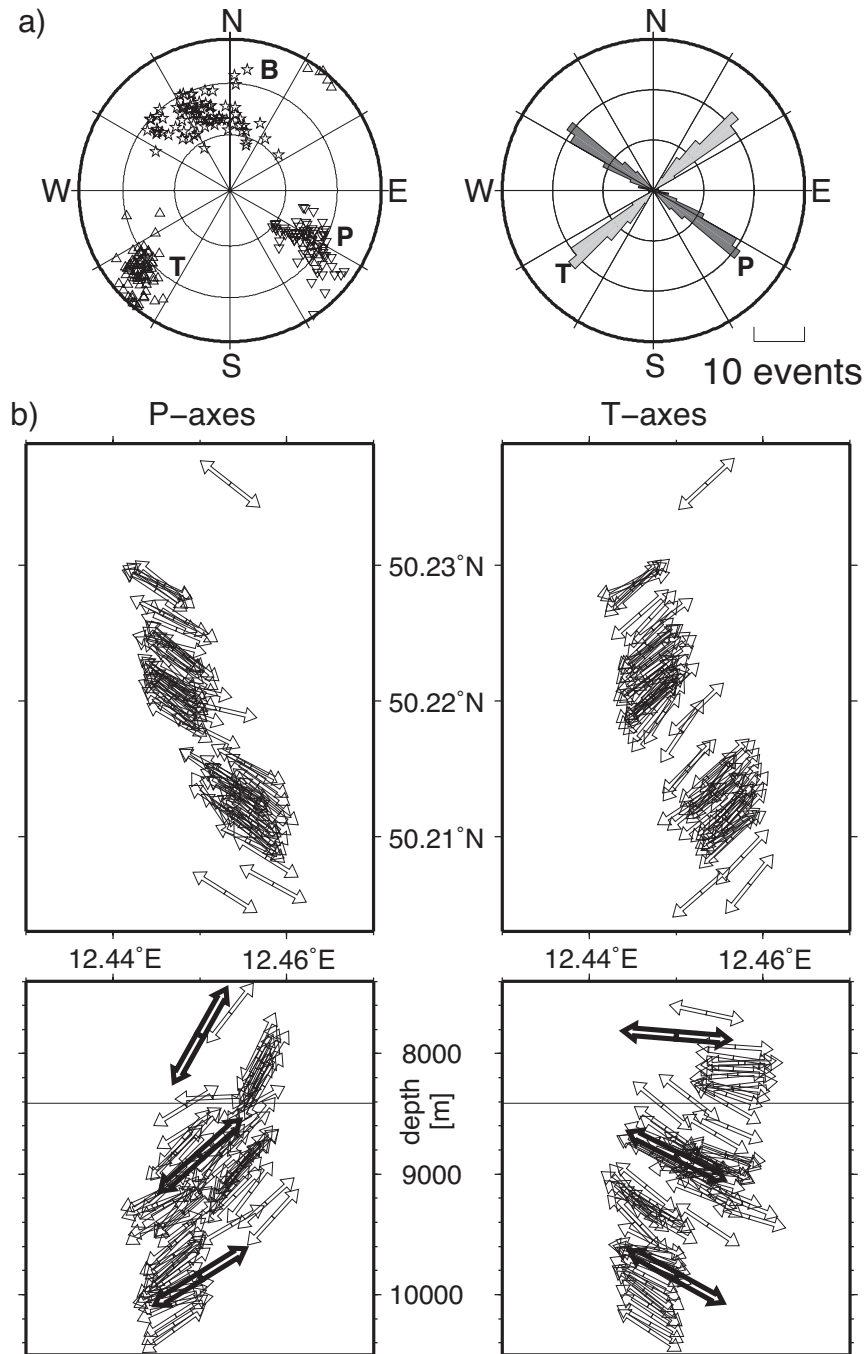


Figure C.23: As in Fig. C.22 but for stress directions obtained using model II. See Appendix B.4 for model specifications.

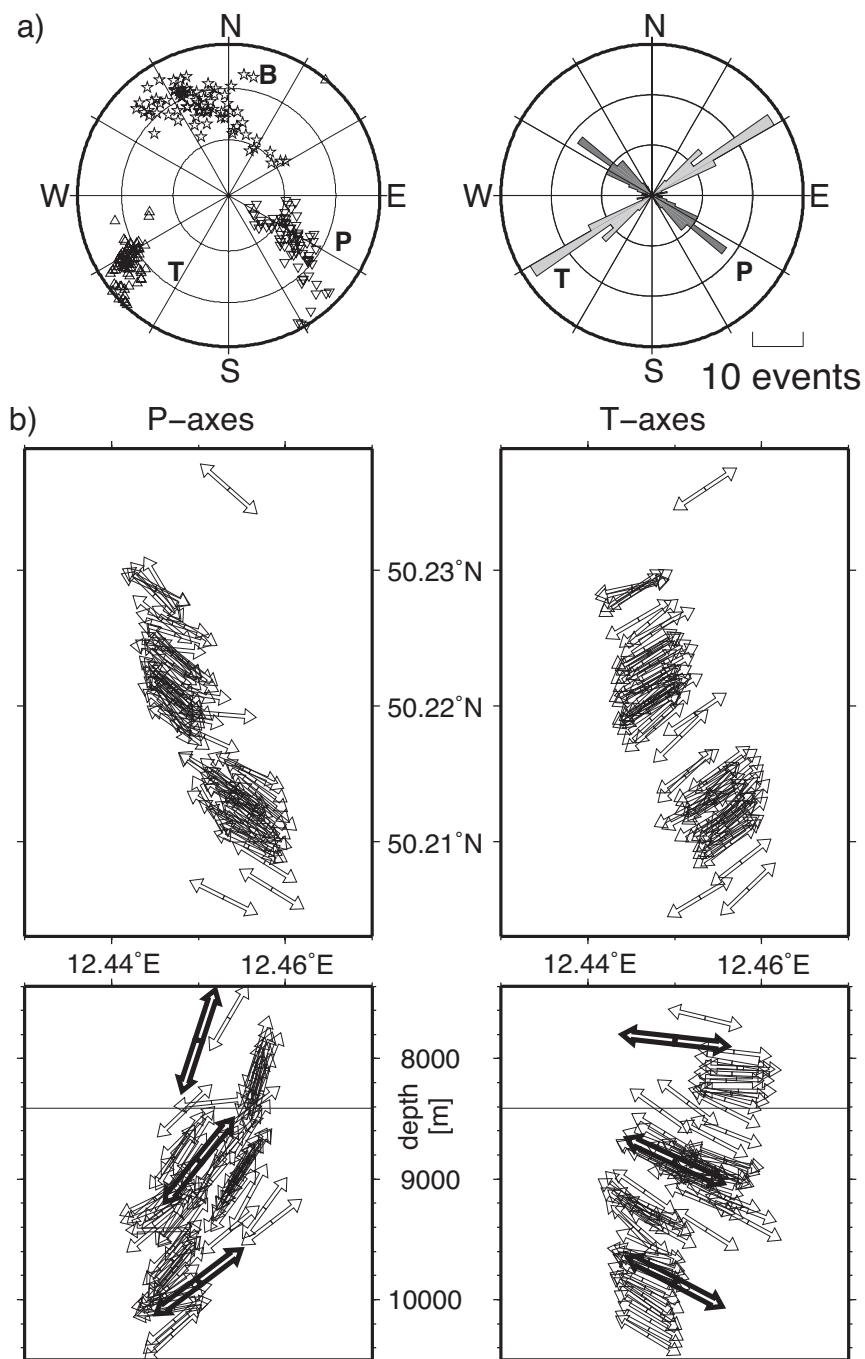


Figure C.24: As in Figs. C.23 and C.22 but for stress directions obtained using model III. See Appendix B.5 for model specifications.

## Curriculum Vitae

- 2003 to date Scientist and PhD student at the University of Potsdam, FR Germany
- 2005 MAGMA research stipend at the Charles University of Prague and the Geophysical Institute of the Academy of Sciences of the Czech Republic
- 2002 DAAD graduate stipend at the Charles University, Prague, Czech Republic
- 2002 Scientific co-worker at the University of Leipzig, FR Germany
- 2002 Diploma degree in geophysics, University of Leipzig, FR Germany
- 1996-2002 Studies in geophysics, University of Leipzig, FR Germany
- 1999-2000 Erasmus undergraduate stipend, University of Leeds, U.K.
- 1998 Pre-diploma in geophysics, University of Leipzig, FR Germany
- 1996 Nurse assistant at the infirmary Hôpital Français de Saint Louis, Jerusalem, Israel
- 1996 Nurse assistant at the infirmary R.-Koch Klinik, Leipzig, FR Germany
- 1994-1995 Civilian service (in lieu of army) at the infirmary R.-Koch Klinik, Leipzig, FR Germany
- 1994 Abitur, A.-Ph.-Reclam Gymnasium, Leipzig, FR Germany
- May 28, 1976 Born in Leipzig, GDR